

# **The Aerosol Limb Imager: Limb Scattered Polarized Radiance Images Using an Acousto-Optic Filter for Stratospheric Aerosol Profiling from a Stratospheric Balloon**

A Thesis Submitted to the  
College of Graduate Studies and Research  
In Partial Fulfillment of the Requirements  
for the Degree of Doctor of Philosophy

In the Department of Physics and Engineering Physics  
University of Saskatchewan  
Saskatoon

By

Brenden J. Elash

© Copyright Brenden John Elash, July, 2016. All rights reserved.

### **Permission to Use**

In presenting this thesis in partial fulfilment of the requirements for a Postgraduate degree from the University of Saskatchewan, I agree that the Libraries of this University may make it freely available for inspection. I further agree that permission for copying of this thesis in any manner, in whole or in part, for scholarly purposes may be granted by the professor or professors who supervised my thesis work or, in their absence, by the Head of the Department or the Dean of the College in which my thesis work was done. It is understood that any copying or publication or use of this thesis or parts thereof for financial gain shall not be allowed without my written permission. It is also understood that due recognition shall be given to me and to the University of Saskatchewan in any scholarly use which may be made of any material in my thesis.

Requests for permission to copy or to make other use of material in this thesis in whole or part should be addressed to:

Head of the Department of Physics and Engineering Physics

University of Saskatchewan

Saskatoon, Saskatchewan S7N 5E2

## ABSTRACT

Stratospheric aerosol has been measured extensively from satellite platforms over the past three decades and is an important factor in the climate change discussion. Instruments capable of measuring vertically resolved aerosol extinction profiles are in decline with few future endeavours, if any, are planned to fill the hole left by the loss of current instruments. The Aerosol Limb Imager (ALI) is an optical remote sensing instrument designed to image scattered solar irradiance from the atmospheric limb. These measurements are used to retrieve spatially resolved information of the stratospheric aerosol distribution, including spectral extinction coefficient and particle size. Here we present the design, development and test results of an ALI prototype. The instrument design uses a large aperture Acousto-Optic Tunable Filter (AOTF) to image the sunlit stratospheric limb in a selectable narrow wavelength band ranging from the visible to the near infrared. Additionally, through the nature of the AOTF, ALI is a polarized instrument recording the polarized limb radiance which is a relatively new concept as current techniques measure the total radiance. A study to address if there are any major advantages or concerns in measuring the linear polarization for aerosol is also addressed within this work.

The long term goal of this work is the eventual realization of ALI on a satellite platform in low earth orbit, where it can provide high spatial resolution observations, both in the vertical and cross-track dimensions. The ALI prototype was tested on a stratospheric balloon flight from the Canadian Space Agency (CSA) launch facility in Timmins, Canada, in September 2014. Preliminary analysis of the hyperspectral images indicate that the radiance measurements are of high quality, and we have used these to retrieve vertical profiles of stratospheric aerosol extinction coefficient from 650–950 nm, along with one moment of the particle size distribution.

## ACKNOWLEDGMENTS

The work presented here would not be possible with the contributions of many individuals and organizations. Without these individuals and organizations I would not have been able to partake in this education journey through optics and atmospheric science. I would like to thank the Institute for Space and Atmospheric Studies, the University of Saskatchewan, the Natural Sciences and Engineering Research Council, the Centre National d'Etudes Spatiales, and the Canadian Space Agency for their financial support.

Members of my research team have been monumental to assisting in the completion of this project. Thanks to Paul Loewen for building and testing the electronics for ALI; Seth Dueck creating the polarized version of SASKTRAN-HR as well as the guidance given using the polarized model; Landon Rieger for help and advice in using the retrieval package; Dr. Nick Lloyd for his assistance in the designing and testing of the flight software; and Dr. Douglas Degenstein for overall advice and knowledge during the project.

To my supervisor, Dr. Adam Bourassa, I would extend a sincere thanks for the wonderful opportunity to work alongside him in this endeavor. Without his guidance, knowledge, and enthusiasm this project would not be what it became.

Finally, I would like to thanks my family and friends for their support throughout this work

*To my family: Johanna, Amy, Kaitlyn, and Chris*

## TABLE OF CONTENTS

	<u>page</u>
<b>ABSTRACT.....</b>	<b>iii</b>
<b>ACKNOWLEDGMENTS .....</b>	<b>iv</b>
<b>LIST OF TABLES .....</b>	<b>x</b>
<b>LIST OF FIGURES .....</b>	<b>xi</b>
<b>LIST OF ABBREVIATIONS .....</b>	<b>xix</b>
<b>1 INTRODUCTION.....</b>	<b>1</b>
<b>2 BACKGROUND .....</b>	<b>5</b>
2.1 Introduction.....	5
2.2 Stratospheric Aerosol.....	8
2.2.1 Aerosol Sources .....	9
2.2.2 Aerosol Microphysics .....	10
2.2.3 Climate Effects.....	12
2.3 Aerosol Measurements.....	14
2.3.1 In-situ-Based Measurements .....	14
2.3.2 Occultation .....	15
2.3.3 Lidar .....	17
2.3.4 Limb Scatter .....	18
2.4 Radiative Transfer.....	21
2.4.1 Scalar Radiative Transfer .....	21
2.4.2 Vector Radiative Transfer .....	25
2.4.3 Rayleigh Scattering .....	27
2.4.4 Mie Scattering .....	27
2.4.5 SASKTRAN Radiative Transfer Model .....	30
2.5 Inversion Techniques .....	31
2.6.1 Optimal Estimation .....	32
2.6.2 Levenberg-Marquardt .....	33
2.6.3 Multiplicative Algebraic Reconstruction Technique .....	33
2.6 ALI Prototype Instrument and Stratospheric Balloon Flight.....	34
2.6.1 ALI Specifications .....	34
2.6.2 ALI Instrument Design Process Overview .....	36
<b>3 INSTRUMENT DESIGN.....</b>	<b>38</b>
3.1 Introduction.....	38
3.2 AOTF Theory and Background .....	38
3.2.1 Solution to the Acoustic Equation .....	39
3.2.2 Diffraction Efficiency .....	44
3.2.3 Diffraction Angle .....	45

3.2.4 Tuning Curve .....	48
3.3 Optical Chain Development.....	50
3.3.1 AOTF Operation .....	51
3.3.2 Telecentric System Prototype .....	53
3.3.3 Telescopic System Prototype .....	60
3.3.4 ALI Optical Design .....	65
3.3.5 Correction to the Optical Design.....	70
3.4 Opto-Mechanical Design and Thermal Balancing.....	71
3.4.1 Opto-Mechanical Design .....	72
3.4.2 Baffle Design .....	77
3.4.3 Light Tight Case.....	82
3.4.4 Thermal Considerations .....	83
<b>4 CALIBRATIONS AND CONTROL SOFTWARE .....</b>	<b>85</b>
4.1 Introduction.....	85
4.2 Control Software .....	85
4.3 AOTF Calibration .....	89
4.3.1 Tuning Curve Analysis .....	89
4.3.2 Point Spread Function .....	93
4.3.3 Diffraction Efficiency .....	94
4.4 ALI Calibrations and System Test.....	95
4.4.1 Exposure Time Determination .....	95
4.4.2 DC Offset Removal.....	97
4.4.3 Dark Current Correction .....	98
4.4.4 Stray Light Calibration.....	99
4.4.5 Relative Flat-Fielding Correction .....	101
4.5 Integrated Testing .....	104
<b>5 STRATOSPHERIC BALLOON FLIGHT AND AEROSOL RETRIEVALS .....</b>	<b>106</b>
5.1 Stratospheric Balloon Flight .....	106
5.1.1 Preflight Preparations.....	106
5.1.2 Balloon Flight .....	110
5.2 Limb Measurements.....	113
5.3 Aerosol Retrievals.....	119
5.3.1 Aerosol Extinction Retrieval Methodology .....	120
5.3.2 Particle Size Retrieval Methodology .....	124
5.3.3 Aerosol Extinction Retrievals .....	128
5.3.4 A Sample Particle Size Retrieval .....	133
5.4 Results and Future Improvements .....	134
<b>6 THE SENSITIVITY TO POLARIZATION IN STRATOSPHERIC AEROSOL RETRIEVALS FROM LIMB SCATTERED MEASUREMENTS .....</b>	<b>137</b>
6.1 Introduction.....	137
6.2 Background and Forward Model .....	138

6.2.1 Polarized Scattered Sunlight and Stratospheric Aerosols .....	138
6.2.2 SASKTRAN-HR Model .....	143
6.2.3 Model Scenarios.....	144
6.3 Methodology .....	146
6.4 Analysis.....	150
6.4.1 Difference in Scalar Retrievals using a Scalar or Vector Model .....	150
6.4.2 Fraction of Limb Signal due to Aerosol.....	152
6.4.3 Potential for Retrieval Bias .....	157
6.4.4 Precision Analysis.....	159
6.5 Conclusions.....	164
<b>7 CONCLUSION .....</b>	<b>166</b>
<b>LIST OF REFERENCES.....</b>	<b>170</b>
<b>A ALI HARDWARE COMPONENTS.....</b>	<b>183</b>
A.1 Optical Components.....	183
A.1.1 Optical Lenses .....	183
A.1.2 Polarizers.....	183
A.1.3 AOTF .....	184
A.2 Opto-Mechanical and Electrical Components .....	185
A.2.1 RF Driver .....	185
A.2.2 QSI CCD Camera.....	185
A.2.3 OCELOT Computer .....	185
A.2.4 Opto-Mechanical Pieces.....	186
<b>B ALI SOFTWARE COMMANDS .....</b>	<b>187</b>
B.1 List of Commands for ALI Software .....	187
B.1.1 EnableScience.....	188
B.1.2 DisableScience .....	188
B.1.3 EnableRF .....	188
B.1.4 DisableRF .....	189
B.1.5 EnableAutoSendStats .....	189
B.1.6 DisableAutoSendStats .....	189
B.1.7 SetScienceMode .....	189
B.1.8 ReloadConfig.....	190
B.1.9 LdCusCnf .....	190
B.1.10 LdCusExp.....	190
B.1.11 GetFile .....	191
B.1.12 EndCurrentScienceCycle.....	191
B.1.13 SetExposureScaleFactor .....	191
B.1.14 UpdateExposureTimeCurve .....	191
B.1.15 EnableCheckRfTemps.....	192
B.1.16 DisableCheckRfTemps.....	192
B.1.17 ResetHousekeeping .....	192

B.1.18 DumpConfig .....	192
B.1.19 SetBitsPerSecond .....	192
B.1.20 EnableAutomation .....	193
B.1.21 DisableAutomation .....	193
B.1.22 SetAutomationTimeout .....	193
B.1.23 EnableGps .....	193
B.1.24 DisableGps .....	193
B.1.25 EnablePulse .....	193
B.1.26 DisablePulse .....	193
B.2 List of ALI Science Modes .....	194
B.2.1 Invalid Mode .....	194
B.2.2 Calibration Mode .....	194
B.2.3 Aerosol Mode .....	195
B.2.4 H <sub>2</sub> O Mode .....	195
B.2.5 O <sub>2</sub> Mode .....	196
B.2.6 Custom Mode .....	197
B.2.7 Aerosol Constant Exposure Time Mode .....	197
B.3 List of ALI Exposure Modes .....	197
B.3.1 Invalid Mode .....	197
B.3.2 Calibrated Exposure Mode .....	198
B.3.3 Custom Exposure Mode .....	198

## LIST OF TABLES

<u>Table</u>	<u>page</u>
<b>Table 3-1:</b> Telecentric Test System Optical specifications .....	55
<b>Table 3-2:</b> Telescopic Prototype System Optical Parameters .....	61
<b>Table 3-3:</b> Final ALI optical specifications.....	68
<b>Table 3-4:</b> Revised ALI optical specifications .....	71
<b>Table 4-1:</b> Location of ALI temperature sensors. ....	88
<b>Table 4-2:</b> Estimated balloon flight exposure times. ....	97
<b>Table 6-1:</b> Different particle size distributions used to test the sensitivity of the aerosol retrieval. ....	145
<b>Table 6-2:</b> The SSA dependence of the normalized co-variance for the horizontal and vertical polarization retrievals. The given numbers are the mean with the standard deviation for each geometry across all wavelengths. Note that the SSA of 90° for the vertical polarization has been removed due to the poor signal in this region.....	162
<b>Table A-1:</b> Lens used in ALI and their specifications. ....	183
<b>Table A-2:</b> AOTF Specifications. ....	184
<b>Table A-3:</b> QSI CCD camera specifications. ....	185
<b>Table A-4:</b> Opto-mechanical components used in ALI .....	186
<b>Table B-1:</b> ALI operational science modes.....	194
<b>Table B-2:</b> ALI calibration science mode specifications. ....	195
<b>Table B-3:</b> ALI aerosol science mode specifications.....	195
<b>Table B-4:</b> ALI H <sub>2</sub> O science mode specifications. ....	196
<b>Table B-5:</b> ALI O <sub>2</sub> science mode specifications.....	196
<b>Table B-6:</b> ALI operational exposure time modes.....	197

## LIST OF FIGURES

<u>Figure</u>	<u>page</u>
<b>Figure 2-1:</b> Sample log-normal distribution for typical non-volcanic stratospheric aerosol .....	11
<b>Figure 2-2:</b> Bimodal particle size distributions fits from OPC. (a) Distributions from a volcanic period after the Mount Pinatubo eruption recorded in 1993. (b) Distributions from a background aerosol period recorded in 1999. Both of the aerosol distribution measurement are from 20 km altitude with the solid line being the fine mode and the dashed line is the coarse mode. Figure is recreated from Figure 5 of <i>Deshler et al.</i> (2003). .....	12
<b>Figure 2-3:</b> An occultation instrument monitoring the atmosphere by scanning the atmosphere by looking directly at the sun. ....	16
<b>Figure 2-4:</b> Lidar instrument showing a measurements in both the nadir and off-nadir lines of sight.....	18
<b>Figure 2-5:</b> Limb scattering geometry measurement for an instrument where single and multiple scattering events occur.....	19
<b>Figure 2-6:</b> (a) Change in scattering cross section for Rayleigh and Mie scattering over wavelength. The Mie scattering uses a log-normal distribution with a mode width of 1.6 and a mode radius of 0.08 $\mu\text{m}$ . (b) The first term of scattering matrix, $P_{11}(\Theta)$ , for Rayleigh and Mie scattering across scattering angle.....	30
<b>Figure 3-1:</b> Geometry for the AOTF wave derivation assuming the acousto wave is along the x-axis and the AO interaction occurs along the z axis over an interaction length, $L$ . The parameters $ri$ , $ki$ , and $\theta i$ are the position vector, wave vector, and angle of the incident electric field and similarly for the diffracted electric field. Figure recreated from <i>Xu and Stroud</i> (1992).....	41
<b>Figure 3-2:</b> A standard non-collinear AOTF experiential set up. The crystal is assumed to infinitely long in the y direction. Figure recreated after <i>Guenther</i> (1990) number 14B-1.....	47
<b>Figure 3-3:</b> General Layout of an AOTF. A randomly polarized incoming light source hits the front surface of the birefringent crystal. The black bar below the crystal is the piezoelectric transducer that produces the RF signal and forms the acousto wave represented by the grey arrow. The momentum matching Bragg diffraction occurs and monochromatic polarized light (-1 order) exits the AOTF at a constant angle with the 0th order and +1 order being blocked by an optical stop.....	48
<b>Figure 3-4:</b> The wave vectors generated by the AOTF experiment set up in Figure 3-2. From the above figure $ke$ and $ko$ are the wave vectors of the extraordinary and	

ordinary axis of the AOTF crystal. Originally published as Figure 1 in *Elash et al.* (2016) ..... 49

**Figure 3-5:** (a) An AOTF undergoing Bragg diffraction with an unpolarized input incident wave with a RF wave applied represented by the arrow. After the diffraction event four output signals are formed: the zeroth order and first order ordinary (o) and extraordinary (e) signals. However the only optical path that remains at a constant angle no matter the applied RF wavelength is the first order extraordinary diffracted signal. (b) Two linear polarizers are added to the system, the first linear polarizer removes the ordinary polarization from the outputs with the dotted lines and the second linear polarizer removes undiffracted extraordinary light shown by the dashed line. This configuration is the “AOTF-on” state. (c) The system in (b) without a RF wave so no Bragg diffraction is occurring. Once again the first linear polarizer removes the ordinary polarization represented by the dotted line and the second linear polarizer removes the extraordinary light shown by the dashed line. This configuration is the “AOTF-off” state. Originally published as Figure 2 in *Elash et al.* (2016) ..... 52

**Figure 3-6:** A standard paraxial ray tracing diagram. The aperture is located to make the system telecentric in the image plane and  $f$  is the focal length of the lens. ..... 53

**Figure 3-7:** Ray Tracing diagram simulation of the telecentric lens system preformed using Code V. The elements in the system are the following: (1) Optical Stop and telecentric aperture. (2) 100 mm focal length plano-convex lens. (3) Brimrose AOTF. (4) 100 mm focal length plano-convex lens. (5) Telecentric Aperture. (6) 75.6 mm focal length plano-convex lens. (7) Imaging plane. It should be noted that the x and y scales are not the same in this image. Also, in the lab a polarizer is added in front and behind the AOTF as well as prisms after the AOTF..... 54

**Figure 3-8:** Quantum efficiency of the Kodak KAF-1603ME contained within the QSI CCD camera is represented by blue curve. Quantum efficiency provided by QSI Scientific. ..... 56

**Figure 3-9:** The effect on the optical path of converging light bundles as they pass through a material of index of refraction  $n(\lambda)$ . When the index of refraction strongly depends on wavelength, as in the AOTF, the optical path length can experience great changes that alters the focal point of the system..... 56

**Figure 3-10:** Code V simulation of the spot size for the telecentric system at focus at 800 nm. The spots are shown for 0.0, 1.5 and 2.6 degree fields of view at 600 nm (blue) and 800 nm (green). The full spot sizes for the 600 nm spots are 0.16, 0.22, and 0.25 mm for 0.0, 1.5, and 2.6 degrees fields respectively, with the corresponding 800 nm spot sizes being 0.024, 0.053, 0.094 mm. The black circles represent the Airy disk for each specific wavelength and FOV. ..... 58

<b>Figure 3-11:</b> The top left is the original test image used for the experiment. The top right, bottom left, and bottom right are the images recorded through the telecentric system at 650, 750, and 850 nm. The system is focused at 800 nm.....	59
<b>Figure 3-12:</b> Ray Tracing diagram of the telescopic lens system simulated by Code V. The elements in the system are the following: (1) 100 mm focal length plano-convex lens. (2) Location where field stop is located to limit stray light (3) 100 mm focal length plano-convex lens. (4) Brimrose AOTF. (5) 75.6 mm focal length plano-convex lens. (6) Imaging plane. It should be noted that the x and y scales are not the same as Figure 3-7. Also, in the lab a polarizer is added in front and behind the AOTF as well as prisms behind the AOTF.....	61
<b>Figure 3-13:</b> Vertical displacement of a collimated bundle of light cause by a material of index of refraction $n(\lambda)$ .....	62
<b>Figure 3-14:</b> Code V simulation of the spot size for the telescopic system. The spots are shown for 0.0, 1.5 and 3.0° fields of view at 600 nm (blue) and 800 nm (green). The full spot sizes for the 600 nm spots are 0.004, 0.045, and 0.122 mm for 0.0, 1.5, and 3.0° fields respectively, with the corresponding 800 nm spot sizes being 0.096, 0.081, 0.047 mm. The black circles represent the Airy disk for 600 nm wavelength and each FOV.....	63
<b>Figure 3-15:</b> The top left is the original test image used for the experiment. The top right, bottom left, and bottom right are the images recorded through the telescopic system at 650, 750, and 850 nm. The system is focused at 800 nm.....	64
<b>Figure 3-16:</b> Final optical design for ALI with a Code V ray tracing diagram. The elements in the system are: (1) 150 mm focal length plano-convex lens. (2) Field stop. (3) 100 mm focal length plano-convex lens. (4) Vertical (extraordinary) linear polarizer. (5) Brimrose AOTF. (6) Horizontal (ordinary) linear polarizer. (7) 50.4 mm focal length bi-convex lens. (8) Imaging plane. Originally published as Figure 4 in <i>Elash et al.</i> (2016).....	66
<b>Figure 3-17:</b> MTF analysis performed by Code V for the final ALI design used in campaign. The 7 pixel running average corresponds to a spatial frequency of 15.5 cycles/mm. ....	67
<b>Figure 3-18:</b> The final optical layout of ALI's optical chain from the top and profile perspectives with the components being the following: (1) 150 mm plano-convex lens with 25.4 mm diameter. (2) Field Stop. (3) 100 mm plano-convex lens with 50.8 mm diameter. (4) Optical rail system. (5) Vertical (extraordinary) linear polarizer. (6) Brimrose AOTF. (7) Rotation Stage. (8) Horizontal (ordinary) linear polarizer. (9) 50 mm bi-convex lens with 25.4 mm diameter. (10) QSI 616s CCD camera. (11) Optical rail. ....	73

<b>Figure 3-19:</b> The custom mounting hardware design to mount the AOTF and QSI CCD camera into ALI's opto-mechanical design. Left: Custom AOTF mounting hardware. Right: The five piece QSI CCD camera mounting hardware.	75
<b>Figure 3-20:</b> ALI opto-mechanical system with three degree horizontal tilt and designed baffle discussed in section 3.4.2. Originally published as Figure 5 in <i>Elash et al. (2016)</i> .	76
<b>Figure 3-21:</b> (a) Start of the optical baffle geometry method. The red lines are the marginal rays and the green line is the first ray that can enter the system without encountering at least three surfaces. (b) The first internal vane has been added and the location of the next vane is being determined. (c) The second internal baffle has been added and since the green line intersects with the critical baffle no more baffle are required. (d) Additional interior vanes and an external vane have been added to ensure a height to pitch ratio of 0.5 to improve the baffle's capabilities to reduce stray light.	79
<b>Figure 3-22:</b> A cross-section view of the ALI baffle system. All dimensions on the drawing are in millimeters and the sloped black lines represent the 6 degree FOV.	80
<b>Figure 3-23:</b> ALI baffle vain profile. Dimensions are in millimeters.	81
<b>Figure 3-24:</b> Final ALI optical and opto-mechanical assembly.	82
<b>Figure 3-25:</b> ALI optical system with light tight case attached. Three degree horizontal tilt not present in this image.	82
<b>Figure 4-1:</b> A complete flow diagram showing interaction between all the software modules on the on board ALI flight computer.	86
<b>Figure 4-2:</b> Telecentric test experiential setup for AOTF parameter determination. All lenses and apertures are represented by the same symbol.	90
<b>Figure 4-3:</b> (a) A row averaged image taken from the AOTF of the point spread function when the tuning frequency of the AOTF was at 124.96 MHz. (b) The FWHM for each of the determined wavelengths for the AOTF. The FWHM at 600 nm is 1.5 nm and as the wavelengths get longer the FWHM increases to 4.9 nm at 1080 nm. (c) The calibration curves for the AOTF RF versus the diffracted wavelength which contains the data points recorded and fit curves. (d) The percent error with respect to the measured frequency for the two best fit curves in the previous panel. Originally published as Figure 6 in <i>Elash et al. (2016)</i> .	92
<b>Figure 4-4:</b> Simulated scalar radiances from the SASKTRAN-HR in blue and red with the radiance on the left side and the scaling factor in black with the value on the right side.	96

<b>Figure 4-5:</b> The DC offset curve (Equation 4.5) is seen in black where the lab and flight calibration data is shown in blue. The counts on the vertical axis are the counts that need to be removed to account for the DC offset. ....	98
<b>Figure 4-6:</b> The dark current from the calibration images over a series of camera temperatures and exposure times. ....	99
<b>Figure 4-7:</b> A calibration image after stray light removal has been performed where the measured wavelength is 750 nm with a 1 second exposure time. Vignetting can be seen as moving away from center of the image. Additionally the last 1° of the horizontal FOV is on the right side is lost due to strong contamination from reflections within the system. Originally published as Figure 7 in <i>Elash et al.</i> (2016). ....	100
<b>Figure 4-8:</b> The blackbody emittance curve from Equation 4.6 normalized to 775 nm. ....	102
<b>Figure 4-9:</b> The flat fielding coefficients for 750 nm. ....	103
<b>Figure 5-1:</b> Side of the QSI CCD with the panel that contains the vacuum seal opened. The orange o-ring seen in the cavity is removed from the chamber to open the vacuum seal to the camera's CCD chip. ....	108
<b>Figure 5-2:</b> The ALI instrument is mounted on board the CARMEN-2 gondola (top shelf on the right). ALI located next to SHOW, another Canadian instrument with collaboration between ABB, York University, and the University of Saskatchewan. ALI has its red tag cover over the optical entrance to protect the instrument from dust and other contaminates. Thermal insulation has been added to the instrument and during the flight sun side is on the side of SHOW. Some of the reflective layer was blacked out to not cause additional stray light into SHOW optical path. ....	109
<b>Figure 5-3:</b> (a) The GPS data from ALI during the Nimbus 7 mission generated via Google Earth. The colour of the line represents the absolute speed of the gondola during the mission and the blue, green, red colours represent speeds of approximately 10, 70, and 140 km/h. Important landmarks are noted on the image. The end of mission represents the end of the primary aerosol mission. No GPS data was collected from ALI after power down. The location of image 208 is the red label. (b) The temperature and altitude profiles from the Nimbus 7 flight. The time of image 208 is shown by the cyan vertical line and first light measured by ALI occurs at the magenta vertical line. Originally published as Figure 8 in <i>Elash et al.</i> (2016). ....	111
<b>Figure 5-4:</b> During the flight the calibrated exposure times was updated. The blue curve represents the exposure times from the ground calibration and the red curve is the recalibration during the flight. The black curve is the percent change in between the pre-flight calibrated results and the during flight calibration. ....	112

- Figure 5-5:** Stray light removal technique is performed using image 208 which is a 750 nm measurement. The top panel is the image after the DC offset has been removed from the measurement. The middle panel is the associated AOTF-off image and stray light features are seen in the upper right of the image as well as light being registered in the entire right side of the image. The final panel is the first panel minus the second panel and the abnormal gradient has been removed from the final image, leaving a cleaner radiance profile. ..... 115
- Figure 5-6:** (a) Final calibrated 750 nm image, taken at 13:57 UTC located at 48.55°N, 80.00°W with a SZA and SSA of 63° and 98° respectively. (b) The same 750 nm image with the mean of the profile removed from the image leaving the residual signal that shows thin clouds in the troposphere. Originally published as Figure 9 in *Elash et al.* (2016)..... 116
- Figure 5-7:** Averaged ALI relative radiance vectors from 12 of the 13 wavelengths from the Nimbus 7 flight. Each panel presents the radiance vectors from a different wavelength measured which is denoted in the top right corner. The dashed lines are radiance profiles where the SZA is greater than 90° and solid lines are profile where the SZA is less than 90°. Originally published as Figure 10 in *Elash et al.* (2016). ..... 118
- Figure 5-8:** Relative radiances spectrally from 650 nm to 950 nm as measured from ALI at approximately 14:20 UTC consisting of images number 204 to 216 looking 90° in the azimuth from the sun facing southwards. These spectral profiles are presented at several tangent altitudes with a horizontal look direction of 0°. The shading represents the error on the radiances. Originally published as Figure 11 in *Elash et al.* (2016)..... 119
- Figure 5-9:** (a) The black, blue, red curves represent the measurement vector, first term of Equation 5.6, and second term of Equation 5.6 using image 208 (b) A collection of all of the measurement vectors at 750 nm during the mission with a SZA less than 90°. (c) Image 208 measurement vector with associated error represented by the shading. ..... 121
- Figure 5-10:** Reproduced from Figure 4 of *Rieger et al.* (2014). For OSIRIS scan 6432001 aerosol measurement vectors were calculated at 22.5 km. (A) The three size distributions used in the study. (B) The measurement vectors calculated via the SASKTRAN simulation (C) The relative percent difference of the fine and representative distributions with respect to the bimodal distribution. A 1% error is the radiance yields an uncertainty in the bimodal measurement vector shown by the grey shading. ..... 125
- Figure 5-11:** Computed with the optical properties of the SASKTRAN-HR engine. This variation of the cross section with respect to the mode radius and width allows for some determination of the particle size distribution through the Angström exponent. .... 127

<b>Figure 5-12:</b> An example of three aerosol retrievals from images 206, 208, and 214, with center wavelengths of 750, 850, and 950 nm respectively are vertically displayed in the figure from top to bottom. The left column shows the measurement vector, $\mathbf{y}$ , in black with the retrieved forward model, $\mathbf{F}$ , in blue. The center column shows the ratio of the measurement vector over forward model known as $\alpha$ and is the convergence factor between the ALI measurement and the forward model. For both of the first two columns, the black line is barely visible due to the very good agreement of the forward model. The final column is ALI aerosol extinction in blue with the associated error represented by the light blue shading. ....	130
<b>Figure 5-13:</b> Left is the retrieved aerosol extinction profiles from the last complete imaging cycle consisting of images 205 to 216 from the 0.0° horizontal line-of-sight. Right is the 750 nm ALI aerosol extinction in blue with its error represented by the shading compared to the 750 nm extinction measured by OSIRIS in red with its error represented by the shading. Originally published as Figure 12 in <i>Elash et al. (2016)</i> .....	131
<b>Figure 5-14:</b> (a) Image 208 (750 nm) re-retrieved using an albedo of 0 and 1 compared to the original albedo used from OSIRIS. (b) Using the determined zenith pointing error from section 5.2, image 208 is retrieved again using the maximum possible pointing error compared to the original. ....	132
<b>Figure 5-15:</b> The left panel shows the convergence of two sample particle size retrievals, blue and red represent an initial state of 0.08 and 0.12 $\mu\text{m}$ mode radius respectively. Both initial states converge to the same value over approximately 3 iterations in the particle size retrieval method. The middle panel shows the final Angström exponents determined from images 204-216. The shading represents the error associated with the least squares fit. The right panel shows a typical least squares fit of the retrieved extinction values over wavelength to determine the Angström exponent at model altitude of 14.5 km. Originally published as Figure 13 in <i>Elash et al. (2016)</i> .....	134
<b>Figure 6-1:</b> (Top) The fraction of a linear polarization (left is horizontal and right is vertical) over the total radiance for molecular air density. (Bottom) The change in the fraction of linear polarization between an atmosphere that contains aerosol and one with only molecular air density.....	142
<b>Figure 6-2:</b> The two aerosol profiles used in this study. The blue is a background aerosol extinction levels, and the red curve is a representative aerosol profile after the Nabro eruption. ....	145
<b>Figure 6-3:</b> Percent differences between the vector retrieved aerosol extinction profiles and the scalar retrieval from simulated total radiance measurements. Each column represents a different particle size distribution (see Table 6-1). ....	151
<b>Figure 6-4:</b> (Top) For a horizontal (left) or vertical (right) linear polarization the percent of the signal that is attributed to aerosol, $\delta$ . (Bottom) The change in the fraction	

of the limb signal due to aerosol when compared to the total radiance for the horizontal (left) and vertical (right) polarization ( $\Delta\delta$ ). The simulation uses a geometry of SZA=45° and SSA=60°, with the albedo being 0 and the aerosol state the background profile with particle size distribution 1. Take note the red-blue scale is non-symmetric..... 153

**Figure 6-5:** Dependence of the fraction of the limb spectra due to aerosol on solar scattering angle (left panels) for total radiance (top), horizontal polarization (middle) and vertical polarization (bottom), and the magnitude of the radiance for each case (right panels). Note the low signal near SSA of 90 degrees for the vertical polarization which would be problematic for terminator orbits. ..... 154

**Figure 6-6:** The ratio of the linearly polarized radiance to the total radiance for horizontal (left) and vertical (right) orientations. Note that the scale for each plot is different. The simulation was performed with a SSA of 60 degrees with volcanic aerosol loading for a tangent altitude of 20 km. ..... 156

**Figure 6-7:** The mean percent difference between the retrieved aerosol extinction profile with an assumed particle size distribution and the true state corresponding to the indicated particle size distribution (see Table 6-1). Error bars represent one standard deviation of the variability across all viewing geometries. Results shown are for 750 nm and 20 km altitude. ..... 159

**Figure 6-8:** The wavelength dependence of the co-variance for the horizontal and vertical polarization retrievals normalized to the total radiance case. The faded line represent one standard deviation of the variability encountered across all input parameters. The top panel is for an instrument design and/or operation that compensates for changing signal levels with polarization and viewing geometry, and the bottom panel is for uncompensated measurements. .... 161

**Figure A-1:** The transmission and extinction ratios of the LPVIS100 used in ALI. .... 184

## LIST OF ABBREVIATIONS

ALI	Aerosol Limb Imager
ALTIUS	Atmospheric Limb Tracker for the Investigation of the Upcoming Stratosphere
AO	Acousto-Optic
AOTF	Acousto-Optical Tunable Filter
BEO	Back End Optics
CALIPSO	Cloud-Aerosol Lidar and Infrared Path_nder Satellite Observations
CATS	Cloud Aerosol Transport System
CCD	Charged-Coupled Device
CNES	Centre National d'Etudes Spatiales
CSA	Canadian Space Agency
DC	Direct Current
FEO	Front End Optics
FOV	Field of View
FWHM	Full Width Half Max
GPS	Global Positioning System
ICESat	Ice, Cloud, and land Elevation Satellite
IR	InfraRed
MART	Multiplicative Algebraic Reconstruction Technique
MTF	Modular Transfer Function
NASA	National Aeronautics and Space Administration
NIR	Near InfraRed
OMPS	Ozone Mapping and Pro_le Suite
OPC	Optical Particle Counter
OSIRIS	Optical Spectrograph and Infra-Red Imaging System
RF	Radio Frequency
SAGE	Stratospheric Aerosol and Gas Experiments
SASKTRAN-HR	SASKTRAN High Resolution
SCIAMACHY	SCanning Imaging Absorption spectroMeter for Atmospheric CHartographY
SME	Solar Mesosphere Experiment
SNR	Signal to Noise Ratio
UTLS	Upper Troposphere and Lower Stratosphere

# CHAPTER 1

## INTRODUCTION

The atmosphere of the Earth is a dynamic, evolving system dependent upon its composition. The concentration of various atmospheric species is dependent upon altitude, geographical location, season, and time of day. These species interact with the incoming sunlight to absorb, scatter, and re-emit the incoming radiance originating from the sun. Using spectroscopy, concentrations of different species can be determined to discover the composition of the atmosphere. Over a period of time, changes to the composition caused by natural and anthropogenic sources can be used to infer changes and trends, some of which are related to climate change. One important species in determining the radiative forcing effect is stratospheric sulfuric aerosol. These aerosols are submicron-sized droplets of sulfuric acid that scatter solar irradiance away from earth causing a cooling effect to the surface temperature. The source gasses that form these aerosols arise from the burning of fossil fuels, biomass burning, marine processes and form what is often referred to as the “background” aerosol layer. A large unpredictable perturbation of this layer occurs after large volcanic eruptions that can inject large quantities of sulfur directly into the stratosphere.

Instrumentation has been deployed over the past decades to monitor the atmospheric state from the ground, sky, and in space using many different methods. The evolution of the atmosphere needs to be monitored in the future and to do so, new instrumentation is required. Using the techniques from current generation instrumentation combined with advancements in technology, the capabilities of the next generation of satellite instruments will be able to monitor the earth with greater efficiency and higher resolutions.

Aerosol has been monitored globally from satellite platforms since the 1970s. The most notable method used is known as solar occultation, such as the NASA SAGE missions. These instruments

acquired vertical aerosol profiles, however they were limited to the number of measurements that can be acquired per day due to each measurement requiring a sunrise or sunset. Following occultation, other techniques were implemented onboard satellites with the ability to measure aerosol. One such technique is limb-scatter geometry, such as OSIRIS onboard the Odin spacecraft, which achieves greater global coverage since it only requires sunlit atmosphere and also maintains vertical resolution. Stratospheric aerosol monitoring has continued to the present day from various platforms, including the previously mentioned as well as others, which has allowed a long global time series to determine trends in aerosol extinction over the past few decades. However, the current instruments are ageing and many are operating past their estimated lifetimes with few, if any, scheduled to replace the ageing instruments.

The continued atmospheric monitoring of stratospheric aerosol is essential since it is an important component of the climate equation due to its overall nature to cause cooling of the planetary surface. Recently, increases in stratospheric aerosol have been linked to the so-called “global warming hiatus” and the gradual increase in stratospheric aerosol has been attributed to small volcanic eruptions. Continued global coverage of stratospheric aerosol is essential to continue to monitor the climate. Additional missions and instrument prototypes are required for the near future.

In this work, the design and test of a new passive satellite-based remote sensing instrument, named the Aerosol Limb Imager (ALI), is presented, which images the polarized limb radiance of the atmosphere to determine stratospheric aerosol profiles using a novel filtering technology. ALI measures the atmosphere using two dimensional imaging to acquire cross-track and vertical profiles giving additional measurement resolution. Current limb instruments do not measure the cross-track profile and only the vertical. The addition of the cross track will allow for more

spatially dense measurement points which will allow better determination of atmospheric species such as aerosol and how it dynamically interacts with its environment. This instrument, although a prototype for a satellite instrument, has been tested on a stratospheric balloon flight and was designed specifically for this platform. Slight alterations to the design are needed for deployment on to a satellite platform mission.

In this work, Chapter 2 outlines the background physics of the atmosphere on which this project is based including an overview of stratospheric aerosol. This includes its discovery and discussion about the importance of aerosol in the atmosphere, the effect on climate, sources of aerosol, and microphysical properties. Following, an overview of the different techniques used to measure aerosols is presented. This includes techniques used in in-situ measurements like optical particle counters and nephelometers and satellite based methods such as occultation and limb scatter. Then a brief overview of radiative transfer theory is covered starting with the scalar representation and moving into the more complete polarized, or vector, theory needed for this work. Lastly is a brief discussion of the SASKTRAN-HR model used within this work and inverse methods to determine atmospheric parameters from radiance measurements.

Chapter 3 starts with an overview of Acousto-Optics Tunable Filters (AOTF), which is the novel filtering device at the core of the ALI system. The background physics and practical application of this device are covered with a focus on the advantages and disadvantages to using this filter in remote sensing applications. Following is a discussion of the possible optical layouts for ALI and the testing and underling choice for the optical system design. Chapter 4 discusses the calibration and testing of the final instrument as well as the control software used during stratospheric balloon flight.

Chapter 5 is a presentation of the ALI test flight on a stratospheric balloon in Timmins, Ontario in 2014. The results from the measurements recorded from the flights are also presented including calibrated images, retrieved aerosol profiles, precision estimates, and particle size estimation. These results are compared to current satellite measurements and a discussion about the quality of the ALI retrievals is presented.

Since ALI is inherently a linearly polarized instrument to be used in a future space monitoring mission, a study was undertaken to determine the full effect of the polarized measurement on the aerosol retrieval capability. Furthermore, the optimal geometry for a limb scatter polarized instrument was also determined in this same study. This was done by probing the solution space with a large range of input parameters, and the results of this study are the focus of Chapter 6.

## CHAPTER 2

## BACKGROUND

### 2.1 Introduction

Stratospheric aerosol plays an important role in the global radiative forcing balance by scattering solar irradiation and causing an overall cooling effect that depends on the particle size distribution and the concentration (*Kiehl and Briegleb*, 1993; *Stocker et al.*, 2013). These climate effects are an important and recent focus of research due to the potential contribution of stratospheric aerosol to the so-called global warming hiatus (*Solomon et al.*, 2011; *Haywood et al.*, 2014; *Fyfe et al.*, 2013) and efforts to quantify the variability and trends in the global stratospheric aerosol load are underway with various ground-based and satellite data sets (*Rieger et al.*, 2015; *Ridley et al.*, 2014).

Since its discovery with stratospheric balloon observations (*Junge et al.*, 1961), stratospheric aerosol has been measured with various techniques, although due to the variability of physical composition and particle size, the observations are always limited to some degree and no single measurement technique can fully determine the full range of aerosol properties unambiguously. In-situ balloon observations continue to be used and have provided highly valuable data sets, including most notably the long time series of Optical Particle Counter (OPC) measurements from Laramie, WY (*Deshler et al.*, 2003; 2008; *Kovilakam et al.*, 2015). Aircraft-borne nephelometers (*Beuttell and Brewer*, 1949; *Charlson et al.*, 1969) acquire detailed in-situ measurements, providing, for example, plume composition (*Murphy et al.*, 2014), but are spatially limited to the aircraft track. Ground based lidars have been used to do detailed studies of the extent of volcanic aerosol plumes (*Chazette et al.*, 1995; *Sawamura et al.*, 2012) and provide valuable insight into long term local variability and trends in the aerosol layer. For example, lidar observations were used by *Hofmann et al.* (2009) to first report the observed increase in stratospheric aerosol over

approximately the last decade. However, the global distribution, which can only really be obtained with satellite observations, provides invaluable insight into aerosol processes and variability. A good example of this is the use of satellite observations by *Vernier et al.* (2011b) to determine that the increased stratospheric aerosol load reported by *Hofmann et al.* (2009) was in fact due to a series of relatively minor, mostly tropical, volcanic eruptions.

Several recent studies have highlighted the requirement for continued global stratospheric aerosol observations and especially the need to resolve, both vertically and horizontally, aerosol in the lowermost stratosphere and the upper troposphere. This is the case for tracking the evolution of aerosol from volcanic eruptions, which can have a substantial effect on the aerosol optical depth in the lowermost stratosphere (*Ridley et al.*, 2014; *Andersson et al.*, 2015). Furthering the understanding of the transport of aerosol near and across the tropopause would also benefit from higher spatial and temporal resolution observations. This is evident in the case of volcanic plumes, such as that from Nabro in 2011, the transport and origin of which has been studied extensively and the conclusions are somewhat controversial (*Bourassa et al.*, 2012c; 2013; *Vernier et al.*, 2013; *Fromm et al.*, 2013; 2014; *Fairlie et al.*, 2014; *Clarisso et al.*, 2014). However, this is also the case for the formation of background-level aerosol, particularly in the region of the Asian and North American monsoons, which have been identified as a source of substantial, seasonal and highly structured aerosol formation from precursor tropospheric source gases (*Vernier et al.*, 2011a; *Neely et al.*, 2014; *Thomason and Vernier*, 2013).

Continued stratospheric aerosol observations from space are drastically needed though few, if any, planned missions with such capability are underway. In this work, we present the design and test of a prototype instrument for potential future satellite-based stratospheric aerosol observation. The Aerosol Limb Imager (ALI) concept is a relatively small, low-cost, low-power, passive

instrument, suitable for microsatellite deployment with the capability to provide high spatial resolution measurements, both vertically and horizontally, of the visible/NIR aerosol extinction coefficient. The basic idea is to leverage the clear advantages of the limb scatter technique as a passive, and therefore low mass and low power, means to obtain daily global coverage, with a two dimensional hyperspectral imager for filling cross-track observation.

The ALI instrument concept is built around the use of an Acousto-Optic Tunable Filter (AOTF), which is a novel filtering technology that provides the ability to rapidly select the central wavelength of an image with no moving parts. These filters, which have recently been developed as large aperture imaging quality devices, operate very efficiently in the red and near infrared spectral range, which is a well matched spectral range for limb scatter sensitivity to aerosol and cloud (*Rieger et al.*, 2014). Additionally, the spectral bandpass of the AOTF, which is typically between 3-6 nm at these wavelengths, is very suitable for the broadband scattering characteristics of the aerosol limb signal. The two dimensional imaging nature of the design provides the capability to achieve at least sub-kilometer resolution at the tangent point, which is on the order of the scale size of the upper troposphere and lower stratosphere (UTLS) aerosol features mentioned above.

It should be noted that the basic instrument design concept of ALI is very similar to that of the Atmospheric Limb Tracker for the Investigation of the Upcoming Stratosphere (ALTIUS) (*Dekemper et al.*, 2012), which is a Belgian instrument concept from the Belgian Institute for Space Aeronomy (BIRA). ALTIUS is designed to measure limb scattered sunlight; however, it also has solar, stellar, and planetary occultation modes and is scientifically focused on trace gas measurements, particularly for ozone, whereas ALI is optimized for aerosol observation.

## 2.2 Stratospheric Aerosol

In the late 18<sup>th</sup> century, it was known that atmospheric temperature decreased with altitude and a theory had been raised that at a specific altitude the temperature must eventually go to absolute zero (*Hoinka*, 1997). This lead to a series of balloon campaigns, which were noisy and unreliable due to the technology available (*Hoinka*, 1997), to discover this mysterious altitude in the atmosphere. However, in the late 19<sup>th</sup> century the technology used in these sounding balloons had improved to a point where the atmospheric temperature could be accurately measured and it was found that at approximately 12 km an inversion point was discovered where the temperature started to increase and thus the tropopause, which separates troposphere and the stratosphere, was discovered. The stratosphere is the region of the atmosphere above the temperature inversion of the troposphere, where atmospheric temperature increases, and the lower bound of the stratosphere is in-between 10 and 16 km from the high latitudes to the tropics (*Andrews*, 1987). The stratosphere, which extends up to approximately 50 km, is thermodynamically stable and fairly dry (*Boucher*, 2015). The characteristic stability of the region limits vertical transport of the stratosphere, leading to long lifetimes, spanning from months to years, for non-volatile species (*Volk et al.*, 1997; *Brasseur and Solomon*, 2005)

The stratosphere undergoes exchange of air with the troposphere though a series of dynamical processes including tropical convection, polar vortices, and tropopause folding (*Holton et al.*, 1995). Meridional circulation within the stratosphere is dominated by the slow Brewer-Dobson circulation, although zonal circulation is much faster (*Plumb and Eluszkiewicz*, 1999). Some chemicals can cross the tropopause thermal barrier into the stratosphere which allows for chemicals reactions to occur. One such reaction forms stratospheric sulfate aerosol, discovered by *Junge et al.* (1961) through stratospheric balloon sondes. Sulfate aerosols are droplets of hydrated sulfuric acid ( $\text{H}_2\text{SO}_4$ ) formed from the oxidation of sulfur compounds, primary OCS and  $\text{SO}_2$

(*Brock et al.*, 1995). This stable layer of aerosol exists in the stratosphere from the altitude of the tropopause to approximately 30 km.

### **2.2.1 Aerosol Sources**

The sources for sulfate aerosol are primarily produced in the troposphere and formed through both natural and anthropogenic processes. These sulfur sources enter the atmosphere in various ways and undergo some form of chemical reactions to form sulfate aerosol within the stratosphere.

One primary source of this sulfur is OCS which originates from marine processes, biomass burnings, and industry (*Kettle et al.*, 2002; *Notholt et al.*, 2003). OCS has a long lifetime in the troposphere and low solubility allowing for a significant portion to reach the stratosphere where some of it oxidizes and hydrates to form sulfate aerosol ( $H_2SO_4$ ) and adds to the background aerosol layer (*Crutzen*, 1976).

Another source of sulfur is  $SO_2$ , which originates in the troposphere through industry from the burning of fossil fuels. Sulfur dioxide ( $SO_2$ ) has a short lifetime in the troposphere, and its concentration varies regionally. This sulfur hydrates into sulfate aerosol, which can enter the stratosphere through atmospheric processes (*Thomason and Peter*, 2006). A second source of  $SO_2$  is from volcanic eruptions; which, although highly variable in location and time, can inject a large amount of sulfur directly into the stratosphere which undergoes hydroxyl chemistry and is converted into sulfate aerosol. Volcanos can inject such large amounts of sulfur that they in fact dominate the stratospheric aerosol layer perturbing the background levels. Examples of this perturbation of the aerosol layer were noted during the volcanic eruptions of El Chichon in 1982 (12-20 Tg of sulfur) (*McCormick and Swissler*, 1983; *Hofmann and Rosen*, 1983) and Mount Pinatubo in 1991 (20-30 Tg of sulfur) (*McCormick and Veiga*, 1992). However, after the Mount Pinatubo eruption a volcanically quiescent period occurred where aerosol layers returned to

background. Following this period, a series of smaller volcanic eruptions have increased the background aerosol layer in the amount of 4-7% per year from 2000 to 2009 (*Vernier et al.*, 2011b) and has continued to the present day. Several examples of these small volcanic eruptions include Kasatochi (1.2-2.2 Tg) (*Prata et al.*, 2010), Nabro (1.0- 1.5 Tg) (*Clarissee et al.*, 2016), Calbuco (0.2 -0.5 Tg), and Kelut (0.1-0.3 Tg) (*Carn et al.*, 2016).

## 2.2.2 Aerosol Microphysics

These sulfur sources undergo a series of reactions to be converted into H<sub>2</sub>SO<sub>4</sub> and have been found to form spherical, liquid droplets of aerosol that consist of approximately 25% H<sub>2</sub>O and 75% H<sub>2</sub>SO<sub>4</sub> (*Rosser*, 1971; *Wang et al.*, 1989). These droplets coagulate into various sizes on the order of 0.05 to 1.0 μm depending on the various contributions and stages of the processes of nucleation, evaporation and condensation (*Junge et al.* 1961; *Brock et al.*, 1995; *Bingen et al.*, 2004). A log-normal distribution is often used to approximate the particle size of aerosol in the form of

$$\frac{dn(r)}{dr} = \frac{n_0}{r \ln(\sigma_g) (2\pi)^{1/2}} \exp\left(-\frac{\ln^2(r/r_g)}{2 \ln^2(\sigma_g)}\right) \quad (2.1)$$

where  $n_0$  is the aerosol number density,  $r_g$  is the mode radius, and  $\sigma_g$  is the mode width (*Jäger and Hofmann*, 1991; *Hamill et al.* 1997). In this case, the particle radii are distributed normally over the logarithm of the radius. For a typical non-volcanic background aerosol, with a mode radius and mode width of 0.08 μm and 1.6 respectively (*Thomason*, 1991), the log-normal distribution is shown in **Figure 2-1**.

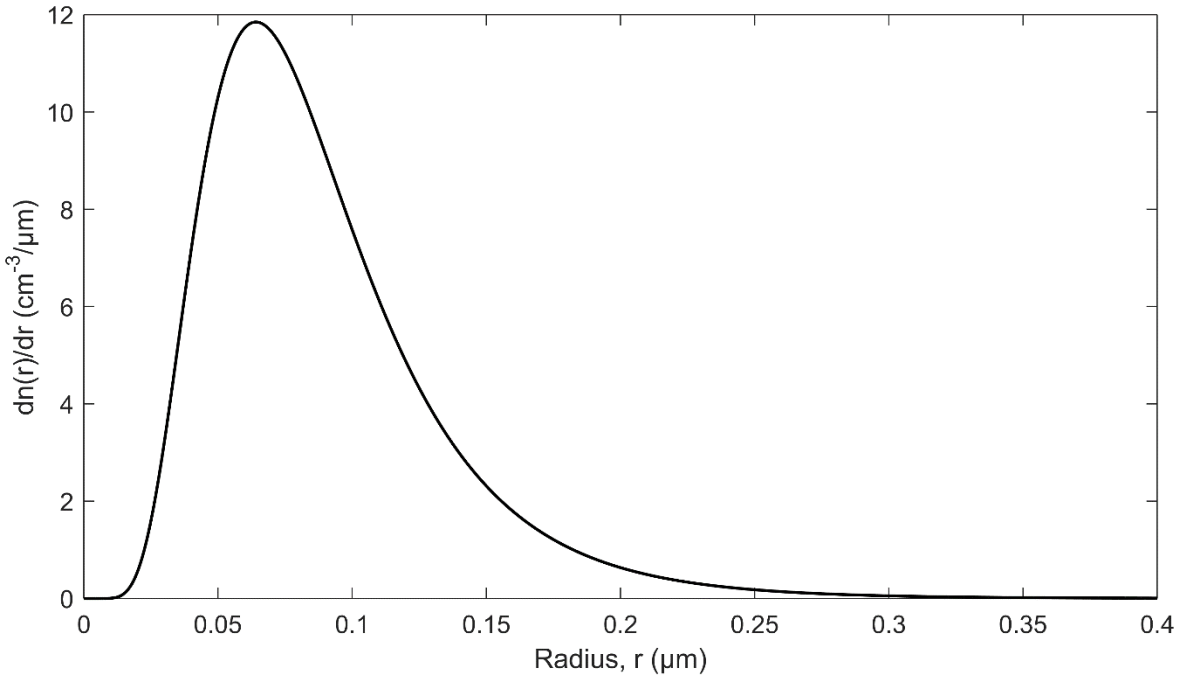


**Figure 2-1:** Sample log-normal distribution for typical non-volcanic stratospheric aerosol.

Optical Particle Counters (OPC) have been used on board stratospheric balloon flights from Laramie, Wyoming over the past 40 years to measure particle sizes in bins between 0.15 to 2.0  $\mu\text{m}$  (*Deshler et al.*, 2003). These measurements provide a valuable if somewhat unique long term set of size-resolved measurements of sulfate aerosol. These particle size distributions can be considered to be primarily unimodal, known as a fine mode, over non-volcanic periods and can be used as an acceptable distribution to approximate background periods. But during volcanic episodes, a bimodal log-normal distribution of aerosol particles, which includes a coarse mode, is more representative of stratospheric aerosol (*Deshler et al.*, 2003; 2008; *Kovilakam et al.*, 2015). The coarse mode has larger particles than the fine mode and complicates the determination of aerosol microphysical parameters since the number of required parameters has increased to six: a number density for both the fine and coarse mode, two mode radii, and two mode widths. Figure 5 from *Deshler et al.* (2003), recreated in Figure 2-2, demonstrates two bimodal particle size distributions from balloon OPC. The first distribution is from a volcanic period in 1993 after the

Mount Pinatubo eruption and another from a background period in 1999. It should be noted that even though a bimodal distribution is found for the background case in Figure 2-2, the number density of the coarse mode is very small and can generally be ignored in non-volcanic periods so a unimodal approximation is sufficient.

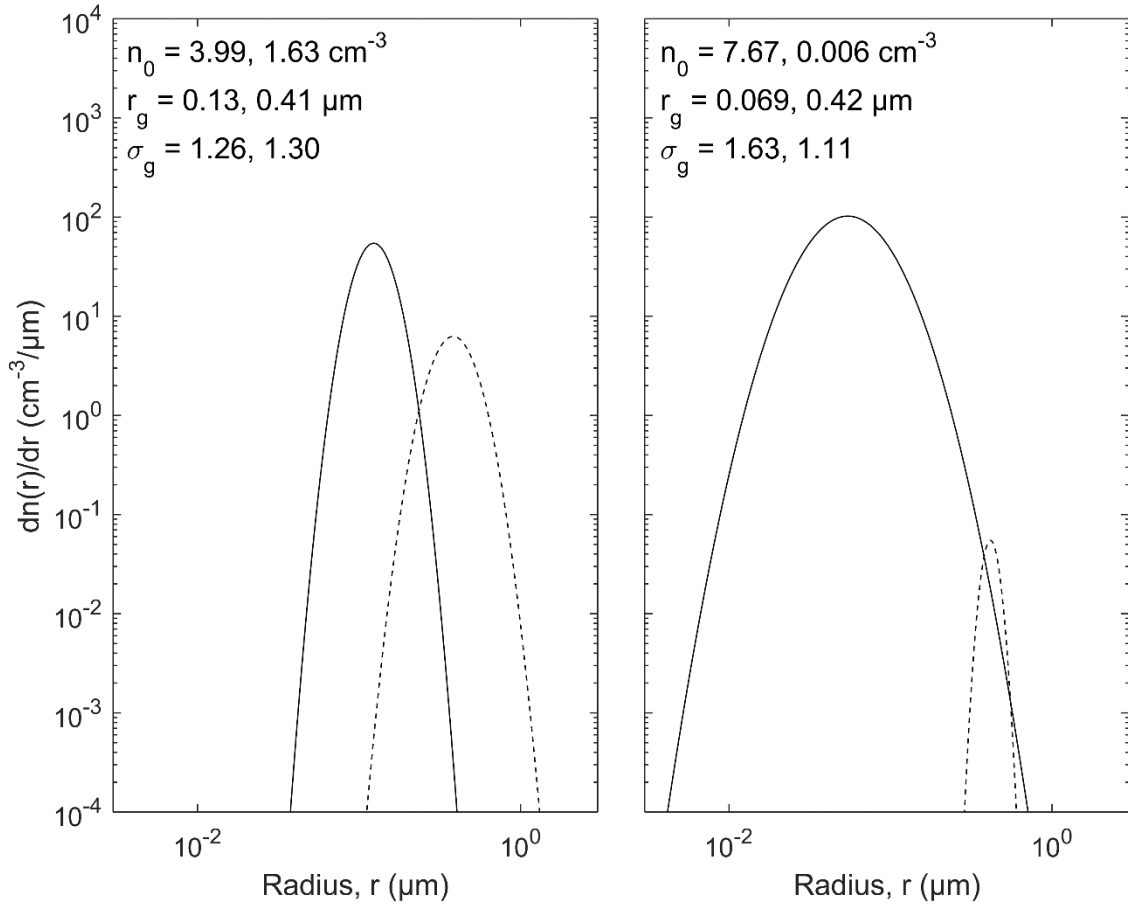


**Figure 2-2:** Bimodal particle size distributions fits from OPC. (a) Distributions from a volcanic period after the Mount Pinatubo eruption recorded in 1993. (b) Distributions from a background aerosol period recorded in 1999. Both of the aerosol distribution measurement are from 20 km altitude with the solid line being the fine mode and the dashed line is the coarse mode. Figure is recreated from Figure 5 of *Deshler et al. (2003)*.

### 2.2.3 Climate Effects

Stratospheric aerosol can have several effects on the climate of the planet, and particularly due to the volcanic contribution, there is a large amount of uncertainty in the overall effect (*Solomon et al., 2007*). Through the so-called “direct effect”, aerosol particles scatter incoming

visible solar radiation away from earth increasing the albedo causing a cooling of the surface of the planet (*Lacis et al.*, 1992). The albedo is the amount of incoming solar irradiance that is reflected back to space. A secondary direct effect from aerosols, which is highly dependent on aerosol particle size distribution, is a greenhouse-like effect that is caused by scattering of infrared radiation emitted from the earth's surface (*Kiehl and Briegleb*, 1993). Aerosol also introduces a so-called “indirect effect” to the radiative balance. This is also known as the cloud albedo effect. This is caused by condensation of water onto existing aerosol particles. These become cloud condensation nuclei and stimulate cloud formation, which leads to an increase of the planetary albedo, which then also contributes to cooling the planet's surface. These types of cloud forming particles also tend to increase the overall lifetime of the cloud, increasing the overall cloud coverage and thus increasing the planetary albedo (*Charlson et al.*, 1992). Overall, the cooling effect of the aerosol particles dominates the warming effect and cools the surface of the planet (*Solomon et al.*, 2011).

Background aerosol periods result in relatively small cooling from stratospheric aerosols but this can greatly change during periods of volcanic activity where the layer can be greatly perturbed. After the eruption of Mount Pinatubo in 1991 the sulfate aerosol load was increased by 5 to 10 fold causing cooling of the lower atmosphere by  $0.5^{\circ}\text{C}$  (*McCormick et al.* 1995; *Soden et al.*, 2002) and 0.1 to  $0.3^{\circ}\text{C}$  on the surface (*Thompson et al.*, 2009; *Canty et al.*, 2013). And the surface temperatures did not return to pre-Pinatubo level until approximately three years after the eruption as the atmosphere filtered out the additional aerosol (*Hansen et al.*, 1996). More recently, a series of small to moderate volcanic eruptions have increased the background stratospheric aerosol layer (*Vernier et al.*, 2011b). This additional volcanic aerosol load has been proposed to be linked to a larger cooling effect, known as the global warming hiatus (*Solomon et al.*, 2011;

*Haywood et al., 2014; Fyfe et al., 2013).* Recently, the temperature of the surface has not risen the amount expected from climate models, and this disagreement has been proposed to be linked to the increase in stratospheric aerosol known as the global warming hiatus.

Even with the current knowledge of the cooling effect of aerosol on climate, there is a large uncertainty to the magnitude of the cooling effect due to the unknowns in aerosol microphysical parameters. To be able to fully resolve the effect of aerosol, new instrumentation is required that has the capabilities to not only determine aerosol concentration in higher resolutions, vertically, globally, and temporally, but also must be able to determine some form of particle size distribution information. This additional information will reduce the uncertainty of the effect of aerosol on climate.

### **2.3 Aerosol Measurements**

Two fundamental methods are used to measure aerosol concentrations within the atmosphere. Two such methods are ground based and in-situ measurements which give good detail and information about a specific localized area. However, these measurements are limited in scope as they do not have global coverage that is inherent in satellite instrumentation. Both ground-based instruments and satellites have important roles in monitoring the planet's aerosol content and each of these methods have inherent advantages and disadvantages. An overview is given on some of the common methods to determine aerosol and why using different methods helps to increase the overall accuracy and precision of merged data sets.

#### **2.3.1 In-situ-Based Measurements**

In-situ measurement are typically performed using balloon- or aircraft-based platforms. In-situ balloon instruments directly measure aerosol particles during the ascent and can determine the particle size distributions. The OPC is an active instrument that uses light source internal to the device to optically count aerosol particles. This type of instrument has been launched from

Laramie, Wyoming since 1971, and has successfully measured aerosol mixing ratio and particle size distributions (*Deshler et al.*, 2003; 2008; *Kovilakam et al.*, 2015). Furthermore, aircrafts have been used to carry nephelometers to acquire detailed in-situ measurements (*Beuttell and Brewer*, 1949; *Charlson et al.*, 1969) including plume composition (*Murphy et al.*, 2014) but are limited spatially to the aircraft track.

In-situ measurements yield high quality direct measurements of aerosol from the altitude that the instrument is currently situated unlike remote sensing applications from satellites. However, these types of instruments only give aerosol parameters from a localized region, like the Laramie, Wyoming OPC, or have very few or limited flights. In order to achieve full global coverage satellite remote sensing instruments are needed to fill the spatial gap.

### **2.3.2 Occultation**

Satellite instrumentation capable of measuring stratospheric aerosol has been in use since the 1970s, beginning with limb sounding solar occultation measurements, and its operational geometry can be seen in Figure 2-3. Solar occultation measurements have provided a reliable, accurate and essentially continuous long term record of vertically resolved aerosol extinction coefficient measurements, mostly from the series of Stratospheric Aerosol and Gas Experiment (SAGE) instruments including SAGE I in 1979, SAGE II in 1984, and SAGE III in 2001 (*Russell and McCormick*, 1989; *Thomason and Taha*, 2003). These SAGE measurements, which have a vertical resolution of approximately 1 km, have generally compared well with ground-based and in-situ measurements, although there are challenges associated with determining microphysical parameters and comparison between instruments can be challenging (*Russell and McCormick*, 1989; *Kovilakam et al.*, 2015). However, solar occultation is generally a robust and stable technique as it directly measures atmospheric optical depth, along with the exo-atmospheric solar spectrum with each scan, allowing for straightforward retrieval of aerosol extinction coefficients

(*Damadeo et al.*, 2013). The major drawback to occultation instruments is that a sunrise or sunset event is required to perform a measurement limiting is the number of scans per day to 16-48 measurements depending on the orbit.

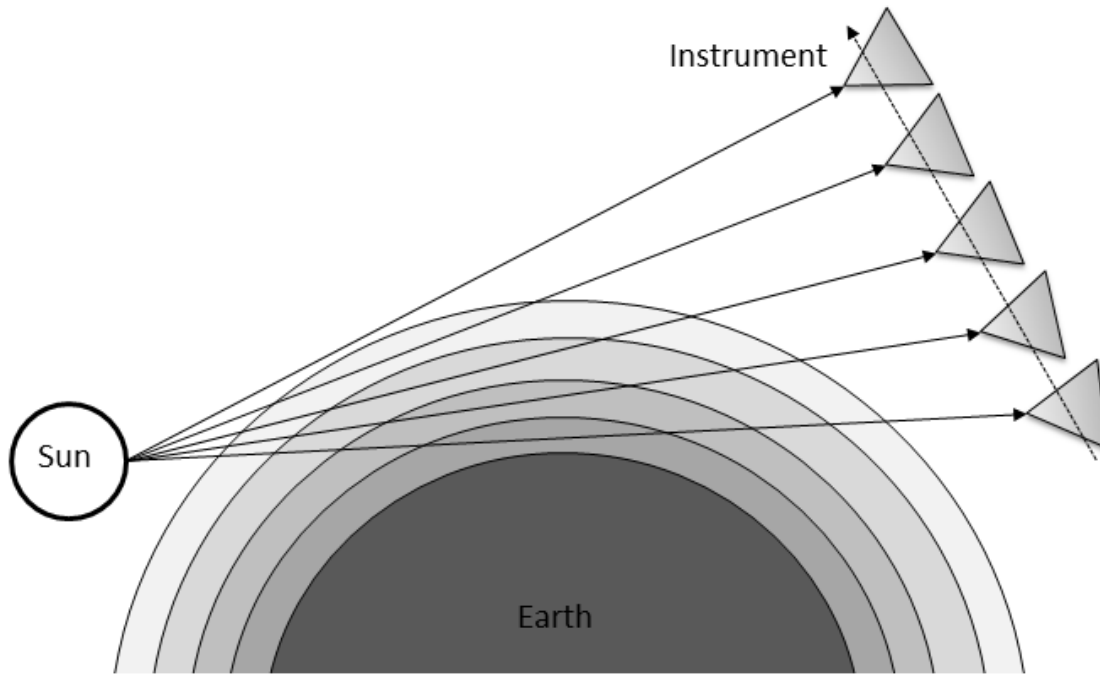


**Figure 2-3:** An occultation instrument monitoring the atmosphere by scanning the atmosphere by looking directly at the sun.

The series SAGE missions came to an end in 2006 with the failure of SAGE III and the occultation measurements have continued from the currently operational MAESTRO and ACE-Imager instruments on SciSat (*McElroy et al.*, 2007; *Gilbert et al.*, 2007) and have had some success producing stratospheric aerosol extinction products (*Vanhellemont et al.*, 2008; *Sioris et al.*, 2010). Furthermore, a manifestation of SAGE III is planned for deployment on the International Space Station in 2016 (*Cisewski et al.*, 2014) to continue the occultation aerosol record.

### 2.3.3 Lidar

A method known as lidar can determine atmospheric parameters through the pulsing of a laser and measuring of the intensity of the backscattered laser light at different wavelengths and polarizations. Lidar has been used at ground based facilities to measure aerosol layers dating back to the 1960s (*Fiocco and Grams*, 1964) and are still used today. More recently lidar instruments have been used on satellite missions including the Ice, Cloud, and land Elevation Satellite (ICESat) from 2002 to 2010 (*Schutz et al.*, 2005) and Cloud-Aerosol Lidar and Infrared Pathfinder Satellite Observations (CALIPSO) which launched in 2006 (*Winker et al.*, 2007). More recently Cloud Aerosol Transport System (CATS) (*Chuang et al.*, 2013) has been mounted on the international space station in 2015 with a three year planned mission. Traditional lidar instruments have looked in the nadir direction (either straight down or up) however some instruments have looked slightly off-nadir, both can be seen in Figure 2-4 for a space based geometry. Lidar measurements have been used to determine aerosol plumbs from volcanos (*Chazette et al.*, 1995; *Sawamura et al.*, 2012) and long term trends (*Hofmann et al.*, 2009).

CALIPSO is a joint mission developed between the National Aeronautics and Space Administration (NASA) and the Centre National d'Etudes Spatiales (CNES) of the United States and France respectively. It uses a two wavelength polarized lidar system to achieve high resolution aerosol and cloud retrievals along the satellite's orbital track with global coverage from 82°S to 82°N (*Young and Vaughan*, 2009). CALIPSO nominally measures backscatter profiles approximately every 300 m along track with approximately 200 m vertical resolution. However, the stratospheric backscatter signal is weak and requires averaging of only the night time measurements over several days and typically yielding resolutions of 0.5 km vertically and 500 km horizontally (*Vernier et al.*, 2011b). Additionally, the uncertainty in the calibration with respect to the molecular background is on the order of the stratospheric aerosol signal and leads to a potential

bias in the stratospheric measurements (*Rogers et al.*, 2011). CALIPSO was launched in 2006 and although it is presently still operational, it is also operating beyond its design lifetime.

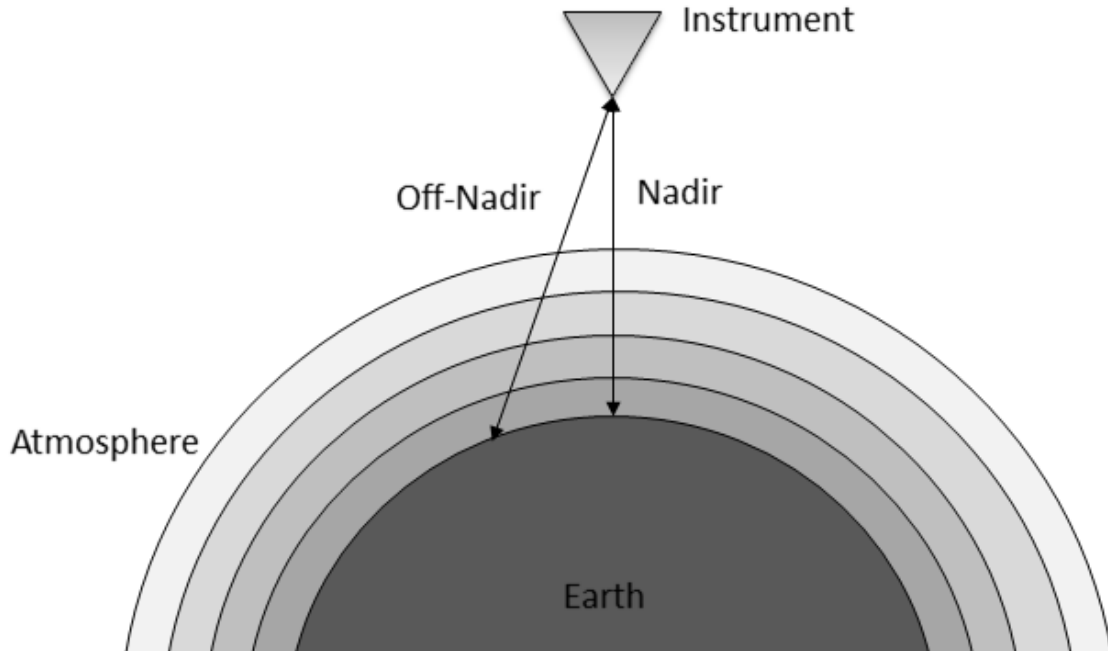


Figure 2-4: Lidar instrument showing a measurements in both the nadir and off-nadir lines of sight.

#### 2.3.4 Limb Scatter

The limb scatter technique measures light that is scattered into the line of sight of the instrument from atmospheric interactions. These scattering interactions can undergo either single or multiple scattering events. Single scatter is when light from the sun interacts with a particle in the atmosphere and scatters it directly into the line of sight of the instrument. Multiple scatter is when the photon of light undergoes several scattering events before entering the line of sight including scattering off of multiple particles in the atmosphere or scattering off of the ground. These events can occur any number of times before entering the instrument. The geometry for the limb scatter technique can be seen in Figure 2-5 and defines the fundamental angles for this method. All angles are defined from the tangent point, which is the point where the distance between the line of sight

and the surface of the earth is minimized, represented by the black dot. The Solar Zenith Angle (SZA) is the angle between the local vertical and the direction of the sun; the Solar Scattering Angle (SSA) is defined to be the angle between the direction of the sun and the line of sight and the Solar Azimuth Angle (SAA) is the angle between the projection of the sun on the plane of the line of sight and the line of sight. These angles can also be seen on Figure 2-5.

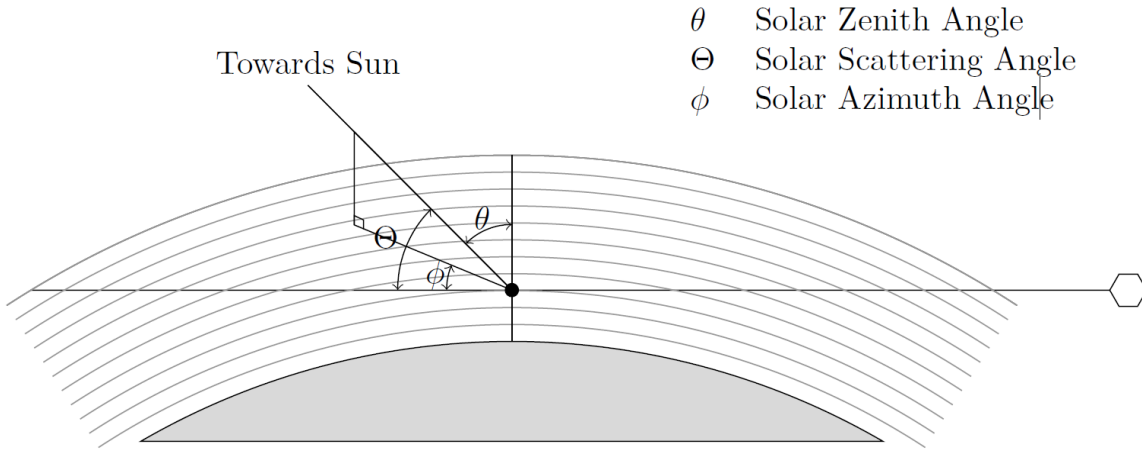


Figure 2-5: Limb scattering geometry measurement for an instrument where single and multiple scattering events occur.

The limb scatter method yields relatively good vertical resolution and allows for measurements to be taken during any daylight period with good Signal to Noise Ratio (SNR), however it requires the use of a complex forward model to calculate the scattering events along with some a priori knowledge of the aerosol scattering cross section in order to retrieve the extinction coefficient profile. The model needs to accurately determine the effect of multiple scatter since it consists of 10-50% of the measured signal depending of the specific geometry and wavelength (*Oikarinen et al., 1999*). Furthermore, due to the complex nature of the problem; a large amount of computational time and memory is required for an accurate calculation.

The first use of limb scatter was on the Solar Mesosphere Explorer (SME) (*Barth et al., 1983*) to measure mesospheric ozone profiles in 1981. Much later, other limb scatter instruments were

launched into low earth orbit that had the capability to determine aerosol extinction including the Optical Spectrograph and InfraRed Imaging System (OSIRIS) launched on the Odin satellite in 2001 (*Llewellyn et al.*, 2004) and the SCanning Imaging Absorption spectrOMeter for Atmospheric CHartographY (SCIAMACHY) on Envisat launched in 2002 (*Bovensmann et al.*, 1999). Both of these instruments are scanning grating spectrometers which can gather a single tangent point and scans the atmosphere to complete a vertical profile.

The OSIRIS version 5.07 data product provides 750 nm extinction profiles at approximately 2 km vertical resolution (*Bourassa et al.*, 2007) and has been shown to agree relatively well, generally within 30%, with SAGE II and SAGE III occultation measurements (*Bourassa et al.*, 2012b; *Rieger et al.*, 2015). The SCIAMACHY instrument uses a retrieval technique essentially similar to OSIRIS to retrieve aerosol profiles at 750 nm with approximately 3 km vertical resolution (*Ernst et al.*, 2012; *von Savigny et al.*, 2015). However SCIAMACHY observations ceased with the demise of Envisat in 2012 and although OSIRIS continues to operate, it is now in the sixteenth year of a mission designed for two years.

The most recently launched limb scatter instrument is the Ozone Mapping Profiler Suite Limb Profiler (OMPS-LP) on the Suomi-NPP satellite in 2011. Although similar in spectral range and vertical resolution to OSIRIS, OMPS-LP is an imaging spectrometer that vertically images the limb in a single measurement. The imaging capability of OMPS-LP provides a decrease in the time required to obtain a limb profile and so increases the along track sampling. Recent work on the feasibility of aerosol retrieval from OMPS-LP measurements show promising results (*Rault and Loughman*, 2013).

An instrument that is currently under development is ALTIUS (*Dekemper et al.*, 2012), which is a Belgian instrument concept from the Belgium Institute for Space Aeronomy. ALTIUS is

designed to image limb scattered sunlight, both vertically and horizontally across the track through the use of the Acousto-Optic Tunable Filter (AOTF) technology (see section 3.2) and additionally has solar, stellar, and planetary occultation modes. ALTIUS is scientifically focused on trace gas measurements, particularly for ozone and the instrument has three channels, each channel with a separate AOTF, measuring wavelengths from 250-2000 nm which could eventually be used for aerosol extinction measurements.

The limb scatter technique is selected for the ALI instrument. ALI also uses an AOTF to spectrally image the filtered scattered signal. This technique was selected due to the relatively lax measurement requirement of only requiring sunlit atmosphere to be able to record a high number of quality measurements. Additionally, the imaging nature of the AOTF will allow quick measurements that are used to retrieve vertical profiles of aerosol extinction.

## **2.4 Radiative Transfer**

To use the limb scatter technique to determine aerosol extinction and particle size information, an understanding of radiative transfer is required. However, modeling the complex scattering interactions of light within the atmosphere is difficult. In this section, an overview of scalar radiative transfer is performed, followed by the necessary modifications to form polarized radiative transfer equations. A description of scattering interactions important to aerosols is also developed. Finally, an overview of the SASKTRAN radiative transfer model used within this work is provided.

### **2.4.1 Scalar Radiative Transfer**

The scattering and absorption processes in the atmosphere are non-trivial and an adequate method to model this interaction is needed. The following presents a derivation of radiative transfer equations for the atmosphere with scalar radiance which does not account for polarization. In order to accurately discuss radiative transfer, a coordinate system must first be defined. If we assume

that a ray of light,  $I$ , is propagating in a given direction,  $\hat{\Omega}$ , and starts at a location,  $s_0$ , with the initial position of  $\mathbf{r}_0$ , then the position of the ray along the path direction can be completely defined by its path length,  $s$ . The basis of path length is used to define the radiative transfer equations.

The fundamental theory for radiative transfer is known as Beer-Lamberts law. The law describes the change in intensity or radiance of light,  $dI$ , as it interacts with a thin layer of space or atmosphere,  $ds$ . The thin layer has particles which affect the attenuation of the light which is dependent on the number of particles,  $n$ , and the particle cross section,  $\sigma$ . If there are several different particles, the attenuation is a summation of the number densities and cross sections. The Beer-Lambert Law gives the following form

$$\frac{dI(s)}{ds} = -I(s) \sum_i n_i(s) \sigma_i(s). \quad (2.2)$$

The extinction of the particles is a measure of the loss of light over a given distance and is defined as

$$k(s) = \sum_i n_i(s) \sigma_i(s). \quad (2.3)$$

Integrating Equation 2.2 forms the following result

$$I(s_1) = I(s_0) e^{-\int_{s_0}^{s_1} k(s') ds'}. \quad (2.4)$$

The optical depth,  $\tau(s)$ , is defined as the extinction over the path length simplifying Equation 2.4 to

$$I(s_1) = I(s_0) e^{-\tau(s)}. \quad (2.5)$$

The above gives the radiance at point  $s_1$  after it has gone through attenuation from  $s_0$ .

Although this form of the Beer-Lambert's Law is useful for describing the loss of light through scattering or absorbing from an initial source though a medium, the atmosphere also has incoming

light that is scattered into the line of sight from other directions or emitted from particles. To account for this additional source of light a source term,  $J$ , is added to Equation 2.2 to yield

$$\frac{dI(s)}{ds} = k(s)(J(s) - I(s)). \quad (2.6)$$

Using the fact that the change in optical depth is defined as

$$d\tau = -k(s)ds \quad (2.7)$$

Equation 2.6 is rearrange into

$$\frac{dI(\tau)}{d\tau} = I(\tau) - J(\tau). \quad (2.8)$$

Using the following derivative

$$\frac{d}{d\tau}(I(\tau)e^{-\tau}) = \frac{dI(\tau)}{d\tau}e^{-\tau} - I(\tau)e^{-\tau} \quad (2.9)$$

and substituting it into Equation 2.8 yields

$$\frac{d}{d\tau}(I(\tau)e^{-\tau}) = -J(s)e^{-\tau}. \quad (2.10)$$

This form can now be integrated over the optical depth giving

$$I(\tau)e^{-\tau} - I(\tau_0)e^{-\tau_0} = - \int_{\tau_0}^{\tau} J(\tau')d\tau'. \quad (2.11)$$

Selecting the reference point at the observer to be  $\tau_0 = s_0 k(s_0) = 0$  and converting the equation back to path lengths yields

$$I(s_0) = I(s)e^{-\tau(s)} + \int_s^{s_0} k(s')J(s')ds' \quad (2.12)$$

which gives the radiance as seen from an observer at a point,  $s$ , along the line of sight.

With the full form of the radiative transfer equation, the source term must be determined. In the atmosphere there are three sources of additional radiation, thermal emissions, photochemical reactions, and scattered light. For wavelengths from the visible to the near infrared (*i.e.*

wavelengths less than 2  $\mu\text{m}$ ) there is little contributions from thermal emissions. Furthermore, as long as wavelengths where photochemical reactions occur are avoided this source term can also be ignored. This leaves the only significant source of light to be added into the line of sight to be from scattered sunlight. The source term for scattered sunlight is given by

$$J(s, \hat{\Omega}) = \frac{k_{scat}(s)}{k(s)} \int_{4\pi} I(s, \hat{\Omega}') p(s, \theta) d\hat{\Omega}'. \quad (2.13)$$

The diffuse radiance is given by  $I(s, \hat{\Omega}')$  and is the radiation scattered into the line of sight from all directions. The phase function,  $p(s, \theta)$ , described the probability that a ray of light is scattered from a direction,  $\hat{\Omega}'$ , into the line of sight propagation direction,  $\hat{\Omega}$ . The scattering angle,  $\theta$ , is defined as

$$\cos(\theta) = \hat{\Omega}' \cdot \hat{\Omega}. \quad (2.14)$$

Lastly,  $k_{scat}(s)$  is the extinction only caused by scattering and not absorption. The term  $\frac{k_{scat}(s)}{k(s)}$  only allows the fraction of particles that scatter radiation, and not absorb it, to contribute to the source term.

As a final note, the calculation of the diffuse radiance is what makes this a computationally heavy problem. To completely solve for the diffuse radiance, the radiance at every point in the atmosphere must be determined. Furthermore, the light can be scattered multiple times in the atmosphere, requiring a diffuse radiance for each order of scatter. Each successive scattering adds smaller contributions to the final radiance at the observer. Through this iterative process the full multiple scatter solution to the radiative transfer equation is

$$I(s_0) = \sum_{i=1}^{\infty} [I_i(s)] e^{-\tau(s)} + \int_s^0 k(s') \sum_{i=1}^{\infty} [J_i(s')] ds'. \quad (2.15)$$

The multiple scatter term is calculated until the contribution is sufficiently small to be negligible.

### 2.4.2 Vector Radiative Transfer

The scalar radiative transfer equation works well for systems that do not measure polarized light as the effect of polarization on the total radiance is small. However, for instruments that measure polarized light, a vector radiative transfer equation is required. Before polarization can even be discussed, a method to quantify polarization must be defined which is the Stokes vectors.

The Stokes vectors are given as

$$\mathbf{I} = \begin{bmatrix} I \\ Q \\ U \\ V \end{bmatrix}, \quad (2.16)$$

where  $I$  is the scalar or total radiance,  $Q$  is the difference between horizontal polarization to vertical polarization,  $U$  is the difference between  $+45^\circ$  diagonal polarization to  $-45^\circ$  polarization, and  $V$  is the difference between the counter clockwise circular polarization to clockwise polarization (*Bickel and Bailey, 1985*). Using a reference frame where the local x-axis is defined to be the horizontal polarization leads to the following definition for the Stokes vector

$$\begin{aligned} I &= \langle E_x \rangle^2 + \langle E_y \rangle^2 \\ Q &= \langle E_x \rangle^2 - \langle E_y \rangle^2 \\ U &= 2\text{Re}(\langle E_x \rangle \langle E_y^* \rangle) \\ V &= 2\text{Im}(\langle E_x \rangle \langle E_y^* \rangle) \end{aligned} \quad (2.17)$$

The electric field aligned with the x and y-axis are  $E_x$  and  $E_y$  respectively, the star is the complex conjugate, and Re and Im are the “real part of” and “imaginary part of” respectively. The degree of polarization can be determined with the Stokes vectors. If the equality  $I^2 = Q^2 + U^2 + V^2$  holds true then the light is fully polarized, otherwise it is only partially polarized if  $I^2 > Q^2 + U^2 + V^2$ .

With the addition of polarization, the radiative transfer and source term equations (Equations 2.12 and 2.13) need to be rewritten with polarization state included. The polarized radiative transfer equation are

$$\mathbf{I}(s_0) = \mathbf{I}(s)e^{-\tau(s)} + \int_s^0 k(s')\mathbf{J}(s')ds' \quad (2.18)$$

$$\mathbf{J}(s, \widehat{\Omega}) = \frac{k_{scat}(s)}{k(s)} \int_{4\pi} \mathbf{L}(\theta_2)\mathbf{P}(s, \theta)\mathbf{L}(\theta_1)\mathbf{I}(s, \widehat{\Omega}')d\widehat{\Omega}', \quad (2.19)$$

which are the vector radiative transfer and source term equations respectively (*Mishchenko et al.*, 2002). With polarization a scattering reference frame is defined and incoming radiance is rotated into the scattering frame multiplied by the scattering matrix,  $\mathbf{P}(s \theta)$ , then returned to the original propagation frame. The rotation matrix is defined as

$$\mathbf{L}(\theta) = \begin{bmatrix} 1 & 0 & 0 & 0 \\ 0 & \cos(2\theta) & \sin(2\theta) & 0 \\ 0 & -\sin(2\theta) & \cos(2\theta) & 0 \\ 0 & 0 & 0 & 1 \end{bmatrix} \quad (2.20)$$

where  $\theta$  is the angle between the propagation and scattering reference frame. The radiance and the source terms are now Stokes vectors in 4 by 1 matrices and the scattering matrix,  $\mathbf{P}(s \theta)$ , is a 4 by 4 tensor that is related the probability of the incoming light to be scattered in the propagation direction with a specific polarization. As a note, the operation of  $\mathbf{L}(\theta_2)\mathbf{P}(s, \theta)\mathbf{L}(\theta_1)$  is commonly referred to as the phase matrix. The polarization equation adds extra computation and memory consumption since the polarization must be computed at each scattering in the radiative transfer equation, which is nontrivial, and stored in memory, which is four times the size of a standard scalar radiance calculations.

With the complete vector polarized radiative transfer expression the two scattering interactions that pertain to determining aerosol will be described. The first interaction is Rayleigh scattering which defines the scattering of the background atmosphere, and Mie scattering which determines how incoming light scatters from aerosol particles.

### 2.4.3 Rayleigh Scattering

Rayleigh scatter is the scattering performed by the molecular background atmosphere, *i.e.* by molecules of the air. The first calculation of molecular atmospheric scattering cross sections was by Lord Rayleigh where he assumed the molecules were dielectric spheres with radii much less than the wavelength of the light. Later, the King correction was added to the Rayleigh scattering cross section,  $\sigma_{ray}$ , to yield the following expression

$$\sigma_{ray} = \frac{128\pi^5 \alpha_0^2}{3\lambda^4} \frac{6 + 3\rho_n}{6 - 7\rho_n}, \quad (2.21)$$

which is highly dependent on wavelength,  $\lambda$ , which is in cm. The parameters  $\alpha_0$  and  $\rho_n$  are the volume polarizability, in  $\text{cm}^{-3}$ , and the depolarization ratio, which is unitless (*Sneep and Ubachs*, 2005).

The other important quantity for scattering is the scattering matrix. For Rayleigh scattering, the vector model scattering matrix is given by the Rayleigh-Gans approximation (*Mishchenko et al.*, 2002)

$$\mathbf{P}(\Theta) = \frac{3}{4} \begin{bmatrix} 1 + \cos^2 \Theta & -\sin^2 \Theta & 0 & 0 \\ -\sin^2 \Theta & 1 + \cos^2 \Theta & 0 & 0 \\ 0 & 0 & 2\cos\Theta & 0 \\ 0 & 0 & 0 & 2\cos\Theta \end{bmatrix}. \quad (2.22)$$

Each component of the scattering matrix itself is smooth which allows for easy and accurate calculation for Rayleigh scattering.

### 2.4.4 Mie Scattering

For larger particles, like sulfate aerosol, Rayleigh scattering no longer holds since the size of the particles is on the order of the wavelength and Mie scattering must be used. *Mie* (1908) solved Maxwell's equations in a general sense with a solution using spherical Bessel and Henkel functions. Only the fundamental Mie scatter equation is presented here but a full derivation of Mie

scatter can be found in *van de Hulst* (1957). The scattering cross section from Mie theory is given by

$$\sigma_{mie} = \frac{2\pi}{k^2 r^2} \sum_{l=1}^{\infty} (2l+1) (|a_l|^2 + |b_l|^2), \quad (2.23)$$

where  $k$  is the wavenumber,  $r$  is the particle radius and the coefficients  $a_l$  and  $b_l$  are given by

$$a_l = \frac{\Psi'_l(nkr)\Psi_l(kr) - n\Psi_n(nkr)\Psi'_l(kr)}{\Psi'_l(nkr)\zeta_l(kr) - n\Psi_l(mkr)\zeta'_l(kr)}, \quad (2.24)$$

$$b_l = \frac{n\Psi'_l(nkr)\Psi_l(kr) - \Psi_n(nkr)\Psi'_l(kr)}{n\Psi'_l(nkr)\zeta_l(kr) - \Psi_l(mkr)\zeta'_l(kr)}. \quad (2.25)$$

The index of refraction of the particle is given by  $n$ , and  $\Psi_l$  and  $\zeta_l$  are the normalized half-integer order Bessel functions of the first kind and Henkel functions of the second kind respectively. The scattering matrix for Mie scatter for a vector solution has the following form (*Hansen and Travis*, 1974)

$$\mathbf{P}(\Theta) = \frac{2\pi}{k^2 \sigma_{mie}} \begin{bmatrix} S_1 S_1^* + S_2 S_2^* & S_1 S_1^* - S_2 S_2^* & 0 & 0 \\ S_1 S_1^* - S_2 S_2^* & S_1 S_1^* + S_2 S_2^* & 0 & 0 \\ 0 & 0 & S_1 S_2^* + S_2 S_1^* & i(S_1 S_2^* + S_2 S_1^*) \\ 0 & 0 & -i(S_1 S_2^* + S_2 S_1^*) & S_1 S_2^* + S_2 S_1^* \end{bmatrix}. \quad (2.26)$$

The terms in the scattering matrix,  $S_1$  and  $S_2$ , are known as the amplitude functions and are given by

$$S_1(\Theta) = \sum_{l=1}^{\infty} \frac{2l+1}{l(l+1)} \left[ a_l \frac{1}{\sin\Theta} + b_l \frac{d}{d\Theta} \right] P_l^1(\cos\Theta), \quad (2.27)$$

$$S_2(\Theta) = \sum_{l=1}^{\infty} \frac{2l+1}{l(l+1)} \left[ b_l \frac{1}{\sin\Theta} + a_l \frac{d}{d\Theta} \right] P_l^1(\cos\Theta), \quad (2.28)$$

where  $P_l^1$  are the Legendre polynomials.

In the atmosphere, various particle sizes occur and a log-normal distribution (Equation 2.1) is assumed for aerosols. In order to determine effective scattering cross-section, a weighted average over the particle radius is performed

$$\sigma_{eff} = \frac{\int_0^{\infty} \sigma_{mie}(r)n(r)dr}{\int_0^{\infty} n(r)dr}. \quad (2.29)$$

The weighted average is similarly performed to determine the effective phase matrix for a particle size distribution.

There are stark differences between Rayleigh and Mie scattering cross sections and scattering matrices. Using standard atmospheric conditions, a comparisons of the extinctions and thus the scattering cross sections against the wavelength can be seen in Figure 2-6a. The wavelength to the fourth dependence is noted in Rayleigh scattering, in blue, (Equation 2.21) whereas Mie scattering, in red, does not have this dependence. Due to the difference the significance of Mie scattering becomes more predominant as wavelength increases. Further the scattering matrix is also radically different (Figure 2-6b). Taking a look at the first term of the scattering matrix,  $P_{11}(\Theta)$ , the Rayleigh term is smooth with even forward and back scattering and small amount of scattering seen in 90° scattering angle. The scattering term for Mie on the other hand has a very strong tendency for forward scattering compared with few scatter events happening for scattering angles past 90°. Further, for certain wavelengths and size parameters the Mie phase matrix can have oscillations super imposed onto the curve making the phase matrix even more complex than Rayleigh scattering.

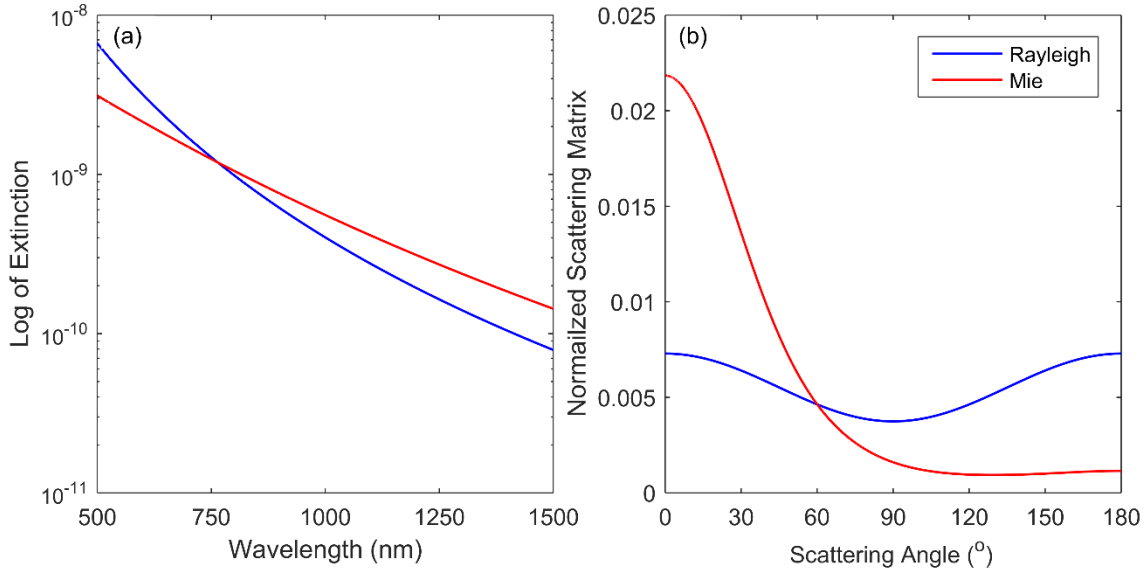


Figure 2-6: (a) Change in scattering cross section for Rayleigh and Mie scattering over wavelength. The Mie scattering uses a log-normal distribution with a mode width of 1.6 and a mode radius of 0.08  $\mu\text{m}$ . (b) The first term of scattering matrix,  $\mathbf{P}_{11}(\Theta)$ , for Rayleigh and Mie scattering across scattering angle.

It should be noted that although the theory is well founded to calculate the Mie scattering cross sections and phase matrices, in practice it is computationally intensive since the terms consist of infinite sums of Bessel and Henkel functions. Work done by *Wiscombe* (1980) has allowed for effective computation of the Mie scattering coefficients, which has been implemented into the SASKTRAN radiative transfer engine.

#### 2.4.5 SASKTRAN Radiative Transfer Model

The SASKTRAN radiative transfer was first developed to solve the scalar radiative transfer equation in a fully spherical atmosphere for both single and multiple scatter with a one dimensional atmosphere, *i.e.* considering the variation in altitude only (*Bourassa et al.*, 2008). The first source term,  $J_1$ , is the sunlight from the sun attenuated and scattered into the instrument line of sight, and it is assumed the incoming solar irradiance encounters the earth in parallel randomly polarized rays. To include higher order terms, a successive orders method is used to simulate second, third and higher orders of scattering within the atmospheric model. Another important assumption in

the SASKTRAN model is that the ground reflection is assumed to have a depolarizing Lambertian distribution, which will evenly distribute the incoming radiance evenly in all outgoing directions with the efficiency of the planetary albedo.

Recent upgrades have been performed on SASKTRAN and have led to a new engine known as SASKTRAN High Resolution or SASKTRAN-HR (Zawada *et al.*, 2015) which has expanded the model to be able to perform radiative transfer calculations with a fully three dimensional atmosphere. This update allows the model to vary the atmospheric concentrations in not just the vertical direction, like the original SASKTRAN, but in both of the horizontal geometries (*i.e.* latitude and longitude), allowing for true variances observed in the atmosphere.

The most important update to the SASKTRAN-HR model for this work is the addition of the ability to calculate the vector or polarized radiances (Dueck *et al.*, 2016). Using the vector model allows for SASKTRAN to compute the Stokes vectors in the reference frame of the model, which can be rotated into any desired frame of reference through the use of a provided basis by SASKTRAN-HR. The polarization output from SASKTRAN-HR performs polarized calculations up to an arbitrary order scattering interaction, all scattering past this arbitrary scattering are assumed to be scalar.

## 2.5 Inversion Techniques

Remote sensing methods indirectly measure the atmosphere and require a method to be able to transform the measurement into a physical atmospheric quantity. This process is known as a measurement inversion or inverse problem. A measurement vector,  $\mathbf{y}$ , is constructed from the spectral radiance that has sensitivity to the desired physical parameter while reducing sensitivity to other physical parameters as much as possible. A forward model (*i.e.* SASKTRAN-HR),  $\mathbf{F}(\mathbf{x}, \mathbf{b})$  is used to compute the measurement vector using an input state,  $\mathbf{b}$ , and physical parameter state,

$\mathbf{x}$ . The length of the measurement vector and state vector are  $m$  and  $n$  respectively. It is important to note that the length of the measurement vector and state vector do not have to be the same. This leads to the following formation

$$\mathbf{y} = \mathbf{F}(\mathbf{x}, \mathbf{b}) + \boldsymbol{\epsilon}, \quad (2.30)$$

where  $\boldsymbol{\epsilon}$ , is the measurement noise and needs to be inverted to yield the physical result.

The inverse is found directly if it is assumed that there is no measurement error and the problem is linear. Using an initial guess or a priori,  $\mathbf{x}_a$ , the retrieved parameter state can be found through

$$\mathbf{y} = \mathbf{K}(\mathbf{x} - \mathbf{x}_a) + \mathbf{F}(\mathbf{x}_a, \mathbf{b}), \quad (2.31)$$

$$\hat{\mathbf{x}} = \mathbf{x}_a + \mathbf{K}^{-1}(\mathbf{y} - \mathbf{F}(\mathbf{x}_a, \mathbf{b})). \quad (2.32)$$

The Jacobian is represented by  $\mathbf{K}$ , and is the partial derivative of the forward model to the state vector. The Jacobian is an  $m \times n$  matrix. However, remote sensing methods are generally non-linear and are associated with measurement noise; additionally numerical approximation are used to calculate the forward model and Jacobian. These issues make the direct method generally ineffective and iterative methods are used. This section will briefly cover common methods used for atmospheric inversions.

### 2.6.1 Optimal Estimation

Commonly a Bayesian approach is often used to update the atmospheric state known as optimal estimation (Rodgers, 2000). This method uses statistical knowledge of the a priori and state parameter with measurement noise to determine the probability that the state parameter is  $\mathbf{x}$  given a measurement of  $\mathbf{y}$  and is given by

$$P(\mathbf{x}|\mathbf{y}) = \frac{P(\mathbf{y}|\mathbf{x})P(\mathbf{x})}{P(\mathbf{y})}. \quad (2.33)$$

A solution is found by maximizing the probability of  $P(\mathbf{x}|\mathbf{y})$ . If it can be assumed that the measurement vector and a priori have Gaussian distributions the above can be solved to yield

$$\hat{\mathbf{x}} = \mathbf{x}_a + \mathbf{S}_a \mathbf{K}^T (\mathbf{K} \mathbf{S}_a \mathbf{K}^T + \mathbf{S}_\epsilon)^{-1} (\mathbf{y} - \mathbf{K} \mathbf{x}_a). \quad (2.34)$$

The covariance matrices of the a priori and measurement error are  $\mathbf{S}_a$  and  $\mathbf{S}_\epsilon$  respectively. This equation is iterated until a coverage solution is found for non-linear problems. It should be noted that if the probability state of the a priori are unknown or is not well modeled by a Gaussian distribution this method can find inaccurate or biased results.

### 2.6.2 Levenberg-Marquardt

The Gauss-Newton method has been classically used to solve for non-linear inversion problems. However, if the initial guess is far from the solution and if the solution space is not well described by a quadric the method will fail. *Levenberg* (1944) proposed another method for the non-linear least squares fit that was later modified by *Marquardt* (1963) given as

$$\hat{\mathbf{x}}^{(n+1)} = \hat{\mathbf{x}}^{(n)} + (\mathbf{K} \mathbf{K}^T + \gamma^{(n)} \mathbf{D})^{-1} \mathbf{K}^T (\mathbf{y} - \mathbf{F}(\hat{\mathbf{x}}^{(n)}, \mathbf{b})), \quad (2.35)$$

known as the Levenberg-Marquardt algorithm. The damping factor,  $\gamma$ , reduces the step size in iteration to keep the problem in a linear region. If this damping factor is small the method approaches the Gauss-Newton method whereas if  $\gamma$  is large the method steps down the direction of the gradient descent. The diagonal matrix,  $\mathbf{D}$ , is a scaling matrix for the damping factor since the state vector may have different dimensions and magnitudes resulting in the benefit of larger step sizes in more linear areas of the solution space. However, the determination of the damping factor can be difficult to determine from numerical methods and usually an ad hoc method is used.

### 2.6.3 Multiplicative Algebraic Reconstruction Technique

The Multiplicative Algebraic Reconstruction Technique (MART) is a form of relaxation techniques similar to Chahine relaxation (*Chahine*, 1970). The MART algorithm has the modification of a weighting matrix,  $\mathbf{W}$ , which relates the importance of each measurement vector,  $k$ , and tangent altitude,  $j$ , to each retrieved state altitude,  $i$ . The algorithm is given by

$$\hat{x}_i^{(n+1)} + \hat{x}_i^{(n)} \sum_k \sum_j \frac{y_{jk}}{F_{jk}(\boldsymbol{x}^{(n)}, \boldsymbol{b})} W_{ijk}. \quad (2.36)$$

Unlike the previous methods, this method allows for computation of the state vector without the computation of the Jacobian or any matrix inversions allowing for a fast and efficient algorithm. Further, the MART algorithm requires the measurement vector to be positive for the method to converge to a solution. For atmospheric retrievals, including aerosols, the measurement vector is generally positive and is not a large limitation. Additionally, for single wavelength aerosol retrievals only one measurement vector is commonly used (*Bourassa et al.*, 2007; 2012b) and the measurement vector summation from Equation 2.36 can be dropped.

## 2.6 ALI Prototype Instrument and Stratospheric Balloon Flight

The work presented here is focused on the design of the Aerosol Limb Imager (ALI), a polarized limb scatter instrument that spectrally images the atmosphere. The central feature of ALI is the use of the novel technology known as an AOTF which has the ability to rapidly select the central filtered wavelength with no moving parts. AOTFs have recently been developed with large apertures and high quality crystals allowing for imaging capabilities. This permits AOTF use in new applications, such as the ALI instrument, with the ability to achieve sub-kilometer resolution, both horizontally and vertically. The AOTF technology operates efficiently in the red to near infrared which is well-matched for limb scatter sensitivity to aerosol and clouds (*Rieger et al.*, 2014) and has a typical spectral bandpass of 3-6 nm which is ideal for the broadband scattering characteristics of aerosol.

### 2.6.1 ALI Specifications

The goal of ALI is a future satellite mission to be able to monitor aerosol concentration and microphysics globally from space, however the ALI presented here has been designed for a stratospheric balloon platform since it was the only available platform for testing. This platform

has resulted in some changes to the required design parameters for the instrument. To sufficiently measure spectral radiance from a stratospheric balloon platform the following specifications and their relevance will be described below.

The balloon is estimated to have a float altitude of 35 km and ALI will need to measure the atmosphere from a tangent altitude of the ground or 0 km to the float altitude of 35 km. This results in ALI needing a minimum vertical field of view of  $6^\circ$  to measure the entire region of interest. It is important to note that for a satellite platform the required field of view would be reduced to approximately  $1^\circ$ . Further, the aerosol structural features discussed in section 2.2 are generally on the order of a kilometer and to resolve these features a minimum spatial resolution of 250 m vertically is required. Similar specifications are used for the horizontal (cross-track) direction to be able to maintain optical unity and allow the use of spherical optics.

Spectrally, aerosol particles scatter over a broadband range; however particle sensitivity, which is currently hard to determine, increases with the near IR measurements. ALI will be able to measure wavelengths from 600-1200 nm. Since the aerosol (Mie) scattering cross section varies slowly with wavelength, measurements at every 25-50 nm within the range are required. Furthermore, this slow varying cross section also allows for low spectral resolution with a spectral bandpass requirement of less than 10 nm.

The nature of measuring limb scattered images results in a situation where the lower altitudes have high signal and the upper altitudes have low signal. Therefore signal to noise levels are the most important at the high altitudes due to the exponential signal drop-off. The highest measurement altitudes (*i.e.* 30-35 km) require that the signal to noise ratio must remain above 1 to be able to use these high altitude measurements to determine aerosol extinction. Additionally, the

system will be able to take an image on the order of a second to achieve a high number of measurements.

Finally, due to the limitations of the stratospheric balloon platform both mass, power consumption, and thermal rages are a concern. The balloon platform can only sustain so much mass and has a limited amount of power. As such, the total mass of ALI must remain below 50 kg and power draw below 80 W is required. Furthermore, the balloon will be floating in atmospheric conditions that are colder than -40°C resulting in freezing concerns. Additionally, heating from direct sunlight can bake the instrument resulting in concerns of overheating. In order to mitigate these concerns ALI must be thermally stable within all equipment's standard operating ranges.

## **2.6.2 ALI Instrument Design Process Overview**

The AOTF provides a novel and new method of being able to record spectral images of the atmosphere. However, the use of an AOTF has specific optical requirements which complicates the optical design on the system. A large focus of this work is the designing and testing of the optical system to verify excellent performance with the AOTF which is the focus of Chapter 3. Once the optical design is finalized, calibration is undergone and control software is written to prepare ALI for its stratospheric balloon flight from Timmins, Ontario in 2014 and is the focus of Chapter 4. Additionally, Chapter 5 is focused on the stratospheric balloon launch and post-flight analysis including raw image conversion and the retrieving of aerosol. The retrieved aerosol is compared to OSIRIS measurements to verify the quality of the measurements recorded by ALI. Finally, since ALI inherently measures polarized radiance due to the nature of the AOTF, special consideration had to be given to the orientation of the AOTF within the system. Measuring a linear polarized light instead of measuring the total radiance, like current generation instruments, changes the sensitivity of the instrument to aerosol. To verify good sensitivity during the future space

missions a study was performed, contained in Chapter 6, to determine the advantages and disadvantages to measuring linear polarized light instead of the total radiance.

# CHAPTER 3

## INSTRUMENT DESIGN<sup>1</sup>

### 3.1 Introduction

Aerosol is an important component to the climate equation and new instruments with higher density and resolution measurements are required for the near future. These instruments will need to have the ability to determine both aerosol concentration as well as particle size information in better understand the effect of aerosol on the global climate. This chapter discusses the ALI instrument with the goal of measuring high quality aerosol profiles to fulfill the need of future scientific monitoring. The design of ALI is covered from the initial planning to the completed optical and opto-mechanical system. First, a discussion of the Acousto-Optical Tunable Filter (AOTF) is presented that covers the solution of the wave equation, diffraction efficiency, output diffracted angle, and tuning curve. Following is a discussion of the trade-offs of the two primary optical design layouts considered for the instrument. Then the final optical specifications of the chosen design are presented along with the opto-mechanical aspects of the instrument

### 3.2 AOTF Theory and Background

The fundamental piece of technology used in the ALI design is an AOTF, which provides tunable narrow band filtering of an incident optical signal with fast response times and no moving parts. The use of AOTF technology for space based initiatives is only recently possible due to the recent advances in creating AOTFs with the ability to maintain imaging quality performance over a wide acceptance angles. This section discusses the theory behind the AOTF.

---

<sup>1</sup> Portion of sections 3.3.1, 3.3.2, 3.3.3, and 3.3.4 as well as **Error! Reference source not found.**, **Error! Reference source not found.**, **Error! Reference source not found.**, and Figure 3-20 were originally published in *Elash et al. (2016)*

### 3.2.1 Solution to the Acoustic Equation

The AOTF is a device that through phonon-phonon interaction and a Bragg-like diffraction process allows a broadband light source to be filtered and the output can be captured as an image. Two primary types of AOTFs exist, collinear (*i.e.* the acoustic wave is aligned with the incident beam, (*Harris and Wallace, 1969*)) and non-collinear (*i.e.* the acoustic wave and the optical beam do not propagate collinearly in the crystal, (*Chang, 1977*)) configurations, and both use an optically anisotropic medium (*Saito and Yano, 1976*). An anisotropic medium is a material that is transparent and has a different index of refraction based upon the polarization state of the incoming light and its propagation direction, commonly called birefringence. For imaging purposes, a wide aperture is required and such AOTFs have been developed (*Gass and Sambles, 1991*) and are currently readily available.

To effectively utilize to AOTF in a precision optical instrument, it is imperative to understand the detailed principle of operation. The AOTF undergoes a phenomena known as an Acousto-Optic (AO) effect which describes the interaction between sound and light waves within the medium, generally a crystal. The AOTF used in this work operates in the Bragg diffraction regime which will be assumed for this derivation. Understanding the interactions between the light and the sound (acousto) waves within the crystal leads to an understanding of the functionality of the device. For an AO interaction within the AOTF there are three fundamental signals, the first two are light waves that are represented by an incident and diffracted (or filtered) electric fields and the third is a sound wave that is an applied Radio Frequency (RF) wave. Solving the AO wave equation for an AOTF will determine the form of the incident and diffracted waves in terms of optical and medium parameters. This is useful for to determine the primary characteristics of the operation of the device such as diffraction efficiency and wavelength calibration. The RF wave

exerts a stress on the crystal within the AOTF and this stress is the basis to solve the AO wave equation.

The derivation will start with the determination of the AO wave equation starting from Maxwell's equations. Amperes law and Faradays law are the foundation for the wave equation and are presented as

$$\nabla \times \mathbf{E} + \frac{\partial \mathbf{B}}{\partial t} = 0 \quad (3.1)$$

$$\nabla \times \frac{\mathbf{B}}{\mu} = \mathbf{J} + \frac{\partial(\epsilon \mathbf{E})}{\partial t} \quad (3.2)$$

where  $\mathbf{E}$  is an electric field,  $\mathbf{B}$  is an magnetic field,  $\mathbf{J}$  is the current density,  $\mu$  is the permeability, and  $\epsilon$  is the permittivity. By taking the curl of the Equation 3.1, combining it with Equation 3.2, and assuming that the AOTF crystal is non-conductive (*i.e.*  $\mathbf{J} = 0$ ) along with the identity  $\nabla \times (\nabla \times \mathbf{E}) = \nabla(\nabla \cdot \mathbf{E}) - \nabla^2 \mathbf{E}$  and assuming the crystal has no net charge (*i.e.*  $\nabla \cdot \mathbf{E} = 0$ ) gives the simplified wave equation in the form

$$\nabla^2 \mathbf{E} = \mu_0 \frac{\partial^2(\epsilon \mathbf{E})}{\partial t^2}. \quad (3.3)$$

The RF or sound wave creates a stress wave within the crystal that causes a modulation within the crystal effecting the dielectric permittivity. Since the dielectric permittivity is not a constant with time, it induces a susceptibility yielding the following form

$$\nabla^2 \mathbf{E} - \mu_0 \epsilon \frac{\partial^2 \mathbf{E}}{\partial t^2} = \frac{\mu_0}{\epsilon_0} \frac{\partial^2 \mathbf{P}}{\partial t^2} \quad (3.4)$$

where  $\mathbf{P}$  is the induced polarization due to the stress in the AO medium given by  $\mathbf{P} = \epsilon_0 \Delta \chi \mathbf{E}$  and  $\Delta \chi$  is the change in the susceptibility. It is important to note that if the input electric field is linearly polarized (*i.e.* ordinary polarization) then the stimulated electric field has a different linear polarization state (*i.e.* extraordinary polarization) (Voloshinov, 1996). It is standard to define the

input electric field as the incident field and output electric field as the diffracted field. Remembering that the crystal is birefringent, the indices of refraction for the two wave fronts will have differing indices of refraction. Using this standard the susceptibility is given by  $\Delta\chi = -n_i^2 n_d^2 p \mathbf{S}$  where  $n_i$  and  $n_d$  are the indices of refraction for the incident and diffracted electric fields and  $p$  is the elasto-optic coefficient which is dependent on medium and orientation of the crystal used and  $\mathbf{S}$  is the strain wave induced by the acousto wave. As mentioned earlier a solution for this equation is presented in the Bragg region meaning there will only be first order diffraction effects.

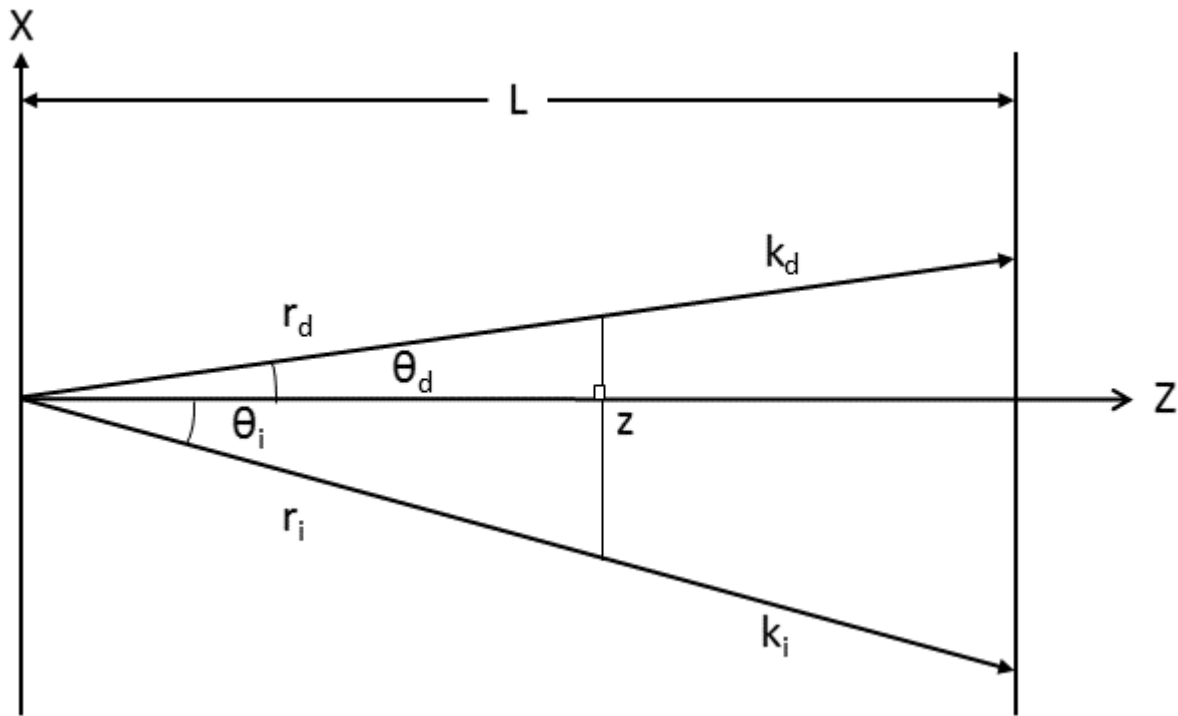


**Figure 3-1:** Geometry for the AOTF wave derivation assuming the acousto wave is along the x-axis and the AO interaction occurs along the z axis over an interaction length,  $L$ . The parameters  $r_i$ ,  $k_i$ , and  $\theta_i$  are the position vector, wave vector, and angle of the incident electric field and similarly for the diffracted electric field. Figure recreated from Xu and Stroud (1992)

Assuming the incoming electric field is a plane wave, which is valid since most waves enter the device with a large radius of curvature, the above differential equation can be solved. A standard

acousto-optical geometry is used in the solution and is shown in Figure 3-1. The acoustic wave is propagating in the x direction of the crystal causing a stress wave which leads to the modulation of the index of refraction within the acoustic region of the crystal denoted by  $L$ . The system is orientated such that the acousto interaction occurs along on the z axis and the electric field entering the device is a plane wave described by

$$\mathbf{E}_i(\mathbf{r}, t) = \frac{1}{2} \mathbf{E}_i(z) \exp[j(\omega_i t - \mathbf{k}_i \cdot \mathbf{r})] \quad (3.5)$$

and the diffracted electric field is described as

$$\mathbf{E}_d(\mathbf{r}, t) = \frac{1}{2} \mathbf{E}_d(z) \exp[j(\omega_d t - \mathbf{k}_d \cdot \mathbf{r})] \quad (3.6)$$

where  $\omega$  and  $\mathbf{k}$  are the angular frequencies and wave vectors for the incident and diffracted beam.

The modulation caused by the acoustic wave is a strain on the crystal given as

$$\mathbf{S}(\mathbf{r}, t) = \frac{1}{2} \mathbf{S}(z) \exp[j(\Omega t - \boldsymbol{\kappa} \cdot \mathbf{r})] \quad (3.7)$$

where  $\Omega$  is the angular frequency of the RF wave, and  $\boldsymbol{\kappa}$  is the acousto wave vector.

Equations 3.5 through 3.7 are used to determine the coupled wave equations by using them in the acousto wave equation, Equation 3.4. The induced polarization is formed by the incident wave interacting with the strain wave resulting in  $\mathbf{P} = \epsilon_0 \Delta \chi \mathbf{E}$ . The polarization wave will in turn stimulate the diffracted electric field yielding the first half of the coupled equations in the form

$$\frac{dE_d(z)}{dz} - j\Delta k E_d(z) = -j \frac{n_i^2 k_d}{4 \cos \theta_d} p S E_i(z) \exp[j(\mathbf{k}_d - \mathbf{k}_i - \boldsymbol{\kappa}) \cdot \mathbf{r}] \quad (3.8)$$

$$\frac{dE_d(z)}{dz} - j\Delta k E_d(z) = j \frac{v_i}{2L} E_i(z) \exp[j(\mathbf{k}_d - \mathbf{k}_i - \boldsymbol{\kappa}) \cdot \mathbf{r}]$$

where  $\Delta k$  is the difference between the group and phase wave vectors of the diffracted electric field,  $L$  is the length of the AO interaction, and  $v_i = -n_i^2 k_d p S L / 2 \cos(\theta_d)$ . However, once the interaction between the incident electric field forms the diffracted field, the diffracted field in turn

interacts to form a polarization wave that stimulates the incident wave yielding the second coupled equation

$$\frac{dE_i(z)}{dz} = -j \frac{n_d^2 k_i}{4 \cos \theta_i} p S^* E_d(z) \exp[j(\mathbf{k}_i - \mathbf{k}_d - \boldsymbol{\kappa}) \cdot \mathbf{r}] \quad (3.9)$$

$$\frac{dE_i(z)}{dz} = j \frac{v_d}{2L} E_d(z) \exp[j(\mathbf{k}_i - \mathbf{k}_d - \boldsymbol{\kappa}) \cdot \mathbf{r}],$$

with  $v_i = -n_d^2 k_i p S L / 2 \cos(\theta_i)$ . From the previous coupled equations, a very crucial concept for the operation of the AOTF is revealed known as the momentum matching criteria. The value of the exponential term needs to be very small or equal to zero (*i.e.*  $\mathbf{k}_i = \mathbf{k}_d \pm \boldsymbol{\kappa}$ ) for the previous coupled equations to have a useful solution. The momentum matching criteria is an important result and will be used to find the tuning curve and diffraction angle within the AOTF. For efficient Bragg diffraction, the geometry is set up such that the difference of the wave vectors for the incident electric field is small or zero. Finally,  $v_i$  and  $v_d$  are the optical phase shift and the effective optical phase shift is defined as  $v_{id}^2 = v_i v_d$ .

Solving the coupled wave equations assuming momentum matching criteria yields the following solutions

$$E_i(z) = \exp\left(j \frac{\Delta k}{2} z\right) \left( A_1 \cos \frac{Tz}{L} + A_2 \sin \frac{Tz}{L} \right) \quad (3.10)$$

$$E_d(z) = \exp\left(j \frac{\Delta k}{2} z\right) \left( B_1 \cos \frac{Tz}{L} + B_2 \sin \frac{Tz}{L} \right) \quad (3.11)$$

where  $T = \left(v_i v_d + \frac{\Delta k^2}{4}\right)^{\frac{1}{2}}$  which is proportional to the inverse of wavelength. It should be noted that the frequency of the diffracted wavelength is  $\omega_i \pm \Omega$  though the coupled interaction. To find the unknown coefficients, the boundary conditions of the system, are used

$$E_i(0) = E_i, \quad E'_i(0) = 0, \quad E_d(0) = 0, \quad E'_d(0) = \frac{v_i}{2L} E_i. \quad (3.12)$$

Solving for the coefficients yields

$$\mathbf{E}_i(z) = E_i \exp\left(j \frac{\Delta k}{2} z\right) \left( \cos \frac{Tz}{L} - j \frac{\Delta k L}{2T} \sin \frac{Tz}{L} \right) \quad (3.13)$$

$$\mathbf{E}_d(z) = E_i \exp\left(j \frac{\Delta k}{2} z\right) \left( \frac{v_i}{2T} \sin \frac{Tz}{L} \right). \quad (3.14)$$

With the completed forms of the incident and diffracted fields the diffraction efficiency and the shape of the point spread function can be determined.

### 3.2.2 Diffraction Efficiency

The diffraction efficiency,  $\eta$ , of the AOTF is ratio of the energy of the incident electric field compared to the energy of the diffracted electric field at the end of the acoustic interaction region given by

$$\eta = \frac{|E_d(L)|^2}{|E_i(0)|^2} = \left(\frac{v_i}{2}\right)^2 \left(\frac{\sin T}{T}\right)^2 \cong \left(\frac{v_{id}}{2}\right)^2 \left(\frac{\sin T}{T}\right)^2. \quad (3.15)$$

This form yields the common sinc function shape for the spectral Point Spread Function (PSF) of an AOTF from a point object or source. The PSF describes the spectral bandwidth of the filtering capabilities of the device and is the limited factor to the spectral resolution of the AOTF. This limit must be sufficiently small enough (approximately less than 10 nm) to be able to accurately resolve aerosol from atmospheric measurements. Additionally, this form can be altered to better identify how to increase the diffraction efficiency of an AOTF. The diffraction efficiency is converted into a form that uses the RF driving power assuming exact momentum matching (*i.e.*  $\Delta k = 0$ ) and that the interaction is occurring within a birefringent medium. The RF driving power is the amplitude at which the piezoelectric transducer pumps the RF signal into the AO medium. The average energy flow of the acoustic power is defined by

$$P_a = \frac{\rho v^3 S^2 H L}{2} \quad (3.16)$$

where  $\rho$  is mass density of the medium,  $v$  is the acoustic velocity in the crystal,  $H$  and  $L$  is the height and length of the acoustic wave interaction region. Another variable that is defined is the acousto-optic figure of merit,  $M_2$ , which is completely determined by the medium properties defined by

$$M_2 = \frac{n_i^3 n_d^3 p^2}{\rho v^3} \quad (3.17)$$

and is a measure of how efficient a medium can undergo the AO effect.

Using Equations 3.16 and 3.17 along with the definition of  $T$  and rearranging Equation 3.15 yields the following for the diffraction efficiency

$$\eta = \sin^2 \left( \frac{\pi}{\lambda \sqrt{\cos \theta_i \cos \theta_d}} \sqrt{\frac{M_2 L P_a}{2H}} \right). \quad (3.18)$$

The efficiency of the diffraction at a wavelength,  $\lambda$ , can be increased through design considerations. First, a medium should be picked that yields the largest possible AO figure of merit. Second, the active region of the AO interaction should be narrow and long increasing the  $L/H$  ratio. And lastly, the driving power of RF wave should be large enough to equate the component inside of the sinusoid function in Equation 3.18 to  $\pi$ . It should be noted that increasing the RF power too high can have the possibility of deceasing the AOTF diffraction efficiency.

### 3.2.3 Diffraction Angle

Although the wave equations are useful in determining the diffraction efficiency, PSF, and the form of the electric fields, it is not useful to determine the angle of the diffracted wave or the RF acousto wave to wavelength relation known as the tuning curve (covered in the section 3.2.4). Instead the momentum matching criteria realized through Equations 3.8 and 3.9 are used.

The diffraction angle is analyzed using the interaction between the acoustic sound wave and the phonon light by

$$\mathbf{k}_i = \mathbf{k}_d \pm \boldsymbol{\kappa} \quad (3.19)$$

known as the momentum matching criteria. For this analysis, only the +1 order diffraction interaction is performed although a similar analysis can be performed for the -1 case. The wave vectors are defined as

$$|\mathbf{k}_i| = \frac{2\pi n_i}{\lambda}, \quad (3.20)$$

$$|\mathbf{k}_d| = \frac{2\pi n_d}{\lambda}, \quad (3.21)$$

$$|\boldsymbol{\kappa}| = \frac{2\pi F}{v}. \quad (3.22)$$

The RF frequency is given by  $F$  which is related to the angular frequency by  $\Omega = 2\pi F$  and the speed of the acousto wave within the crystal is given by  $v$ . It is assumed that the extraordinary light undergoes the momentum matching through the device.

A standard acousto optical experimental setup, which can be seen in Figure 3-2, is used to determine the diffraction angle. Using Equation 3.19, the x component of the wave vector is

$$k_x = k_i \sin \theta_i = k_d \sin \theta_d + \kappa \quad (3.23)$$

and the magnitude of the diffracted wave vector is

$$k_d = \frac{\omega_d}{c} = \frac{\omega_i - \Omega}{c}. \quad (3.24)$$

Combining the results from Equation 3.23 and Equation 3.24 the angular deviation of the diffracted source is

$$\sin \theta_d = \frac{c(k_i \sin \theta_i - \kappa)}{\omega_i - \Omega}. \quad (3.25)$$

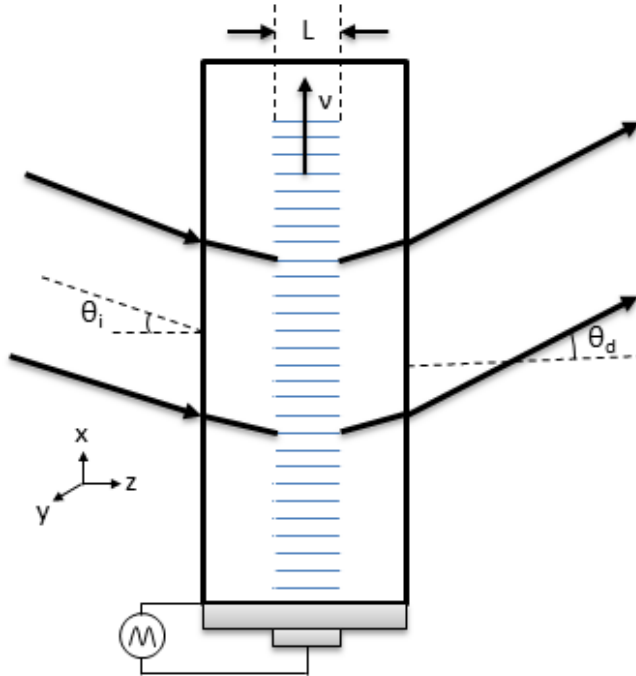


**Figure 3-2:** A standard non-collinear AOTF experimental set up. The crystal is assumed to infinitely long in the y direction. Figure recreated after *Guenther* (1990) number 14B-1.

The diffracted light leaves the AOTF at a different angles depending on the RF which translates to angular movement of diffracted beam as the wavelength is scanned. In order for the device to be usable in an imaging optical system, the diffracted light must always leave the device following the same path no matter what wavelength is being filtered. Thus, a crystal wedge or compensator is fashioned to the back of the device to compensate for this effect using a correcting prism like effect causing the diffracted beam to always leave the device at the same angle. A general optical layout with the deflection in the optical path and an attached compensating wedge is shown in Figure 3-3.

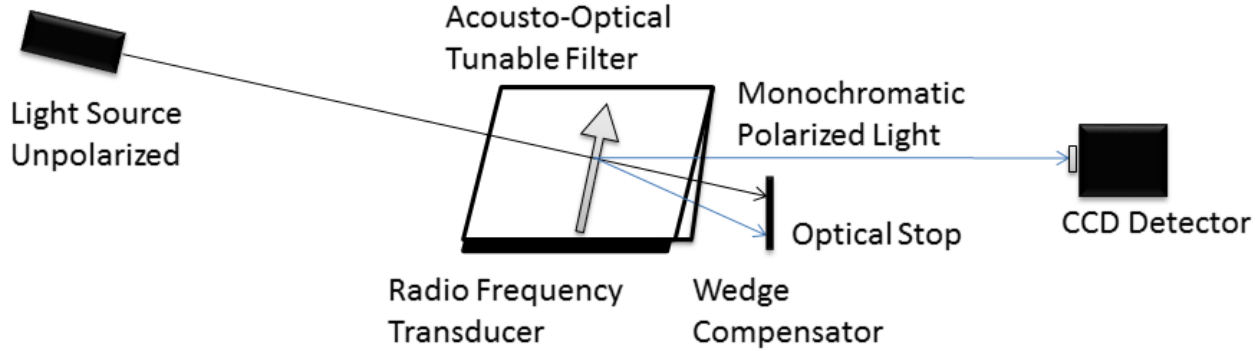


**Figure 3-3:** General Layout of an AOTF. A randomly polarized incoming light source hits the front surface of the birefringent crystal. The black bar below the crystal is the piezoelectric transducer that produces the RF signal and forms the acousto wave represented by the grey arrow. The momentum matching Bragg diffraction occurs and monochromatized polarized light (-1 order) exits the AOTF at a constant angle with the 0th order and +1 order being blocked by an optical stop.

### 3.2.4 Tuning Curve

The tuning curve is the AOTF relationship between the diffracted wavelength and the applied RF. The analysis is performed using the momentum matching criteria stated in Equation 3.19. Figure 3-4 shows the wave vectors in the orientation of a tellurium oxide ( $\text{TeO}_2$ ) crystal in a birefringent orientation where  $\alpha$  is the propagation angle of the acoustic wave with respect to the crystal orientation.

The wave vector diagram can be used to define the incident and diffracted indices of refraction in terms of the ordinary and extraordinary indices of refraction in the following

$$n_i = \left( \frac{\sin^2(\theta_i + \alpha)}{n_e^2} + \frac{\cos^2(\theta_i + \alpha)}{n_o^2} \right)^{-\frac{1}{2}}, \quad (3.26)$$

$$n_d = n_o. \quad (3.27)$$

If the difference in the index of refraction is small, as it is for  $\text{TeO}_2$ , Equation 3.26 can be approximated as (Voloshinov *et al.*, 2007)

$$n_i = n_o + \Delta n \sin^2(\theta_i + \alpha), \quad (3.28)$$

where  $\Delta n$  is the difference between the extraordinary and ordinary indices of refraction (*i.e.*  $\Delta n = n_e - n_o$ ). The wave vectors, seen in **Error! Reference source not found.**, of the system need to follow the momentum matching criteria from Equation 3.19. Separating the wave vectors into their directional components with respect to the propagation angle,  $\alpha$ , the tangential and perpendicular directions respectively are

$$k_i \cos \theta_i = k_d \cos \theta_d, \quad (3.29)$$

$$k_i \sin \theta_i - \kappa = k_d \sin \theta_d. \quad (3.30)$$

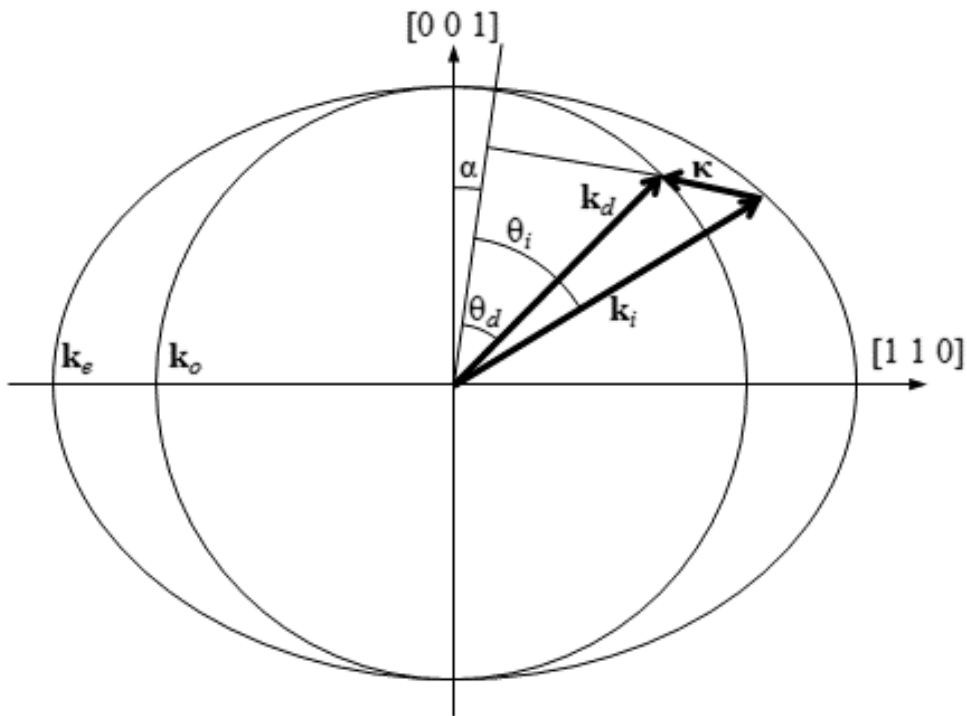


**Figure 3-4:** The wave vectors generated by the AOTF experiment set up in Figure 3-2. From the above figure  $k_e$  and  $k_o$  are the wave vectors of the extraordinary and ordinary axis of the AOTF crystal. Originally published as Figure 1 in *Elash et al.* (2016).

The tangential and perpendicular directions of the wave vector can be used in combination with the wave vectors definitions (Equations 3.20-3.22, and 3.29-3.30) to yield

$$\lambda = \frac{v}{F} \left[ n_i \sin \theta_i - (n_o^2 - n_i^2 \cos^2 \theta_i)^{\frac{1}{2}} \right]. \quad (3.31)$$

The above can be approximated as

$$\lambda = \frac{\Delta n v}{F} \frac{\sin^2(\theta_i + \alpha)}{\sin \theta_i} \quad (3.32)$$

assuming difference in indices of refraction is small (Equation 3.28) (*Voloshinov and Mosquera, 2006*). This equation has several implications to the operation of the device which affects the design possibilities in an imaging system. First, the wavelength diffracted by the AOTF is inversely related to frequency of the RF wave. Second, the wavelength of the diffracted signal is dependent on the angle of incidence of the incoming wave therefore passing a signal though the AOTF at different incident angles results in different outgoing wavelengths. Also, through the described interaction, the diffracted light goes through a 90° rotation in polarization (*Voloshinov, 1996*). As a final note, it is important to note that the indices of refraction are sensitive to temperature changes which can alter the tuning curve calibrations, generally corresponding to a 1 nm change per 10 °C for TeO<sub>2</sub>. Using the basis of the theory behind the AOTF the device can successfully be used to create a spectral imaging system for limb scatter measurements.

### **3.3 Optical Chain Development**

The ALI design goal is a simple optical system that essentially images a single wavelength at a time through the use of an AOTF. However, the AOTF operation requires important instrument design considerations to account for its optical operation (*Suhre et al., 2004*). First, a brief overview of AOTF operational states is discussed. Then is a brief introduction to the two optical systems considered for ALI and an overview of the final ALI optical design. The final design images the atmosphere with a resolution on the order of 200 m for both vertical and cross-track special dimensions with a wavelength range of 650-950 nm which corresponds to the usable range of the QSI CCD to be used in the system. Code V optical design software was used to assist in the designing and analyzing the performance of both of the optical designs and final optical system.

### 3.3.1 AOTF Operation

This section describes the two fundamental states of the AOTF used throughout the rest of this work but first is the general operation of the device itself. The general operation of the AOTF is shown in **Error! Reference source not found.a**. An RF wave is applied and there is one input, the unpolarized broadband incident ray, and four output signals. The birefringence of the crystal splits the zeroth order ordinary and extraordinary polarizations into two separate outputs. The RF wave interacts with the incoming radiance to form the first order extraordinary and ordinary diffracted beams with polarizations rotated by 90°. Further, only the first order extraordinary polarization remains at a consistent angle due to the compensation mentioned in section 3.2.3.

When the AOTF is used in any experiments or design, the removal of the unwanted polarizations are desired to achieve high quality low contamination images. As such, a linear polarizer is always placed in front of the AOTF to remove the ordinary polarization and a linear polarizer is placed behind the AOTF to remove the zeroth order extraordinary polarization. When an RF wave is applied to the crystal with the polarizers, as seen in **Error! Reference source not found.b**, the AOTF is considered to be in the on or “AOTF-on” state with only the first order extraordinary wave passing through the system. When an RF wave is not applied to the crystal and the polarizers are present, as seen in Figure 3-5c, the AOTF is considered to be in the off or “AOTF-off” state with no outputs from the system. These two states, “AOTF-on” and “AOTF-off” are used throughout the remainder of this work to describe these two operational modes of the AOTF.

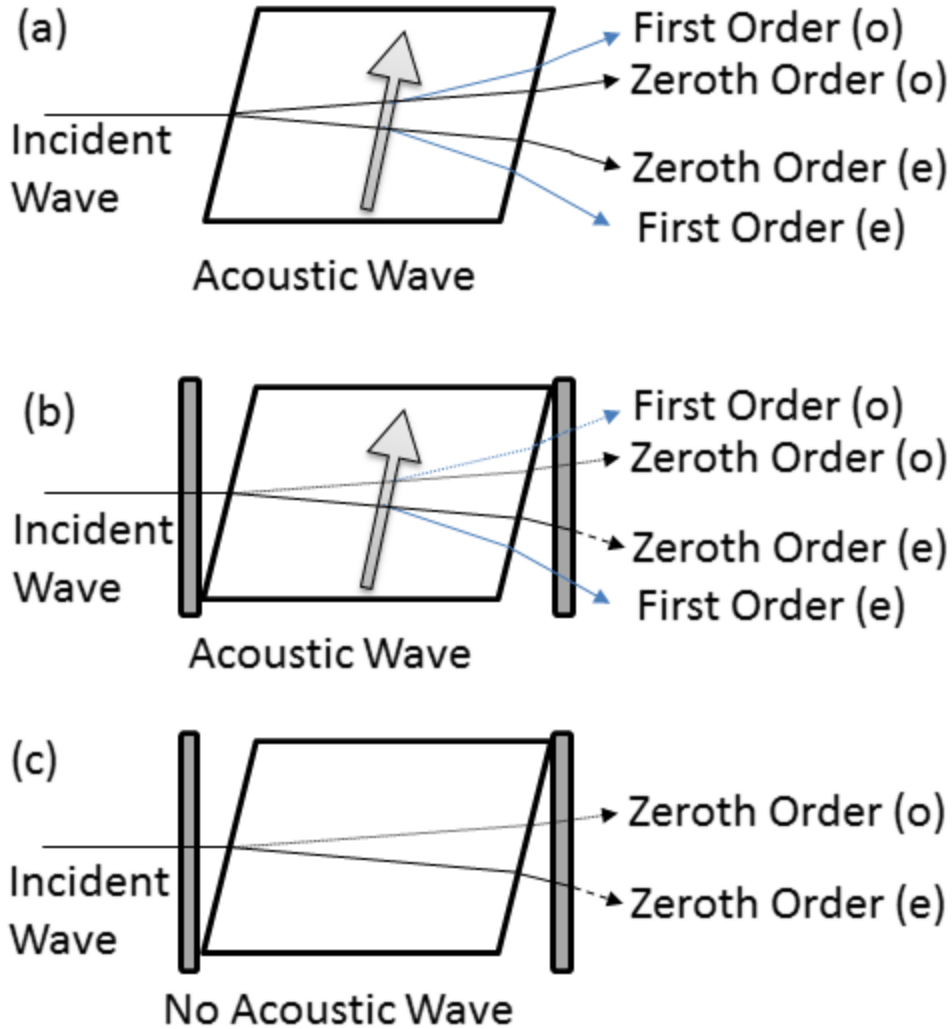


**Figure 3-5:** (a) An AOTF undergoing Bragg diffraction with an unpolarized input incident wave with a RF wave applied represented by the arrow. After the diffraction event four output signals are formed: the zeroth order and first order ordinary (o) and extraordinary (e) signals. However the only optical path that remains at a constant angle no matter the applied RF wavelength is the first order extraordinary diffracted signal. (b) Two linear polarizers are added to the system, the first linear polarizer removes the ordinary polarization from the outputs with the dotted lines and the second linear polarizer removes undiffracted extraordinary light shown by the dashed line. This configuration is the “AOTF-on” state. (c) The system in (b) without a RF wave so no Bragg diffraction is occurring. Once again the first linear polarizer removes the ordinary polarization represented by the dotted line and the second linear polarizer removes the extraordinary light shown by the dashed line. This configuration is the “AOTF-off” state. Originally published as Figure 2 in Elash *et al.* (2016).

An AOTF for ALI was acquired from Brimrose of America (model number TEAFI10-0.6-1.0-MSD) with a Gooch and Housego driver (model number 64020-200-2ADMDFS-A). The AOTF

has a large aperture that is of imaging quality. It is optically tuned for a range of 600 nm to 1200 nm corresponding to an RF range of 156 to 75 MHz. Further the spectral resolution is 1.6 nm at 633 nm and broadens to 6.3 nm at 1153 nm with an approximate diffraction efficiency of 60% across the spectral range. The AOTF is made from a tellurium dioxide ( $\text{TeO}_2$ ) birefringent crystal. The extraordinary light is diffracted at  $2.7^\circ$  off of the optical axis of the device with a 10 mm by 10 mm optical aperture with a minimum separation angle of  $6.4^\circ$  between the zeroth and first order. The acceptance angle is  $2^\circ$  from the normal, which defines the angular spread where the AOTF undergoes efficient Bragg diffraction (Xu and Shroud, 1992). A detailed overview of the AOTF specifications can be found in appendix A.1.3.

### 3.3.2 Telecentric System Prototype

The first optical system considered for ALI is a telecentric system which allows for the images without perspective. Before the telecentric design is discussed a basic explanation of a telecentric system is described.

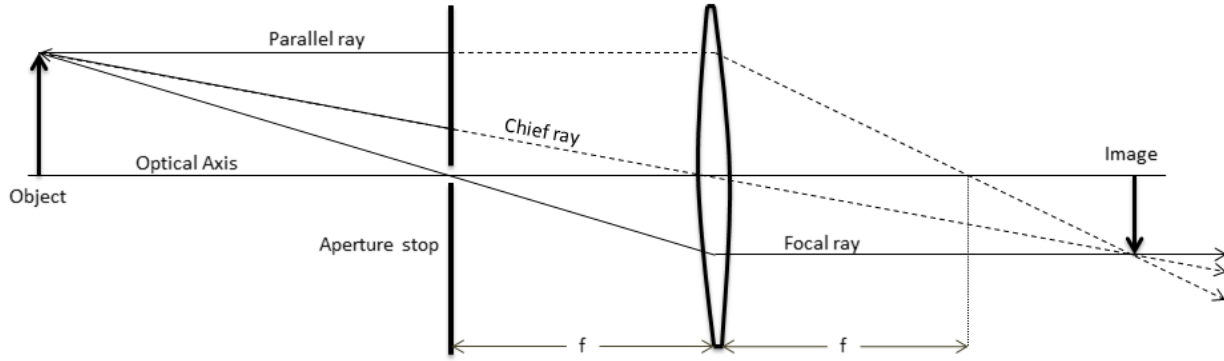


**Figure 3-6:** A standard paraxial ray tracing diagram. The aperture is located to make the system telecentric in the image plane and  $f$  is the focal length of the lens.

To describe the concept behind the telecentric system, a basic ray tracing image is shown in Figure 3-6 where three paraxial rays are drawn using a simple biconvex lens. To make this simple biconvex system telecentric in image space, an aperture is added to the system on the object side

at the focal point of the lens. The theoretical idea is to have an aperture so small that only the focal ray can pass through it. All of the other rays, including the chief and parallel ray, are blocked from entering the system. Now the image is only defined by a single ray and it is in focus everywhere on the image side of the system, and therefore has an infinite depth of field. However, an aperture that is so small proposes a few problems in practice. First, a hole of such a small size would cause diffraction effects that would dominate the imaging qualities of the system. Second, such a small aperture would let so little signal through that very long exposure times would be needed or a low Signal to Noise Ratio (SNR) would result. So in practice a larger aperture is used at the focal point. Now the system no longer has an infinite depth of field, but still retains a large depth of field and remains almost the same size no matter where the image plane is located. It should be noted that a telecentric system in object space can be created by putting the aperture on the image side of the lens causing the object to always be the same size in the image no matter where it is physically located.

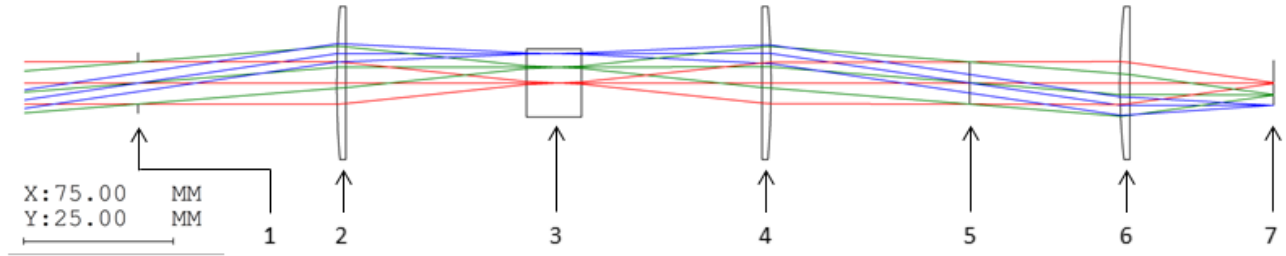


**Figure 3-7:** Ray Tracing diagram simulation of the telecentric lens system preformed using Code V. The elements in the system are the following: (1) Optical Stop and telecentric aperture. (2) 100 mm focal length plano-convex lens. (3) Brimrose AOTF. (4) 100 mm focal length plano-convex lens. (5) Telecentric Aperture. (6) 75.6 mm focal length plano-convex lens. (7) Imaging plane. It should be noted that the x and y scales are not the same in this image. Also, in the lab a polarizer is added in front and behind the AOTF as well as prisms after the AOTF.

A telecentric layout in both image and object space has advantages and disadvantages for the imaging quality of the AOTF system. An advantage is since the wavelength filtered by the AOTF is dependent on the incident angle (Equation 3.32) and from the ray tracing diagram (Figure 3-7),

all lines of sight enter with approximately the same angular spread so the filtered image has consistent wavelength and spectral point spread function. However, two problems are added to the system. First, a blurring effect is added to the final image dependent on wavelength, which is discussed below in greater detail. As well, this method is sensitive to any surface defects of the crystal since the light enters the crystal in focused bundles.

A test optical system was designed with Front End Optics (FEO) to be telecentric in both object and image space with Back End Optics (BEO) to resize the image to fit on the CCD. A list of the specifications can be seen in Table 3-1 and a ray tracing diagram from a Code V simulation is shown in Figure 3-7. The AOTF has an optical aperture of 10 mm by 10 mm and is the field stop of the system. This is a physical limit of the device and causes the Field Of View (FOV) to be limited. In order to image the vertical limb from the ground to float altitude of a stratospheric balloon, typically 35 km, a  $6^\circ$  FOV is required. Also, with the current set up of 100 mm focal length lenses, the rays of light from each line of sight enter the AOTF at the maximum acceptance angle, which is  $2^\circ$ . This allows the maximum amount of light to enter the device to achieve highest possible throughput.

**Table 3-1:** Telecentric Test System Optical specifications

Parameter	Value
Effective focal length (mm)	75.6
Front End Optics Magnification	1.00
Back End Optics Magnification	0.756
Field Of View ( $^\circ$ )	5.7 x 5.7
F-number	14.28

The image is focused on a 16-bit digital QSI 616 CCD with 1536x1024 pixels and a mechanical shutter that allows an integration time between 0.01 seconds to 240 minutes. The CCD chip itself is a Kodak KAF-1603ME with micro lenses to improve the quantum efficiency of the device and its spectral characteristics can be seen by the blue curve in Figure 3-8.

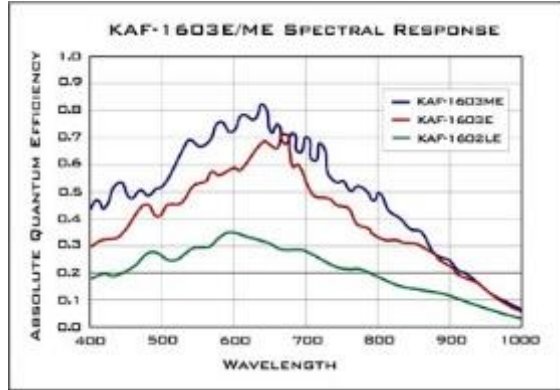


**Figure 3-8:** Quantum efficiency of the Kodak KAF-1603ME contained within the QSI CCD camera is represented by blue curve. Quantum efficiency provided by QSI Scientific.

The overall design has several aspects that make it a good system for imaging. First, all of the bundles of light entering the AOTF have the same angular spread. As seen in Equation 3.32, the diffracted wavelength depends on the incoming angle. With the telecentric layout all points of the imaging plane have the same angular dependence so the entire image is of the same wavelength and have the similar spectral PSF.

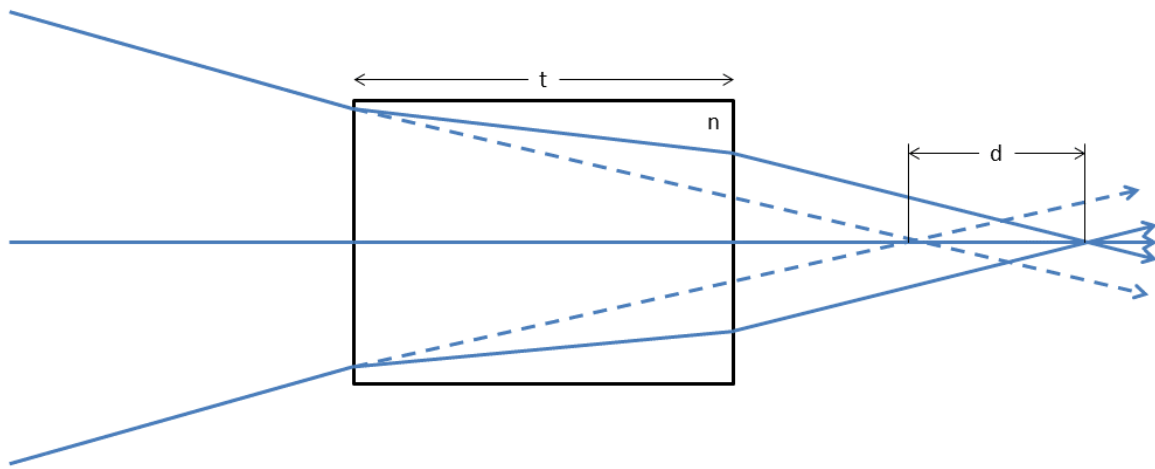


**Figure 3-9:** The effect on the optical path of converging light bundles as they pass through a material of index of refraction  $n(\lambda)$ . When the index of refraction strongly depends on wavelength, as in the AOTF, the optical path length can experience great changes that alters the focal point of the system.

However, despite its benefits, there are a few drawbacks to consider in the design as well. First, the optical path between the two 100 mm focal length lens is 200 mm in air for the prototype,

however the AOTF is made of tellurium dioxide ( $\text{TeO}_2$ ) or paratellurite and has a high index of refraction and dispersion given by (*Uchida, 1971*)

$$n_o^2 = 1 + \frac{2.584\lambda^2}{\lambda^2 - 0.1342^2} + \frac{1.157\lambda^2}{\lambda^2 - 0.2638^2}, \quad (3.33)$$

$$n_e^2 = 1 + \frac{2.823\lambda^2}{\lambda^2 - 0.1342^2} + \frac{1.542\lambda^2}{\lambda^2 - 0.2631^2}, \quad (3.34)$$

for the ordinary and extraordinary polarizations respectively. The high dispersive property, or Abbe number results in a change in the distance in the optical path,  $d$ , given by

$$d = \frac{n(\lambda) - 1}{n(\lambda)} t, \quad (3.35)$$

where  $n(\lambda)$  is the index of refraction with a wavelength dependence and  $t$  is the thickness of the crystal. The AOTF crystal causes the optical path in air to be lengthened by  $d$ , as can be seen in Figure 3-9. In order to compensate, the length  $d$  must be added to the path to account for the discrepancy, however the adjustment can only be compensated for a specific wavelength and thus a defocusing of the image plane occurs for other wavelengths. The severity of this problem can be seen in Figure 3-10 from a Code V simulation of the spot size of the optical system which was optimally focused for 800 nm. In this simulation, a grid of rays is passed through the system for each FOV and using ray tracing the final location for each FOV on the image plane are determined. The black circles represent the Airy disks, which are the minimum possible spot size possible due to diffraction for each wavelength of light. The spot sizes at 800 nm are on the order of 24  $\mu\text{m}$  at the center, which is diffraction limited, and 94  $\mu\text{m}$  at the edge of the FOV. However, for the same optical layout the 600 nm spot sizes are all greater than 160  $\mu\text{m}$  which causes a noticeable blurring in the recorded image. For a system using a telecentric system, this defocusing of the image plane would require additional compensating optics to correct the change in the path length or the detector of the system would need to be actively moved as wavelength is scanned. However, the

f-number could be increased to increase the system's depth of field to reduce the defocusing effect caused by the AOTF, but the same effect causes a reduction in signal throughout leading to longer exposure times.

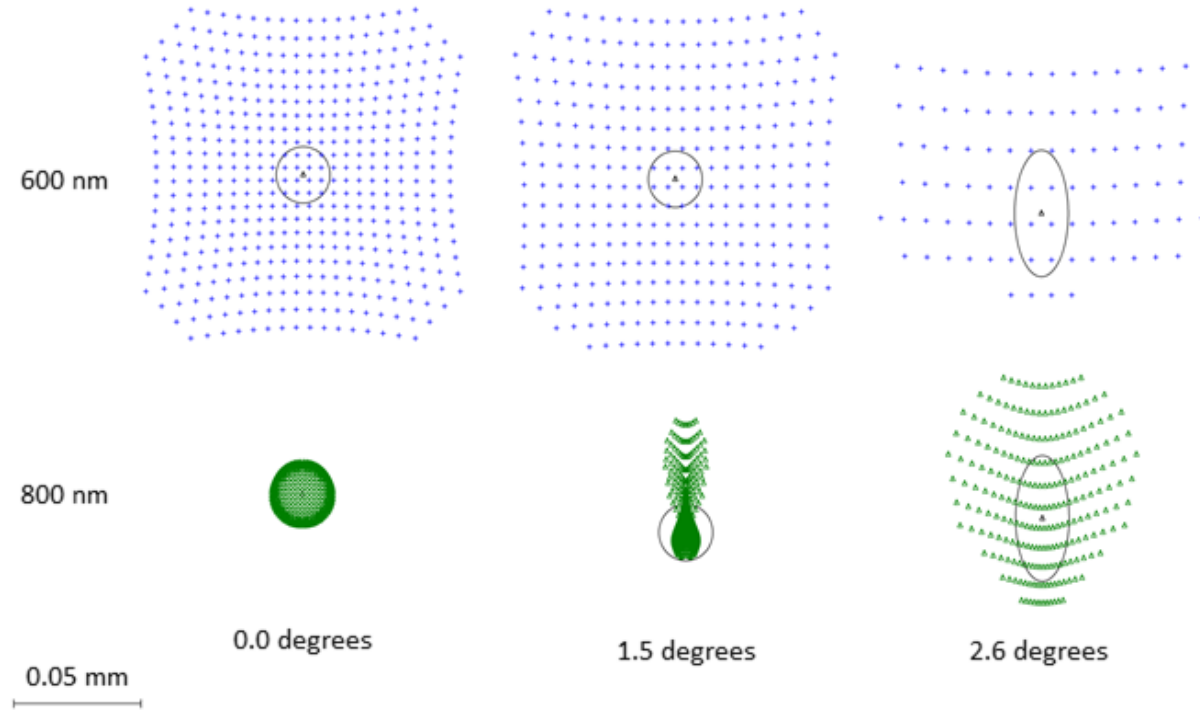


**Figure 3-10:** Code V simulation of the spot size for the telecentric system at focus at 800 nm. The spots are shown for 0.0, 1.5 and 2.6 degree fields of view at 600 nm (blue) and 800 nm (green). The full spot sizes for the 600 nm spots are 0.16, 0.22, and 0.25 mm for 0.0, 1.5, and 2.6 degrees fields respectively, with the corresponding 800 nm spot sizes being 0.024, 0.053, 0.094 mm. The black circles represent the Airy disk for each specific wavelength and FOV.

The telecentric system was breadboarded in the lab and used to image EIA 1956 standard resolution chart and the results of the test can be seen in **Error! Reference source not found.** The experimental set up is similar to the system in Figure 3-7 except for two fundamental differences. The Code V software can perform analysis for only one polarization and neglects the bend in the optical axis caused by the AOTF. However, these two issues can be dealt with sufficiently in the lab. The unwanted polarization is removed by adding a polarizer before and after the AOTF (Figure 3-5b and Figure 3-5c). The light that is actively diffracted through the AOTF is

the light that enters the AOTF crystal with extraordinary polarization. The polarizer before the device stops the ordinary polarization from entering the AOTF and the second polarizer, orientated  $90^\circ$  to the first, on the posterior of the AOTF is used to only let the diffracted extraordinary light through and removes the non-diffracted extraordinary polarization light. As mentioned in section 3.2.4, the polarization of the diffraction beam is rotated by  $90^\circ$  (Voloshinov, 1996). The second issue to be handled is that the AOTF bends the optical path by  $2.7^\circ$ . Two prisms were added after the AOTF to straighten out the optical path; the optical path past the prisms is parallel to the original optical path and is offset by approximately a millimeter and obscures a part of the FOV. The resolution chart was positioned so that the loss of the FOV due to the prism compensation was accounted for by a shift in the vertical location of the resolution chart.

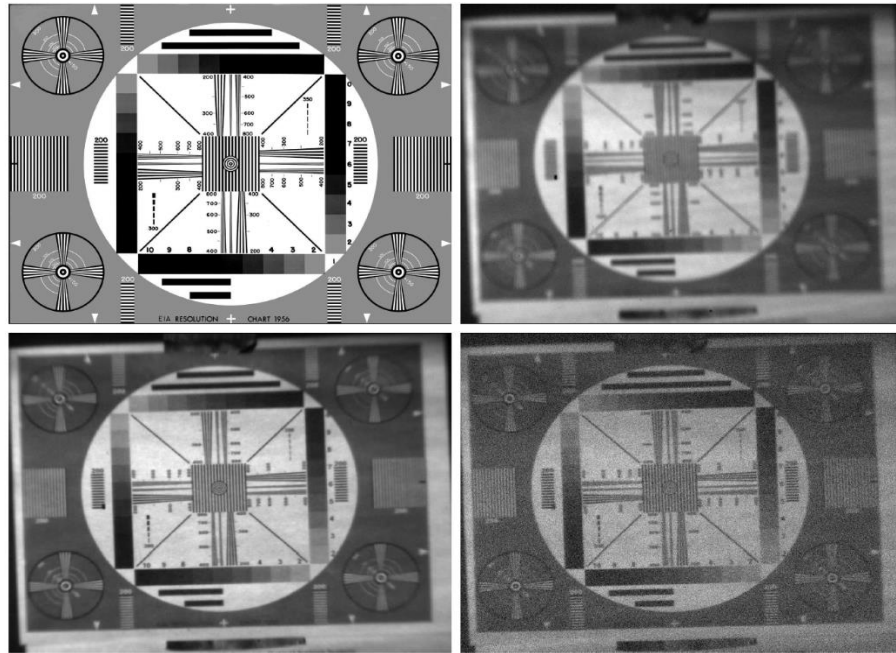


**Figure 3-11:** The top left is the original test image used for the experiment. The top right, bottom left, and bottom right are the images recorded through the telecentric system at 650, 750, and 850 nm. The system is focused at 800 nm.

The two images were taken, an “AOTF-off” and “AOTF-on” image, at every 25 nm at wavelengths between 600 and 1000 nm using a 30 second exposures imaged on the QSI CCD

camera. The “AOTF-off” image was subtracted from the “AOTF-on” image to approximately remove the dark current, DC offset, and stray light. Three sample images can be seen in Figure 3-11 with the optics focused at 800 nm and the image blurring that was simulated in the spot size diagram can be easily noticed in the 650 nm wavelength image. The center lines of the resolution chart are unable to be resolved from each other compared to the 750 nm image. A unique line of sight can be resolved every 2 pixels in the center of the 750 nm image which corresponds to 150 m resolution at the tangent point from the balloon platform, and a 4-5 pixel resolution near the edge corresponding to about a 200 m resolution. Also due to the efficiencies of the CCD and the charts ability to reflect the longer wavelengths of light the SNR at the 850 nm image in the bottom right panel is rather low, and can be visibly seen by looking at the grainy quality of the image.

### **3.3.3 Telescopic System Prototype**

The second optical system in consideration is a telescopic optical system configuration consisting of a standard telescope for the FEO with a focusing lens. The front lens, known as the objective lens, is used to focus an object at infinity to the focal point of the lens, then a second lens, the eyepiece is used to increase the optical power of the system, that is to increase the angular size of the image with respect to the angular size of the object. The eyepiece lens is located at a combined distance of the focal lengths of both the objective and eyepiece and causes the image to be focused at infinity. However for our system the telescope is used to focus the light in order to enter the AOTF at an angle less than its acceptance angle as well as to reject light rays outside of the desired FOV. The light from each line of sight in the telescopic system enters the AOTF collimated and is focused through the BEO onto the QSI 616 CCD discussed in section 3.3.2. A detailed simulation Code V layout and ray tracing of the optical design can be seen in Figure 3-12.

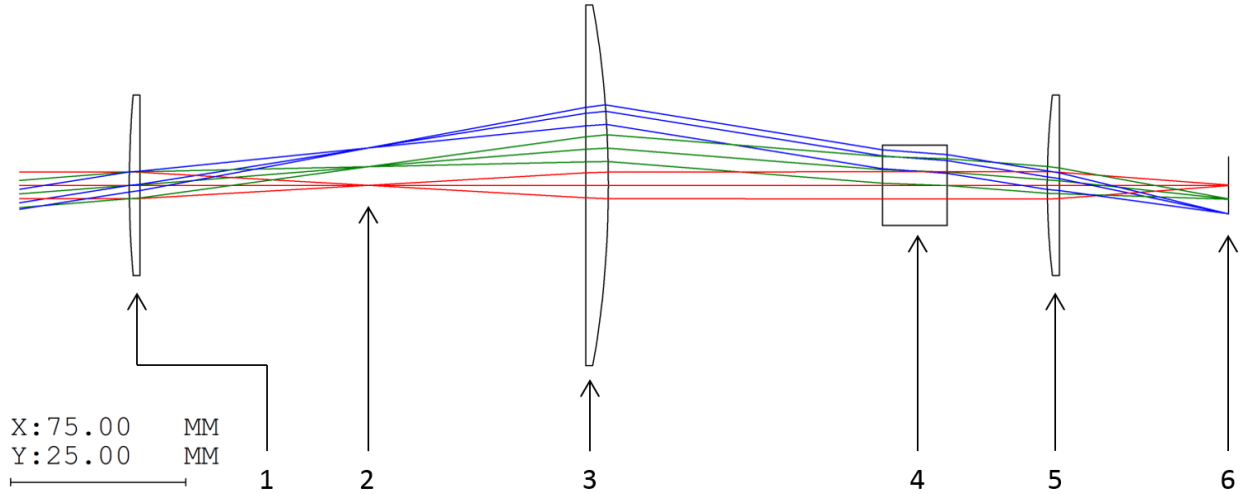


**Figure 3-12:** Ray Tracing diagram of the telescopic lens system simulated by Code V. The elements in the system are the following: (1) 100 mm focal length plano-convex lens. (2) Location where field stop is located to limit stray light (3) 100 mm focal length plano-convex lens. (4) Brimrose AOTF. (5) 75.6 mm focal length plano-convex lens. (6) Imaging plane. It should be noted that the x and y scales are not the same as Figure 3-7. Also, in the lab a polarizer is added in front and behind the AOTF as well as prisms behind the AOTF.

The telescopic prototype was designed with as many similar components and specifications as possible to the telecentric prototype in order to allow accurate comparisons of the systems without major optical effects and aberrations caused by using different materials, sizes, and focal length lenses. The optical specifications of this system are given in Table 3-2. However, there are a few fundamental differences. First, the aperture stop is located at the front lens which limits the rays of light that can enter the system, unlike the telecentric design that has a front aperture stop at the focal length of the first lens.

**Table 3-2:** Telescopic Prototype System Optical Parameters.

Parameter	Value
Effective focal length (mm)	75.6
Front End Optics Magnification	1.00
Back End Optics Magnification	0.756
Field Of View (°)	6.0 x 6.0
F-number	20

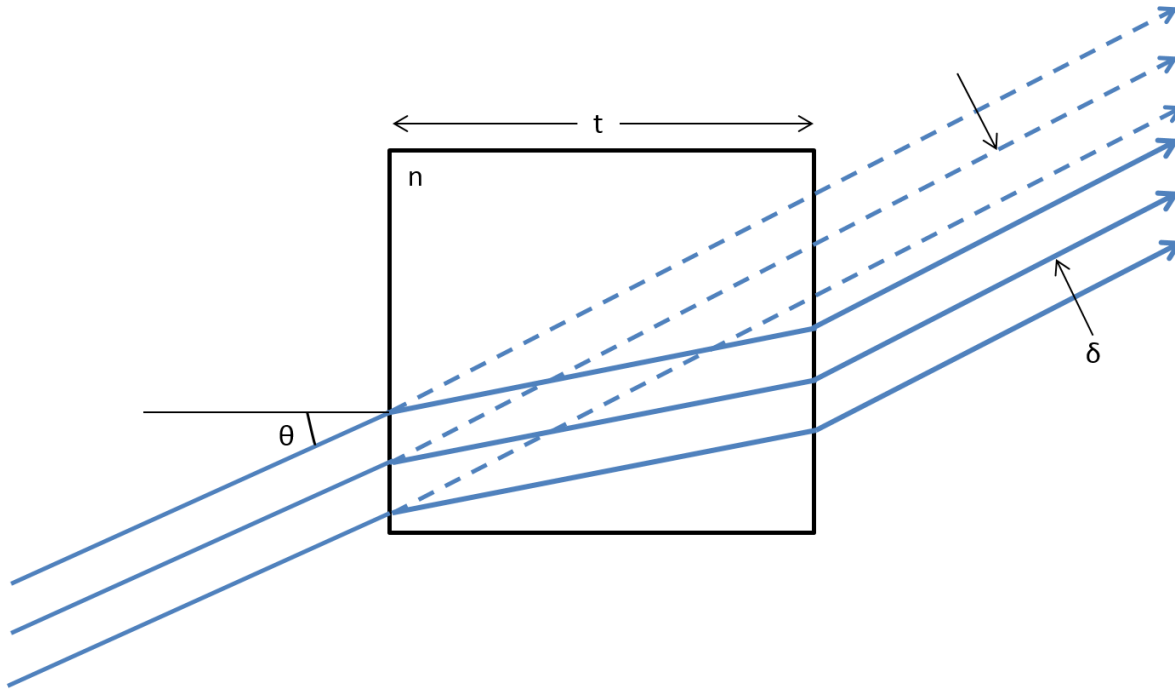


**Figure 3-13:** Vertical displacement of a collimated bundle of light cause by a material of index of refraction  $n(\lambda)$ .

The second fundamental change to the optical system is that the AOTF now has collimated light passing through the device, unlike the telecentric system, and this has a few changes to improve and degrade the imaging quality of the system. First, the primary light passing through the AOTF from a single line of sight is entering the AOTF at the same angle, so the image has a smaller spectral PSF than the telecentric counterpart; however, each line of sight is diffracted with a different fundamental wavelength due to the angular dependence in the AOTF Bragg diffraction wavelength determination (Equation 3.32). The final image has a smaller spectral bandpass but there is a wavelength gradient radiating out from the center of the image. Second, since the light now passes through the AOTF collimated, the focal point of the image no longer changes with wavelength. Instead, a lateral displacement of each line of sight occurs based on the angle of incidence and the diffracted wavelength which causes a slight magnification of the image. The lateral displacement that occurs is given by the following relation

$$\delta = n(\lambda) - 1 \frac{t\theta}{n(\lambda)} \quad (3.36)$$

where  $\delta$  is the displacement from the original path; causing a slight magnification change based on the wavelength of the light being diffracted and  $\theta$  is the incident angle on the crystal. However, this wavelength dependent change is at worst 50 micrometers for the test configuration. The effect can be seen in Figure 3-13. The last change to the system is the focusing power it possesses, as can be seen in the spot diagrams in Figure 3-14. The change in spot size due to wavelength is primarily due to the chromatic aberrations of the optical lenses. If it is desired to remove the chromatic aberration one option is to replace the lenses with mirrors in the flight version, the second option is to use achromatic doublets. The system is diffraction limited for 600 nm for all lines of sight and for 800 nm at 3.0 degrees. Also the difference in location of the spot sizes is caused by the magnification effect discussed above.

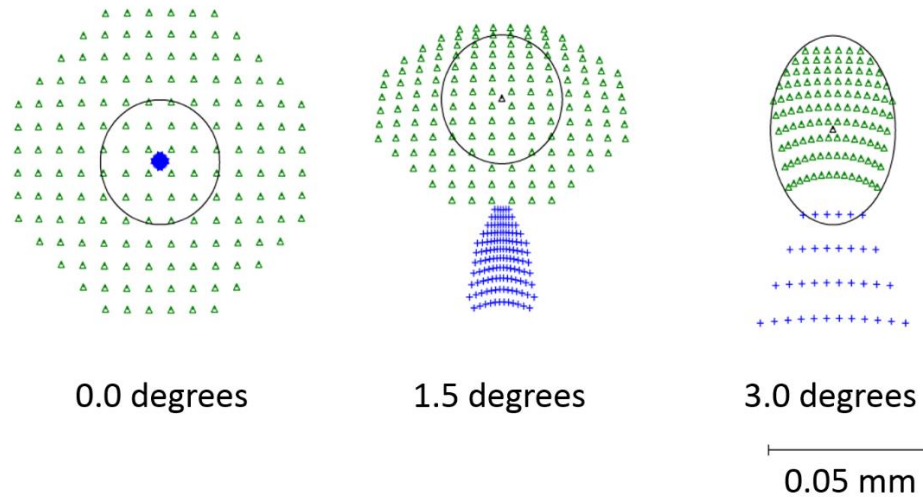


**Figure 3-14:** Code V simulation of the spot size for the telescopic system. The spots are shown for 0.0, 1.5 and 3.0° fields of view at 600 nm (blue) and 800 nm (green). The full spot sizes for the 600 nm spots are 0.004, 0.045, and 0.122 mm for 0.0, 1.5, and 3.0° fields respectively, with the corresponding 800 nm spot sizes being 0.096, 0.081, 0.047 mm. The black circles represent the Airy disk for 600 nm wavelength and each FOV.

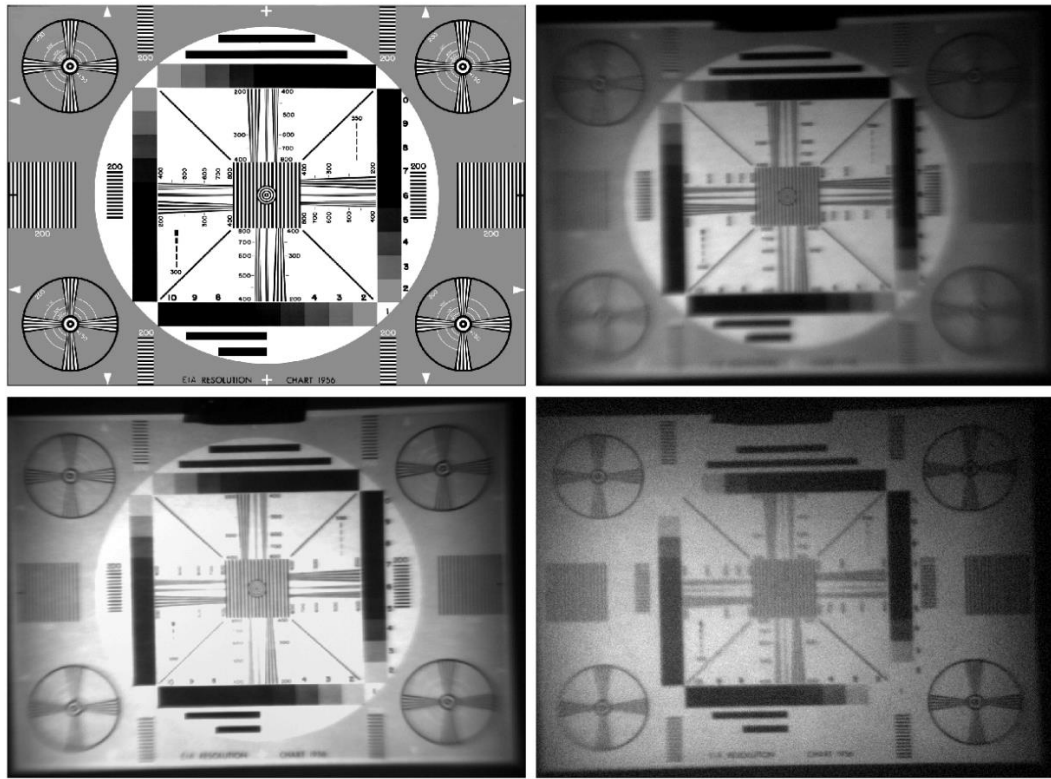


**Figure 3-15:** The top left is the original test image used for the experiment. The top right, bottom left, and bottom right are the images recorded through the telescopic system at 650, 750, and 850 nm. The system is focused at 800 nm.

An experimental resolution test was set up with the telescopic system with two polarizers and prisms added to the optical chain in the similar fashion to the section 3.3.2 experimental set up. The QSI CCD was also used with the same 30 second integration time. The results of this test can be seen in **Error! Reference source not found.**. Once again the image at 750 nm is the sharpest of the three but the center lines of the EIA 1956 test chart are distinguishable at all of the wavelengths. The blurring of the 650 nm image is caused by the chromatic aberrations of the lens and the prisms. Furthermore the prisms are removed in the final design reducing the aberrations. Also, the magnification issue discussed above is relatively insignificant in the test images and the small changes can be accounted for in the calibration of the final instrument. Lastly, the resolution

target's poor ability to reflect NIR radiation of the light source causes the 850 nm image to also have a low SNR. This issue is not be a concern for the final system.

### 3.3.4 ALI Optical Design

In light of the requirements for imaging aerosol, we have chosen a telescopic design for the ALI prototype. Since the wavelength gradient across the image is small compared to the slowly varying aerosol scattering cross section, the fixed image plane is preferable for the improvement it provides in spatial imaging, particularly as we desired to use as simple as possible an optical design.

We used a very simple three lens optical layout with commercial off-the-shelf components. Two lenses before the AOTF form a simple telescope for the Front End Optics (FEO), and a single focusing lens behind the AOTF comprises the Back End Optics (BEO). The AOTF is oriented such that the detected image is formed from the diffracted beam of the vertically polarized, *i.e.* extraordinary, light (defined at the entrance aperture). A linear polarizer (ThorLabs model number LPVIS100) with an extinction ratio greater than  $10^5$  is placed at the back of the FEO to remove the incoming horizontal, or ordinary, polarized beam. The diffracted extraordinary beam undergoes a  $90^\circ$  rotation in polarization so a second linear polarizer, oriented at  $90^\circ$  to the first, is used after the AOTF but before the BEO to remove the undiffracted beam. This is shown schematically in **Error! Reference source not found.b**. Note that even with the high extinction ratio of the polarizers, a not insignificant fraction of light that is intended to be blocked passes through the system. The diffracted extraordinary signal comprises at most a  $\sim 10$  nm bandpass fraction of one polarization such that the unabsorbed broadband signal from the polarizers can be on the same order of intensity as the diffracted signal.

The extraordinary diffracted light is  $2.7^\circ$  from the optical axis and to compensate, the entire optical chain after the AOTF is mechanically aligned with this direction. The BEO forms the image of the signal on a QSI 616s 16 bit CCD with 1536 by 1024 pixels. A ray tracing diagram for ALI's

optical system was created using the Code V optical design software and can be seen in **Error!**

**Reference source not found.** No corrections were attempted to reduce chromatic or spherical aberrations within the system and the system exhibits coma due to a large FOV and the curvature of the lenses near the edge of the FOV. Analysis with Code V shows that the distortion due to these effects across the center two degrees of the FOV is a change of less than 1% across the entire wavelength range. The final one degree shows a distortion of less than 4%. Finally the lateral displacement in the telescopic test configuration has been reduced in the final design to be on the order of a micrometer and is consider to be negligible.

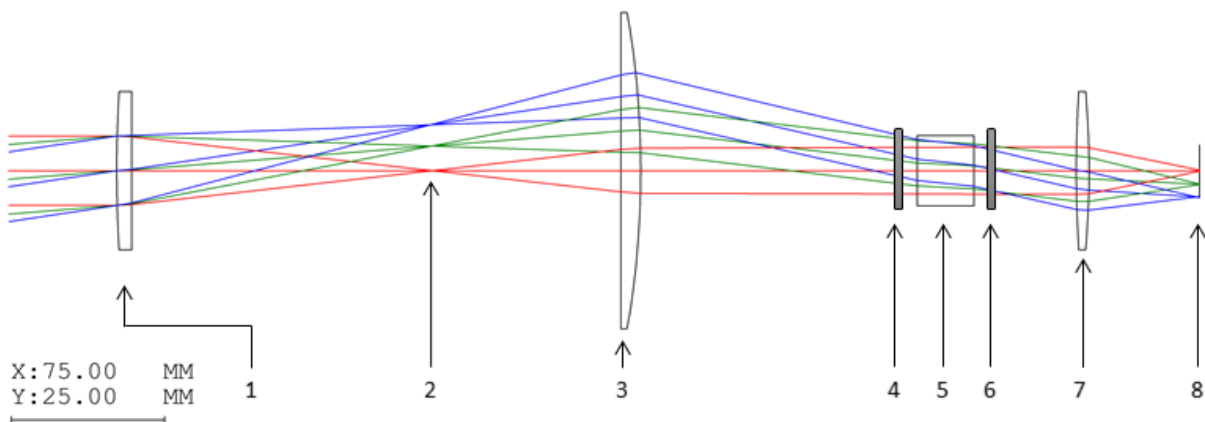


**Figure 3-16:** Final optical design for ALI with a Code V ray tracing diagram. The elements in the system are: (1) 150 mm focal length plano-convex lens. (2) Field stop. (3) 100 mm focal length plano-convex lens. (4) Vertical (extraordinary) linear polarizer. (5) Brimrose AOTF. (6) Horizontal (ordinary) linear polarizer. (7) 50.4 mm focal length bi-convex lens. (8) Imaging plane. Originally published as Figure 4 in *Elash et al. (2016)*.

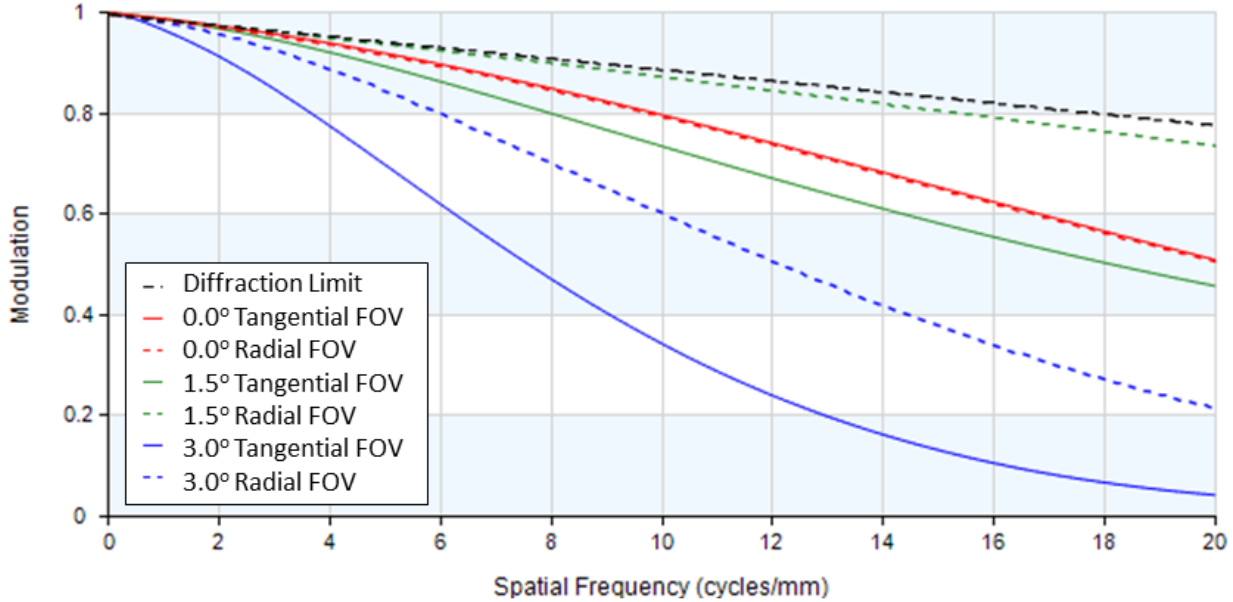


**Figure 3-17:** MTF analysis performed by Code V for the final ALI design used in campaign. The 7 pixel running average corresponds to a spatial frequency of 15.5 cycles/mm.

An analysis was also performed to determine the minimum resolution required to achieve a Modular Transfer Function (MTF) of 0.3 across the entire FOV for all wavelengths (Smith, 2000). The MTF is an optical measure of the system's ability to resolve line pairs per millimeter where a line pair is a white line followed by a black line. Generally, when increasing line pairs per millimeter leads to a decrease in the resolvability of an optical system. The MTF can be found computationally through

$$MTF(f) = \frac{I(f)_{max} - I(f)_{min}}{I(f)_{max} + I(f)_{min}}, \quad (3.37)$$

where the MTF is dependent on the frequency,  $f$ , of the line pairs,  $I(f)_{max}$  is the maximum intensity of the measured pair, and  $I(f)_{min}$  is the minimum. The MTF can vary differently with respect to tangential and radial directions of the optic system. To obtain a minimum MTF of 0.3 across the entire field, except for the 3° tangential or perpendicular FOV, a seven pixel running average is required, corresponding to a MTF frequency of 15.5 line pairs per millimeter. The 3°

tangential field being below the detection threshold of 0.3 is not a large concern since the SNR is low at the edges of the FOV and primality results in a loss of cross-track resolution at the ground and float altitude tangent points which are not critical for analysis. Furthermore, when the FOV is  $2.7^\circ$  from the normal the tangential component is above the 0.3 MTF threshold. The MTF analysis of ALI can be seen in **Error! Reference source not found..** Overall, this corresponds to an average vertical and horizontal resolution of 210 m across the entire ALI FOV at the tangent point.

A tolerance study was also performed with Code V to assess the capability of the system within the tolerances of the mounting equipment. Through a Monte Carlo method, Code V perturbs the placement and shape of the optical components within the system and computes the change in the MTF on the image plane. This analysis determines what optical misalignments or defects will degrade the performance of the system. Performing the analysis on ALI, it was determined that ALI was relatively insensitive to the tolerances of commercial off-the-shelf component used.

**Table 3-3:** Final ALI optical specifications

Parameter	Value
Effective focal length (mm)	74.3
Front end magnification	0.67
Back end magnification	1.27
Entrance Pupil (mm)	9.91
Field of view ( $^\circ$ )	6.0 x 5.0
F-number	7.5
Image size (mm)	9 x 7.5
Image size (pixels)	1000 x 800
Resolved image size (averaged pixels)	143 x 114
Spectral range (nm)	650-950

An experiment to determine the exposure times and entrance pupil of ALI is discussed in the calibrations section specifically in chapter 4 but the results of the experiment were that the ALI entrance pupil was selected at 9.91 mm to yield estimate flight exposure on the order of a second.

Furthermore, a demagnification in the FEO and a magnification in the BEO was added to further increase the light throughput to help reduce the exposure times. A summary of the optical specification for the ALI prototype is given in Table 3-3. It is important to note that a camera could not be acquired to be able to capture the entire desired range 600-1200 nm and instead a reduced range is measured from 650-950 nm. Although quality aerosol extinction measurements can still be made with this range the instrument does lose some sensitivity to particle size distributions.

It should be noted that our choice of a telescopic optical layout for ALI is actually the opposite choice of that made for the ALTIUS design, which uses a telecentric optical layout. For that instrument, the need for spectral resolution for trace gas retrieval makes the decision to use telecentric optics quite clear (*Dekemper et al.*, 2012). Given that basic design difference, the overall optical specifications are quite similar between the ALI and ALITUS prototype instruments (again see Table 3-3 for ALI specifications), although two key differences are noted. First, by using a telescopic layout the maximum FOV for ALI is determined by choosing lenses to ensure light enters ALI within the acceptance angle of the AOTF. This allows for a larger possible FOV than with a telecentric system where the field view is defined by the aperture of the AOTF. Second, the f-number for ALTIUS is 14.32 compared to 7.5 for ALI, which allows ALI to increase light throughput at the cost of slightly higher aberrations in the final image. *Dekemper et al.* (2012) reports that the visible channel of ALTIUS was breadboarded and tested by taking ground based measurements of a smoke stack plume. They used the measurements to retrieve NO<sub>2</sub> slant column density using 10 second exposure times; although, they note that an increase in measurement frequency would improve the instrument capabilities. This also factored into our decision to use telescopic optics to increase throughput for ALI. A final selection for the optical design of ALI was presented in this section as well the justifications used to determine the result. For the final

design of ALI, the telescopic system deemed to be the better option for our scientific purpose to determine aerosol extinction and engineering study to verify the capabilities of using an AOTF in space based remote sensing techniques.

### **3.3.5 Correction to the Optical Design**

It should be noted a correction to the optical design is required that was discovered after the campaign of the instrument during the analysis. The  $3^\circ$  half-angle FOV signal enters the AOTF at an angle of  $2.2^\circ$  from the normal and the acceptance angle of the AOTF is  $2.0^\circ$ . This results in a great loss of diffraction efficiency for approximately the last half degree of the FOV. This error was created when decreasing the f-number of the system to 7.5 to reduce the exposure times, remembering that lower f-numbers have higher light throughput, by adding a FEO magnification. However, this increase in throughput is overcompensated by the loss in diffraction efficiency of the AOTF in the last half degree of the FOV overall resulting in a lower SNR. To rectify this problem a slight change to the optical system is suggested in this section while still using commercial off-the-shelf components.

The main issue results about the front end magnification and the suggestion resolves around keeping a similar optical layout with a smaller demagnification in the FEO, and a compensating demagnification with the BEO to maintain the same final image size. This is performed by replacing the first lens or objective lens of the telescope (element 1 in **Error! Reference source not found.**) to a 125 mm focal length plano-convex lens and compensating the optics such that the distance between the first two lenses is the sum of the two focal lengths of the telescope. The back end lens is also replaced with a 62.9 mm bi-convex lens. This results in the  $3^\circ$  half-angle FOV entering the AOTF at  $1.6^\circ$  well within the acceptance angle of the AOTF. A table of the revised specifications can be found in Table 3-4.

This change results in several secondary changes to the system. First, the f-number is increased up to 8.0 which reduces the throughput of the system over but the last half of a degree of the FOV becomes brighter helping to reduce the vignetting and SNR drop off near the edge of the measured images. Second, the size of the image on the CCD has reduced in size which should decrease the resolution of the instrument but the decrease is partially offset by the larger f-number reducing the system aberration resulting in a final average vertical and horizontal resolution of 260 m.

**Table 3-4:** Revised ALI optical specifications

Parameter	Value
Effective focal length (mm)	78.9
Front end magnification	0.80
Back end magnification	0.98
Entrance Pupil (mm)	9.91
Field of view (°)	6.0 x 5.0
F-number	8.0
Image size (mm)	8.5 x 7.1
Image size (pixels)	945 x 789
Resolved image size (averaged pixels)	135 x 114
Spectral range (nm)	650-950

### 3.4 Opto-Mechanical Design and Thermal Balancing

Upon the finalization of the optical design of ALI, an opto-mechanical system was required for use of a stratospheric balloon. This section gives an overview of the hardware used to transform ALI from a laboratory breadboard to a flight model. The opto-mechanical design discusses the optics component framing within the system, stray light reduction, as well as the addition of a light tight case. Following is a brief overview of the thermal concerns of the system and how the system was designed to minimize the thermal risks.

### 3.4.1 Opto-Mechanical Design

After the optical system had been finalized, an opto-mechanic design to secure the optical components was required. This system needed to be able to withstand the stresses applied to the system during the launch of the stratospheric balloon and to withstand the large thermal changes that could be experienced during the flight to keep the optics in the system aligned and in focus. Furthermore, the system must also meet safety factors for torque and shock forces on the instrument so that it does not become detached from the gondola during the flight. This is to verify the safety of CNES workers who launch the balloon as well as citizens below the gondola during flight.

Consideration for thermal expansion and contraction of the opto-mechanical components also had to be considered when picking materials to house the optical lenses housing system in order to reduce the chance of any torques arising in the optical chain from thermal expansions. To reduce this effect, a consistent material was picked for the complete optical housing so all materials would have the same thermal response to the environment. The chosen material was aluminum since it is commonly used in stratospheric balloon instruments and platforms because of its light weight and relatively inexpensive cost.

With a chosen material the next design parameter was what method to use to house the optics. Commonly, space based instrumentation uses a solid piece of material that is machined into the shape required to be able to house all the optical components. However, this method is relatively expensive and is generally used for finalized space instrumentation and not for design concept prototypes. These types of cases also have a long lead-times for production and manufacturing components which would have been pressing the timeline for the launch date. The other option was to design an optical rail system primarily from off-the-shelf components from optical manufacturers, which would allow the flexibility to be able to make slight modifications to the

design without having to commission a new one-piece case allowing for inexpensive alterations to the ALI optical chain without complete reconstruction. The drawback with only using off-the-shelf components is it may be harder to maintain the alignment and resolution of the system. Considering the prototype nature of the project, the choice was made to go with off-the-shelf opto-mechanical and structural pieces for ALI with the possible limitation in alignment and resolution being classified as an acceptable trade-off.

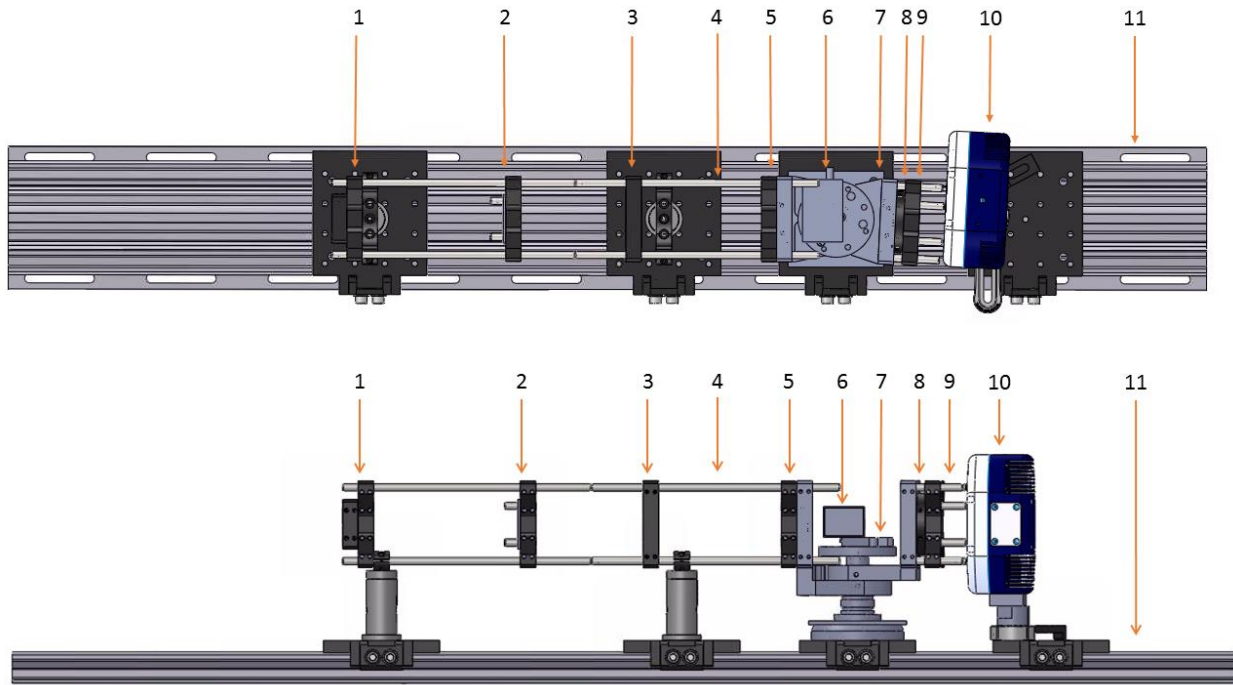


**Figure 3-18:** The final optical layout of ALI's optical chain from the top and profile perspectives with the components being the following: (1) 150 mm plano-convex lens with 25.4 mm diameter. (2) Field Stop. (3) 100 mm plano-convex lens with 50.8 mm diameter. (4) Optical rail system. (5) Vertical (extraordinary) linear polarizer. (6) Brimrose AOTF. (7) Rotation Stage. (8) Horizontal (ordinary) linear polarizer. (9) 50 mm bi-convex lens with 25.4 mm diameter. (10) QSI 616s CCD camera. (11) Optical rail.

Using components from ThorLabs, Edmund Optics, Newport, and McMaster-Carr, an opto-mechanical case was designed for ALI and the optical rail can be seen in Figure 3-18. A single sturdy wide optical rail, element 11, was used as the system base since it has the whole optical chain plus a baffle (discussed in section 3.4.2) mounted to it and would have a low suitability to

torsion. This rail would serve as a base for all the optical mounting. The opto-mechanical chain was connected to the rail using rigid optical aluminum rods. For the optical chain, an optical cage system was used since the four rods surrounding the optic mounts provided a rigid framework that would still allow for fine tuning of the optical elements. The optical cage is element 4 in Figure 3-18. Once the aligning of the optical system was completed, the components were glued into place to prevent slippage during transportation and flight.

During the testing of the breadboarded optical system in the lab, two prisms were used to account for the deviation in the optical chain caused by the AOTF. These prisms were removed in the final design by bending the BEO of the optical chain by  $2.7^\circ$  through a rotation stage (element 7). The removal of the prisms further reduced distortions within the system as mentioned in section 3.3.4.

It should be mentioned that optical lenses for ALI were repurchased for the final system with the addition of antireflection coatings. An antireflection coating would increase the systems efficiency as well as reduce internal reflections. From ThorLabs, a B-type antireflection coating was ordered for the lenses which reduces reflection from each lens surface down to an average of less than 0.50% from 650 to 1050 nm instead of an approximately 8% loss per surface from an uncoated lenses. The lenses also had a 1% tolerance in the focal length and made from grade A NBK7 glass.

A selection of linear polarizers were considered for elements 5 and 8 in the opto-mechanical system. However, the wavelength range of ALI made standard polarizers difficult to locate which limited the possible choices. A nanoparticle linear film polarizer from ThorLabs was eventually decided upon (model number LPVIS100) for ALI since it gave an extinction ratio better than  $10^5$  for 650 to 1200 nm completely covering ALI operating range. The extinction ratio is defined by

the ratio between the maximum transmission when the polarizer's axis is aligned with the signal to the maximum transmission after the polarizer has been rotated by 90°.

For the opto-mechanical design special consideration had to be given to mounting the AOTF and CCD camera. Both of these elements are non-standard sizes in optics and no preexisting components could be purchased to mount these pieces. Therefore custom mounting hardware had to be used to rigidly mount these components. Both components were designed through the use of the SolidWorks design software.

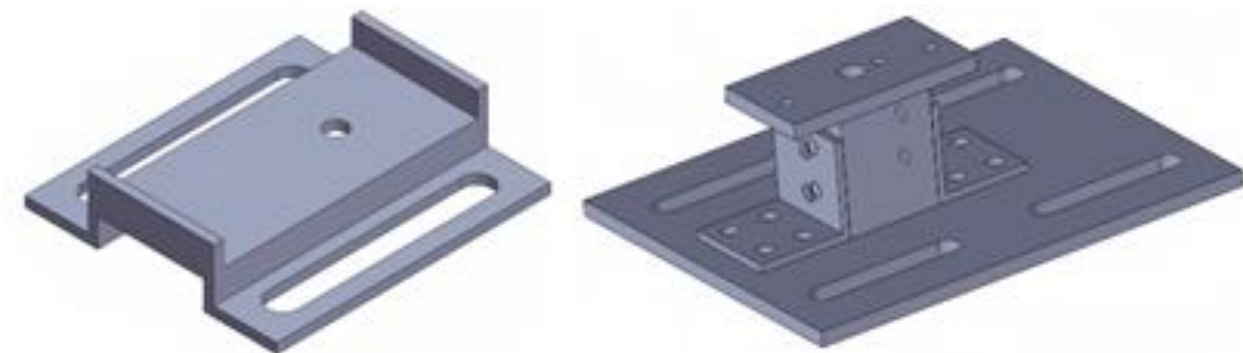


**Figure 3-19:** The custom mounting hardware design to mount the AOTF and QSI CCD camera into ALI's opto-mechanical design. Left: Custom AOTF mounting hardware. Right: The five piece QSI CCD camera mounting hardware.

The AOTF had one usable mounting hole on the bottom of the device to affix it to the optical chain. However, directly mounting the device onto the rotation stage would result in the AOTF being offset downward from the optical path. Furthermore, with only one mounting point there was concern for rotation of the device rotating during the flight which would not be able to be mitigated. A single piece was designed that lightly clamped the AOTF onto the top of the mounting hardware to lock the AOTF's rotation axis. To affix the custom AOTF mount to the optical system four tapped screw holes were utilized on the top of the rotation stage. On the base of the AOTF mount two slot screw holes were used to be able to correctly align the AOTF within the optical chain when affixing it to the rotation stage which can be seen in the left side of Figure 3-19.

The mount for the CCD camera had a different set of requirements; mounting holes were available for use on the bottom of the camera but the camera mount needed to be able to securely hold the relatively heavy camera into place with very little available vertical space (~6 cm) between the base of the rail mount and the camera. A five piece mount was designed that would fit in the tight space and be sturdy to support the mass of the camera seen in the right side of Figure 3-19. The base plate perfectly fits onto the optical rail mount and the slotted holes allow for horizontal alignment of the camera with the optical axis. The vertical alignment to the optical axis is correctly set with the height of the camera mount. Also, the CCD sensor on the QSI camera is offset to one side and the mounting hardware accounts for this displacement.

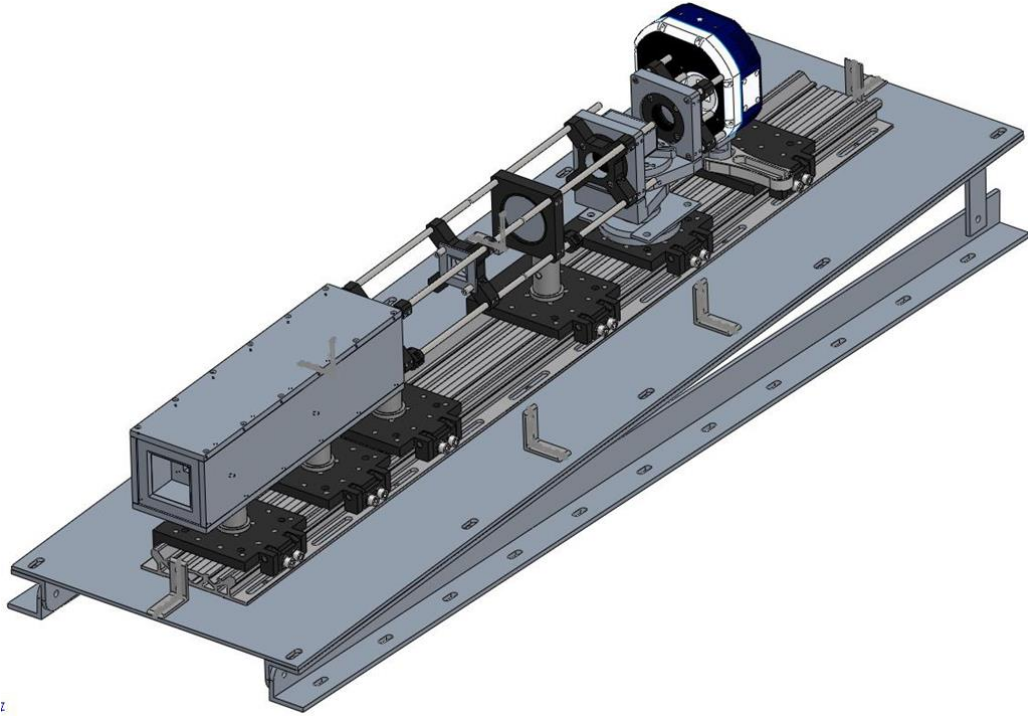


**Figure 3-20:** ALI opto-mechanical system with three degree horizontal tilt and designed baffle discussed in section 3.4.2. Originally published as Figure 5 in *Elash et al. (2016)*.

The ALI system is tilted three degrees from the horizontal so that the FOV of the instrument from the balloon flight geometry would measure from the ground to the balloon float altitude. A

SolidWorks rendition of ALI with the three degree tilt from the horizontal can be seen in Figure **3-20**.

Finally, mounting hardware was tested through simulations done by the CSA to verify that the safety factor of the system was met, which it passed. The test was a stress analysis of the mounting points of the ALI system to the gondola and itself.

### **3.4.2 Baffle Design**

A major concern with any optical instrument is the presence of unwanted or stray light. Two types of stray light are commonly defined: internal and out-of-field stray light. Internal stray light is unwanted light that passes through the system through scattering, reflections, or imperfections in optical elements. Out-of-field stray light is light that enters the optical path but originates from outside of the FOV. A long standing concern in the design of limb scatter instruments is the effective rejection of out-of-field stray light. This is due to the bright surface very near to the targeted limb in combination with the exponentially dropping limb signal with tangent altitude. For ALI test observations from the stratospheric balloon, a front end baffle was incorporated.

When designing a baffle several design aspects need to be determined. Consideration must be given to the length and width of the baffle as a larger, well-designed baffle is able to more efficiently remove out-of-field light but increases the size, mass, and cost of the instrument. Furthermore, the number of vanes in the baffle design must be considered. More vanes help to remove additional out-of-field light but each vane adds an edge that light can scatter off which may introduce more stray light into the system. A balance must be met with the size and number of vanes in the ALI baffle to best remove out-of-field stray light.

The first point of the discussion is the height and width of the baffle. In a baffle system, the larger the baffle is by cross-sectional area the better the baffle can be designed to reduce stray light. However, there is a limited amount of space to build the ALI instrument and the baffle must

share space with optics, electronics and power systems; and as such, a size that fit these constraints had to be selected. An internal height and width of 70.00 mm was chosen since this was the size of the optical rails used to house the optical chain and the instrument could not be any taller than the height of the optical rail to meet size constraints.

The length is also limited by the space available, as well as the FOV and entrance aperture size. The baffle must be short enough so that the size of the FOV does not become larger than the cross-section of the baffle. To maximize the effectiveness of the baffle the longest possible length that could be accommodated was selected and was 300 mm in length.

Also, one always needs to make sure the optical stop located within the baffle is placed at the same location as the optical design. If the location of the optical stop is changed from the baffle design, it affects the performance of the instrument itself. If the optical stop is moved further from the optical design specifications, the FOV remains the same but limits the amount of light that enters the system. Thus changing the overall f-number of the system either increases the exposure times or decreases the SNR. The other case is if the optical stop is moved closer to the optical system. The opposite problem occurs which is more light enters the system than the system was designed for causing an excess of stray light and rendering the baffle ineffective.

The baffle system is designed such that it minimizes the percentage of out-of-field stray light that enters the system without encountering at least three baffle surfaces. This method, the optimal baffle geometry, is standardly used in optics to minimize stray light (*Fischer, 2008*). In the system, the baffles are spaced in such a way that little stray light cannot enter the system without coming into contact with at least three surfaces reducing the overall intensity of the stray light.

The optimal baffle geometry design method is described. In Figure 3-21a the base baffle case is formed with the critical baffle vane at the entrance to the optical system (-250 mm) and a second

vane is located closest to the optical chain. It should be noted that a reduction in the length of the baffle to 250 mm occurred so that an exterior baffle could be added to reduce surface reflections. The marginal rays of the optical system is represented by the red line.

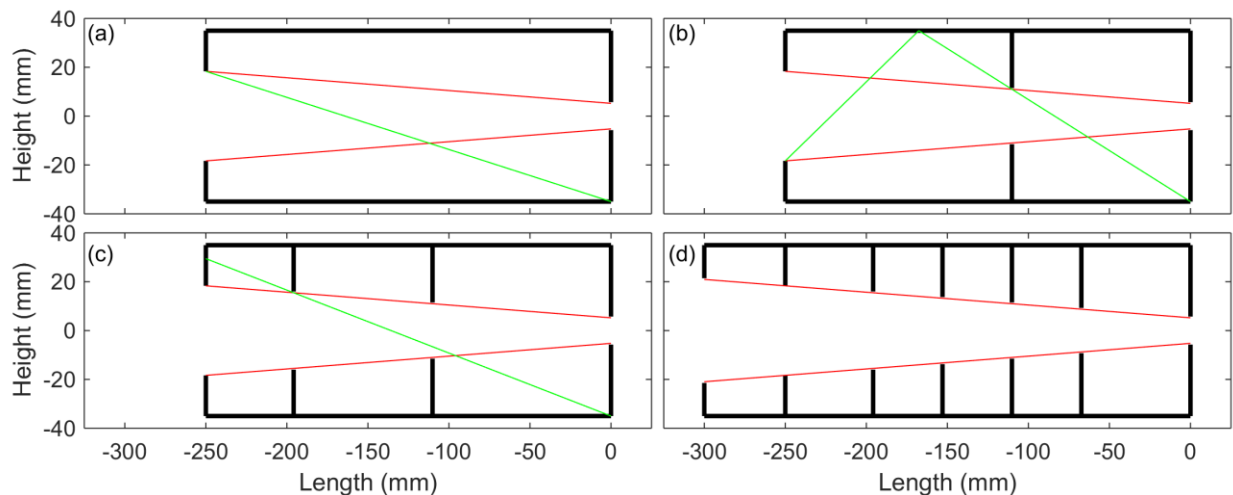


**Figure 3-21:** (a) Start of the optical baffle geometry method. The red lines are the marginal rays and the green line is the first ray that can enter the system without encountering at least three surfaces. (b) The first internal vane has been added and the location of the next vane is being determined. (c) The second internal baffle has been added and since the green line intersects with the critical baffle no more baffle are required. (d) Additional interior vanes and an external vane have been added to ensure a height to pitch ratio of 0.5 to improve the baffle's capabilities to reduce stray light.

Next, an indicator line is drawn from the bottom right corner of the baffle to the opposite tip of the critical baffle, represented by the green line. This line represents the first ray that can enter the system without coming into contact with at least three surfaces. The next vane is added where the indicator line and marginal ray intersects, and has been added in Figure 3-21b.

The next indicator line goes from the bottom corner to just passing the newly inserted vane and encounters the outer side of the baffle wall. The line goes through a reflection and passes just by the critical baffle once again. The intersection of the second segment of the indicator line and marginal ray is where the second vane is added as in Figure 3-21c.

The process is then repeated to determine the location of any additional vanes. For the ALI baffle, the indicator line no longer is able to reflect upon the top baffle surface and therefore the minimum level of baffles have been achieved. However, two extra internal baffles and one external baffle were added to the design (Figure 3-21d). The exterior baffle was added to help further reduce stray light from surface reflection by shielding the critical baffle from the direct ground reflections. The additional interior baffles were added to achieve a height to pitch ratio greater than 0.5. If the height to pitch ratio is less than 0.5, additional stray light enters the optical system due to the high amount of empty space within the baffle (Fischner, 2008).

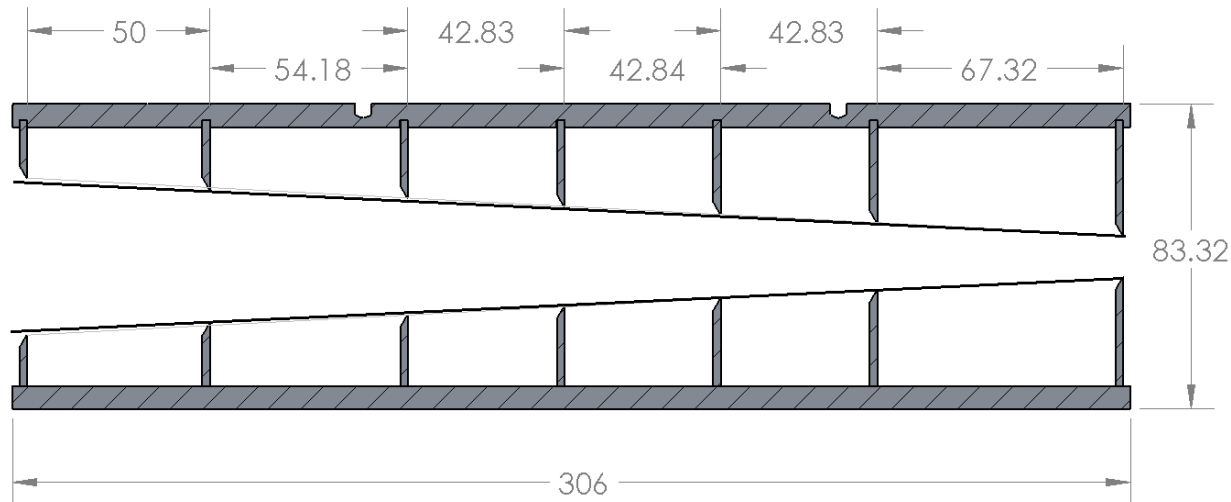


**Figure 3-22:** A cross-section view of the ALI baffle system. All dimensions on the drawing are in millimeters and the sloped black lines represent the 6 degree FOV.

With the completed design, a drawing needed to be created to machine the baffle accounting for machining tolerances. With the exception of the critical baffle all of the edges of the vanes were reduced in size by 0.5 mm so that they could be produced within possible machining tolerances and not limit the FOV by being too tall. A SolidWorks version of the baffle can be seen in Figure 3-22 which accounts for the thickness of the materials and machining tolerances.

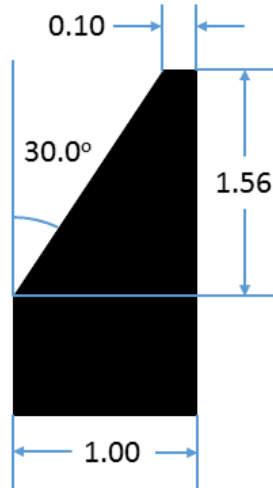


**Figure 3-23:** ALI baffle vane profile. Dimensions are in millimeters.

Ideally, the edges of the vanes would be machined to a fine blade. However, this is not practical for two reasons. First, the baffle's edges would be prone to damage causing dents or grooves in the vane cross-section possibly producing unwanted scattering effects. Second, it is only possible to machine the tips so fine with tolerances without reducing the height of the vane.

**Error! Reference source not found.** shows the profile for the baffle vanes as they were machined. A final assembly of the optical system can be seen in Figure 3-24.

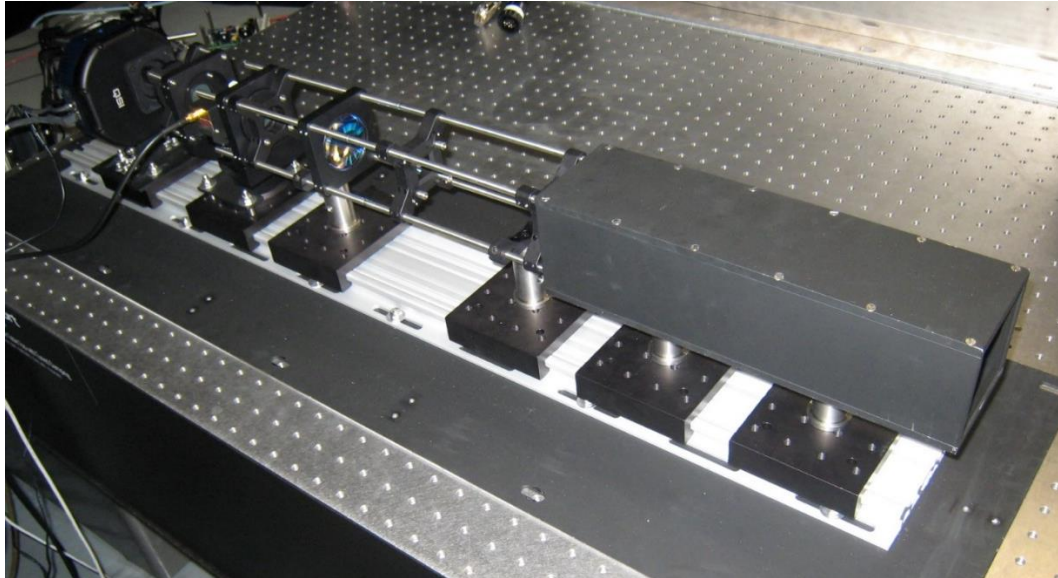


**Figure 3-24:** Final ALI optical and opto-mechanical assembly.

### 3.4.3 Light Tight Case

To complete the opto-mechanical design, a light tight case was required. The case was made out of aluminum and every connection point in the case was overlapped, through interlocking pieces, to verify the rejection of the light. The light tight case was clamped onto the base plate of ALI and a final rendition of ALI can be seen in Figure 3-25.

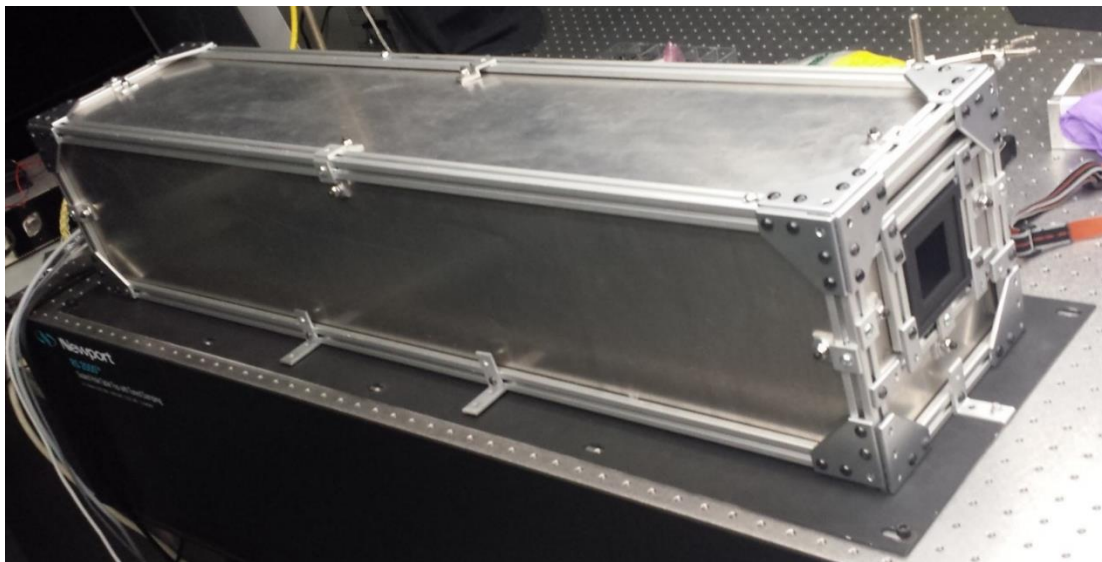


**Figure 3-25:** ALI optical system with light tight case attached. Three degree horizontal tilt not present in this image.

### **3.4.4 Thermal Considerations**

An instrument, like ALI, has to survive the possibility of extreme temperatures during a flight on a stratospheric balloon. The extreme temperatures arise through various processes, first the instrument must survive the ascent through the tropopause where temperatures can reach -70°C and must survive the float temperatures which can be as cold as -50°C. Conversely, being exposed to direct sunlight causes heating that would result in instrument failure due to overheating. Furthermore, ALI using simple opto-mechanical design means there is no active thermal control and, with the reduced atmospheric density at approximately a float altitude of approximately 35 km convective cooling could not be relied on for thermal control. Following is a discussion of various thermal concerns within ALI.

The electronics are stored within two aluminum cases, a computer case and power supply case. All components within the two cases are all rated for an extended thermal range (-40 to 85°C) except the RF driver which has an operational thermal range of 0 to 50°C. The extended range of the all other electronic components reduces the concern since this case is not be exposed directly to the elements as they are sheltered via insulation and, from consultation with the CSA and CNES teams, the internal temperature of the electronics area from previous missions have reached a coldest temperature of approximately -20°C during normal flight operations.

However, the RF driver does not fall into the specified temperature range, which is a problem, and the driver also produces a large amount of heat that is convectively cooled in the laboratory which is not possible at float due to the reduced atmospheric pressure. Since the RF driver is a fundamental piece of hardware, failure in the component would result in a primary system failure.

To mitigate the risk, several considerations are made with regards to the RF driver. First, a RF driver with a cooling plate is purchased to better allow for conductive thermal control and without

any method of cooling the driver on the gondola the driver would overheat and fail. So the driver is mounted to the aluminum case such that the cooling plate would be in direct contact with the surface of the case, and the case would be mounted on the gondola such that the surface of the case would be against the aluminum mounting surface on the gondola. This allows a large amount of heat to be dumped to the gondola to keep the RF driver within the operating range. Second, the driver freezing was not as large of a concern since the driver produced enough heat to sustain its temperature. However, the driver would be both on and off during the mission for different imaging modes which may result in freezing or overheating. A temperature sensor is used to monitor the driver and the control software on board ALI has a safety measure built in that would automatically turn the driver off if it reached 50°C or turn on if the temperature dipped below 0°C.

Another region of concern was the housing of the optical system which would be directly exposed to the elements. The optics would expand and contract based on the temperature and CCD camera had an operating temperature of -40 to 20°C. Furthermore, the CCD primarily used convection to cool the camera; by recommendation from QSI, fans were disabled as they would rip apart due to the low atmospheric pressure since the rotation speed is based on air resistance. To mitigate the thermal risk, a twofold approach was taken. First, the optical housing was surrounded in foam to thermally insulate it from the cold experienced during darkness and ascent through the tropopause. Second, the foam insulation was covered in a reflective material to reduce direct warming from the radiation from the sun.

# CHAPTER 4

## CALIBRATIONS AND CONTROL SOFTWARE<sup>2</sup>

### **4.1 Introduction**

A finalized ALI instrument has been developed and constructed through careful considerations of optical and opto-mechanic concerns. The special requirements of the AOTF and balloon platform were met within the design of the system. However, the completed system required calibration and testing to achieve high quality measurements. Additionally, control software to operate the system from the balloon platform is required. This chapter focuses on discussion of the control software written for ALI and following are the calibrations preformed to achieve high quality radiance measurements. For the calibration experiments the AOTF used in ALI is characterized followed by the calibration of the entire system. Finally, a fully integrated test of the ALI system is underwent as a final test before the stratospheric balloon flight in Timmins, Ontario.

### **4.2 Control Software**

During the stratospheric balloon flight, software is required in order to control the instrument from the ground and have it operate in the air. Two separate software packages were developed to accomplish the communication and control systems required for the mission. First, a ground control platform that communicated to ALI which received diagnostic information, completed images, and sent commands to be processed. The second software package was the onboard system that controls the instrument systems.

The ground control software contains the module that is responsible for establishing communication with ALI, handling any loss of information during data transfer, decoding the data from the ALI flight software, as well as uploading commands to the instrument. The software

---

<sup>2</sup> Portion of sections 4.3.1, 4.3.2, 4.3.3, 4.4.4 and 4.4.5 as well as **Error! Reference source not found.**, and Figure 4-7 were originally published in *Elash et al. (2016)*

onboard ALI is more complicated with different modules to handle the different aspects of the hardware and control systems. The onboard ALI computer system is a Debian Linux operating system with multi-threaded C++ based software that controls the hardware and science data collection operation. The onboard computer is a VersaLogic PC-104 OCELOT computer with fanless operation and a thermal operating range of -40 to 85°C. The flight software contains five different modules to handle different functions of the system. The five modules are the main module, communication module, diagnostics module, science module, and local storage represented in Figure 4-1 by blue, green, orange, purple, and yellow respectively. A brief overview of each will follow.

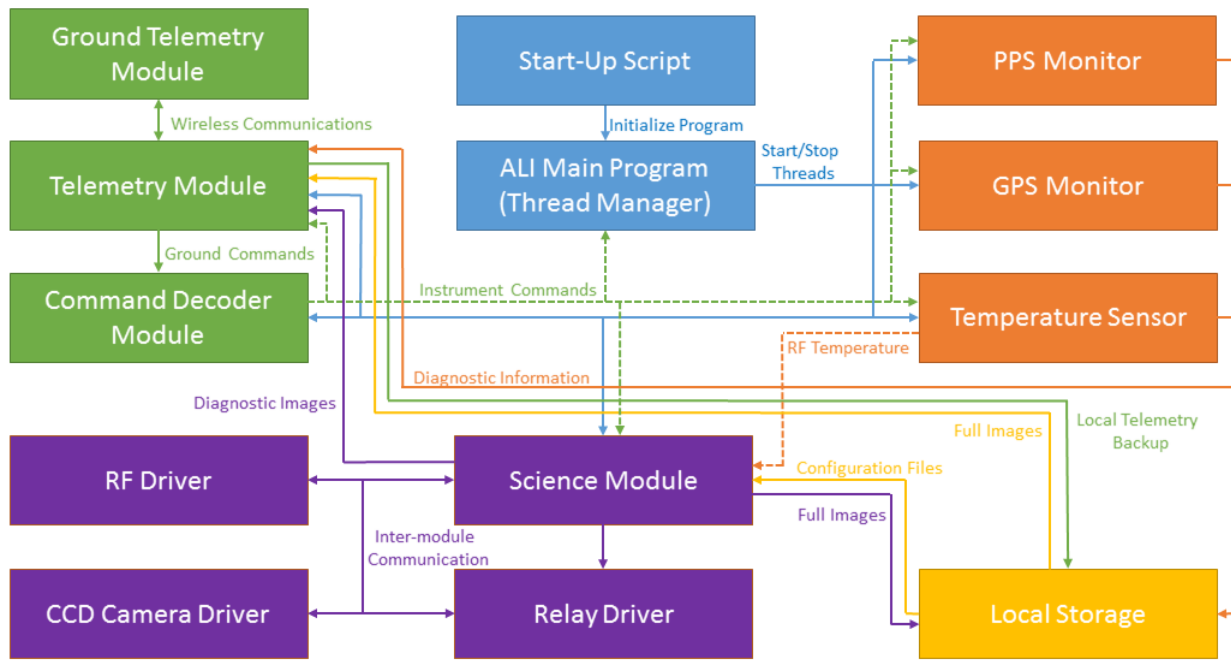


**Figure 4-1:** A complete flow diagram showing interaction between all the modules of ALI software on the on board ALI flight computer.

The main module consists of a bash script which initiates the ALI C++ flight program during startup and can be restarted from the ground upon a software failure. Once the main program has

been started by the script, the thread manager initializes all of the individual threads for the other processes and then waits for a termination command to close the ALI flight software.

The first module started by the thread manager is the communications module which operates the telemetry or communication between other modules as well interactions with the ground control software. The module sends and receives all data packets that are outgoing and incoming through UDP protocol as required by the CSA and CNES specifications. Also, data rate limits were imposed on the instruments to avoid one instrument using all the bandwidth to transfer data from the gondola. For ALI the limit was 100,000 bits per second. The communication module was responsible for verifying that this limit was obeyed when encoding into packets and sending them to the ground. Also, uploaded commands are decoded and sent to the command decoder which takes all the incoming commands from the ground, parses the information, and sends the commands to the proper modules. A full list of commands can be found in section B.1

The diagnostic module manages the Global Positioning System (GPS) information, pulse per second ping, and voltage and temperature sensors. The GPS monitor records the current location and height of the instrument from the front of ALI optical instrument. The pulse per second is a signal that is sent out from the gondola's SIREN module (a device used for the gondola's communications and telemetry system) every second. It is a constant signal between all instruments on board to correlate each systems data to each other. The voltage sensors verify that the voltage levels stay within the electronics specified ranges. Lastly, the temperature sensor module reads all of the temperature sensors from a one line temperature sensing device, where all temperature sensors are connected with a simple RS-232 connection. The locations of the temperature sensors can be seen in Table 4-1 and the locations attempt to achieve a complete temperature profile of the instrument. All information gathered by the diagnostic module is sent to

the telemetry system so the ground user can determine the state of the system and make any required changes. The data is also stored on the local hard drive (solid state) onboard ALI for use when ALI is recovered after the flight.

**Table 4-1:** Location of ALI temperature sensors.

Number	Sensor Location
1	Aluminum wall of electronics case
2	Cooling plat of RF Driver
3	OCELOT CPU heatsink
4	Aluminum wall of power supply case
5	5 V power supply transducer
6	12 V power supply transducer
7	Front of ALI baffle just inside system
8	On the CCD camera

The science module operated the ALI instrument, the acquisition of data, and directly controls the relay to the RF driver, the QSI CCD camera, and the RF driver. The science module loads program defaults upon startup from local storage or program settings can be altered from ground control. Each of the modes for data acquisition has its own configuration file and the supported modes are a calibration mode, an aerosol mode, an H<sub>2</sub>O mode, an O<sub>2</sub> mode, a constant exposure time aerosol mode, and a custom mode. The details for these mode can be found in appendix B.2.

When the science operations are enabled ALI loads in an operational mode as specified from the ground. The science mode controls all of the hardware and process the imaging cycle and two types of images are created. Full images that contain the entire image are sent to local storage due to bandwidth considerations and diagnostic images are transmitted to the ground that contains the required information to verify the success of the flight operations and instrument in case the local solid state data is not recoverable after the balloon flight. When the mode is completed the same modes are repeated unless ALI has received a command to stop acquiring images or is queued to start another mode.

Each diagnostic image contains five complete vertical columns of measurements with statistics on the entire image, including percentages of saturated and under-saturated pixels, as well as the location and time of the measurement and the current state of ALI. There are two reasons to include diagnostic images. First, having diagnostics on every image gives the users real time information if the measured data is saturated or under exposed and adjustments can be made during the mission. The second reason is there is no guarantee that when the gondola lands ALI will survive. The balloon can land in water or crash land destroying the stored data. In case of such events, some data is sent down for every image so analysis and results can still be acquired from the ALI mission and can be used to verify the feasibility of the technology. Lastly, any extra bandwidth that is not allocated to other processes is used to transmit complete images down to the ground for complete horizontal and vertical verifications of the ALI instrument.

### **4.3 AOTF Calibration**

The calibration of the AOTF is performed within this section. The AOTF is from Brimrose of America and the specifications can be found in appendix A.1.3. The AOTF needed to be fully calibrated to expand upon the factory specifications to be able to accurately use the AOTF within the ALI system. The calibrations preformed on the AOTF are:

- A tuning curve analysis
- A point spread function analysis
- Diffraction efficiency determination.

#### **4.3.1 Tuning Curve Analysis**

A tuning curve related the applied RF wave to the diffracted wavelength, and must be accurately known to determine the wavelength being measured, and directly affects the aerosol retrieval. The form of the tuning curve can be seen in Equation 3.32. To determine the curve for the AOTF within

ALI a test optical set up was devised in the lab to determine the central diffracted wavelength as a function of the selected RF,  $F$ .

For this analysis, a telecentric test layout was used, the details of which are described in section 3.3.2. An advantage of the telecentric testing layout is that the wavelength dependence of the acousto effect from the incident angle, noted in Equation 3.32, is removed since all the lines of sight enter the AOTF with the same angular spread. The experimental set up consisted of the AOTF centered between two 100 mm focal length lenses to optimally fill the AOTF aperture. Linear polarizers were inserted before and after the AOTF to remove unwanted polarizations. An aperture was set up in front and behind the AOTF in the optical chain at the focal length of the front and back lenses respectively and opened to 5 mm to complete the telecentric experimental layout. The high front end f-number of 20 required long integration times to capture sufficient signal. It also enabled the system to have a much higher degree of telecentricity. Two prisms were used to compensate for the  $2.7^\circ$  off axis bending to set the light parallel to the optical path. A standard 100 W tungsten halogen bulb was used as a light source. The front end optics had no magnification and back optics were used to match the f-number of the spectrometer's input optics. The layout can be seen in Figure 4-2.

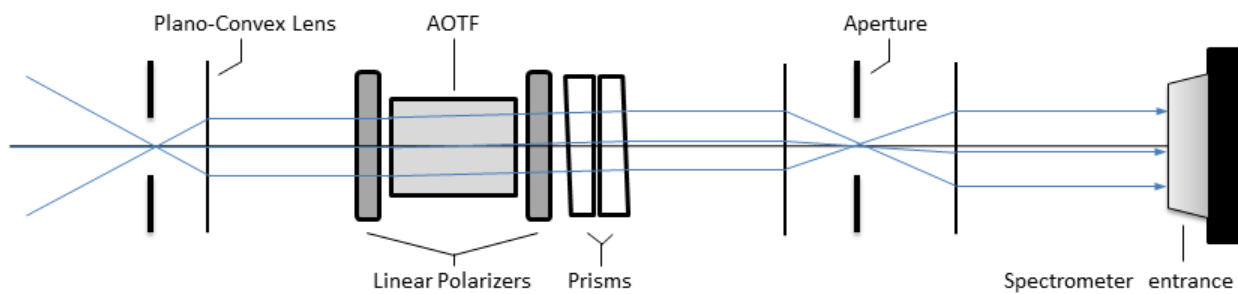


**Figure 4-2:** Telecentric test experiential setup for AOTF parameter determination. All lenses and apertures are represented by the same symbol.

The output is passed into a HORIBA iHR320 spectrometer with a 1200 lines/mm grating blazed at 750 nm and is imaged on a Synopse 354308 front-illuminated CCD detector with 1024x256 pixels. The CCD is thermoelectricity cooled to -75°C to reduce any significant dark current contributions to the measurements. The signal entering the spectrometer optics were well collimated and limited the amount of stray light.

Images were taken at a set of RFs spaced every 150 kHz from 160 MHz to 75 MHz nominally corresponding to a 1 nm resolution. The spectral images were recorded with the spectrometer slit at 0.5 mm making the minimum Full Width Half Max (FWHM) of the spectrometer 1.175 nm with a normal distribution, which is less than the minimum factory specified resolution of 1.6 nm. The final recorded spectra would be a convolution of the PSF of the AOTF and spectrometer, however this will have a small effect on the determined spectral resolutions by making them appear to be slightly larger than the AOTF itself, but with the broadband nature of aerosol scattering this is not a large concern since the true PSF will be better than that measured. At each RF two images were taken with a 15 second integration time: one with the AOTF in its on state and another with the AOTF in its off state. The stray light, dark current, and the DC bias are recorded in the image with the AOTF off and can be removed from the AOTF spectral image by taking the image with the AOTF on and subtracting the image with the AOTF off. Since the recorded spectra are spatially aligned in the images all of the rows of the CCD are summed together to get the total count measurement at each wavelength. The maximum value of each spectra is taken to be the central diffracted wavelength through the AOTF at each respective RF. A typical spectral measurement result can be seen in **Error! Reference source not found.a**.

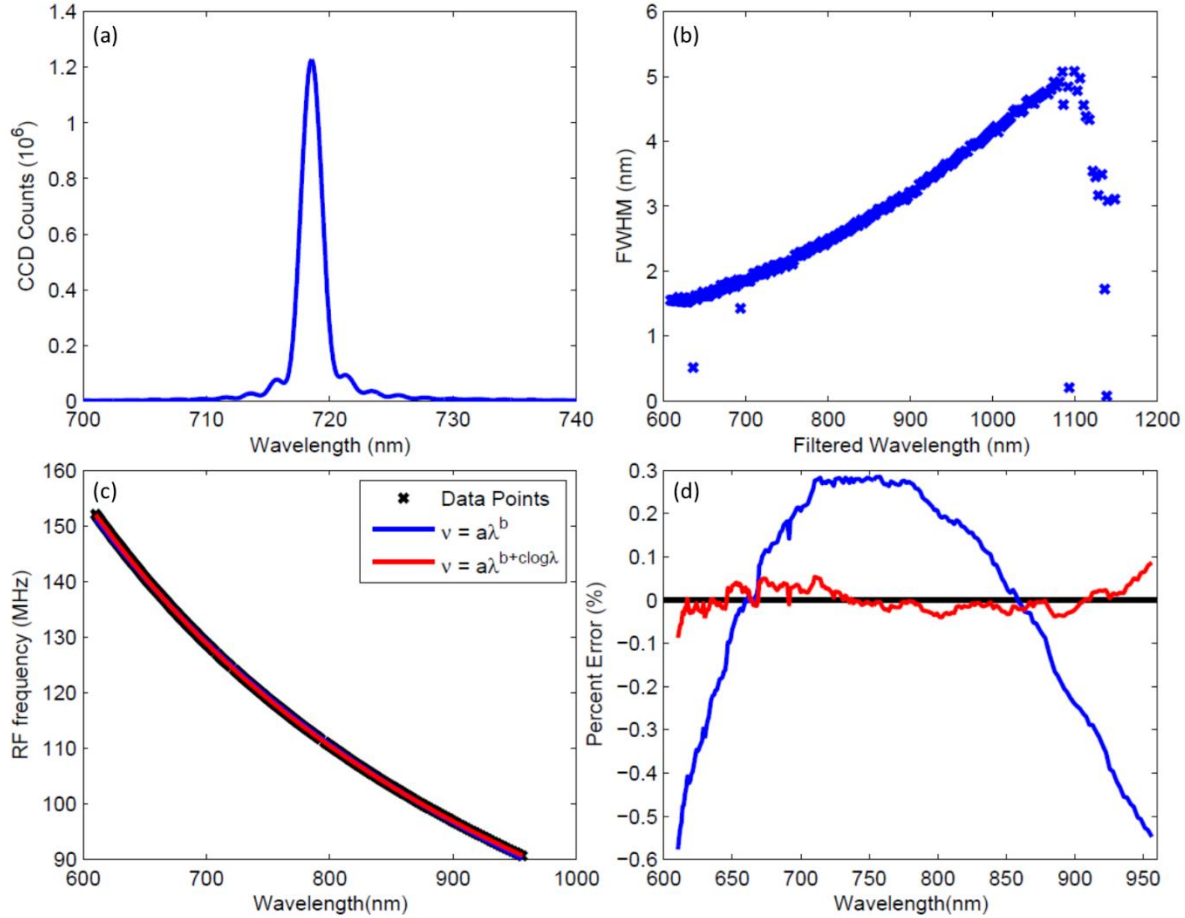


**Figure 4-3:** (a) A row averaged image taken from the AOTF of the point spread function when the tuning frequency of the AOTF was at 124.96 MHz. (b) The FWHM for each of the determined wavelengths for the AOTF. The FWHM at 600 nm is 1.5 nm and as the wavelengths get longer the FWHM increases to 4.9 nm at 1080 nm. (c) The calibration curves for the AOTF RF versus the diffracted wavelength which contains the data points recorded and fit curves. (d) The percent error with respect to the measured frequency for the two best fit curves in the previous panel. Originally published as Figure 6 in Elash *et al.* (2016).

The maximum values from each of the images were determined and the corresponding wavelengths. The tuning curve from section 3.2.4 (Equation 3.32) was not used since some of the AOTF parameters were not known and an imperial fit was used instead. It was noted that the curve appear to follow a power function of the form

$$F = a\lambda^b. \quad (4.1)$$

A linear least squares fit was performed in log space finding the coefficients  $a$  and  $b$ . The fit was performed and appeared to match the data quite well but a relative error analysis was preformed and it was seen that there was only an agreement better than 0.6% near the edges. An improved fit was provided by a modified power function in the form of

$$F = a\lambda^{b+c\log\lambda}. \quad (4.2)$$

The results of these fits can be seen in **Error! Reference source not found.c** and Figure 4-3d. The agreement of this form is better than 0.1% throughout the whole wavelength range and the determined tuning curve is

$$F = \exp(19.793)\lambda^{-3.381+0.168\log\lambda} \quad (4.3)$$

where  $\lambda$  is in nanometers and  $F$  is in megahertz with a 0.1% error in the central wavelength. Additionally the AOTF will undergo temperature changes during the flight. However, even when considering the temperature changes during the balloon flight, the AOTF would experience a maximum wavelength drift of 2.5 nm during the mission which is acceptable for the slowly varying broadband scattering of aerosol. Furthermore, it should be noted that even though the AOTF optical range is 600 nm to 1200 nm, our analysis only measured wavelengths from 600 nm to 1080 nm due to the low quantum efficiency of the CCD beyond this range.

### 4.3.2 Point Spread Function

The spectral Point Spread Function (PSF) of the AOTF was also determined using the same set of data that was used for the tuning curve calibration. The spectral PSF was found by determining the FWHM for each wavelength. These results are shown in Figure 4-3b. The sidelobes in Figure 4-3a are a known AO effect discussed in section 3.2.2 as a result of Equation 3.17 from the induced RF wave and for the Brimrose AOTF amounts to 8 to 14% of the total signal depending on wavelength. As noted in the previous section the PSF of the AOTF and the spectrometer are

convolved in this analysis. Even with this widening bias to the spectral PSF, the AOTF spectral resolution is well within the limits that are required in order to determine aerosol extinction in the upper troposphere and lower stratosphere (see section 2.6.1).

#### **4.3.3 Diffraction Efficiency**

An experiment was performed on several wavelengths to determine the RF power that yielded the highest throughput through the AOTF using a collimated light source. For the AOTF in ALI, the maximum throughput occurred when the RF power was at the recommended limit of the AOTF, which was 2 W. Following this, the diffraction efficiency of the AOTF was determined by using two sets measurements. The first is the experimental data used to perform the wavelength calibration, and the second is measurements of the intensity of the incident collimated light beam. The light in both experiments was linearly polarized and aligned with the polarization axis of the AOTF; for the second set the AOTF was simply removed from the optical chain. It should be noted that the attenuation of the AOTF crystal itself was not determined independently and is combined with the diffraction efficiency. We are more concerned about signal throughput of the device so the combination of the effects is acceptable. The incident light source was then measured with the same iHR320 spectrometer and Synapse CCD with identical settings. By taking the ratio of the intensity at the diffracted wavelength to the incident intensity the diffraction efficiency was determined. It was found to vary between 54 and 64% across the measured spectral range. Equation 3.18 was not used to determine a theoretical diffraction efficiency due to unknown AOTF parameters such as interaction length. However, our results agree with the experimental diffraction efficiencies supplied from Brimrose with the AOTF.

It should be noted that the diffraction efficiency changes also with respect to incoming angle and this experimental determination only measured the diffraction efficiency at normal incidence (*Xu and Stroud, 1992*). It is acceptable to only perform these measurement normal incidence since

the loss of signal is small as long as the incident angle remains within a certain range known as the acceptance angle. For the AOTF used in ALI the acceptance is  $2^\circ$ .

#### **4.4 ALI Calibrations and System Test**

A series of pre-flight laboratory calibrations were performed on complete ALI instrument. The instrument was characterized as a complete system to provide calibrated radiance and estimate flight exposure times. The following calibration measurements were performed on ALI:

- Exposure time determination
- DC offset removal
- Dark current correction
- Stray light calibration
- Relative flat-fielding correction

##### **4.4.1 Exposure Time Determination**

An experiment for ALI was performed to determine exposure times for the stratospheric balloon flight as well as the entrance pupil size of the system. On July 12, 2014 from 13:00 to 16:00, during clear conditions, ALI was placed on the roof of a building ( $52.13^\circ\text{N}$   $106.63^\circ\text{W}$ ) pointing approximately  $90^\circ$  in the azimuth from sun and measurements were recorded with variety of exposure time (0.01 to 120 seconds) and wavelengths (600 to 1000 nm). The exposure times that would achieve a three quarter full well on the ground were determined for each wavelength. However, the exposure times were needed for the balloon geometry, not on the ground, where the change in altitude greatly changes the spectral radiance which alters the exposure times.

To address this issue a radiative transfer model is needed. A radiative transfer model has been developed at the University of Saskatchewan over the past 15 years. Using the scalar SASKTRAN-HR (*Bourassa et al.*, 2008; *Zawada et al.*, 2015) radiative transfer model, discussed in detail in section 2.4.5, radiance profiles were simulated from a ground-based geometry and a simulated

balloon flight geometry. The simulated radiance profiles for the ground based and balloon flight geometry are seen in **Error! Reference source not found.**. A scaling factor,  $\beta$ , is based on the ratio of the ground based and balloon based geometries and is used to adjust the integration times. The scaling factor can be used in combination with the ground based determined integration times,  $t_g$  in the following

$$t_b = t_g \beta = t_g \frac{I_b}{I_g}, \quad (4.4)$$

where  $t_b$  is the integration time from the balloon platform, and  $I_b$  and  $I_g$  are the simulated scalar radiances from the balloon and ground respectively. The scaling factor can be observed in black in Figure 4-4 and the estimated balloon geometry exposure times are located in Table 4-2.

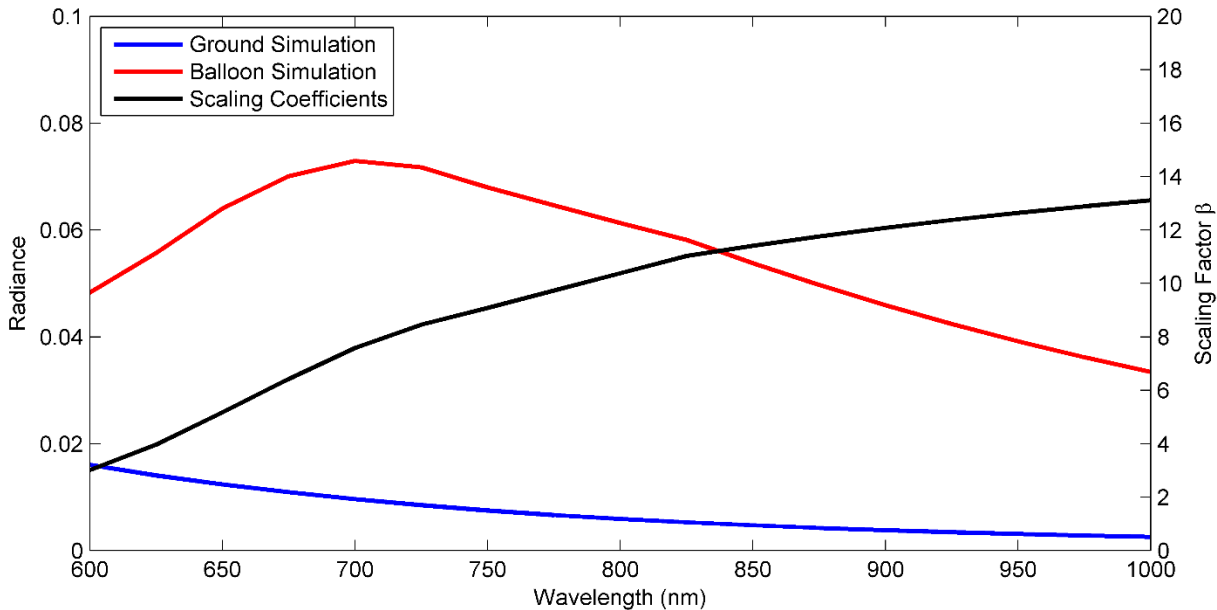


**Figure 4-4:** Simulated scalar radiances from the SASKTRAN-HR in blue and red with the radiance on the left side and the scaling factor in black with the value on the right side.

The exposure times determined were designed to be on the order of a second during the flight which was performed by selecting an appropriate entrance pupil size of 9.91 mm; however, there was some uncertainty with the exposure times determined. The radiances used from the

SASKTRAN-HR model were scalar since the vector model was still in development. ALI is a polarized instrument so the effect polarization would have on the scaling factors was unknown. To account for the unknown effect from the lack of simulated polarized radiances, the software was designed to be able to change the exposure time curve during the mission as required. Finally the read out speed of the CCD camera was slow compared to the exposure times and on average took 20 second per image, which greatly reduced the measurement density.

**Table 4-2:** Estimated balloon flight exposure times.

Wavelength (nm)	Exposure Time (s)
650	2.00
675	2.00
700	1.39
725	0.38
750	0.10
775	0.10
800	0.10
825	0.33
850	0.47
875	0.48
900	1.00
925	2.00
950	2.00

#### 4.4.2 DC Offset Removal

The DC offset is a bias that is applied to the analogue to digital converter inside the CCD camera that causes a bias in the final count values for the image and needs to be removed in order to be able to get the pure measurement counts from the instrument. It is usually assumed that the DC offset for a CCD is a constant across the operating temperatures and exposure times of the device; however, the DC offset for the camera used in ALI exhibited a temperature dependence. Dark images were acquired in the laboratory to be used in the calibration. Additionally, a calibration mode was used on the ascent of the balloon during the campaign that acquired dark images which

were used to further calibrate the DC offset. All of the dark images were taken with the shortest possible exposure time of 0.01 s to reduce any dark current contribution from the images. The mean value of the counts for each image was determined and was used to determine the DC offset. The standard deviation of the counts for each image ended up being approximately 2% of the average value. Using this data, a curve was fit to determine the DC offset with respect to temperature. The curve is in the form of

$$\text{DC offset} = 0.00659T^3 - 0.09202T^2 - 3.5368T + 64305127 \pm 2\%, \quad (4.5)$$

where  $T$  is the temperature of the detector in degrees Celsius to determine the offset that needed to be removed and is plotted in Figure 4-5.

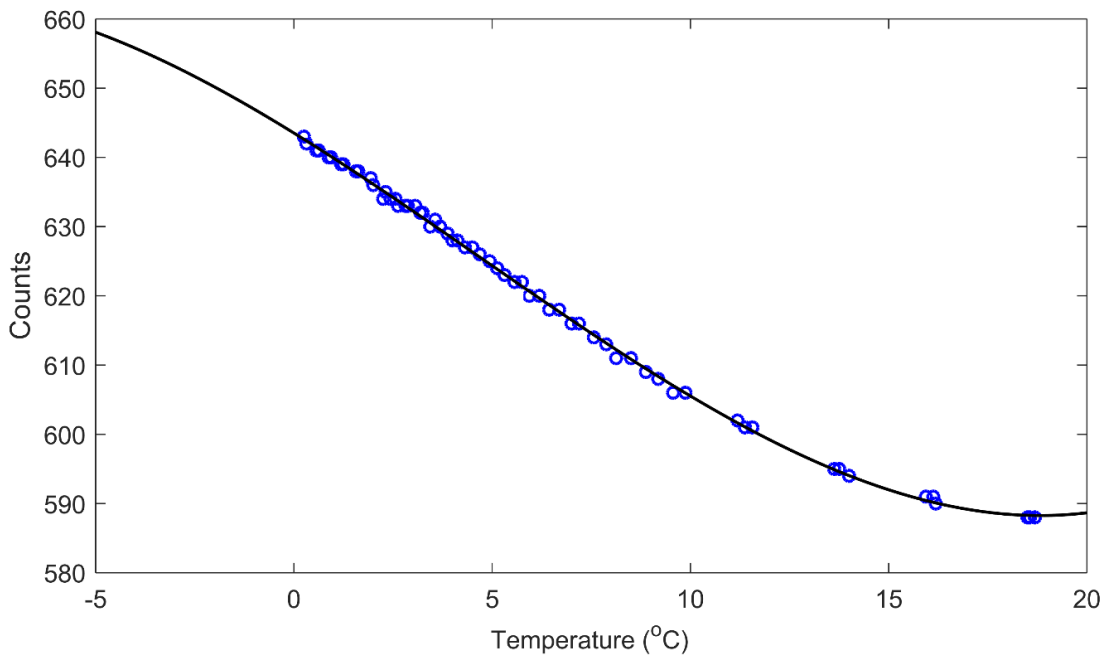
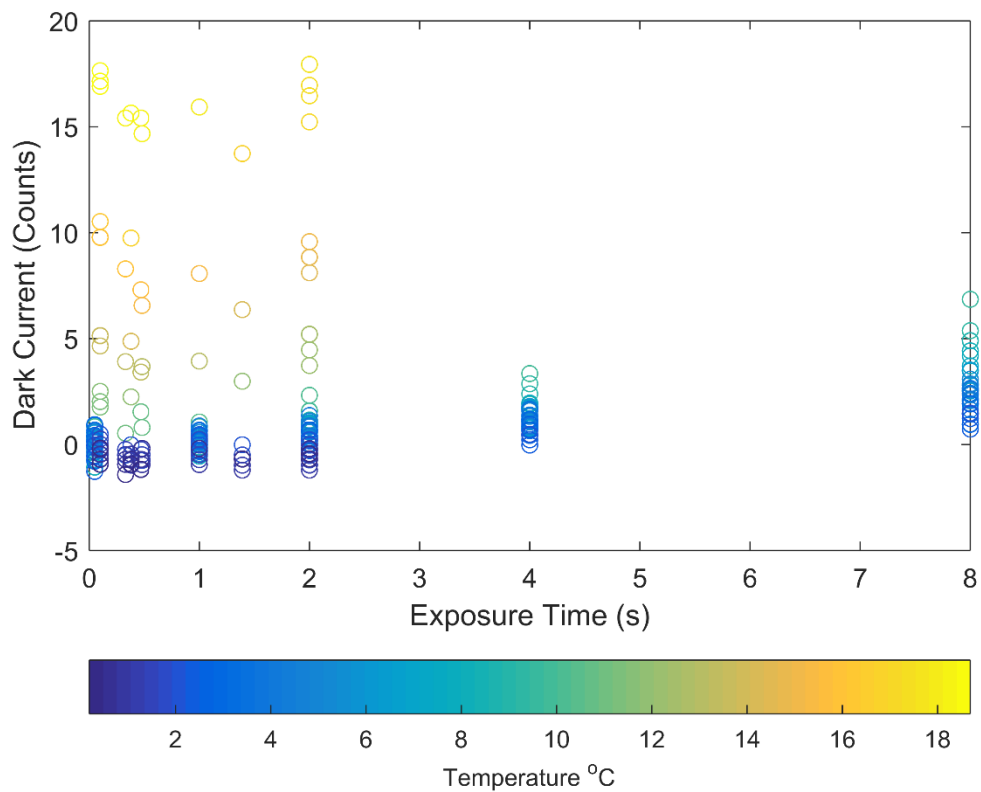


**Figure 4-5:** The DC offset curve (Equation 4.5) is seen in black where the lab and flight calibration data is shown in blue. The counts on the vertical axis are the counts that need to be removed to account for the DC offset.

#### 4.4.3 Dark Current Correction

The dark current is thermal energy that builds up in the CCD detector. It grows linearly with exposure time and nonlinearly with temperature. By using images taken in darkness with a variety

of exposures time, the dark current can be determined by looking at the residual after the DC offset has been removed using the curve developed in the previous section. The residual of the counts for the calibration dark image can be seen in Figure 4-6. During the campaign, the operating temperature of the camera was less than 10°C throughout the entire flight and most exposure times were less than five seconds leaving a very small dark current contribution in the measurement images at worst seven counts. The seven count dark current was small compared to the DC offset and was considered to be an addition noise source added to the error for the radiances. With the removal off the CCD artifacts of DC offset and dark current stray light additional system calibrations of stray light and relative flat fielding could be performed.



#### 4.4.4 Stray Light Calibration

A laboratory experiment to characterize the stray light in the ALI system was performed. Two types of stray light exist; the first is out-of-field stray light, *i.e.* signal that enters the optical path that originates outside of the FOV. The second is internal stray light, which is caused by scattering, reflections or other imperfections in the optical elements. As mentioned previously, stray light removal is critical for limb scatter measurements.

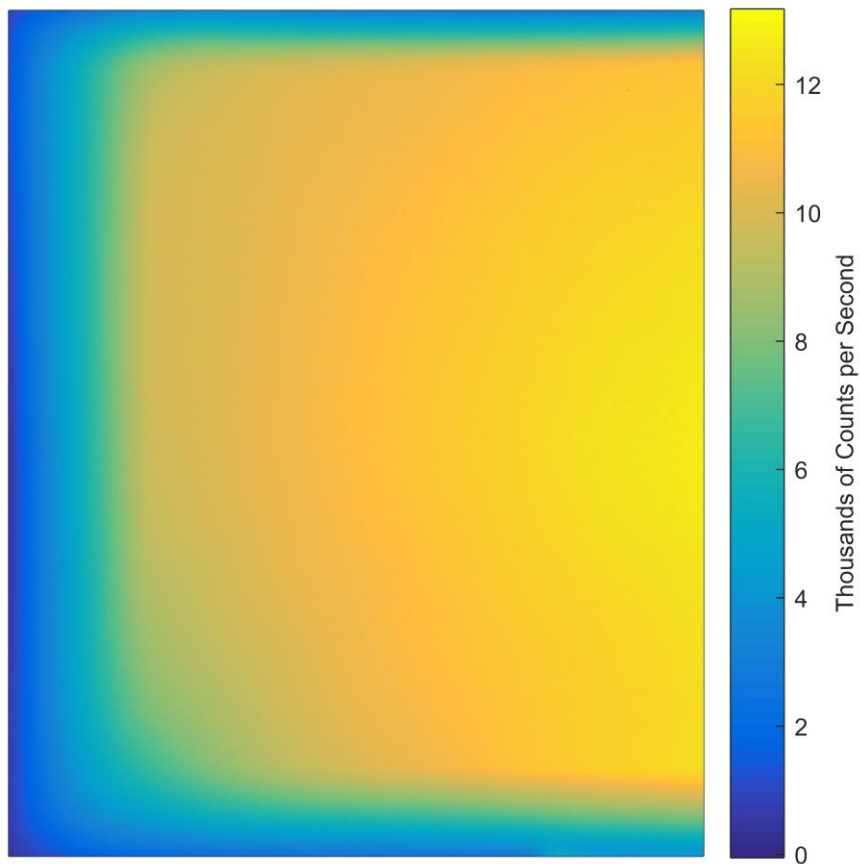


**Figure 4-7:** A calibration image after stray light removal has been performed where the measured wavelength is 750 nm with a 1 second exposure time. Vignetting can be seen as moving away from center of the image. Additionally the last  $1^\circ$  of the horizontal FOV is on the right side is lost due to strong contamination from reflections within the system. Originally published as Figure 7 in Elash *et al.* (2016).

The use of the AOTF has potential to increase the amount of internal stray light due to the fact that the undiffracted beam and the unmeasured polarization also propagate through the system.

However, the diffraction interaction only occurs when the acoustic wave signal is applied, so without the acoustic wave the recorded measurement only contains the stray light in the system. Using this unique characteristic of the AOTF, the stray light of the system was measured in the laboratory. A 250 W quartz-tungsten light source was passed through a dispersing screen and onto the entrance aperture of ALI, effectively filling the entire aperture and all angles within the FOV. Using a variety of exposure times, ranging from 0.1 to 60 s and wavelengths from 650 to 950 nm in 25 nm intervals, this diffuse source was imaged twice, once with the AOTF in its off state, with no driving acoustic wave, and once with the AOTF in its on state, with the acoustic wave applied. For each pair of measurements the image with the “AOTF-off” only contains stray light in the system, and the “AOTF-on” image contains the stray light combined with the image of the diffuse source. Subtracting the “AOTF-off” image from the “AOTF-on” image yields a final image that contains only the image of the diffuse source. A typical example of a resulting image is shown in Figure 4-7. The observed vignetting is caused by the aperture of the AOTF, expected from the ray tracing model, and light entering the AOTF outside the acceptance angle. Note that this method also partially removes dark current associated with the detector. This two-image method was used operationally during the balloon measurement campaign such that images captured had a corresponding “AOTF-off” image immediately obtained with the same exposure time. For the calibration images an average stray light to signal ratio of  $2.5 \cdot 10^{-2}$  was noted.

#### **4.4.5 Relative Flat-Fielding Correction**

By using a simple optical layout as chosen for the prototype, light gets blocked by the AOTF's aperture causing a vignetting on the images. As the FOV is increased, so is the vignetting. Furthermore, the extreme range of the FOV, approximately the last half degree in each direction, is outside the acceptance angle of the AOTF which causes a loss of diffraction efficiency. Both of these effects also need to be calibrated out of the measurements to achieve final radiances. The

flat-field calibration corrects optical and detector level differences in the system across the FOV such that a calibrated image of a perfectly diffuse source yields a constant value across the image. The resulting images from the diffuse source described above were used to determine the flat fielding corrections for ALI. These were determined in two steps: spatial and spectral.

The experimental measurements from the stray light calibration mentioned above was also used to perform the relative flat-fielding calibration. For the spatial correction, for each image at a given wavelength, each pixel was scaled to the mean value of the center 25x25 pixels. A series of images was used to determine the mean flat fielding coefficient for each wavelength which had no more than a 4% standard deviation.

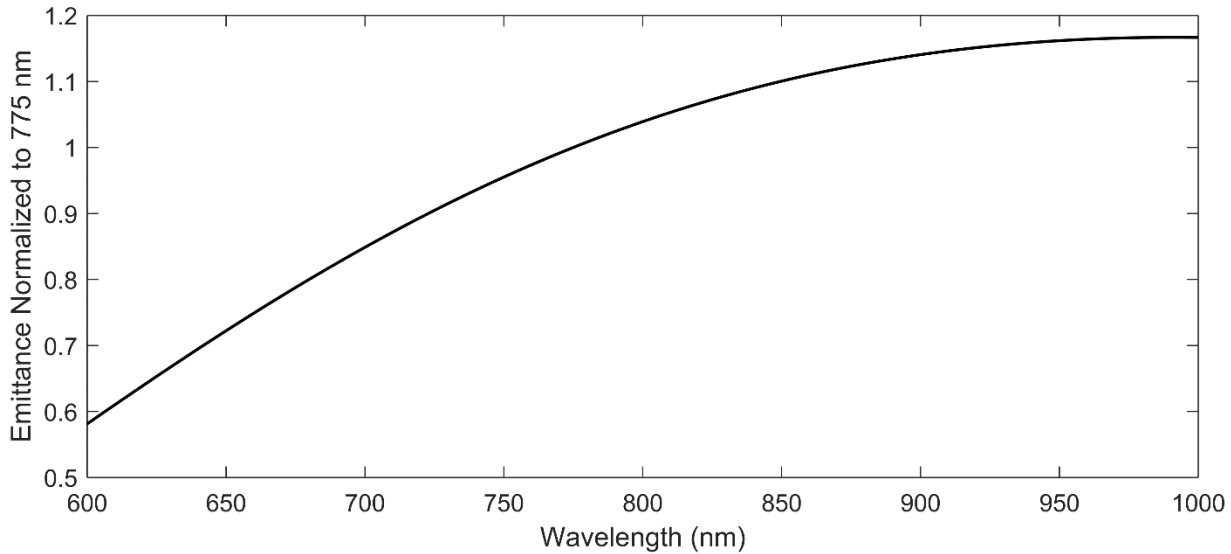


**Figure 4-8:** The blackbody emittance curve from Equation 4.6 normalized to 775 nm.

For the spectral calibration, ALI is most sensitive at 775 nm so this wavelength was chosen as the reference wavelength of a relative spectral calibration. All flat-fielding corrections were then scaled to the blackbody curve of a tungsten halogen bulb normalized to 775 nm assuming an operating temperature,  $T$ , of 3300 K using a method by *Kosch et al.* (2003). The blackbody emittance,  $E(\lambda, T)$ , of a filament bulb is given by

$$E(\lambda, T) = \varepsilon(\lambda, T) \frac{2\pi c}{\lambda^4} \frac{1}{\exp\left(\frac{hc}{\lambda kT}\right) - 1}, \quad (4.6)$$

where  $\varepsilon(\lambda, T)$  is the emissivity of the tungsten filament,  $c$  is the speed of light,  $h$  is Planck's constant, and  $k$  is Boltzmann's constant. The emissivity values for tungsten were acquired by work done by *Forsythe and Worthing* (1925) and used to compute the spectral emittance of the bulb normalized to 775 nm seen in Figure 4-8.

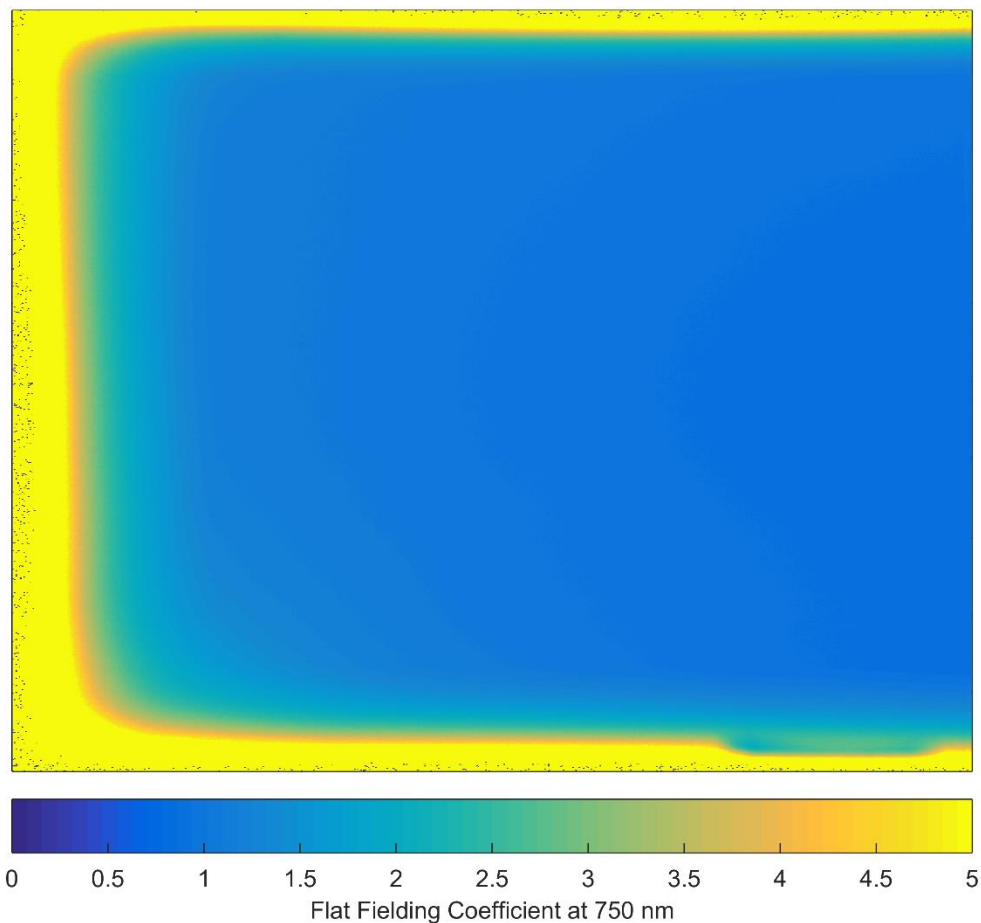


**Figure 4-9:** The flat fielding coefficients for 750 nm.

An example of the flat fielding coefficients for 750 nm can be seen in Figure 4-9. A majority of the coefficient for the central FOVs are near unity which yield good sensitivity throughout most of the image. However, due to the vignetting and the loss of diffraction efficiency near the edges

of the image, the flat fielding values in these regions are larger than the more central FOVs. It should be noted that the relative flat-fielding is the final calibration for ALI and the final radiances are relative to 775 nm. No absolute calibration was performed due to lack of availability of an appropriately calibrated source. For a future iteration of ALI, an absolute calibration would be strongly suggested to be performed.

#### **4.5 Integrated Testing**

With the completion of the ALI instrument, including the optical chain, power and electronics hardware, and system software, a full system test was performed, including a mass and power check. All of the individual components of the system have been tested and verified but a complete integrated test was required to assure no undesired cross-communications occurs between ALI itself and other instruments. ALI was set up in a flight configuration to simulate the launch of the balloon. During the test, ALI was completely controlled from a ground station computer over a local area network to simulate the stratospheric balloon's communication interface. All commands were sent to ALI from the ground station and the simulation performed a full but shortened mission plan, which including pre-flight checks, launch, science measurement acquisition, and mission termination. During the simulation, the temperature and pressure during the flight could not be simulated. However the electronics were pressure tested separately and no issues were noted.

The full integration testing occurred on August 18, 2014, along with a second instrument, the OSIRIS development model (*Kozun 2015; Taylor, 2015*) which was flown alongside ALI during the Timmins campaign. The OSIRIS development model was connected to the same local network, as would be the case during the flight, to be a further test for both ALI and OSIRIS to locate any cross communication problems between multiple instruments.

The testing suite for ALI consisted of testing the pre-flight commands to verify full systems operation, ascent operational mode, science operational mode, and system power down. Each

mode tested the various states of ALI during the balloon mission. Further, all of the possible commands for ALI were also tested in various orders to verify no issues with their operation.

The full integration test found a few minor software bugs that were not found prior, but no major problems were noted with ALI itself or any cross communication problems with the OSIRIS development model. The minor software issues were patched and tested on ALI before a final stable version of the software was loaded onto both the ground and flight computer systems and were considered to be the final flight version for the mission. Finally ALI's power consumption and mass were checked to verify that they were within the requirements as listed in section 2.6.1. The total mass was  $37.4 \text{ kg} \pm 5\%$  and the average power draw was  $70 \text{ W} \pm 10\%$  with a peak draw of  $80 \text{ W} \pm 10\%$  which are within the specification of the mission.

# CHAPTER 5

## STRATOSPHERIC BALLOON FLIGHT AND AEROSOL RETRIVALS<sup>3</sup>

### **5.1 Stratospheric Balloon Flight**

After the completion of the calibrations and the system tests on August 18, 2014, ALI was transported to Timmins, Ontario to prepare for the balloon launch. ALI underwent integration and testing on the gondola from August 25, 2014 until September 18, 2014. During this balloon campaign, there were seven balloon launches with ALI being a part of the seventh balloon. The flight of ALI took place on September 19, 2014.

This Chapter explains the procedure used once ALI and the team arrived in Timmins to prepare to integrate the instrument onto the gondola for the stratospheric balloon flight. Once completed ALI was integrated onto platform and tests were performed. Following, the mission flight is presented including flight path and calibrated relative radiance images. Next, this chapter presents the results from the Timmins campaign including aerosol extinction profiles, and an example of particle size instance during the flight. Finally, is a conclusions section the gives an outlook of the success of mission, results, as well as future improvement that can be made to a later iteration of ALI.

#### **5.1.1 Preflight Preparations**

The Canadian Space Agency (CSA) balloon launch facility in Timmins, Ontario is located at the Victor M. Power Airport ( $48.47^{\circ}\text{N}$   $81.33^{\circ}\text{W}$ ). ALI arrived at the base on August 25, 2014 with a launch window from September 8 to 14, 2014. In between the arrival of ALI and the balloon

---

<sup>3</sup> Portion of sections 5.1.1, 5.2, 5.3.1, 5.3.3, 5.3.4 and 5.4 as well as Figure 5-3, Figure 5-6, Figure 5-7, Figure 5-8, Figure 5-13, and Figure 5-15 were originally published in *Elash et al. (2016)*

launch, ALI had to be verified to have survived transportation, a seal within the CCD needed to be removed, thermal insulation needed to be added, and finally, ALI needed to be integrated onto the Centre National d'Etudes Spatiales (CNES) CARMEN-2 gondola.

ALI was unpacked and set up on a test bench at the launch facility. A visual inspection occurred to verify that no obvious damage occurred to the instrument during transportation. Once completed, ALI was connected to its electronics and power boxes and was powered on. A ground station computer was used to connect to ALI and perform a system check, including verification of automated startup, establishment of telemetry connection, ensuring that the system powered on correctly with no errors and that the science operation program functioned. This test verified that no functional problems occurred to the instrument during transportation, and all temperature and voltage sensors, GPS module, and CCD camera were reporting valid diagnostic values.

An imaging check was performed to verify that no optical components suffered damage or slippage during transportation. An EIA 1956 resolution target was illuminated by a 250 W tungsten halogen light source and was imaged by ALI to verify the optical layout. The recorded images were very similar to the ones taken in the laboratory before leaving Saskatoon.

Following the successful test of ALI, final preparations were needed prior to beginning integration with CARMEN-2. First, the CCD used by ALI had a sealed chamber that was in a vacuum state designed to be at atmospheric pressure and requires unsealing before the flight. This unsealing is done in order to not develop a strong pressure gradient between the CCD chamber and the low pressure of a 35 km environment which could cause permanent catastrophic damage to the CCD detector. At the launch facility, ALI was taken to a semi-clean area to unseal the CCD chamber. A panel was removed on the side of the camera and the seal to be removed can be seen in Figure 5-1. The orange o-ring was removed with associated sealing components and the vacuum

seal was broken. The chamber panel was replaced and ALI was moved back to the integration hall and another set of test resolution targets were taken to verify the correct operation of ALI. All resolution targets were similar with the set before the chamber was unsealed except there was approximately a 5% drop in counts which may have been caused by unsealing the chamber or a change in the lighting conditions of the resolution target. With all optical and electronic verifications complete the thermal insulation discussed in section 3.3.4 were added to ALI.



**Figure 5-1:** Side of the QSI CCD with the panel that contains the vacuum seal opened. The orange o-ring seen in the cavity is removed from the chamber to open the vacuum seal to the camera's CCD chip.

With the completion of the thermal management, ALI was ready to be mounted onto the CARMEN-2 gondola. ALI can be seen mounted on the CARMEN-2 gondola in Figure 5-2**Error!** **Reference source not found.** and ALI used the power and communication subsystems of CARMEN-2. Testing was performed with collaboration from the CARMEN-2 team to verify that

there were no issues between ALI and CARMEN-2's systems. A problem was found in the communication module, named SIREN, between ALI and the ground station computer. With assistance from the CARMEN-2 team, the correct Ethernet settings were determined and a patch to the ALI operation code was applied.



**Figure 5-2:** The ALI instrument is mounted on board the CARMEN-2 gondola (top shelf on the right). ALI located next to SHOW, another Canadian instrument with collaboration between ABB, York University, and the University of Saskatchewan. ALI has its red tag cover over the optical entrance to protect the instrument from dust and other contaminants. Thermal insulation has been added to the instrument and during the flight sun side is on the side of SHOW. Some of the reflective layer was blacked out to not cause additional stray light into SHOW optical path.

During the integration phase, it should be noted that several instruments were also being verified with the CARMEN-2 systems alongside ALI for integration onto the gondola including four other Canadian instruments, such as the OSRIS development model (*Kozun, 2015; Taylor, 2015*) and SHOW which measures water vapour.

The CNES gondola is an actively pointed gondola with azimuthal pointing precision better than 1' with the use of an onboard star tracker. ALI was orientated so it would be maintained at 90° from the azimuthal direction of the sun, with an overall southern FOV during the mission.

### **5.1.2 Balloon Flight**

The flight plan for the CARMEN-2 gondola was once float altitude was reached and the sun had risen ALI, OSIRIS, and SHOW would perform their operational missions for the first four hours of the campaign. The operational objectives for ALI included a dark imaging suite for calibration purposes and an aerosol imaging suite for aerosol measurements. A secondary goal was to test the sensitivity to aerosol of ALI with respect to SSA by recording images at various azimuth directions. After the end of the ALI mission, the instrument was to be powered off and other instruments on CARMEN-2 were to gather measurements.

The flight of CARMEN-2 was delayed past its launch window of September 8 to 14, 2014 due to poor weather conditions. On September 19, 2014 at 05:35 UTC (01:35 local time) ALI was launched as part of the Nimbus 7 mission from the CSA Timmins balloon launch facility. During the launch, the sky was clear with light winds allowing for a safe and uneventful launch. The ascent of the gondola occurred in darkness and reached its flight altitude of 36.5 km at 8:17 UTC. First light was observed by ALI at 9:39 UTC and spectral images were recorded until 14:42 UTC. ALI was powered off at 17:15 UTC.

A visualization of the flight path with major landmarks noted can be found in Figure 5-3a. Temperature profiles for the ambient atmosphere and instrument are shown in Figure 5-3b. The black curve is the ambient atmospheric temperature at the gondola altitude and location during the flight as obtained from ECMWF reanalysis (*Dee et al.*, 2011). The blue, green, and red are from temperature sensors onboard ALI located on the baffle, camera, and RF driver respectively. The baffle temperature sensor was attached just on the inside of ALI right by the entrance aperture for

the system and monitors the temperature at the front of the system. The camera sensor is attached to the back of the CCD camera and the RF driver sensors measures the surface temperature of the RF driver. ALI was thermally insulated to keep the system warm whereas the baffle temperature sensor is relatively uninsulated from the extreme cold of the tropopause. The effect of the cold tropopause can be seen on the gondola at approximately 6:00 UTC. The cooling effect can even be seen on the interior CCD and RF driver sensors which are isolated from the exterior temperature. After the internal temperature drop, the system reaches an equilibrium temperature until the sun rises and solar radiation comes into contact on the instrument at approximately 10:00 UTC at which point there is an increases in the system's temperature. The temperature of the system are kept within operating range with the aid of the reflective material during the flight.

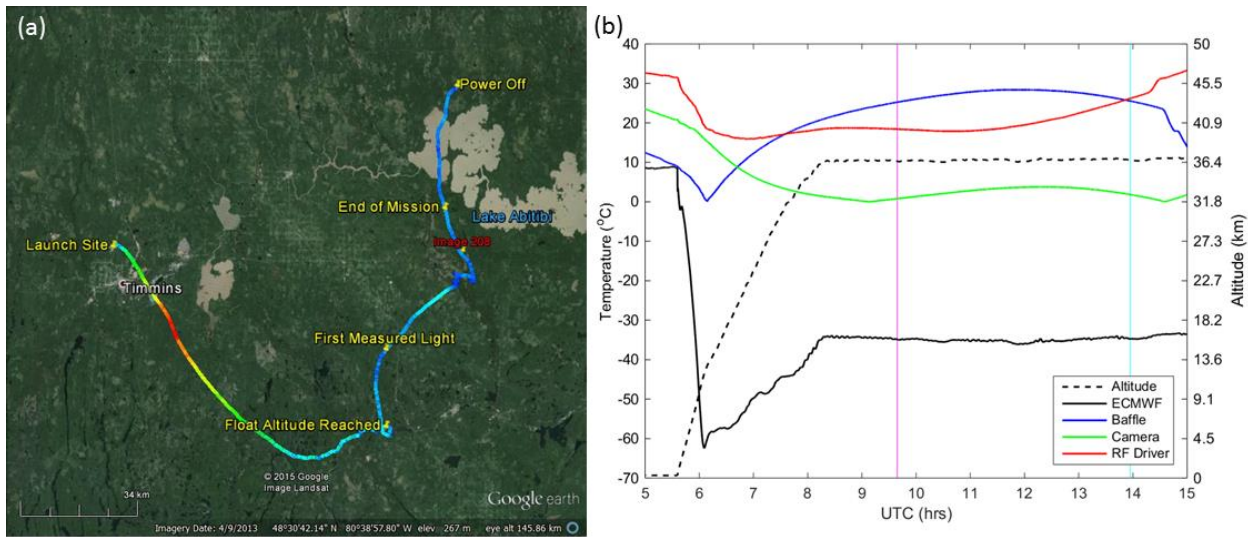


**Figure 5-3:** (a) The GPS data from ALI during the Nimbus 7 mission generated via Google Earth. The colour of the line represents the absolute speed of the gondola during the mission and the blue, green, red colours represent speeds of approximately 10, 70, and 140 km/h. Important landmarks are noted on the image. The end of mission represents the end of the primary aerosol mission. No GPS data was collected from ALI after power down. The location of image 208 is the red label. (b) The temperature and altitude profiles from the Nimbus 7 flight. The time of image 208 is shown by the cyan vertical line and first light measured by ALI occurs at the magenta vertical line. Originally published as Figure 8 in *Elash et al. (2016)*.

During the mission, ALI operated in two primary acquisition modes, a calibration mode and an aerosol imaging mode. The first mode, the calibration mode, was primarily used during ascent when the gondola was in darkness and intermittently between the aerosol mode during sunlit conditions. During this mode, the filtering of the AOTF was not enabled and the system imaged essentially only dark current during the ascent in darkness and stray light during sunlit conditions. Eight exposures are taken in the calibration mode with 0.05, 0.1, 0.5, 1, 2, 3, 5, 10 second exposure times.

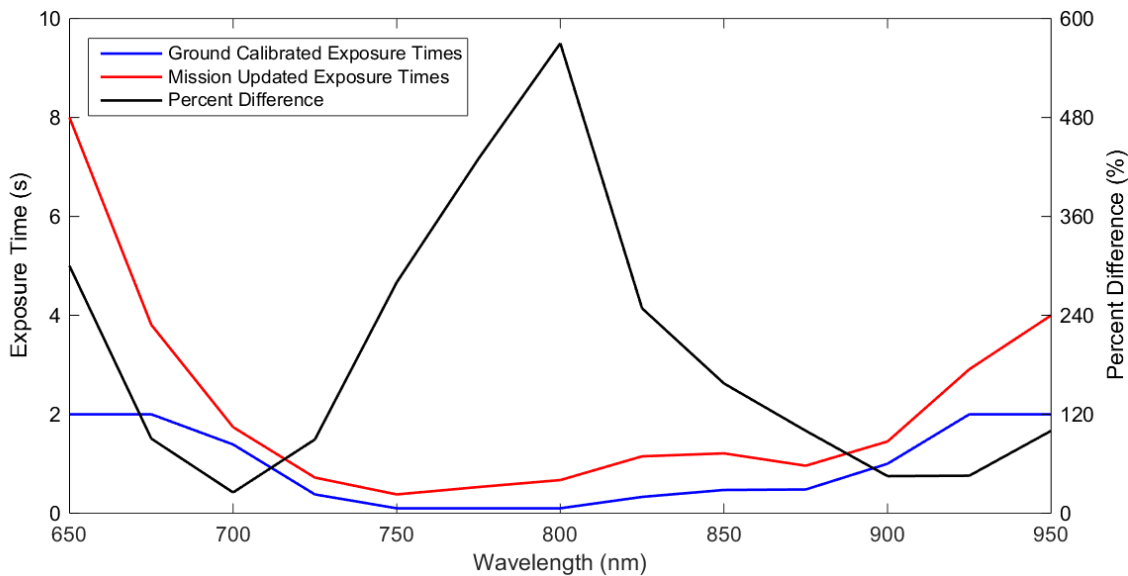


**Figure 5-4:** During the flight the calibrated exposure times was updated. The blue curve represents the exposure times from the ground calibration and the red curve is the recalibration during the flight. The black curve is the percent change in between the pre-flight calibrated results and the during flight calibration.

The second operational mode, the aerosol mode, recorded measurements in a cycle that contained 13 pairs of images across the spectral range (650-950 nm every 25 nm), the pairs being a calibration image with the “AOTF-off” and an image of the limb. Each cycle took approximately 10 minutes with each measurement set taking approximately 45 seconds to acquire with initial exposure times shown in Figure 5-4 in blue, which were the exposure times determined during the roof testing of ALI (see section 4.4.1). However, during the flight it was determined that the

calculated exposure times were not long enough and the images were underexposed. The underexposure is believed to be caused by the initial exposure time calibration curves being calculated with simulated scalar radiance since the SASKTRAN-HR polarization module had not yet completed development. So the exposure time curve was recalibrated during the flight using the image statics that were sent down with the house keeping. A comparison of the two exposure time curves with the percent increase can be seen in Figure 5-4. The percent increase is given by

$$\text{Percent Difference} = \frac{t_c - t_u}{t_c} * 100\%, \quad (5.1)$$

where  $t_c$  is the exposure time for the original calibration and  $t_u$  are the updated exposure times calculated from the flight.

The Nimbus 7 flight lasted for 16 hours 19 minutes with a successful landing at 21:54 UTC. During the flight, ALI successfully gathered 216 aerosol images. The gondola landed 70 km from Amos, Quebec or approximately 250 km from the launch facility. CARMEN-2 was recovered by the balloon recovery team and was returned to base on September 21, 2015. ALI was removed from the gondola, repacked and transported back to Saskatoon, Saskatchewan where the measurements could be verified and processed.

## 5.2 Limb Measurements

After the successful post-flight recovery, ALI was unpacked and checked for any damage in Saskatoon, SK on September 25, 2014. No obvious damage had occurred to ALI from the flight and the instrument was tested to verify no internal damage has occurred. There was no damage sustained to ALI from the flight. 216 raw aerosol mode image pairs were obtained from the flight and calibration was performed including pointing alignment discussed below and the image calibrations as detailed in section 4.4.

The images needed to have complete pointing information added since the raw images only had position and altitude information from the onboard GPS. The azimuth and zenith directional information are needed to determine the line of sight of each pixel on the CCD. The CNES team supplied the Solar Azimuth Angle (SAA) information from the flight and was correlated to the images using GPS time. However, no information was supplied about the zenith direction of the gondola, we were just notified that the gondola was zenithally stable throughout the majority of the flight. So some manual calibration of the zenith angle occurred. ALI was tilted at  $3^\circ$  so the zenith is assumed to be  $93^\circ$  for ALI. This starting guess and was not accurate enough since features in the radiance profiles did not retain the same altitude over the course of a few images. To determine a more precise zenith angle, the zenith angle was varied from  $92^\circ$  to  $94^\circ$  in  $0.1^\circ$  intervals and the tangent altitude was calculated for each case. Then the radiance profiles for each zenith angle was compared to find zeniths where the features were aligned. The zenith angle with the optimal alignment was determined to be  $92.6^\circ$  with an uncertainty of  $0.1^\circ$ .

The calibration techniques discussed in section 4.4 were then applied to the raw images to find the final radiances. As an example, image number 208 is used to demonstrate the steps in the calibration on a flight image. Image 208 is recorded with a wavelength of 750 nm and taken at 13:57 UTC with a SZA and SSA of  $63^\circ$  and  $98^\circ$  respectively. The dark current and DC offset have been removed from image 208 using Equation 4.5. Next, the stray light is removed by using the “AOTF-off” or calibration image and removing it from the “AOTF-on” or measurement image. The result of this procedure can be seen in Figure 5-5. In the first panel, abnormal bright spots are noticed in the right side and the top right of the measurement. These same features are noticed in the stray light image. By subtracting the AOTF-off image from the measurement image, a final smooth measurement image is noted in the last panel. Finally, a flat fielding calibration is

performed (see section 4.4.5) and a final calibrated image can be seen in Figure 5-6a. Remember that no absolute calibration was performed on ALI, so the radiance is relative to the 775 nm laboratory calibration in arbitrary units. The error,  $\epsilon$ , on a given pixel for the radiance measurements were given by

$$\epsilon^2 = \epsilon_{read}^2 + \epsilon_{DC}^2 + \epsilon_{dark}^2 + \epsilon_{stray}^2 + \epsilon_{ff}^2, \quad (5.2)$$

where  $\epsilon_{read}$  is the readout uncertainty from the CCD, which is 15 counts at worst,  $\epsilon_{DC}$  is the error in the DC offset calibration,  $\epsilon_{dark}$  is the error from the dark current in the CCD,  $\epsilon_{stray}$  is the error in the stray light calibration, and  $\epsilon_{ff}$  is the error in the flat field corrections.

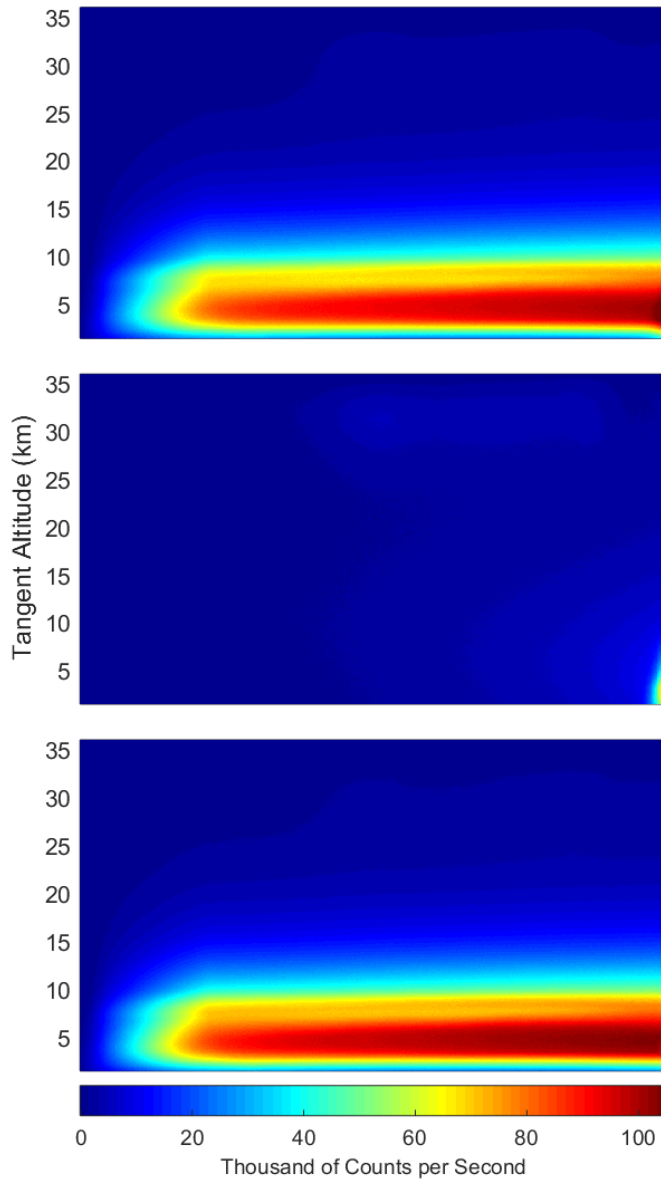


**Figure 5-5:** Stray light removal technique is performed using image 208 which is a 750 nm measurement. The top panel is the image after the DC offset has been removed from the measurement. The middle panel is the associated AOTF-off image and stray light features are seen in the upper right of the image as well as light being registered in the entire right side of the image. The final panel is the first panel minus the second panel and the abnormal gradient has been removed from the final image, leaving a cleaner radiance profile.

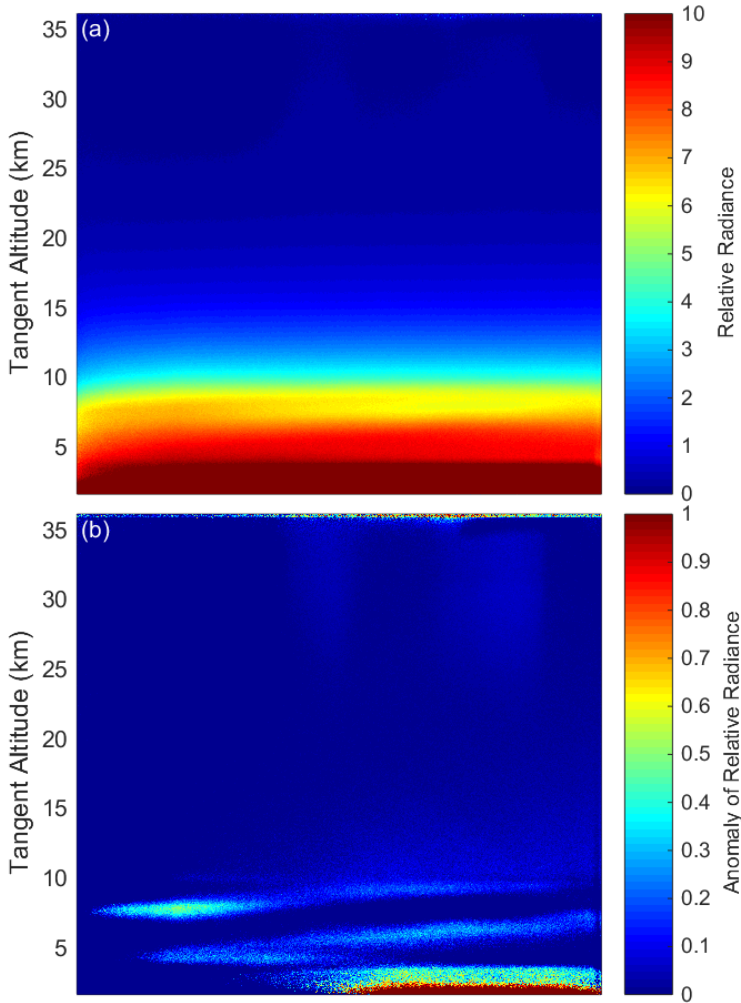


**Figure 5-6:** (a) Final calibrated 750 nm image, taken at 13:57 UTC located at 48.55°N, 80.00°W with a SZA and SSA of 63° and 98° respectively. (b) The same 750 nm image with the mean of the profile removed from the image leaving the residual signal that shows thin clouds in the troposphere. Originally published as Figure 9 in *Elash et al. (2016)*.

From image 208, the horizontal structure across the image is nicely revealed by calculating the mean radiance profile across the image and then removing it from each profile. This is shown in Figure 5-6b, where thin clouds (2 km vertical extent or less) are clearly seen near and below the tropopause level, with substantial variation in tangent altitude across the horizontal FOV. These clouds were also observed from other instruments on board the gondola during the mission (B. Solheim, private communication, 2014). A brief check on the CALIPSO quick-look plots also

shows clouds at a maximum height of approximately 13 km from measurements taken at 08:40 UTC at 47.24°N, 95.25°W, the nearest measurement point to the ALI location and time. Although these images only have a 35 km extent in the horizontal direction, there is also some indication of horizontal variation in radiance significantly above the cloud level, possibly due to real atmospheric variability in the aerosol layer. It should also be noted that some high altitude stray light is also visible in this mean residual image that was not observed in the laboratory tests. For the high altitudes in the range of 27 to 30 km the expected ratio of signal to stray light was estimated to be in between 2-3 but for the campaign the ratio of signal to stray light for some regions dropped down to slightly below one. This may be due to contamination from scattering from a baffle vein or a nearby component of the gondola, although the true cause is unknown.

For ease of further analysis, and to increase the precision of the measurements to a minimum of 0.6 MTF, the images were averaged into cells of 25 pixels horizontally and averaged vertically onto a 1 km tangent altitude grid. The errors for the averaged radiances,  $E$ , is given by

$$E = \left( \frac{1}{(N-n)(M-m)} \sum_{i=n}^N \sum_{j=m}^M (\epsilon_{i,j})^2 \right)^{\frac{1}{2}}, \quad (5.3)$$

where the errors for each pixel,  $\epsilon_{i,j}$ , are summed in vertical,  $i$ , and horizontal,  $j$ , directions from the starting pixel,  $n$  for the vertical and  $m$  for the horizontal, to the final pixel in the average,  $N$  for the vertical and  $M$  for the horizontal. The radiance profiles from the center column of the images for all measurements obtained during the flight are shown in Figure 5-7. The first set of profiles, the dashed lines, which start near zero and move toward larger values, are the measurements that were recorded near and during sunrise (*i.e.* SZA greater than 90°) so the gradual increase is therefore expected. Measurements obtained for SZAs less than 90° are represented by

the solid lines. These radiance profiles follow a similar and expected exponential shape, with some variability at tangent altitudes below 12 km corresponding largely to changing cloud conditions.

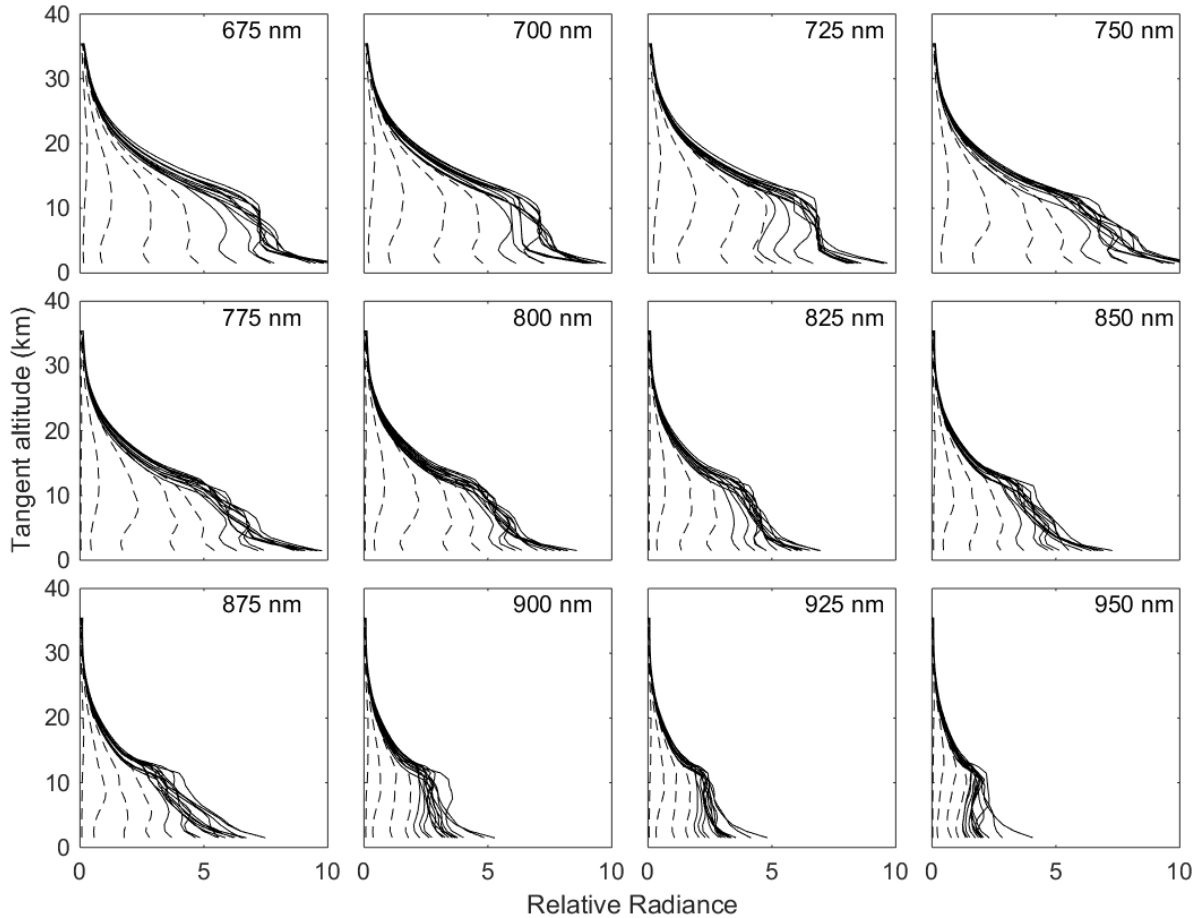


**Figure 5-7:** Averaged ALI relative radiance vectors from 12 of the 13 wavelengths from the Nimbus 7 flight. Each panel presents the radiance vectors from a different wavelength measured which is denoted in the top right corner. The dashed lines are radiance profiles where the SZA is greater than  $90^\circ$  and solid lines are profile where the SZA is less than  $90^\circ$ . Originally published as Figure 10 in Elash *et al.* (2016).

A full cycle of 13 spectral images (numbers 204-216) were used in Figure 5-8 to show the spectrum of relative calibrated radiances at selected tangent altitudes. The estimated uncertainty in the radiance is represented by the shading and was calculated using Equations 5.2 and 5.3. The uncertainty is approximately five percent from 5 to 20 km and increases up to eight percent from 20 to 35 km. The spectra displays the expected and relatively smooth fall off in intensity with

increasing wavelength with Chappuis ozone absorption seen at the lower wavelengths; however, the reason for the peak in the spectra at 875 nm is not known and may be due to an inconsistency in the pre-flight calibration.

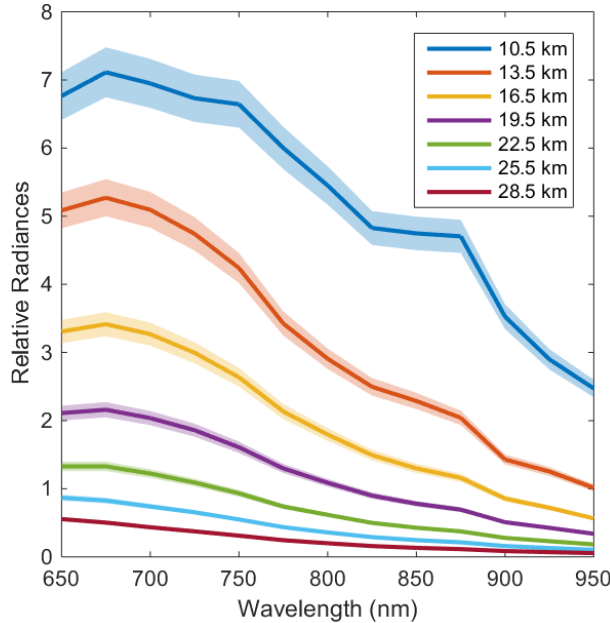


**Figure 5-8:** Relative radiances spectrally from 650 nm to 950 nm as measured from ALI at approximately 14:20 UTC consisting of images number 204 to 216 looking 90° in the azimuth from the sun facing southwards. These spectral profiles are presented at several tangent altitudes with a horizontal look direction of 0°. The shading represents the error on the radiances. Originally published as Figure 11 in *Elash et al. (2016)*.

### 5.3 Aerosol Retrievals

From the successful mission, radiance measurements from ALI needed to be used to determine aerosol parameters. The following sections describe the Multiplicative Algebraic Reconstruction Technique (MART) retrieval method used to determine aerosol and particle size information. The retrieved aerosol profiles from ALI is presented and is compared to the OSIRIS version 5.07 aerosol extinction product. Following, a cycle of aerosol measurements are used to determine a particle size distribution estimate and is contrasted with particle size parameters from other instruments.

### 5.3.1 Aerosol Extinction Retrieval Methodology

A measurement inversion technique is a method used on a measured value and can be converted into a wanted usable physical quantity via an iterative method. A measurement vector,  $\mathbf{y}$ , is constructed that has sensitivity to a desired physical state and is computed with a forward model,  $\mathbf{F}$ , with an input state,  $\mathbf{b}$ , and a wanted physical parameter,  $\mathbf{x}$ . The measurement vector is then calculated with the model and is yielded by

$$\mathbf{y} = \mathbf{F}(\mathbf{x}, \mathbf{b}) + \boldsymbol{\epsilon}, \quad (5.4)$$

where  $\boldsymbol{\epsilon}$  is the noise on the measurement vector.

The inversion of the ALI radiances used a Multiplicative Algebraic Reconstruction Technique (MART), discussed in section 2.6.3, specifically we have applied a slightly modified version of the standard OSIRIS stratospheric aerosol extinction retrieval (*Bourassa et al.*, 2007; 2012b). This inversion algorithm, which is applied from the tropopause to 30 km altitude, assumes log-normal distributed hydrated sulphuric acid droplets (see Equation 2.1) in order to calculate the aerosol scattering cross section from the Mie scattering solution. The modeled radiances for the nonlinear inversion were computed with the SASKTRAN-HR radiative transfer engine using the newly developed vector module for polarization (*Bourassa et al.*, 2008; *Zawada et al.*, 2015; *Dueck et al.*, 2016). The output of SASKTRAN-HR gives the Stokes vectors for the radiance in the model reference frame, which are then rotated into the instrument's coordinate system (see section 2.4.5). Once rotated, the polarization signal required to match the ALI measurement is the vertical polarization given by

$$I_v = \frac{1}{2}(I - Q), \quad (5.5)$$

where  $I$  and  $Q$  are Stokes parameters defined by  $I = \langle E_x^2 \rangle + \langle E_y^2 \rangle$  and  $Q = \langle E_x^2 \rangle - \langle E_y^2 \rangle$ . The variables  $E_x$  and  $E_y$  are the horizontal and vertical component of the electric field in the instrument reference frame.

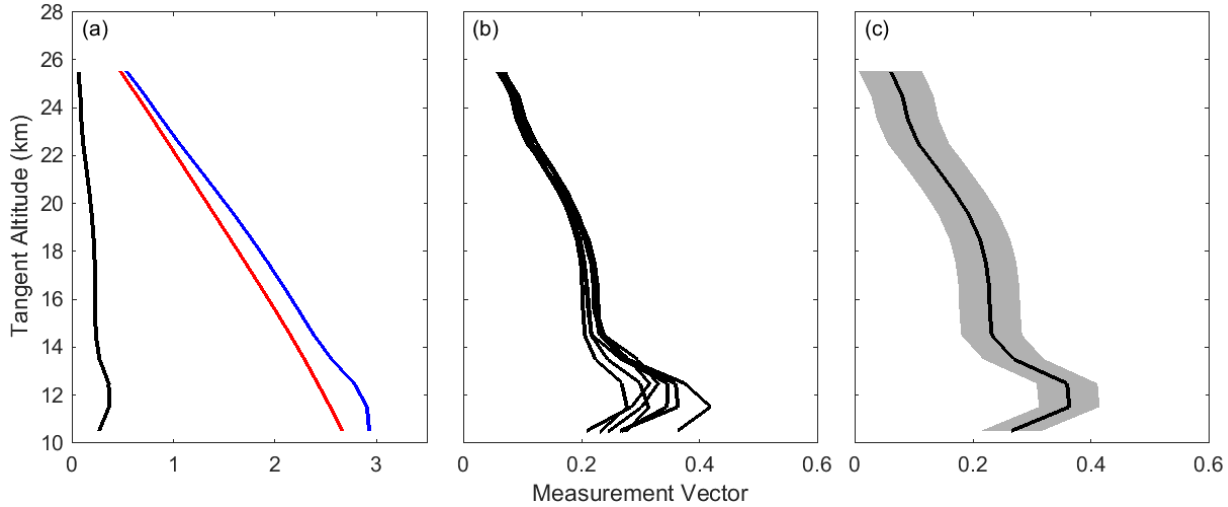


**Figure 5-9:** (a) The black, blue, red curves represent the measurement vector, first term of Equation 5.6, and second term of Equation 5.6 using image 208 (b) A collection of all of the measurement vectors at 750 nm during the mission with a SZA less than 90°. (c) Image 208 measurement vector with associated error represented by the shading.

The relative radiance measurements from ALI are used to create measurement vectors,  $\mathbf{y}$ , as specified in *Bourassa et al.* (2012b) in the form,

$$\mathbf{y} = \log\left(\frac{\mathbf{I}_v(\mathbf{z}, \lambda)}{I_v(z_{ref}, \lambda)}\right) - \log\left(\frac{\mathbf{I}_{v,ray}(\mathbf{z}, \lambda)}{I_{v,ray}(z_{ref}, \lambda)}\right), \quad (5.6)$$

where  $\mathbf{I}_v(\mathbf{z}, \lambda)$  is the measured relative radiance from ALI and  $I_v(z_{ref}, \lambda)$  is the relative radiance at a high reference tangent altitude where there is little aerosol contribution. For the ALI measurements, the highest possible tangent altitude where the signal is above the noise threshold is approximately 30 km tangent height and typical values for  $z_{ref}$  were between 27 and 30 km. The second term in Equation 5.6 uses modeled radiances from SASKTRAN-HR with only the molecular atmosphere to approximately remove the Rayleigh signal. This is done to improve the speed of the convergence of the retrieval (*Bourassa et al.*, 2012b). Figure 5-9a shows the

measurement vector from a 750 nm image (number 208) from the center of the CCD. The final measurement vector,  $\mathbf{y}$ , is shown in the black, with the first term of Equation 5.6 in blue and the second term in red. Removing the Rayleigh component of the signal from the measurement vector increases the sensitivity to aerosol which increases the speed of convergence of the solution. All of the measurement vectors for the 750 nm images from the mission can be seen in Figure 5-9b.

An initial guess state,  $\mathbf{x}_a$ , for the aerosol extinction and an assumed particle size distribution profile are set in the SASKTRAN-HR model. The forward model vector is then constructed similarly to the measurement vector, and used in combination with the measurement vector to update the aerosol extinction coefficient profile using the MART algorithm,

$$\hat{x}_i^{(n+1)} = \hat{x}_i^{(n)} \sum_j \frac{y_j}{F(z_j)} W_{ij} \quad (5.7)$$

where  $\hat{x}_i$  is the aerosol extinction at each model altitude,  $i$  and  $j$  denotes a tangent altitude from the measurements. The forward model result is defined by  $F(z_j)$  and the weighting matrix,  $W_{ij}$ , relates the importance of each element of the measurement vector to each retrieval altitude. It should be noted that this inversion technique is computationally efficient as it allows for the updating of the atmospheric state without calculating the Jacobian (Degenstein *et al.*, 2009). This iterative process is run until the solution has converged and the value of the summation is approximately one and the final aerosol state is determined.

A precision estimate is also required for the retrieved aerosol profiles, an uncertainty estimate on the measurement vector is performed. To yield the uncertainty on the measurement vector at a specific tangent altitude,  $j$ , Equation 5.6 is differentiated and summed in quadrature yielding the following result

$$\delta y_j^2 = \left( \frac{\delta I_\nu(z_j, \lambda)}{I_\nu(z_j, \lambda)} \right)^2 + \left( \frac{\delta I_\nu(z_{ref}, \lambda)}{I_\nu(z_{ref}, \lambda)} \right)^2 + \left( \frac{\delta I_{\nu,ray}(z_j, \lambda)}{I_{\nu,ray}(z_j, \lambda)} \right)^2 + \left( \frac{\delta I_{\nu,ray}(z_{ref}, \lambda)}{I_{\nu,ray}(z_{ref}, \lambda)} \right)^2. \quad (5.8)$$

However, the only uncertainty that is considered is due to the instrument measurement and calibrations, inaccuracies in the SASKTRAN-HR model are ignored. Since the Rayleigh components are modeled, they are dropped from the uncertainty, simplifying the above result to

$$\delta y_j^2 = \left( \frac{\delta I_\nu(z_j, \lambda)}{I_\nu(z_j, \lambda)} \right)^2 + \left( \frac{\delta I_\nu(z_{ref}, \lambda)}{I_\nu(z_{ref}, \lambda)} \right)^2 \quad (5.9)$$

An example of the uncertainty on a measurement vector for image 208 is located on Figure 5-9c.

Once a retrieval has been completed for a measured radiance profile, the result and the uncertainty estimate is then used to estimate the precision in the retrieved extinction. For each altitude, a gain matrix is defined as

$$\mathbf{G} = \frac{d\hat{\mathbf{x}}}{d\mathbf{y}} \quad (5.10)$$

where  $d\hat{\mathbf{x}}$  is the change in the retrieved aerosol extinction and  $d\mathbf{y}$  is the change in the measurement vector. The gain matrix is calculated through successive numerical perturbation of the measurement vector and re-retrieval (Rodgers, 2000). A much faster method to use the Jacobian to determine the uncertainty has been performed (Bourassa *et al.*, 2012a), but makes an assumption that the gain matrix is equal to the inverse of the Jacobian, as typically the averaging kernel is close to the identity matrix. However, this method adds additional uncertainty to the precision estimate and was deemed unsuitable for the balloon campaign. Instead, with a limited set of balloon data, it is feasible to calculate the gain matrix directly. The uncertainty at each retrieved altitude is then given by

$$\mathbf{E} = \mathbf{G}\mathbf{S}_\epsilon\mathbf{G}^T \quad (5.11)$$

where  $\mathbf{S}_\epsilon$  is the covariance matrix of the measurement vector and  $\mathbf{E}$  is the covariance of the retrieved aerosol profile (*Rodgers*, 2000). The covariance matrix is given by

$$\mathbf{S}_\epsilon = \begin{pmatrix} S_{11} & S_{12} & \cdots & S_{1n} \\ S_{21} & S_{22} & \cdots & S_{2n} \\ \vdots & \vdots & \ddots & \vdots \\ S_{m1} & S_{m2} & \cdots & S_{mn} \end{pmatrix} \quad (5.12)$$

where the individual terms are given by

$$S_{\epsilon,ij} = \begin{cases} \left( \frac{\delta I_\nu(z_j, \lambda)}{I_\nu(z_j, \lambda)} \right)^2 + \left( \frac{\delta I_\nu(z_{ref}, \lambda)}{I_\nu(z_{ref}, \lambda)} \right)^2 & i = j \\ \left( \frac{\delta I_\nu(z_{ref}, \lambda)}{I_\nu(z_{ref}, \lambda)} \right)^2 & i \neq j. \end{cases} \quad (5.13)$$

The reported precision for ALI aerosol extinction retrievals is the square root of the diagonal of  $\mathbf{E}$ .

Ideally, the ALI measurements would be used independently to also retrieve ozone in the Chappuis band (600-700 nm range for ALI). However, due to the spectral range of the prototype, only a small fraction of the long wavelength side of the absorption band was captured. For this analysis, we have not retrieved the ozone profile but have set the ozone profile in SASKTRAN-HR to an average of the five closest coincident ozone profiles measured by OSIRIS at the ALI location and time. The ozone cross sections were determined by *Burrows et al.* (1999). The surface albedo used is also from the OSIRIS scans since the two instruments share a similar measurement method and should determine a similar albedo for the cloudy conditions. Preferably, albedo would be determined from ALI following the method of *Bourassa et al.*, 2012b, however due to the lack of an absolute calibration this was not possible.

### 5.3.2 Particle Size Retrieval Methodology

Work done by *Rieger et al.* (2014) has shown that different particle size distributions can affect the aerosol measurement vectors to yield some sensitivity. In his study, he uses an OSIRIS geometry and calculates the respective measurement vectors for a series of particle sizes which

can be seen recreated in Figure 5-10. In panel A, three different log-normal distributions are used to calculate the measurement vector using a simulated atmosphere through SASKTRAN. The three profiles are: a single fine mode particle size distribution with a mode radius and width of 0.08  $\mu\text{m}$  and 1.6 respectively shown in blue, bimodal particle size distribution that simulates volcanic conditions with the mode radius and width of 0.08  $\mu\text{m}$  and 1.6 for the fine mode and 0.4  $\mu\text{m}$  and 1.2 for the coarse mode which is shown in black, and lastly red is a representative size distribution with mode radius and width of 77  $\mu\text{m}$  and 1.75. Panel B shows the measurement vectors calculated with the three distributions across a series of wavelengths. The third panel, panel C, shows the difference of the measurement vectors compared to the bimodal distribution. Sensitivity to particle size is only seen past 800 nm measurements but great sensitivity does not occur until measurement are recorded out to 1200 nm. Furthermore, a 1% error in the radiance yields a relative error in the bimodal distribution measurement vector shown by the gray shading in panel C.

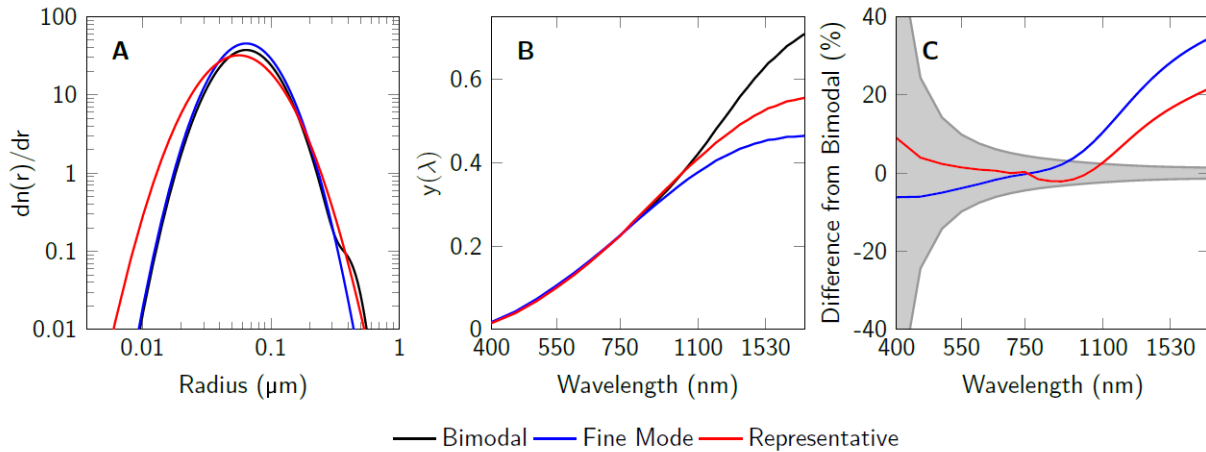


**Figure 5-10:** Reproduced from Figure 4 of Rieger *et al.* (2014). For OSIRIS scan 6432001 aerosol measurement vectors were calculated at 22.5 km. (A) The three size distributions used in the study. (B) The measurement vectors calculated via the SASKTRAN simulation (C) The relative percent difference of the fine and representative distributions with respect to the bimodal distribution. A 1% error in the radiance yields an uncertainty in the bimodal measurement vector shown by the grey shading.

For ALI, measurements were only gathered between 650 and 950 nm in wavelength, due to the low sensitivity of the CCD camera in the NIR. ALI only has sensitivity to particle size from the longer wavelengths and only a small amount. As such, it is not be possible to determine both the mode radius and mode width. Instead, the data from ALI is used to determine an Angström exponent. The Angström exponent is an approximation to Mie scattering since the value of the Angström exponent,  $\alpha$ , is related to the change in scattering cross section which depends on particle size distributions. As such the extinction value changes with a change in cross section.

From

$$\frac{n\sigma}{n_0\sigma_0} = \left(\frac{\lambda}{\lambda_0}\right)^{-\alpha}, \quad (5.14)$$

the particle size profile from a series of wavelengths can be determined from the Angström exponent. Lower Angström exponents correspond to larger particle sizes and vice versa for small particle sizes. The differences between extinction ratios at the different wavelengths can be used to gather an understanding of aerosol particle size in the form of Equation 5.14 where  $n$  is the aerosol concentration, and  $\sigma$  is the scattering cross section. Since the measurements observe relatively the same atmosphere over the time of one complete aerosol cycle the retrieved number densities should be similar. However, the retrievals at each wavelength are determined independently so the number density cannot be cancelled from Equation 5.14. For the 750 nm wavelength, the Mie scattering cross section was calculated for a variety of mode radii and widths and a change in the cross section can be observed in Figure 5-11.

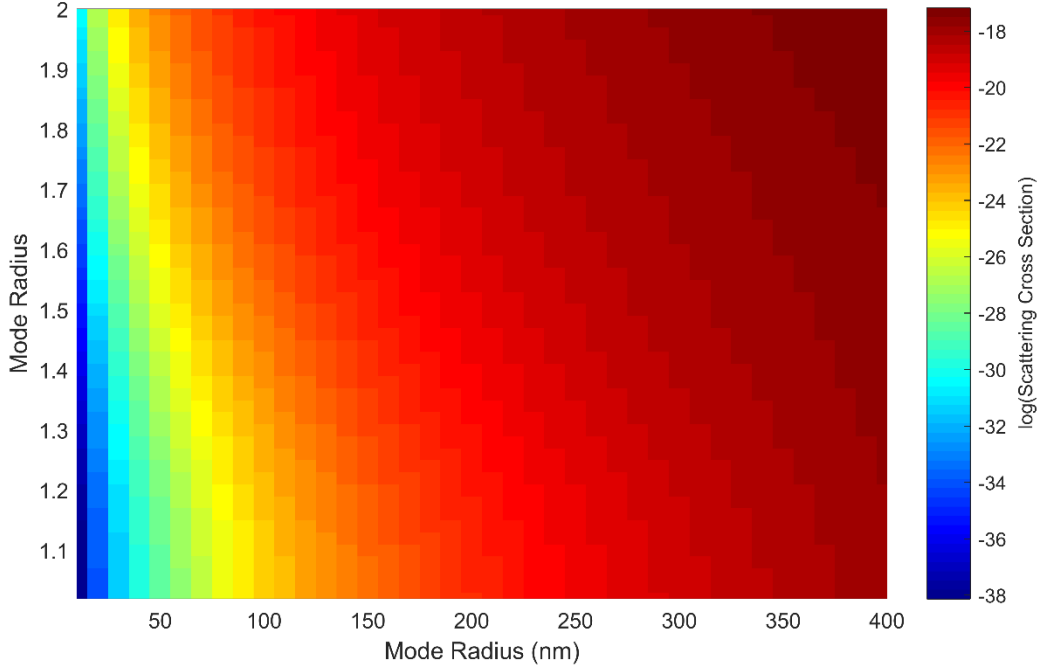


**Figure 5-11:** Computed with the optical properties of the SASKTRAN-HR engine. This variation of the cross section with respect to the mode radius and width allows for some determination of the particle size distribution through the Angström exponent.

The Angström exponent can be determined by fitting a line through a series of spectral points by rearranging Equation 5.14 into the following

$$\alpha = -\frac{\log(n\sigma) - \log(n_0\sigma_0)}{\log(\lambda) - \log(\lambda_0)}. \quad (5.15)$$

The rearrangement demonstrates that the Angström exponent is the simple slope of the log of the extinction over the log of the wavelengths.

Using the retrieved extinction profiles for the complete spectral range, we have attempted a determination of the Angström exponent using a method similar to that outlined by *Rault and Loughman* (2013) for the OMPS-LP analysis. In this method, the independently retrieved extinction profiles at each wavelength and altitude are fit with a straight line in log-wavelength, log-extinction space using a least squares fit. The slope of this line corresponds to the Angström exponent. This is then used to find the best match to the spectral dependence of the Mie scattering

cross section in order to update the particle size distribution. With only one piece of information, the mode-width of the log-normal distribution is fixed to 1.6 and the mode radius is updated. The extinction retrievals are then performed again at each wavelength and the process is iterated until the Angström exponent, corresponding to the determined mode radius, converges.

A precision estimate was also required for the Angström exponent. The method used to is the standard method to calculate uncertainty from the least squares fit. Assuming no uncertainty in the measurement points, the error in the slope is given by

$$\delta\alpha = \frac{s}{SS_{xx}}, \quad (5.16)$$

where  $s$  is

$$s = \sqrt{\frac{SS_{yy} - \alpha SS_{xy}}{n - 2}}, \quad (5.17)$$

and  $SS_{xx}$ ,  $SS_{yy}$ , and  $SS_{xy}$  are the sum of squares of the wavelength, aerosol extinction, and cross term between the wavelength and aerosol extinction and  $n$  is the number of points. However, there is an associated error with each aerosol extinction profile as outlined in section 5.3.1. So to determine the precision of the Angström exponent, accounting for the uncertainty in the aerosol extinction, a Monte Carlo method was used. The uncertainty of the Angström exponent was calculated millions of times and for each calculation a random amount of the error from the known range was added to the extinction. Finally, the mean from all of the uncertainty calculations of all of the least squares fits was used as the precision estimate on the Angström exponent.

### 5.3.3 Aerosol Extinction Retrievals

The complete mission consisted of 216 images that were recorded in illuminated conditions. The MART retrieval method was run on a select complete cycle for the purpose of the analysis, specifically the set of images from 650 to 950 nm consisting of images 204-216. For the purpose

of the retrieval an *a priori* for particle size distribution was used with a mode radius of 0.08  $\mu\text{m}$  and a mode width of 1.6 (Thomason, 1991). A sample of the retrievals can be observed in Figure 5-12 which highlights the 750, 850, and 950 nm retrievals. The left panels show the measurement vector from ALI in black with the forward model radiance profile from SASKTRAN-HR in blue. For each of the wavelengths, the algorithm determines altitudes where the value of the measurement vector is less than the known noise and does not allow aerosol to be retrieved in those regions. Instead, the scaling factor,  $\alpha$ , given by the summation term in Equation 5.7 is scaled to the aerosol profile above and below the last retrieved point to keep the aerosol profile smooth, as discontinuities are nonphysical and can lead to a nonphysical result in the MART algorithm. The middle panel shows the convergence between the measurement vector and the forward model result. The right column of Figure 5-12 is the retrieved aerosol profiles in blue with the associated uncertainty calculated using the method described in the previous section.

The retrieved aerosol extinction profiles for the analysis cycle can be seen in the left panel of Figure 5-13, note the log scale. For the full range of wavelengths, a difference of less than 2% between the measurement vector and forward model is seen throughout the retrieval altitude from approximately 13 to 29 km. Note the behavior of decreasing extinction with increasing wavelength as expected due to the dependence of the cross section with respect to particle size.

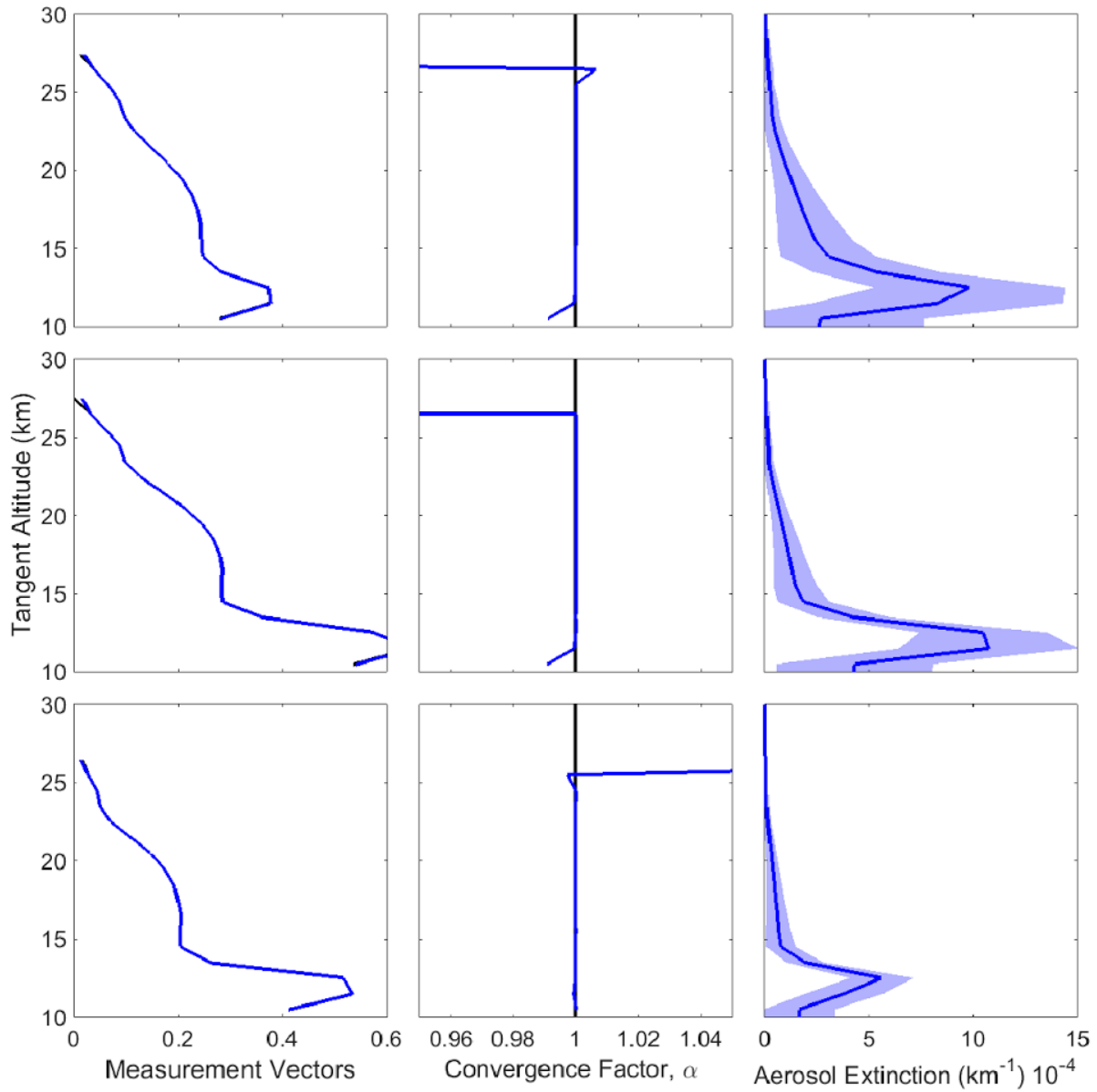


**Figure 5-12:** An example of three aerosol retrievals from images 206, 208, and 214, with center wavelengths of 750, 850, and 950 nm respectively are vertically displayed in the figure from top to bottom. The left column shows the measurement vector,  $\mathbf{y}$ , in black with the retrieved forward model,  $\mathbf{F}$ , in blue. The center column shows the ratio of the measurement vector over forward model known as  $\alpha$  and is the convergence factor between the ALI measurement and the forward model. For both of the first two columns, the black line is barely viable due to the very good agreement of the forward model. The final column is ALI aerosol extinction in blue with the associated error represented by the light blue shading.

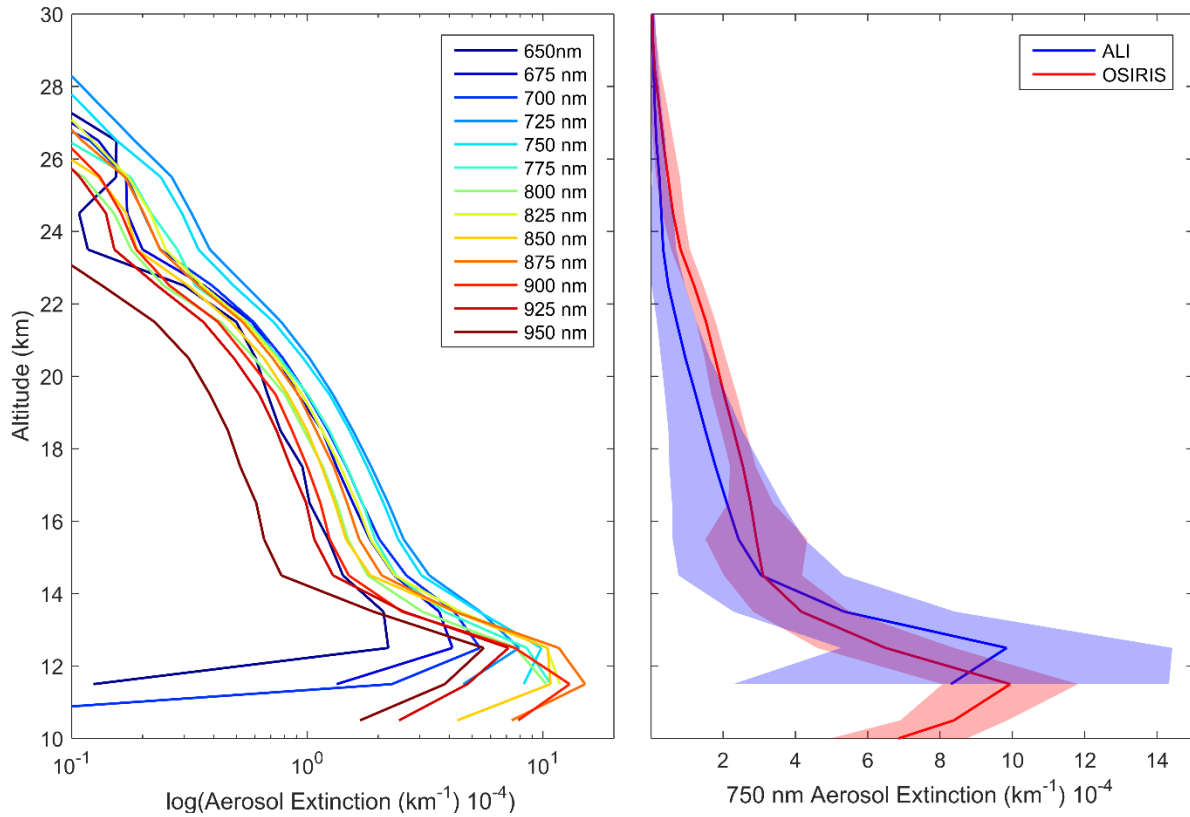


**Figure 5-13:** Left is the retrieved aerosol extinction profiles from the last complete imaging cycle consisting of images 205 to 216 from the  $0.0^\circ$  horizontal line-of-sight. Right is the 750 nm ALI aerosol extinction in blue with its error represented by the shading compared to the 750 nm extinction measured by OSIRIS in red with its error represented by the shading. Originally published as Figure 12 in Elash *et al.* (2016).

The ALI 750 nm aerosol extinction profile is shown in the right panel of Figure 5-13 with the shading representing the precision of the retrieval. The error is strictly based on measurement and instrument uncertainty and neglects any model and atmospheric state uncertainties as previously outlined. The red curve is the average 750 nm aerosol extinction profiles of the same five coincident OSIRIS scans used for the ozone profile. The retrieved extinction profiles from ALI and OSIRIS are within the total retrieval uncertainty. It is encouraging that the instruments follow the same overall profile shape including the stratospheric layer and the steep increase below 15 km. Aerosol is notoriously difficult to validate in remote sensing with various technique and instrument geometries, and yet the SAGE II, SAGE III and OSIRIS differences are generally below 20-30%

up to 30 km (*Bourassa et al.*, 2012b; *Rieger et al.*, 2015) There are also several possible systematic errors not accounted for in the inversion including the choice of retrieval altitude ranges, particle size composition and distributions, stray light, and the high altitude aerosol load.

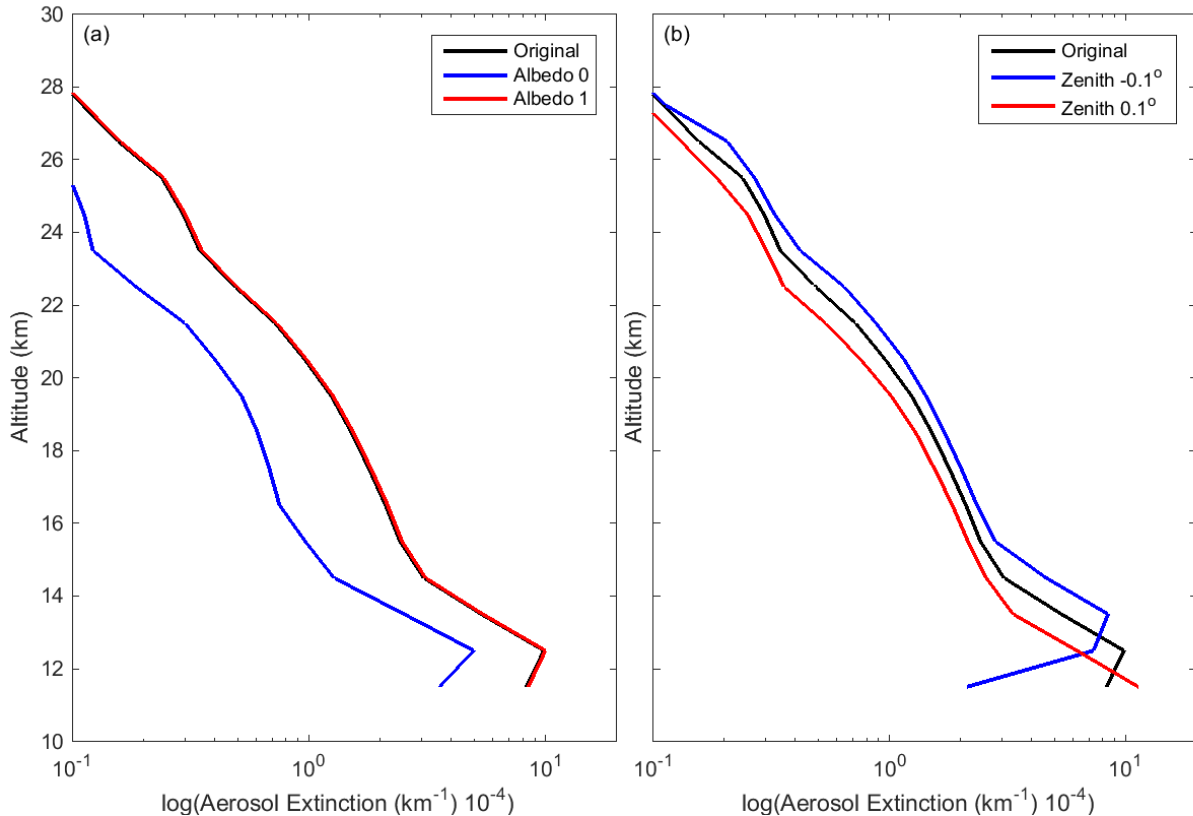


**Figure 5-14:** (a) Image 208 (750 nm) re-retrieved using an albedo of 0 and 1 compared to the original albedo used from OSIRIS. (b) Using the determined zenith pointing error from section 5.2, image 208 is retrieved again using the maximum possible pointing error compared to the original.

As a further note, other issues may have resulted in the disagreement between OSIRIS and ALI, mainly the estimation of the albedo and pointing inaccuracies. For the albedo, vertically linear polarized aerosol retrievals have a much larger sensitivity to albedo. For a scalar retrieval, changing the albedo from zero to one results in approximately a 30% increase in the aerosol extinction, but for a linear polarized measurement this change in albedo can be as large as a 100% increase in aerosol. Image 208 from the ALI campaign was rerun using an albedo of zero and one and the outcome of the retrieval can be seen in Figure 5-14a. Once again, note the log scale, the

albedo used from OSIRIS was 0.79. It should be noted that increasing the albedo higher than the OSIRIS values does not greatly increase the aerosol extinction. However, the retrieved aerosol profile varies by almost a factor of two just from a change in albedo. This may be significant since the albedo seen by a vertically polarized measurement and a total radiance measurement may vary although the true difference between the two type of albedos are unknown. A similar rerun was performed using the error in the zenith pointing discussed in section 5.2. The results of the alteration of the pointing can be seen in Figure 5-14b. From decreasing the zenith angle, the aerosol extinction is increased which could account for the largest discrepancies between the OSIRIS and ALI results at the 20 km range but moves the aerosol peak to a higher altitude causing a further discrepancy with OSIRIS at lower tangent altitudes. However, due to a lack of pointing information from the gondola this is the best estimation that could be performed. For the ALI image the solar scattering angle is 98° and for the five OSIRIS scans they are 77°, 89°, 90°, 91°, 92°, and 93°. With the exception of the forward scatter angles of 77° and 89° from OSIRIS, the scattering angles between OSIRIS and ALI are similar and should not cause a large effect on the retrieved profiles. However from the study performed in Chapter 6 a strong sensitivity to particle size distribution occurs near solar scattering angles of 90 degrees for the vertical polarization which can greatly bias the received aerosol profile. Furthermore, there may be further issues to explore with the polarized measurements and forward model. Finally, regardless, the results are encouraging.

### **5.3.4 A Sample Particle Size Retrieval**

The particle size method outlined above was also applied to this measurement set consisting of images 204 to 216. The retrieved extinction at a given altitude was rejected from the straight line fit if the converged forward model radiance at that altitude was not within 2% of the measurement vector. In the case shown in right of Figure 5-15, at the 14.5 km altitude point, only 10 of the 13

possible wavelengths contributed to the determination of the Angström exponent. The left panel of Figure 5-15 shows the median Angström exponent that was determined after each iteration and convergence can be seen after a couple iterations. The results are shown in the middle panel of Figure 5-15, where the Angström exponent is between 2 and 3 throughout the altitude range from 13 to 22 km. Assuming a mode width of 1.6 yields a median mode radius of 0.077  $\mu\text{m}$ . In comparison to typical levels of background aerosol from the Laramie, Wyoming OPC data (*Deshler et al.*, 2003), the retrieved particle size parameters are certainly within an expected range, although there is a relatively large error bar on the retrieved value, limiting the usefulness of the retrieved particle size information for background aerosol. However, with these error bars, even this limited spectral range would have the sensitivity to detected particle size changes as seen by OSIRIS and SAGE II over recent decades due to small volcanic perturbations (*Rieger et al.*, 2014).

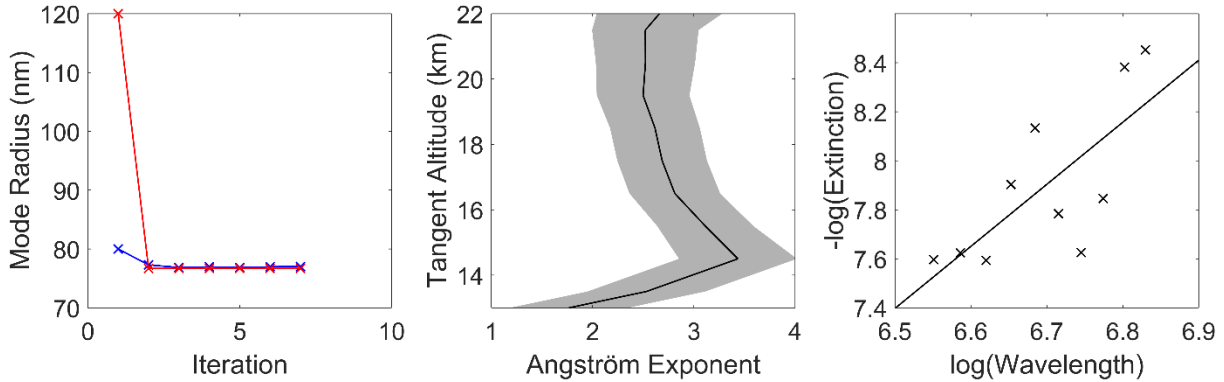


**Figure 5-15:** The left panel shows the convergence of two sample particle size retrievals, blue and red represent an initial state of 0.08 and 0.12  $\mu\text{m}$  mode radius respectively. Both initial states converge to the same value over approximately 3 iterations in the particle size retrieval method. The middle panel shows the final Angström exponents determined from images 204-216. The shading represents the error associated with the least squares fit. The right panel shows a typical least squares fit of the retrieved extinction values over wavelength to determine the Angström exponent at model altitude of 14.5 km. Originally published as Figure 13 in *Elash et al.* (2016).

#### 5.4 Results and Future Improvements

The ALI prototype, which is a telescopic acousto-optic imager, has been used to successfully measure two dimensional spectral images of the atmospheric limb from a

stratospheric balloon. The observed radiances appear to be of high quality and show both vertical and horizontal features of the cloud and aerosol layers. Aerosol extinction coefficient profiles were retrieved from the ALI data that show reasonable agreement with OSIRIS satellite measurements. Furthermore rudimentary particle size microphysics information was also retrieved from the ALI mission. Due to the limited spectral range of the prototype these retrievals was noisy but would still yield sensitivity to large particle size perturbations seen after a volcanic eruption similar to OSRIS or SAGE products and with the extended wavelength range into the NIR the precision could be increased. A satellite version of the ALI instrument would be able to supply global distribution of aerosol extinction and microphysics and assist in continuing the global aerosol record.

No large scale issues were found with the instrument performance; however, some future changes would be recommended. First, an absolute calibration of the instrument would allow ALI to determine the effective of albedo directly, as is done with OSIRIS. This would remove some of the uncertainly in the model inputs and likely yield higher quality results. This is simply a matter of having access to the calibration equipment and preforming the necessary experiments. Also, even with the baffle and the robust method of removing stray light with the cycling of the AOTF, some stray light was still observed in the obtained images. Impact and mitigation of this should be tacked in future iterations of the instrument. An issue to be tackled in a second generation instrument is an added telescope back end to the imager to be able to help remove reflections from the zero order beams from contaminating the final image from internal stray light as occurred in the prototype version of ALI. Also to further reduce this problem Glan-Taylor prism polarizers should replace the nanoparticle linear polarizers. The advantage to the Glan-Taylor prism is rather than attenuate the unwanted polarization it is reflected though total internal reflection

approximately 90 degrees from the optical axis where it can be absorbed away from imaging plane reducing the stray light contamination improving the imaging quality. A camera with faster readout would also greatly increase the number of measurements that can be made with the system and increase the amount of scientific information that could be acquired in a space mission.

Apart from aerosol future iteration of ALI could be used to possibly measure additional atmospheric species with modifications to the possible wavelength range. The current version of ALI was able to measure from 650-950 nm, and expanding out to the NIR and selecting an AOTF with a narrower bandpass the possibility of retrieving a water vapour profile using the water absorption bands around 930 nm would be possible. Further if the AOTF is replaced with a dual octave filter the wavelength range of the device could be expanded, for example 500-2000 nm, and replace the camera with an extended InGa array would allow the addition of an ozone retrieval while still maintaining the ability to retrieve high quality aerosol profiles. Furthermore, the addition of an ozone retrieval has an effect on aerosol retrievals at the shorter wavelengths which would improve the aerosol product at these wavelengths. Lastly, using an extended range AOTF would also allow a short wavelength normalization to the measurement vector like OSIRIS and SCIAMACHY for easier and consistent comparison between various instruments.

# CHAPTER 6

## THE SENSITIVITY TO POLARIZATION IN STRATOSPHERIC AEROSOL RETRIEVALS FROM LIMB SCATTERED MEASUREMENTS

### 6.1 Introduction

Stratospheric aerosol distributions have been monitored on a global scale since the 1970s with satellite instruments using a variety of remote sensing techniques. Remembering that most of the current instruments are operating well past their expected lifetimes, more space monitoring mission are required to continue the stratospheric aerosol monitoring. As noted in the recent review paper by *Kremser et al.* (2015) there is a distinct need for continued monitoring with global coverage of aerosol, particularly extending down to tropopause altitudes.

With the success of the ALI stratospheric balloon mission, a satellite feasibility study as well as a second version for stratospheric balloon testing are under development at the University of Saskatchewan and COM DEV. Additionally, as previously mentioned, a similar polarized instrument is current being developed in Belgium, ALTIUS (*Dekemper et al.*, 2012), which also uses an AOTF for spectral filtering. However, this new method of measuring aerosol has a fundamental difference compared to previous and current limb scatter instruments, it measures linear polarized light and not the total radiance.

The study contained in this chapter will look at polarized radiance measurements from a low earth orbit geometry, similar to that of OSIRIS (*Llewellyn et al.*, 2004) and SCHAMACHY (*Bovensmann et al.*, 1999), and determine the effect of measuring a linear polarization. Although it has been previously shown that the retrieval of stratospheric aerosol extinction profiles from polarized scattered sunlight measurements are possible (Chapter 5, *McLinden et al.*, 1999), the full impact of the polarized measurement has not been systematically studied. In this work we perform

an analysis with simulated polarized measurements to determine first if there are any clear advantages or disadvantages to making the linearly polarized measurement. Further, we investigate which linear polarization and viewing geometries have the largest sensitivities to aerosol, and how the polarized measurements affect the accuracy and precision of the retrieved aerosol product.

## 6.2 Background and Forward Model

In order to investigate the effect of polarization on the sensitivity to aerosol, an accurate model of the polarized limb radiance must be employed. Additionally, a large number of scenarios, including various atmospheric states and viewing geometries, are required to fully probe the solution space. In this section, the basic background describing the polarization state of the limb signal is developed, and the SASKTRAN-HR model and the various model scenarios used for the analysis are described. Based on the useful spectral range for limb scatter observations of stratospheric aerosol, we have limited our discussion to wavelengths from 500-1500 nm.

### 6.2.1 Polarized Scattered Sunlight and Stratospheric Aerosols

All full description of scattering interactions within the atmosphere can be found in section 2.4.2 to 2.4.4. This section will briefly cover the theory and then use it to analyze the polarization state of earth's atmosphere in regards to look direction.

The time-averaged polarization state of partially polarized, incoherent light can be fully characterized by a Stokes vector,

$$\mathbf{I} = \begin{bmatrix} I \\ Q \\ U \\ V \end{bmatrix}. \quad (6.1)$$

where the terms of the Stokes vector, defined in a reference frame, are measures of the total radiance,  $I$ , the difference between horizontal polarization to vertical polarization,  $Q$ , the

difference between  $+45^\circ$  diagonal polarization to  $-45^\circ$  polarization,  $U$ , and the difference between the counter clockwise circular polarization to clockwise polarization,  $V$ . Scattering events modify the polarization state of scattered light. This modification is described by a scattering matrix, which is valid for Stokes vectors defined in a scattering frame. Using a reference frame where the x-axis is defined to be the horizontal polarization and where x and y axes are orthogonal leads to the following definition for the Stokes parameters

$$\begin{aligned} I &= \langle E_x \rangle^2 + \langle E_y \rangle^2 \\ Q &= \langle E_x \rangle^2 - \langle E_y \rangle^2 \\ U &= 2\text{Re}(\langle E_x \rangle \langle E_y^* \rangle) \\ V &= -2\text{Im}(\langle E_x \rangle \langle E_y^* \rangle). \end{aligned} \quad (6.2)$$

The polarization state of light propagating along a ray is stored as a Stokes vector defined in some reference frame. When a scattering event is modelled the Stokes vector is rotated into the scattering frame, multiplied by the scattering matrix, and then rotated into a reference frame in which the scattered Stokes vector is stored and is represented by the following operation,

$$\mathbf{I}^{\text{sca}} = \mathbf{L}(\theta_2)\mathbf{P}(\Theta)\mathbf{L}(\theta_1)\mathbf{I}^{\text{inc}}. \quad (6.3)$$

The outgoing, or scattered, and incoming radiances are represented 4 by 1 matrices, *i.e.* Stokes column vectors, given by  $\mathbf{I}^{\text{sca}}$  and  $\mathbf{I}^{\text{inc}}$ , the rotation matrices are denoted  $\mathbf{L}$  and rotate the incoming ray and scattered ray by rotation angles  $\theta_1$  and  $\theta_2$ . The scattering matrix is a 4 by 4 represented by  $\mathbf{P}(\Theta)$  and is related to the probability that an incoming ray will be scattered at a scattering angle,  $\Theta$ . It also describes the change in polarization state through the elements of the matrix. . The product  $\mathbf{L}(\theta_2)\mathbf{P}(\Theta)\mathbf{L}(\theta_1)$  is sometimes referred to as the phase matrix

For this work, two primary scattering interactions induce and/or modify the polarization state of the light propagating in the atmosphere. These are scattering by the molecular air density and by stratospheric sulfate aerosols. The molecular atmosphere interaction is referred to as Rayleigh

scattering, and has a scattering matrix that is determined from the Rayleigh-Gans approximation (*Mishchenko et al.*, 2002) given by

$$\mathbf{P}(\Theta)_{\text{ray}} = \frac{3}{4} \begin{bmatrix} 1 + \cos^2 \Theta & -\sin^2 \Theta & 0 & 0 \\ -\sin^2 \Theta & 1 + \cos^2 \Theta & 0 & 0 \\ 0 & 0 & 2\cos\Theta & 0 \\ 0 & 0 & 0 & 2\cos\Theta \end{bmatrix} \quad (6.4)$$

where  $\Theta$  is the scattering angle.

For randomly orientated or spherical particles, such as stratospheric aerosol, only six elements of the scattering matrix are required (*van de Hulst*, 1957) which are the following

$$\mathbf{P}(\Theta) = \begin{bmatrix} P_{11}(\Theta) & P_{12}(\Theta) & 0 & 0 \\ P_{12}(\Theta) & P_{22}(\Theta) & 0 & 0 \\ 0 & 0 & P_{33}(\Theta) & P_{34}(\Theta) \\ 0 & 0 & -P_{34}(\Theta) & P_{44}(\Theta) \end{bmatrix} \quad (6.5)$$

Additionally, for spherical particles like stratospheric aerosol only four unique terms are required since  $P_{11} = P_{22}$  and  $P_{33} = P_{44}$ . Spherical aerosol scattering at visible and near-infrared wavelengths is fully described by Mie theory (*Mie*, 1908), for which several standard codes have been developed to calculate scattering cross sections and scattering matrices based on the particle size distribution and index of refraction (*i.e.* *Wiscombe*, 1980). A more detailed discussion can be found in section 2.4.4.

The basic polarization state of the scattered light in the Earth's atmosphere can be understood by first considering a single scattering event of the unpolarized incoming sunlight in a molecular atmosphere. It can be easily seen from the form of the Rayleigh scattering matrix (Equation 6.4) that a single scattering event causes the sky to develop a distinct polarization at a solar scattering angle (SSA) of 90 degrees from the incoming solar beam. The scattered sunlight is linearly polarized in the horizontal orientation, which is parallel to the horizon. The degree of polarization gradually decreases at scattering angles greater than or less than 90 degrees (broadly referred to as

back-scatter and forward-scatter geometries, respectively). In this single scattering scenario, the radiance is completely unpolarized at solar scattering angles of 0 and 180 degrees. If multiple scattering events are taken into account, the degree of polarization is decreased at 90 degrees SSA, and conversely does not become completely unpolarized at SSAs of 0 and 180 degrees assuming horizontal atmospheric unity. Simulations with the SASKTRAN-HR radiative transfer model using an atmosphere of molecular air density show that at 90 degrees SSA, the degree of linear polarization of the limb radiance is approximately 95% for a wavelength of 750 nm. This linear polarization effect is strongest at longer wavelengths (*i.e.* approaching 1500 nm) and decreases, on average by 10%, as the wavelength become shorter (*i.e.* down to 500 nm). This is directly related to the greater contribution from multiple scattering at shorter wavelengths. As the SSA increases from 90 degrees, the degree of linear polarization decreases. It is approximately 20% for a back scatter geometry of 180 degrees, and 30% for a scattering angle of 45 degrees. The ratio of the horizontal polarization over the total radiance and the vertical polarization over the total radiance is shown in the top of Figure 6-1. The strong polarized nature can be noted around SSA of 90 degrees where the radiance is almost complete horizontally polarized.

For an atmosphere that contains both the molecular air density as well as a typical background state of stratospheric sulfate aerosol, both Rayleigh and Mie scattering occur in a weighted fraction according to the optical depth of air and aerosol. Compared to the pure Rayleigh scattering case, the addition of aerosol causes a decrease in the degree of linear horizontal polarization for wavelengths shorter than approximately 750 nm. The bottom two panels of Figure 6-1 show the difference in the ratio of the polarized over the total radiance for the atmosphere with aerosol and one without, this effect has a weak dependence on solar scattering angle, with the most depolarization occurring in forward scatter geometries for short wavelengths. Interestingly, for

longer wavelengths in back-scatter geometries, the opposite occurs. This is due to the changing fraction of scattering from the molecular air density and aerosol because the Rayleigh scattering cross section falls off much more quickly with wavelength than the aerosol cross section (see section 2.4.4). The magnitude of the observed change in linear polarization from a pure Rayleigh atmosphere to that with typical background aerosol is approximately 5-10%, but it obviously varies depending on aerosol loading and the microphysical parameters of the aerosol.

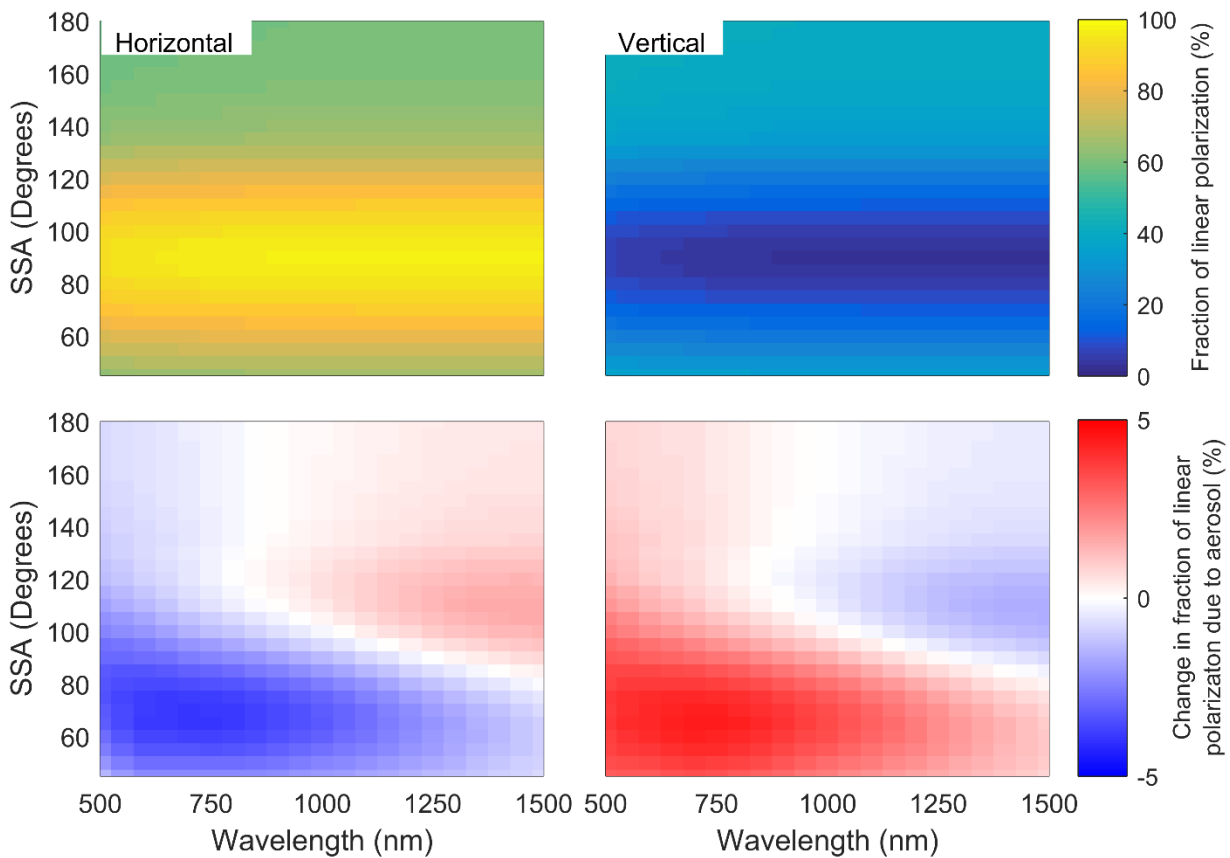


**Figure 6-1:** (Top) The fraction of a linear polarization (left is horizontal and right is vertical) over the total radiance for molecular air density. (Bottom) The change in the fraction of linear polarization between an atmosphere that contains aerosol and one with only molecular air density.

### 6.2.2 SASKTRAN-HR Model

The model used for this work is the SASKTRAN-HR (*Bourassa et al.*, 2007; *Zawada et al.*, 2015) radiative transfer model discussed in section 2.4.5 and a brief overview will follow. The High Resolution module of the SASKTRAN radiative transfer framework (*Bourassa et al.*, 2007; *Zawada et al.*, 2015) was used in this study. The SASKTRAN framework handles built-in and user-specified atmospheric species optical properties and number density profiles, and uses a fully 3D spherical geometry to solve the radiative transfer equation. The High Resolution module uses a successive orders of scattering technique, and solves either the scalar or vector (polarized) radiative transfer equations to arbitrarily many orders of scatter. In this study, the HR module is configured so that for any photon trajectory the first two scatters in the atmosphere (from the Sun) and the final scatter into the instrument line of sight are treated in a fully polarized sense; any intervening scatters treat the photon as randomly polarized. For example: If a photon scatters three times to enter the line of sight, each scatter is treated in a fully polarized sense; if a photon scatters five times to enter the line of sight, the first two scatters are polarized, the photon is then depolarized and scattered twice, and finally undergoes a polarized scatter from its randomly polarized state into the line of sight. This pseudo-polarized approximation has been shown, through comparison against the highly accurate and fully polarized Monte Carlo module of the SASKTRAN-HR framework (*Dueck et al.*, 2016), to approximate the full solution of the vector radiative transfer equation to sufficient accuracy for the wavelengths and geometries of interest in this work. All calculations performed with SASKTRAN-HR in this study assume randomly polarized incident sunlight, and dry air and Mie ( $\text{H}_2\text{SO}_4$ ) scattering events only to model the interaction with the molecular air density and stratospheric aerosol, respectively. Scattering events from the Earth's surface are assumed to be Lambertian and fully depolarizing.

### 6.2.3 Model Scenarios

The impact of using polarized radiance measurements on stratospheric aerosol retrievals is systematically studied with the radiative transfer model by exploring a set of distinct cases that approximately cover the expected range of aerosol parameters, including both particle size and concentration (or extinction) profiles, and viewing geometries. Viewing geometry is an important parameter as even in the case of the total radiance measurements, the geometry can have a substantial effect on the sensitivity of the measurement to aerosol due to the asymmetry of the Mie scattering phase function, *i.e.* element  $P_{11}(\Theta)$  of the scattering matrix (Rieger *et al.*, 2014). There is strong aerosol scattering in the forward direction and so this results in a weaker relative aerosol signal in the back scatter direction.

To probe the space of possible aerosol measurement scenarios, two aerosol extinction coefficient profiles and four particle size distributions were used. The two extinction profiles, nominally specified at 750 nm, correspond to a background aerosol case, typical of the volcanically quiet period of the early 2000's (Deshler *et al.*, 2003), and a volcanically enhanced case which was taken from OSIRIS measurements two months after the Nabro eruption in 2012 (Bourassa *et al.*, 2012c). Both profiles are shown in Figure 6-2. The four particle size distributions were also chosen to represent typical background and volcanically enhanced cases. The background cases are both single mode lognormal distributions with somewhat different, but still typically observed, size parameters. A bi-modal lognormal particle size distribution was used for the volcanically enhanced cases, with one fine mode and one coarse mode, each comprising an equal fraction of the total extinction. All of the parameters of the size distributions are detailed in Table 6-1**Error! Reference source not found.**. These selected distributions are based on in-situ balloon particle counter measurements from Laramie, Wyoming (Deshler *et al.*, 2003). The size distributions were used for translating the extinction profiles, which are specified at 750 nm, to

other wavelengths by scaling the extinction by the ratio of the Mie scattering cross sections corresponding to the size distribution at the two wavelengths.

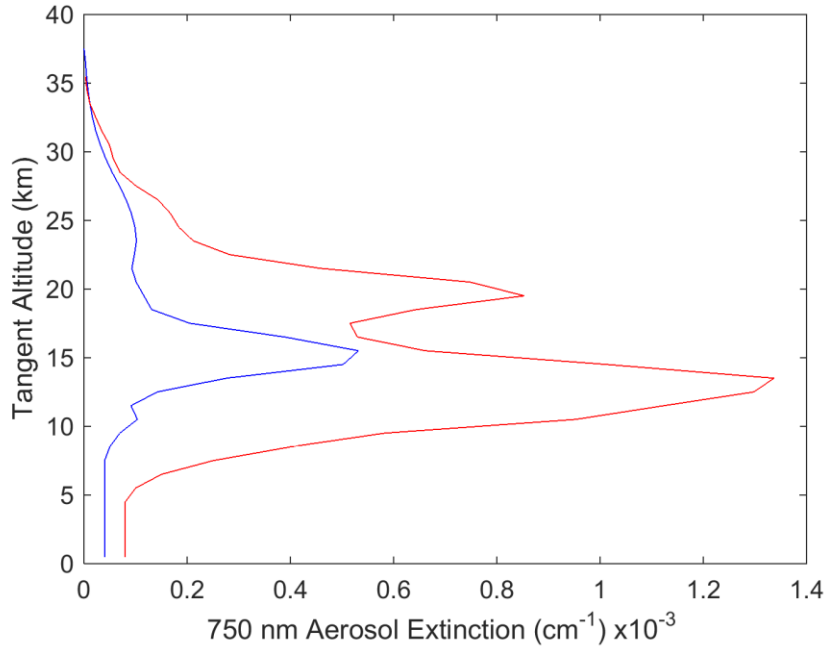


**Figure 6-2:** The two aerosol profiles used in this study. The blue is a background aerosol extinction levels, and the red curve is a representative aerosol profile after the Nabro eruption.

**Table 6-1:** Different particle size distributions used to test the sensitivity of the aerosol retrieval.

Particle size distributions	Fine mode radius (μm)	Fine mode width	Coarse mode radius (μm)	Coarse mode width	Percent extinction coarse mode (%)
1	0.04	1.8	--	--	0
2	0.12	1.25	--	--	0
3	0.04	1.8	0.30	1.15	50
4	0.12	1.25	0.30	1.15	50

To probe the range of possible viewing geometries from low earth orbit, a range of Solar Zenith Angles (SZAs) and Solar Scattering Angles (SSA) were selected. The ranges give representative selections of the possible geometries of a limb scatter instrument in low earth orbits at a range of local times. The selected values for SZA are 15°, 45°, and 75° and for SSA of 30°, 60°, 90°, 120°, 150°, and 180°.

Simulated measurements were performed at wavelengths of 500, 750, 1000, 1250, 1500 nm, which approximately cover for the spectral range commonly used for aerosol retrievals from limb instruments. For example, OSIRIS and SCHIAMACHY aerosol products use the ratio of 750 nm to 470 nm for the aerosol retrieval (*Bourassa et al.*, 2012b; *Ernst et al.*, 2012). Additional longer wavelengths have been shown to provide particle size information from limb scatter measurements (*Rieger et al.*, 2014) and so the 1000-1500 nm wavelength range was also included in this study. Finally, we also performed simulations for Earth surface albedo values of 0 and 1 in order to cover the full range of potential impact.

### **6.3 Methodology**

For the purposes of this study, we have assumed an instrument capable of measuring only the linearly polarized radiance with either a vertical or horizontal orientation. This is representative of newly proposed instruments like ALTIUS (*Dekemper et al.*, 2012) and ALI that use an AOTF and by nature only measure one orientation of linearly polarized radiance. We want to answer the question: If the linear polarization is measured, is this an advantage or a disadvantage over a measurement of the total radiance for aerosol retrievals? Further, is there a preferred orientation of linear polarization?

The polarization states used here are defined as the following: the linearly polarized radiance aligned with the horizon is referred to as the horizontal polarization, and the linearly polarized radiance that is perpendicular to the horizon is referred to as the vertical polarization. We also use the total radiance, or alternatively the scalar radiance, as the reference case. Note that the scalar radiance is not precisely equal to the total radiance. For the work presented here the term “total radiance” refers to the first term in the Stokes vector, which is calculated by the SASKTRAN-HR model when solving the vector radiative transfer equation. The term “scalar radiance” refers to the radiance calculated by the SASKTRAN-HR model when solving the scalar transfer equation.

Using the Stokes parameter formulation, the horizontal polarization is given by  $0.5(I + Q)$  and the vertical polarization is given by  $0.5(I - Q)$ , which can be easily shown from the definitions given in Equation 6.2.

Our study further breaks down this problem into three questions. First, how does the fraction of the limb scatter signal that is due to aerosol vary with aerosol load and viewing geometry for both scalar and polarized measurements? Secondly, does the polarized measurement increase sensitivity to assumptions in the retrieval algorithm and therefore increase potential for biased results? And finally, how does the polarized measurement affect the uncertainty estimate of the retrieved profile?

To explore the first question, simulated measurements were calculated with SASKTRAN-HR using the scenarios described in section 6.2.3, including various wavelengths, geometries, aerosol loading and particle size distributions. These simulated measurements are then used to determine the approximate fraction of the limb signal that is due to aerosol. In each case the model is run with a nominal atmosphere that consists of molecular air density, and climatological ozone and nitrogen dioxide profiles.

The fraction of the limb signal due to aerosol is determined by calculating the radiance without aerosol in the model atmosphere, *i.e.* that due to Rayleigh scattering only,  $I_R$ , and the radiance including aerosol,  $I_A$ . To find the fraction,  $\delta$ , in percentage, of the signal that is attributed to aerosol, the following formulation is used:

$$\delta = \frac{I_A - I_R}{I_A} * 100\%. \quad (6.6)$$

Due to non-linearities from multiple scattering, it is not strictly true that this is the fraction of the signal due to aerosol; however, at most stratospheric tangent altitudes, the wavelengths under study

are quite optically thin and this simple percent difference provides an intuitive approximation of the fraction of the signal due to aerosol.

We explore the second question about the effect of the polarized measurement on the aerosol retrieval using simulated measurements and a retrieval method that is essentially similar to that developed by *Bourassa et al.* (2012b) for OSIRIS. A minor change to the algorithm is made where the measurement vector for this study is not normalized by a shorter wavelength. Although it is advantageous in a retrieval scenario to limit sensitivity to particle size, for this study we explore the worst case scenario under possible limitations of future technology, given that not all instruments may cover a wide enough spectral range for short wavelength normalization.

The limb radiance is calculated using SASKTRAN-HR, again with climatological ozone and NO<sub>2</sub> profiles, for each of the scenarios listed in section 6.2.3. This is taken as a simulated measurement and is then used to retrieve aerosol extinction profiles using the *Bourassa et al.* (2012b) technique. This is done similarly for the total radiance and for each orientation of the linearly polarized radiance. Additionally, a retrieval is performed with the scalar SASKTRAN-HR model to see if there is any substantial difference between using the scalar radiance and the total radiance from the vector model. For each aerosol retrieval, the ozone, NO<sub>2</sub>, and albedo are fixed to the values used in the simulation of the measurement. All four particle size distributions from Table 6-1**Error! Reference source not found.** are used in the simulations, but following *Bourassa et al.* (2012b), the aerosol particle size is fixed in the retrieval to a single mode log-normal with 0.08 μm mode radius and mode width of 1.6. The assumption of a fixed particle size distribution is common in limb scatter retrieval algorithms and this is used to explore sensitivity of the polarized measurements to particle size distributions, and test if the uncertainty in this assumption greatly effects the retrieved extinction.

Lastly, to answer the third question, an uncertainty estimate is performed on these retrievals in order to check the precision of the retrieved aerosol profile. The precision is determined by mapping the covariance of the measurement vector,  $\mathbf{S}_\epsilon$  through the gain matrix,  $\mathbf{G}$ , which describes the sensitivity of the retrieval to the measurement and the respective noise through the following (Rodgers, 2000)

$$\mathbf{E} = \mathbf{G} \mathbf{S}_\epsilon \mathbf{G}^T. \quad (6.7)$$

where  $\mathbf{E}$  is the co-variance matrix for the retrieved aerosol profile. However, the direct calculation of the gain matrix is computationally intensive and numerically requires a retrieval for each measured altitude. A method presented by Bourassa *et al.* (2012a) uses the Jacobian,  $\mathbf{K}$ , to approximate the gain matrix by assuming the problem is linear near the solution state, which is largely a good assumption for limb scatter aerosol retrievals. Using these assumptions, the gain matrix can be determined simply through the inverse of the Jacobian,

$$\mathbf{G} \cong \mathbf{K}^{-1}. \quad (6.8)$$

Rather than specifying an assumed measurement co-variance to study the behavior of the retrieval precision, we simply replace the measurement co-variance in Equation 6.7 with the identity matrix. Thus the resulting terms of  $\mathbf{E}$  are not absolute quantities but are related to the amplification of the measurement noise when mapped to the retrieved state (*i.e.* the larger the values of  $\mathbf{E}$  the larger the uncertainty for the retrieval). The square root of the elements of the diagonal of the aerosol covariance, typically used to represent the error bars on the retrieved profile, are taken as the amplification of the measurement noise.

This method assumes that the radiance measurements regardless of polarization state have exactly the same signal to noise performance, *i.e.* all measurements have the same co-variance. We also consider the case where the instrument is not compensated such that the magnitude of the

various polarization states directly scales the signal to noise performance, *i.e.* the instrument is not compensated to equalize the measurement co-variance when the signal drops due to the measured polarization state. In this scenario the above method must be modified by replacing the identity matrix with the matrix,  $\mathbf{R}$ , to represent the change in signal strength for the various polarizations relative to the scalar case. This matrix is defined as

$$R_{ij} = \begin{cases} \frac{I_{ref,i}}{I_{pol,i}} & \text{for } i = j \\ 0 & \text{for } i \neq j \end{cases} \quad (6.9)$$

The diagonal of the  $\mathbf{R}$  matrix is effectively scaled by the inverse of the magnitude of ratio of the polarized radiance,  $I_{pol,i}$ , to the reference scalar case,  $I_{ref,i}$ , for the measurement altitude,  $i$ .

## 6.4 Analysis

### 6.4.1 Difference in Scalar Retrievals using a Scalar or Vector Model

First, we investigate if there is any significant difference between the use of the scalar radiance and the total radiance for retrievals on measurements of the total radiance. As mentioned above, retrieval algorithms for current limb scatter data sets such as OSIRIS and SCIAMACHY use a scalar radiative transfer model with general success; however, as the total radiance is not generally equal to the scalar radiance, this may lead to biases in the retrieved extinction profile under certain scenarios. Accounting for the vector component in the model alters the overall total radiance from the scalar solution due to multiple scattering interactions between the various polarization states of each successive order of scattering.

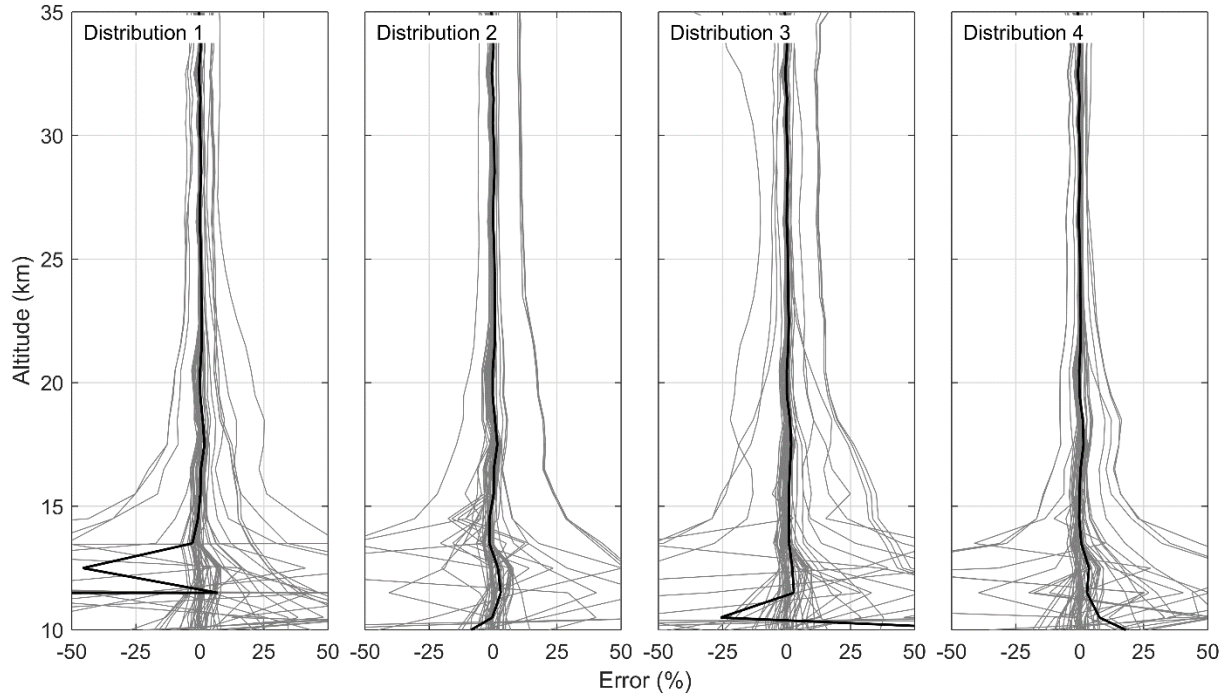


**Figure 6-3:** Percent differences between the vector retrieved aerosol extinction profiles and the scalar retrieval from simulated total radiance measurements. Each column represents a different particle size distribution (see Table 6-1**Error! Reference source not found.**).

The total radiance was simulated with SASKTRAN-HR in vector mode for the full set of wavelengths and viewing geometries, and for the range of aerosol loading scenarios. These were used as input measurements to the retrieval algorithm, which was then performed using both the scalar and vector models. A case-by-case comparison between the retrieved extinctions for the scalar and vector models was performed using a simple percentage difference at each retrieved altitude  $a$  can be seen as the grey lines in Figure 6-3. Furthermore, the mean of the bias for each particle size distribution is shown in solid black. These results, given in Figure 6-3, show that across all wavelengths, the mean percent difference is less than 2% from 15 to 37 km. It should be noted that some of the differences between the two models are removed due to the high altitude normalization in the retrieval. A small number of outlier cases occur where the difference between the retrievals is greater than 7%. All of these cases occur for back scatter geometries and short

wavelengths. The reason for this discrepancy is not well understood, although it certainly arises from the differences between the scalar and total radiance due to polarization interactions from the relatively larger contribution of multiply scattered light at shorter wavelengths. These discrepancies are enhanced by the reduced sensitivity to aerosol in the back scatter geometries. Generally, however, any differences between the use of the scalar and vector model for the retrieval are negligible. In fact, any form of discrepancy essentially vanishes for wavelengths past 1000 nm. Since the use of the vector model can increase calculation times by a factor of at least two, it is certainly justifiable to use the scalar model for the overwhelming majority of scenarios. For the rest of the work presented, any reference to the radiance will only refer to the total radiance,  $I$ , from the vector model.

#### **6.4.2 Fraction of Limb Signal due to Aerosol**

For a typical background aerosol state, the fractional contribution to the total limb radiance from aerosol was calculated from modelled radiances over a series of stratospheric tangent altitudes using the background aerosol profile and particle size distribution 1, given in Table 6-1. Figure 6-4 shows the percent change in this fraction for horizontally and vertically polarized measurements compared to the total radiance. The viewing geometry, which is a typical low earth orbit scenario, is SZA=45° and SSA=60°, and the albedo is set to 0 to remove depolarization from the Lambertian Earth. The top of Figure 6-4 shows the percentage of signal that is attributed to aerosol for both horizontal and vertical linear polarizations,  $\delta$ . As can be seen from the bottom of Figure 6-4, most of the change in the aerosol fraction of the polarized limb signal compared to the total radiance (i.e.  $\Delta\delta = \delta_{tot} - \delta_{pol}$ ) occurs for wavelengths between 500-1000 nm. At these wavelengths the horizontal polarization has a smaller fraction of signal due to aerosol and the

vertical polarization has a larger fraction due to aerosol. Overall the change is small and essentially limited to less than 10%.

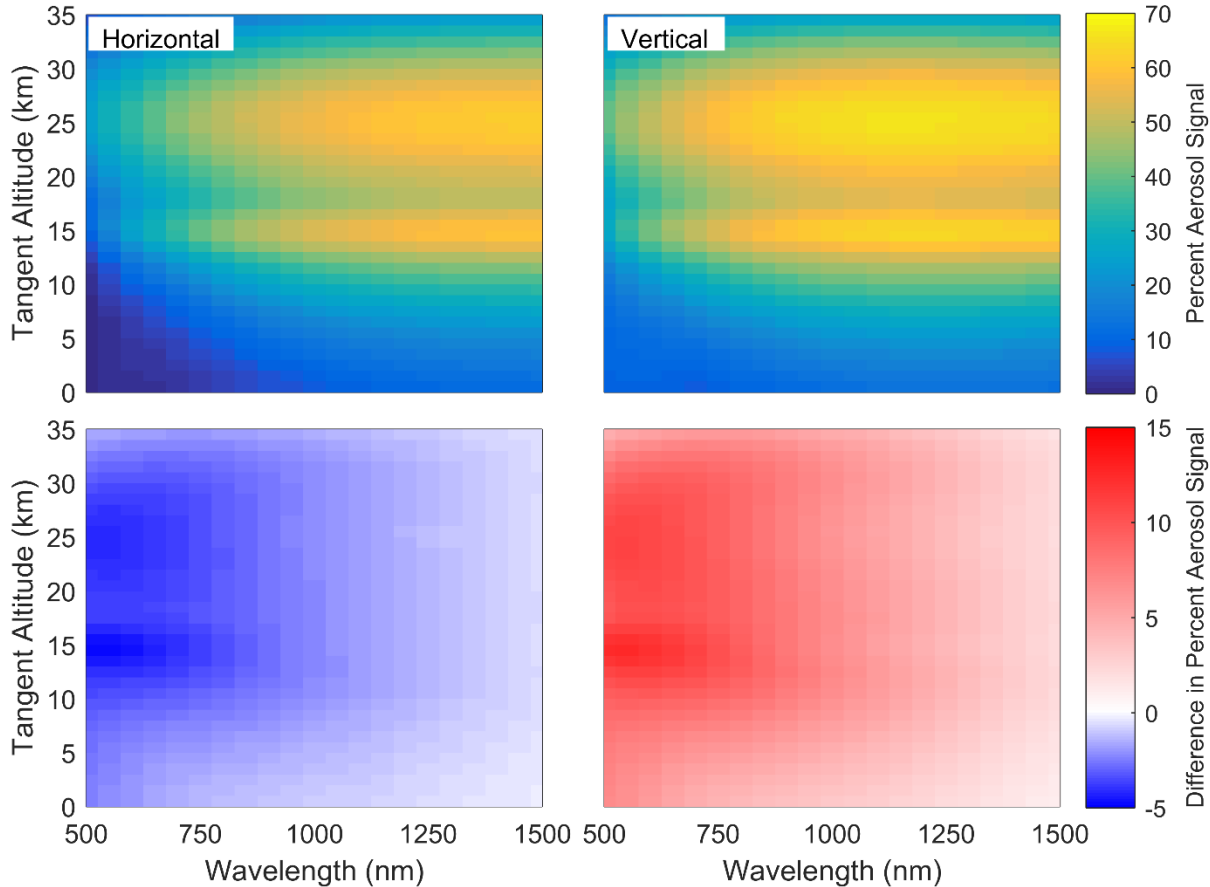


**Figure 6-4:** (Top) For a horizontal (left) or vertical (right) linear polarization the percent of the signal that is attributed to aerosol,  $\delta$ . (Bottom) The change in the fraction of the limb signal due to aerosol when compared to the total radiance for the horizontal (left) and vertical (right) polarization ( $\Delta\delta$ ). The simulation uses a geometry of SZA=45° and SSA=60°, with the albedo being 0 and the aerosol state the background profile with particle size distribution 1. Take note the red-blue scale is non-symmetric.

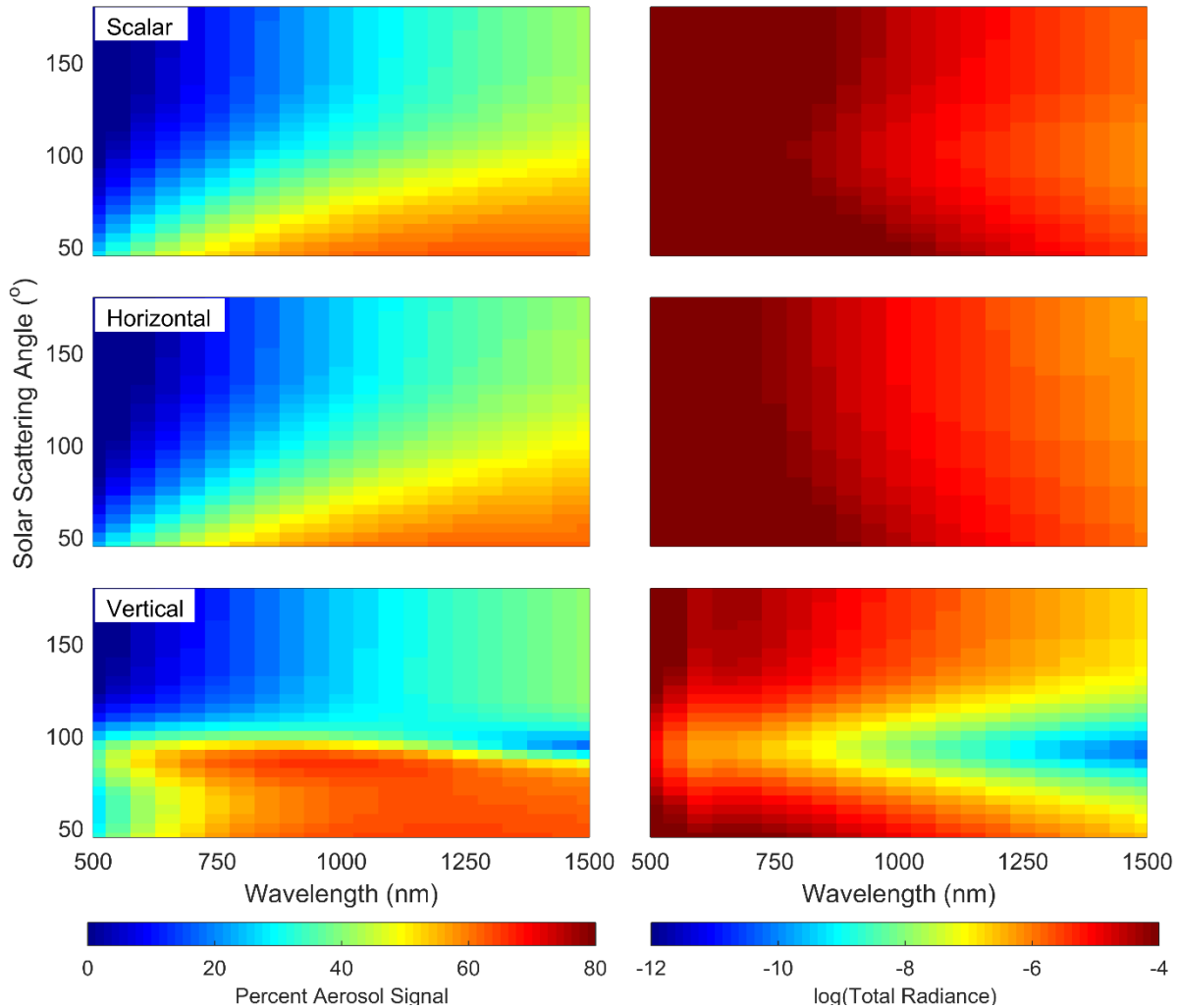


**Figure 6-5:** Dependence of the fraction of the limb spectra due to aerosol on solar scattering angle (left panels) for total radiance (top), horizontal polarization (middle) and vertical polarization (bottom), and the magnitude of the radiance for each case (right panels). Note the low signal near SSA of 90 degrees for the vertical polarization which would be problematic for terminator orbits.

Similar calculations were performed for the range of viewing geometries using the same atmospheric state. Figure 6-5 shows the fraction of limb signal due to aerosol for the total radiance, and both orientations of the linearly polarized radiance. This calculation was performed for 15 km tangent altitude, and other stratospheric tangent altitudes show very similar patterns. An important difference is noted between the forward and back scattering geometries. Remembering the horizontal polarization is given by  $0.5(I + Q)$ , the total and horizontal polarization cases have a

similar dependence on viewing geometry, with the strongest aerosol signal from long wavelengths in the forward scatter direction. The vertical polarization, given by  $0.5(I - Q)$ , has a strong aerosol signal contribution for forward scattering directions, especially at visible wavelengths, in comparison to the total and horizontal polarization cases. For back scattering geometries, somewhat less aerosol signal is observed. For reference, the magnitude of the limb radiance in each case is shown in the right hand column of Figure 6-5 taking note that the high end of the scale is saturated to emphasize the smaller values. It is important to note that the vertical polarization has a very low magnitude at scattering angles near 90 degrees, making vertically polarized measurements in this geometry particularly susceptible to signal-to-noise problems.

These same calculations were performed for the full range of SZAs and found that the SZA affects the fraction of the signal due to aerosol by only less than 1%. Also, when the albedo is changed from 0 to 1, the aerosol signal decreases for all polarizations and wavelengths thus reducing overall sensitivity to aerosol as albedo increases in all cases. Note, however, that the SASKTRAN-HR model assumes that all ground reflection is randomly polarized; the addition of a polarized BRDF model may change the sensitivity to aerosol with higher albedo.

This same analysis was also performed for two other additional polarization orientations, the +45 degree and -45 degree linear polarizations (*i.e*  $0.5(I + U)$  and  $0.5(I - U)$ ) to investigate sensitivity to aerosol. It was found that these two polarization orientations had similar aerosol contribution to the total radiance case with approximately two thirds of the overall signal when compared to the total radiance case.

In general, the contribution to the limb radiance from aerosol for the horizontally polarized and total radiance cases is approximately the same. The vertical polarization has more asymmetry in aerosol signal between forward and back scattering geometries with very low signal magnitude

near 90 degrees scattering angle. Given that essentially all low earth orbit scenarios will cover forward and backward scattering angles, including 90 degrees scattering angle, it is clear that the horizontal orientation overall shows a more favorable response to aerosol. This is particularly true for a terminator orbit such as that for OSIRIS.

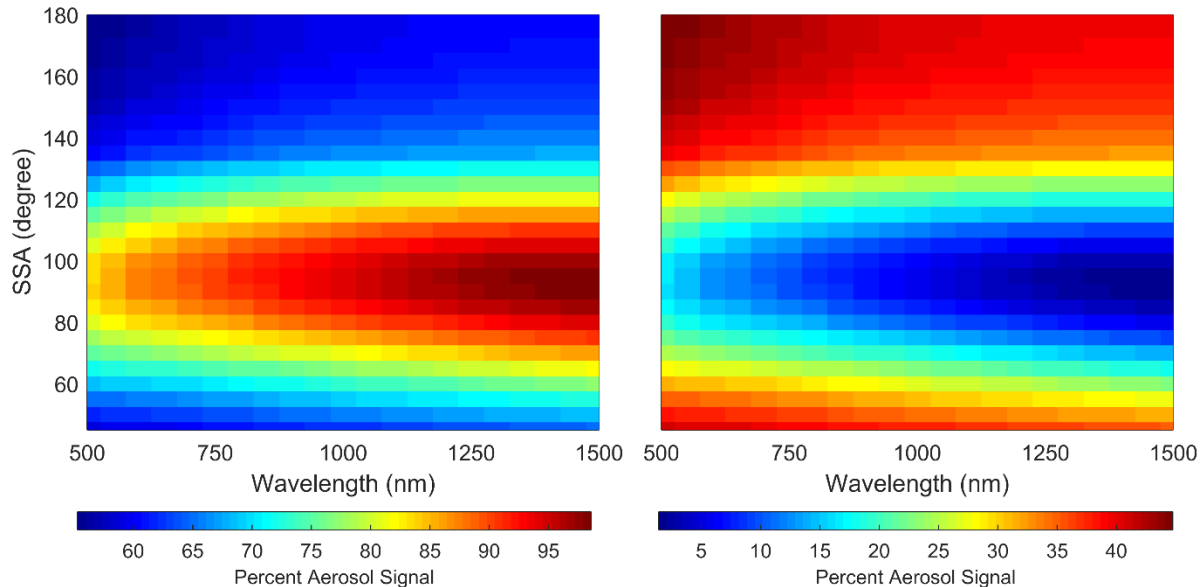


**Figure 6-6:** The ratio of the linearly polarized radiance to the total radiance for horizontal (left) and vertical (right) orientations. Note that the scale for each plot is different. The simulation was performed with a SSA of 60 degrees with volcanic aerosol loading for a tangent altitude of 20 km.

A distinct disadvantage of measuring a linear polarization rather than the total radiance is the loss of overall signal magnitude. In Figure 6-6, the ratio of the polarized radiance to the total radiance is shown for a series of SSAs for a tangent altitude of 20 km, but in this case using the volcanic aerosol extinction profile, which serves to enhance the fraction of signal due to aerosol. Measuring the horizontal polarization results in observing signal levels approximately one half to two thirds of the total radiance, with the greatest effect at the shorter wavelengths. The other forward scatter geometries are similarly affected. For back scatter geometries, the signal levels are also approximately half of the total radiance, but with less spectral dependence. For solar scattering angles near 90°, the horizontal polarization encompasses a large fraction of the total radiance

resulting in signals of 80-95% of the total. Across the full parameter space of viewing geometries, wavelengths, and aerosol loading scenarios, the magnitude of the horizontal polarization is on average 60-70% of the total radiance.

Although the vertical polarization shows a relatively larger fraction of the signal due to aerosol particularly in forward scatter geometries, the overall signal levels are substantially lower. For forward scatter geometries, the magnitude of the vertically polarized radiance is only approximately one third of the total radiance across the spectral range. Back scatter geometries are only slightly better with slightly less than half of the total radiance. Again, near solar scattering angles of  $90^\circ$  the limb radiance is almost fully horizontally polarized and the vertically polarized signal is only 5-20% of the total. On average across the entire parameter space, the vertical polarization component typically accounts for 30-40% of the total signal.

It is clear from this relatively simplistic analysis of the aerosol signal in polarized limb radiance that there are trade-offs between viewing geometries and instrument polarization sensitivity, and changing sensitivity across the spectral range. While there is not an overwhelming case to be made for one particular option over the wide range of scenarios that can be considered, the overall response of the horizontally polarized radiance is essentially similar to the total radiance, but with somewhat reduced magnitude that can most likely be mitigated through instrument design considerations. The vertical polarization has much more widely varying sensitivity to aerosol with very low signal levels near 90 degrees scattering angle, and is a much more challenging choice in terms of instrument performance for aerosol measurements.

#### **6.4.3 Potential for Retrieval Bias**

In this section we directly explore the effect of the polarized measurement on the results of a typical retrieval algorithm through application of the algorithm to simulated measurements across the full parameter space.

We explore the potential of an effect of polarization on the bias in retrieved extinction caused by uncertainty in the assumed particle size distribution. The set of radiances for all cases across the parameter space were again used as simulated input measurements to the retrieval algorithm. This time, retrievals were performed on the horizontally polarized radiance, the vertically polarized radiance, and the total radiance. The radiance calculations in the iterations of the retrieval were set to match the polarization states of the input radiance, but the total solution was used to approximate the total radiance. In all cases, the retrieval was performed using an assumed particle size distribution, which was log-normal with a mode radius and width of 0.08  $\mu\text{m}$  and 1.6 respectively. Note that this assumed size distribution is different than all four of the size distributions used as the “true” state for the simulated input radiances. For the total radiance case, this uncertainty is well known to cause biases of up to 20-30% in retrieved extinction (*Rieger et al.*, 2014). A summary of the differences between the retrieved and true aerosol extinction for 750 nm and 20 km altitude is shown in Figure 6-7 and is similar for altitudes from 17 to 35 km. Errors bars on each point represent one standard deviation of the variability in the results for the range of viewing geometries. These results are representative of the level of agreement also found for other wavelengths and altitudes. There is no substantial difference between the results for the background and volcanic extinction profiles. It should be noted that cases with solar scattering angle of 90° have been removed for the vertical polarization due to the very low values of signal, which manifests as a large dependency on the particle size distribution and a highly biased retrieval. This large bias is very sensitive to scattering angle and is nearly eliminated for even 85° or 95°.

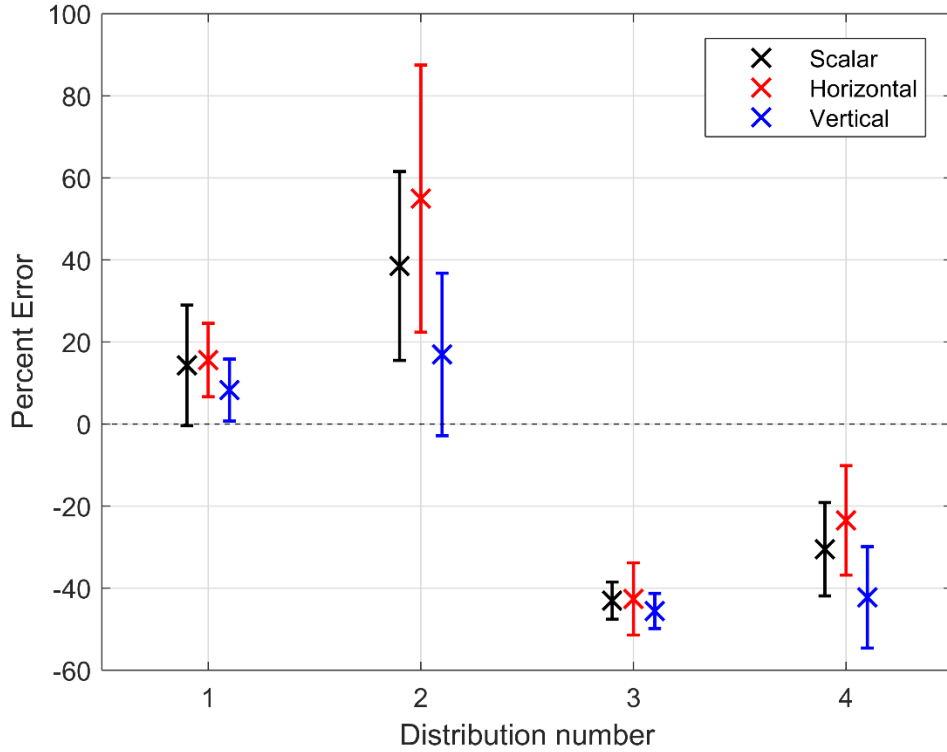


**Figure 6-7:** The mean percent difference between the retrieved aerosol extinction profile with an assumed particle size distribution and the true state corresponding to the indicated particle size distribution (see Table 6-1). Error bars represent one standard deviation of the variability across all viewing geometries. Results shown are for 750 nm and 20 km altitude.

It is clear that the major element of observed bias is simply the difference between the true and assumed particle size distribution. In all four cases there is some difference between the solutions for the various polarization states; however, for each particle size distribution the biases between the polarization states are essentially the same within the variability observed across the various viewing geometries. Neither of the linearly polarized states perform consistently better than the total radiance case; however, they do not perform any worse either (excepting the vertical polarization near 90 degree solar scattering angle), which is an equally important result.

#### 6.4.4 Precision Analysis

Finally, we study the effect of the polarized measurement on the performance of the retrieval in terms of the precision of the results. We again use simulated measurements across the full range

of input parameters as input to the standard retrieval algorithm. Following the methodology outlined in section 6.3, using SASKTRAN-HR the Jacobian matrices were calculated for each retrieved state and used determine the gain matrices, which were then applied as in Equation 6.7 to determine the retrieval precision. It should be noted that not all of the Jacobian matrices could be inverted due to small sensitivity of the lower tangent altitudes (see discussion in *Bourassa et al.*, 2007) and these were removed from the data set (approximately 9% of total cases). This affected a large fraction of the 500 nm cases, so this wavelength was removed from this section of the analysis. As discussed in section 6.3, we approach this problem from two perspectives: (1) an instrument that is compensated in design and/or operation such that measurements regardless of polarization state or geometries have the same signal to noise ratio, and (2) an uncompensated instrument such that the changing signal level with polarization state and viewing geometry affects the signal to noise ratio of the observation.

For the first case, where the signal to noise ratio is compensated such that it is equal for all cases, the measurement co-variance matrix in Equation 6.7 is replaced with the identity matrix, and the relative size of the square root of the diagonal of the resulting aerosol co-variance represents the amplification of the measurement noise. To compare the performance of the various polarization states, the resulting retrieval co-variances for the linearly polarized measurements were normalized by the retrieval co-variances from the total radiance case. The dependence of the results on the various input parameters, such as wavelength and viewing geometry were examined. Very little altitude dependence was observed and so the results were averaged across the retrieved altitude range.

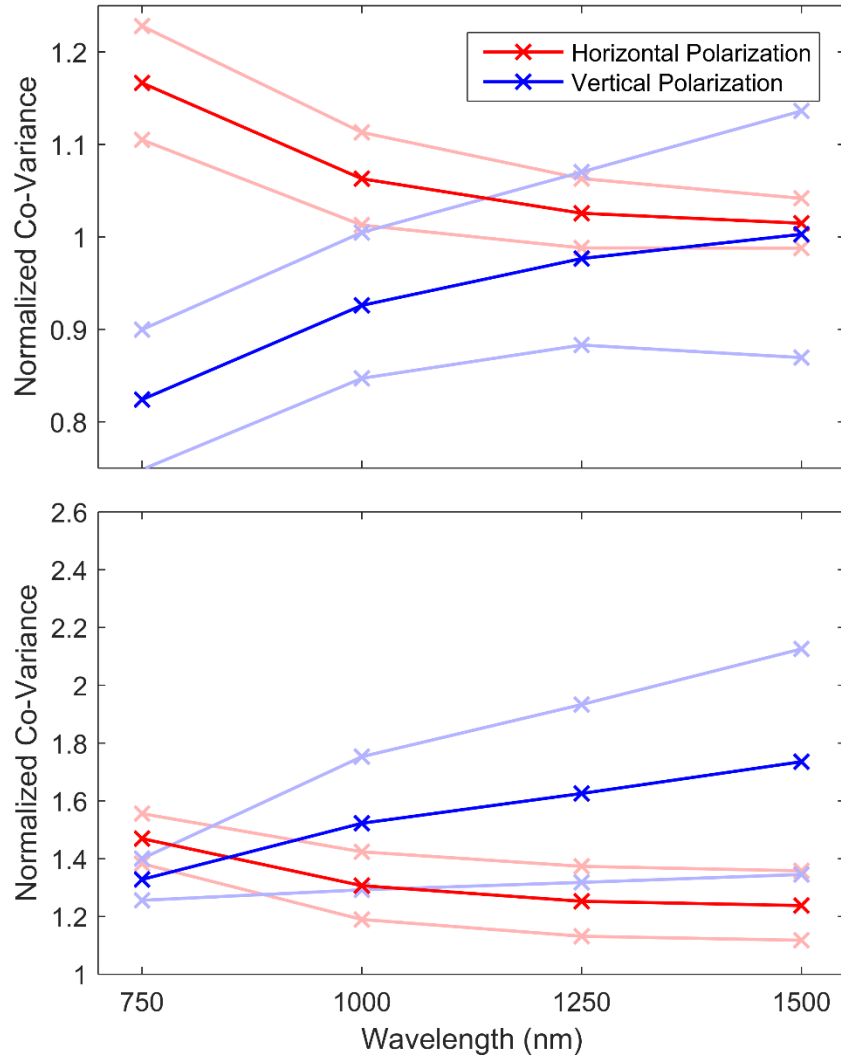


**Figure 6-8:** The wavelength dependence of the co-variance for the horizontal and vertical polarization retrievals normalized to the total radiance case. The faded line represent one standard deviation of the variability encountered across all input parameters. The top panel is for an instrument design and/or operation that compensates for changing signal levels with polarization and viewing geometry, and the bottom panel is for uncompensated measurements.

In Figure 6-8 the normalized co-variance cases were sorted by wavelength using all geometries and atmospheric states. These bins were then averaged for each wavelength shown by the red and blue points for the horizontal and vertical polarization respectively. The fainted colours are one standard deviation from the mean. Each of the means in Figure 6-8 contains between 186 to 229

unique data points and values less than one represent co-variance better than the total radiance case and the opposite for values larger than one.

The resulting normalized co-variances have a substantial dependence on wavelength. The situation where the signal to noise ratio is compensated such that it is equal for all cases is shown in the top panel of Figure 6-8, where the vertical polarization has a smaller co-variance, i.e. better precision, by approximately 20% at the shorter wavelengths than the total radiance retrieval. As wavelength increases to 1500 nm, the precision of the vertical polarization case is approximately equal to that of the total radiance case. The horizontal polarization essentially mirrors the vertical case with higher co-variances than total radiance at short wavelengths and approximately equal at 1500 nm. Recall, however, that the vertical polarization has significantly lower magnitude signal levels and in order for the measurement to be compensated to obtain equal signal to noise levels, an increase in instrument sensitivity or exposure time would be required.

**Table 6-2:** The SSA dependence of the normalized co-variance for the horizontal and vertical polarization retrievals. The given numbers are the mean with the standard deviation for each geometry across all wavelengths. Note that the SSA of 90° for the vertical polarization has been removed due to the poor signal in this region.

Polarization	60°	90°	120°	150°	180°
Horizontal (Compensated)	1.072±0.051	1.090±0.082	1.047±0.078	1.027±0.048	1.023±0.042
Vertical (Compensated)	0.861±0.084	--	0.968±0.157	0.977±0.063	0.980±0.051
Horizontal (Uncompensated)	1.289±0.075	1.225±0.158	1.261±0.165	1.341±0.098	1.360±0.085
Vertical (Uncompensated)	1.576±0.167	--	1.852±0.559	1.527±0.170	1.490±0.130

Across the range of solar scattering angles, the vertical polarization has slightly lower co-variance than the other two cases, except at 90 degrees, which is due to the lack of sensitivity in this region noted previously. Table 6-2 shows the calculated means and standard deviations across SSA for the horizontal and vertical polarizations, note the SSA of 90° is missing due to the poor

signal, and retrieval quality noted in previous sections which results in poor co-variances for this geometry. Furthermore, the variability of the result across all of the other input parameters increases dramatically as the scattering angle approaches 90 degrees. The precision of the retrieval shows very little dependence on the other input parameters such as solar zenith angle, albedo, particle size distribution, and extinction level. On average across all parameters, the retrieved co-variance from the vertical polarization is approximately 15% smaller than the horizontally polarized retrieval.

In the case of an uncompensated instrument, for example where a linear polarizer is added to the optical chain with no other changes in observation, the scaling of the diagonal of the measurement co-variance is used as outlined in section 6.3. Due to the larger magnitude of the signal in the horizontal polarization compared to the vertical polarization, the horizontal cases generally have lower retrieval co-variance, and this effect increases with longer wavelength as seen in the lower panel of Figure 6-8. Note that in this uncompensated case, since the linear polarizations are always some fraction of the total radiance, the co-variance is always larger than the total radiance case (i.e. the normalized co-variances are always greater than 1). Once again very little dependence on solar zenith angle, albedo, size distribution or extinction level was observed. There was also little dependence on solar scattering angle, except for vertical polarization at 90 degrees. On average across all parameters, vertical and horizontal polarizations have approximately a 60% and 30% larger uncertainty than the total radiance case, respectively.

This analysis shows that the main driver of retrieval precision is the signal to noise level of the observation, as would be expected. Again, this leads to instrument design and/or operational considerations in order to maintain retrieval precision at the same level as the total radiance measurement. A main scientific goal of both the ALI and ALTIUS instruments is obtaining high

spatial resolution observations, both vertically and horizontally along, and across, the satellite track. This generally means that images must be collected rapidly and long exposure times are not an affordable luxury. Once more, the relatively higher magnitude signal levels of the horizontal polarization point to this as the more appealing choice of orientation; however, compared to the total radiance case the decreased precision is exaggerated at shorter wavelengths.

## 6.5 Conclusions

We have attempted to address the question of whether or not the measurement of linearly polarized radiance rather than total limb radiance is an advantage or disadvantage with respect to retrievals of stratospheric aerosol. The sensitivity of the polarized limb radiance to aerosol is complex with respect to many parameters, and there are trade-offs in the orientation of the polarization and the orbital viewing geometry. One important point is the very low magnitude of signal observed in the vertical polarization for scattering angles near 90 degrees, which are encountered for a large fraction of observations in low earth orbit, particularly sun-synchronous near-terminator orbits such as for OSIRIS, and the most likely orbit orientation for an ALI satellite mission. More generally, it is important to consider the overall lower magnitude of the linearly polarized radiance, which by definition is a fraction of the total radiance. The horizontal polarization has, on average, higher signal levels than the vertical polarization. It also has a weaker dependence on solar scattering angle that is more similar to the total radiance than the vertical polarization, which is more strongly skewed in the forward scatter direction.

One critical bias in limb scatter retrievals of stratospheric aerosol is due to uncertainty in particle size parameters. We tested four different particle size distribution scenarios, representing background and volcanically perturbed conditions, over a large range of other parameters such as wavelength, viewing geometry, and extinction level and found that there is no significant change in the observed bias for polarized or total radiance measurements. So, with respect to this bias in

stratospheric aerosol retrievals, the linearly-polarized measurement can be used to achieve approximately equal results with only minor advantages and disadvantages between the polarization states.

The polarized measurement can have an effect on the precision of the retrieval, where again the main driver is the magnitude of the signal. The polarization can either increase or decrease the precision and there is an apparent trade-off between signal levels and performance of the vertical or horizontal polarization. This is mostly important at shorter wavelengths since at longer wavelengths the differences are negligible.

In conclusion, we have found no clear advantage to the linearly polarized measurement over the total radiance for aerosol retrievals; however, there are also no clear disadvantages assuming the somewhat lower overall signal levels can be handled in the instrument design or operation. With careful choice of the orientation of the measured polarization with respect to the orbital geometry and desired coverage, an instrument such as ALI or ALTIUS is fully capable of obtaining retrieved aerosol products of very similar quality to an equivalent instrument that measures the total radiance.

## CHAPTER 7

### CONCLUSION

Measurements of aerosol have been used for decades from in-situ measurements through the use of balloons and sondes and globally through the use of satellites. These datasets have been used to determine radiative forcing changes on the earth such as the recent global warming hiatus inferred from the record. However, current generation instruments are aging and operating well beyond their lifetimes. New instrumentation to continue the long term global aerosol dataset is required to continue to monitor climate change. This work has been focused on developing a prototype instrument to capture images of polarized radiance from a limb scatter geometry in order to determine aerosol profiles in two dimensions. ALI is the proposed prototype instrument and was designed as an engineering test to be launched from a stratospheric balloon to determine aerosol extinction and microphysics.

ALI was designed and developed using an AOTF to spectrally filter measured radiance from 650 to 950 nm in two dimensional images with exposure times on the order of seconds. A simple three lens linear optical system using a telescopic layout consisting of the telescope for the FEO and a focusing lens for the BEO to resolve the image was used for ALI. The system had a large FOV of 6° to image from a tangent point on the ground to float altitude (approximately 35 km). This resulted in significant aberrations being present in the last degree of the FOV, which was also partially outside of the acceptance angle of the AOTF. From testing and simulations in Code V optical design software the optical resolution of the instrument was a nominal 210 m both in the vertical and horizontal directions. ALI was calibrated accounting for DC offset, dark current, stray light, flat fielding, and relative spectral calibrations.

The test flight for ALI occurred in Timmins, Ontario from the CSA balloon launch facility. ALI was mounted on board the CNES CARMEN-2 gondola and the launch of the stratospheric

balloon occurred at 05:35 UTC on September 19, 2014 and had a flight duration of 16 hours and 14 minutes. Float altitude was 36.5 km and ALI captured aerosol images for five hours resulting in 216 measurements. These images were used to compute one dimensional aerosol extinction profiles from the flight which agreed well to the nearest OSIRIS scans but had some large discrepancies in extinction values from 20-25 km. This may have been from unaccounted for systematics in the retrieval or the SSA being relatively close to 90° at 98° which is found to yield systematics in the retrieval. Overall, however the results are promising and work on a second iteration of the instrument has already begun as well as a space feasibility study. Furthermore, the particle size retrievals agree with accepted values for the background stratospheric aerosol. A large error bar is associated with the determine particle size since the wavelength range is limited. Even with this limitation, ALI in its current state could notice large particle size trends in the stratosphere, such as the effect of a volcanic eruption. A satellite version of ALI would be able to accurately model aerosol trends on a global basis and be able to continue the global aerosol dataset.

This first prototype ALI instrument has allowed for the measurement of stratospheric aerosol through polarized images and with the continuation of the ALI project some recommendations for future work are suggested. First, an azimuth scan occurred during the flight to test the sensitivity of the measurement to aerosol and provide some verification for the simulation study. These measurements should be analyzed to better understand the correct orientation for the second generation of ALI. A future iteration of ALI that is vertically polarized should be orientated so that the SAA is in between 45-60° to avoid the problematic scattering angles of 80-100° that causes a bias in the retrieved aerosol profile or reorientate the instrument to measure the horizontal polarization instead to avoid this problem.

During the mission, unknown stray light was noted in some of the images and a back end telescopic chain should be added to help further reduce internal stray light from the rejected polarization. Replacing the back end polarizer with a Glan-Taylor prism would allow the unwanted polarization to be reflected off axis and help reduce this stray light issue. Further, the addition of a back end telescope between the AOTF and the camera could further be used to help separate the desired diffracted signal from the undesired outputs in physical space to reduce stray light further. Lastly, the addition of an absolute calibration would allow the direct determination of albedo which would help improve the retrievals due to the highly dependent nature between polarized albedo and retrieved aerosol extinction.

Some recommendations are for the camera that could also improve the quality of the measurements. The addition of a shutter or masked pixels on the CCD would be useful to calibrate DC offset and dark current changes during the flight due to temperature changes. Also an extended range camera and/or AOTF could be used to measure radiances from 500-2000 nm to allow for short wavelength normalization and additional particle size sensitivity.

Since the goal of ALI is a future satellite mission it would be ideal to be able to test a version design for a low earth orbit. However, the second version of ALI is scheduled for another stratospheric balloon launch and must also function from a balloon geometry. Both tests could be performed on the flight of ALI version 2 if it is designed for a low earth orbit geometry with the addition of a front end zoom lens that would be able to change the FOV from space to balloon geometry. Additionally the adaptation of a folded optics design will be required for a space platform and should be tackled in a future iteration. All of these improvements would help to improve the image quality, and space feasibility of the next generation instrument.

With the completion of ALI, a simulation study was undertaken to determine if there was any advantage or disadvantage to measuring a linear polarization over the total radiance for a space mission. Overall it was determined that there is no distinctive advantage to measuring a linear polarization over the total radiance. However, a polarized measurement only observes a fraction of the signal compared to the total radiance case which would need to be mitigated in the optical design or operation. One exception to poor instrument performance is measuring the 90 degree SSA with the vertical polarization due to the extremely low signal levels.

Overall, the ALI mission had a successful first flight and determined aerosol extinction profiles and a moment of particle size information. These profiles compared well to OSIRIS measurements and the particle size parameters were noisy but within the expect values for background aerosol loading. A satellite version of ALI would be able to determine global aerosol profiles from a low earth orbit especially if the horizontal polarization was observed instead the vertical polarization. This success of this mission has allowed for the future development of the ALI platform with two projects currently underway. The first is a second version stratospheric balloon instrument to be flown in the spring of 2017, and the second is a space feasibility study of the performance of ALI from a low earth orbit mission.

## LIST OF REFERENCES

- Andersson, S. M., B. G. Martinsson, J.-P. Vernier, J. Friberg, C. A. Brenninkmeijer, M. Hermann, P. F. van Velthoven, and A. Zahn (2015), Significant radiative impact of volcanic aerosol in the lowermost stratosphere, *Nature communications*, 6, doi:10.1038/ncomms8692.
- Andrews F. G. (1987), *Middle atmospheric dynamics*, Academic Press Inc.
- Angstrom, A. (1964), The parameters of atmospheric turbidity, *Tellus*, 16(1), 64 – 75, doi: 10.1111/j.2153-3490.1964.tb00144.x.
- Barth, C. A., D. W. Rusch, R. J. Thomas, G. H. Mount, G. J. Rottman, G. E. Thomas, R. W. Sanders, and G. M. Lawrence (1983), Solar Mesosphere Explorer - Scientific objectives and results, *Geophysical Research Letters*, 10, 237-240, doi:10.1029/GL010i004p00237.
- Beuttell, R. G., and A. W. Brewer (1949), Instruments for the measurement of the visual range, *Journal of Scientific Instruments*, 26, 357.
- Bickel, W. S., and W. M. Bailey (1985), Stokes vectors, Mueller matrices, and polarized scattered light, *American Journal of Physics*, 53, 468-478 (1985), doi:10.1119/1.14202
- Bingen, C., D. Fussen, and F. Vanhellemont (2004), A global climatology of stratospheric aerosol size distribution parameters derived from sage ii data over the period 1984-2000: 1. methodology and climatological observations, *Journal of Geophysical Research*, 109, doi: 10.1029/2003JD003518.
- Boucher O. (2015), *Atmospheric Aerosols: Properties and Climate Impacts*, Springer.
- Bourassa, A. E., D. A. Degenstein, R. L. Gattinger, and E. J. Llewellyn (2007), Stratospheric aerosol retrieval with optical spectrograph and infrared imaging system limb scatter measurements, *Journal of Geophysical Research*, 112, D10217, doi:10.1029/2006JD008079.
- Bourassa, A. E., D. A. Degenstein, and E. J. Llewellyn (2008), SASKTRAN: A spherical geometry radiative transfer code for efficient estimation of limb scattered sunlight, *Journal of Quantitative Spectroscopy and Radiative Transfer*, 109, 52-73, doi:10.1016/j.jqsrt.2007.07.007.
- Bourassa, A. E., C. A. McLinden, A. F. Bathgate, B. J. Elash, and D. A. Degenstein (2012a), Precision estimate for Odin-OSIRIS limb scatter retrievals, *Journal of Geophysical Research: Atmospheres*, 117, D04303, doi:10.1029/2011JD016976.

Bourassa, A. E., L. A. Rieger, N. D. Lloyd, and D. A. Degenstein (2012b), Odin-OSIRIS stratospheric aerosol data product and SAGE III intercomparison, *Atmospheric Chemistry & Physics*, 12, 605{614, doi:10.5194/acp-12-605-2012.

Bourassa, A. E., A. Robock, W. J. Randel, T. Deshler, L. A. Rieger, N. D. Lloyd, E. T. Llewellyn, and D. A. Degenstein (2012c), Large volcanic aerosol load in the stratosphere linked to Asian monsoon transport, *Science*, 337, 78-81, doi:10.1126/science.1219371.

Bourassa, A. E., A. Robock, W. J. Randel, T. Deshler, L. A. Rieger, N. D. Lloyd, E. Llewellyn, and D. A. Degenstein (2013), Response to comments on "large volcanic aerosol load in the stratosphere linked to Asian monsoon transport", *Science*, 339, 647-647, doi:10.1126/science.1227961.

Bovensmann, H., J. Burrows, M. Buchwitz, J. Frerick, S. Noël, V. Rozanov, K. Chance, and A. Goede (1999), SCIAMACHY: Mission objectives and measurement modes, *Journal of the Atmospheric Sciences*, 56, 127-150, doi:10.1175/1520-0469(1999)056<0127:SMOAMM>2.0.CO;2.

Brasseur G. P. and S. Solomon (2005), *Aeronomy of the Middle Atmosphere: Chemistry and Physics of the Stratosphere and Mesosphere*, 3<sup>rd</sup> edition, Springer.

Brock, C. A., P. Hamill, J. C. Wilson, H. H. Jonsson, and K. R. Chan (1995), Particle Formation in the Upper Tropical Troposphere: A Source of Nuclei for the Stratospheric Aerosol, *Science*, 270, 1650-1653, doi:10.1126/science.270.5242.1650.

Canty, T., N. Mascioli, M. Smarte, and R. Salawitch (2013), An empirical model of global climate—Part 1: A critical evaluation of volcanic cooling, *Atmospheric Chemistry and Physics*, 13(8), 3997–4031, doi:10.5194/acp-13-3997-2013.

Carn, S. A., K. D. Froyd, B. E. Anderson, P. Wennberg, J. Crounse, K. Spencer, J. E. Dibb, N. A. Krotkov, E. V. Browell, J. W. Hair, G. Diskin, G. Sachse, S. A. Vay (2011), In situ measurements of tropospheric volcanic plumes in Ecuador and Colombia during TC4, *Journal of Geophysical Research*, 116, D00J24, doi:10.1029/2010JD014718.

Chahine, M. T. (1970), Inverse Problems in Radiative Transfer: Determination of Atmospheric Parameters, *Journal of Atmospheric Science*, 27, 960-967, doi:10.1175/1520-0469(1970)027<0960:IPIRTD>2.0.CO;2.

Chang, I. C. (1977), Noncollinear tunable acousto-optic filter. Patent.

Charlson, R. J., N. Ahlquist, H. Selvidge, and P. MacCready Jr. (1969), Monitoring of atmospheric aerosol parameters with the integrating nephelometer, *Journal of the Air Pollution Control Association*, 19, 937-942, doi:10.1080/00022470.1969.10469360.

Chazette, P., C. David, J. Lefrere, S. Godin, J. Pelon, and G. Mégie (1995), Comparative lidar study of the optical, geometrical, and dynamical properties of stratospheric postvolcanic aerosols, following the eruptions of El Chichon and Mount Pinatubo, *Journal of Geophysical Research*, 100, 23-195, doi:10.1029/95JD02268.

Chuang, T., P. Burns, E. B. Walters, T. Wysocki, T. Deely, A. Losse, L. Le, B. Drumheller, T. Schum, M. Hart, K. Puffenburger, B. Ziegler, and F. Hovis (2013), Space-based, multi-wavelength solid-state lasers for NASA's Cloud Aerosol Transport System for International Space Station (CATS-ISS), *Proceedings SPIE*, 8599, 85990N. doi:10.1117/12.2005545.

Cisewski, M., J. Zawodny, J. Gasbarre, R. Eckman, N. Topiwala, O. Rodriguez-Alvarez, D. Cheek, and S. Hall (2014), The stratospheric aerosol and gas experiment (SAGE III) on the international space station (ISS) mission, *Proceedings SPIE*, 9241, 924,107-924,107-7, doi:10.1117/12.2073131.

Clarisso, L., P.-F. Coheur, N. Theys, D. Hurtmans, and C. Clerbaux (2014), The 2011 Nabro eruption, a SO<sub>2</sub> plume height analysis using IASI measurements, *Atmospheric Chemistry and Physics*, 14, 3095-3111, doi:10.5194/acp-14-3095-2014.

Crutzen, P. J. (1976), The possible importance of CSO for the sulfate layer of the stratosphere, *Geophysics Research Letters*, 3, 73-76, doi:10.1029/GL003i002p00073.

Damadeo, R. P., J. M. Zawodny, L. W. Thomason, and N. Iyer (2013), SAGE version 7.0 algorithm: application to SAGE II, *Atmospheric Measurement Techniques*, 6, 3539-3561, doi:10.5194/amt-6-3539-2013.

Dee, D. P., S. M. Uppala, A. J. Simmons, P. Berrisford, P. Poli, S. Kobayashi, U. Andrae, M. A. Balmaseda, G. Balsamo, P. Bauer, P. Bechtold, A. C. M. Beljaars, L. van de Berg, J. Bidlot, N. Bormann, C. Delsol, R. Dragani, M. Fuentes, A. J. Geer, L. Haimberger, S. B. Healy, H. Hersbach, E. V. Hlm, L. Isaksen, P. Kllberg, M. Khler, M. Matricardi, A. P. McNally, B. M. Monge-Sanz, J.-J. Morcrette, B.-K. Park, C. Peubey, P. de Rosnay, C. Tavolato, J.-N. Thpaut, and F. Vitart (2011), The ERA-interim reanalysis: configuration and performance of the data assimilation system, *Quarterly Journal of the Royal Meteorological Society*, 137, 553-597, doi:10.1002/qj.828.

Degenstein, D. A., A. E. Bourassa, C. Z. Roth, and E. J. Llewellyn (2009), Limb scatter ozone retrieval from 10 to 60 km using a multiplicative algebraic reconstruction technique, *Atmospheric Chemistry and Physics*, 9, 6521-6529, doi:10.5194/acp-9-6521-2009.

Dekemper, E., N. Loodts, B. V. Opstal, J. Maes, F. Vanhellemont, N. Mateshvili, G. Franssens, D. Pieroux, C. Bingen, C. Robert, L. D. Vos, L. Aballea, and D. Fussen (2012), Tunable acousto-optic spectral imager for atmospheric composition measurements in the visible spectral domain, *Applied Optics*, 51, 6259-6267, doi:10.1364/AO.51.006259.

Deshler, T., M. Hervig, D. Hofmann, J. Rosen, and J. Liley (2003), Thirty years of in situ stratospheric aerosol size distribution measurements from Laramie, Wyoming (41 N), using balloon-borne instruments, *Journal of Geophysical Research*, 108, doi:10.1029/2002JD002514.

Deshler T. (2008), A review of global stratospheric aerosol: Measurements, importance, life cycle, and local stratospheric aerosol, *Atmospheric Research*, 90, 2–4, 223-232, doi:10.1016/j.atmosres.2008.03.016.

Dueck, S., A. E., Bourassa, and D. A. Degenstein (2016), Polarization Additions SASKTRAN Radiative Transfer Model, In Preparations.

Elash, B. J., A. E. Bourassa, P. R. Loewen, N. D. Lloyd, and D. A. Degenstein, (2016), The Aerosol Limb Imager: acousto-optic imaging of limb-scattered sunlight for stratospheric aerosol profiling, *Atmospheric Measurement Techniques*, 9, 1261-1277, doi:10.5194/amt-9-1261-2016.

Ernst, F., C. von Savigny, A. Rozanov, V. Rozanov, K.-U. Eichmann, L. A. Brinkho, H. Bovensmann, and J. P. Burrows (2012), Global stratospheric aerosol extinction profile retrievals from SCIAMACHY limb-scatter observations, *Atmospheric Measurement Techniques*, 5, 5993-6035, doi:10.5194/amtd-5-5993-2012.

Fairlie, T. D., J.-P. Vernier, M. Natarajan, and K. M. Bedka (2014), Dispersion of the Nabro volcanic plume and its relation to the Asian summer monsoon, *Atmospheric Chemistry and Physics*, 14, 7045-7057, doi:10.5194/acp-14-7045-2014.

Fischer, R. E., B. Tadic-Galeb, and P. R. Yoder (2008), *Optical System Design*, 2nd ed., McGraw-Hill.

Fiocco, G., and G. Grams (1964), Observations of the aerosol layer at 20 km by optical radar, *Journal of the Atmospheric Sciences*, 21, 323-324.

Forsythe, W. E., and Worthing, A. G. (1925). The properties of tungsten and the characteristics of tungsten lamps. *The Astrophysical Journal*, 61, 146, doi:10.1086/142880.

Fromm, M., G. Nedoluha, and Z. Charvt (2013), Comment on "large volcanic aerosol load in the stratosphere linked to Asian monsoon transport", *Science*, 339, 647, doi:10.1126/science.1228605.

Fromm, M., G. Kablick, G. Nedoluha, E. Carboni, R. Grainger, J. Campbell, and J. Lewis (2014), Correcting the record of volcanic stratospheric aerosol impact: Nabro and sarychev peak, *Journal of Geophysical Research*, 119, 10,343-10,364, doi:10.1002/2014JD021507.

Fyfe, J. C., N. P. Gillett, and F. W. Zwiers (2013), Overestimated global warming over the past 20 years, *Nature Climate Change*, 3, 767-769, doi:10.1038/nclimate1972.

Gass, P. A., and J. R. Sambles (1991), Accurate design of a non-collinear acousto-optic tunable filter, *Optics Letters*, 16, 429-431, doi:10.1364/OL.16.000429.

Gilbert, K., D. Turnbull, K. Walker, C. Boone, S. McLeod, M. Butler, R. Skelton, P. Bernath, F. Chateauneuf, and M.-A. Soucy (2007), The onboard imagers for the Canadian ACE SCISAT-1 mission, *Journal of Geophysical Research*, 112, doi:10.1029/2006JD007714.

Guenther, R. (1990), *Modern Optics*, 1st edition ed., Wiley and Sons, Inc.

Hamill P., E. J. Jensen, P. B. Russell, and J. J. Bauman (1997), The Life Cycle of Stratospheric Aerosol Particles, *Bulletin of the American Meteorological Society*, 78, 1395–1410, doi:10.1175/1520-0477(1997)078<1395:TLCSOA>2.0.CO;2.

Hansen, J. E., and L. D. Travis (1974), Light Scattering in Planetary Atmospheres, *Space Science Reviews*, 16(4), 527-610, doi:10.1007/BF00168069.

Hansen, J., R. Ruedy, and M. Sato (1996), Global surface air temperature in 1995: Return to pre-Pinatubo levels, *Geophysical Research Letters*, 23(13), 1665-1668, doi:10.1029/96GL01040.

Harris, S. E., and R. W. Wallace (1969), Acousto-Optic Tunable Filter, *Journal of the Optical Society of America* (1917-1983), 59, 744, doi: 10.1364/JOSA.59.000744.

Haywood, J. M., A. Jones, and G. S. Jones (2014), The impact of volcanic eruptions in the period 2000-2013 on global mean temperature trends evaluated in the HadGEM2-ES climate model, *Atmospheric Science Letters*, 15, 92-96, doi:10.1002/asl2.471.

Hofmann D. J. and J. M. Rosen (1983), Stratospheric sulfur acid fraction and mass estimate for the 1982 volcanic eruption of El Chichon, *Geophysical Research Letters*, 10(4), 313-316, doi: 10.1029/GL010i004p00313.

Hofmann, D., J. Barnes, M. O'Neill, M. Trudeau, and R. Neely (2009), Increase in background stratospheric aerosol observed with lidar at Mauna Loa observatory and Boulder, Colorado, *Geophysical Research Letters*, 36, doi:10.1029/2009GL039008, l15808.

Hoinka, K. (1997), The tropopause: Discovery, definition and demarcation, *Meteorologische Zeitschrift*, 6, 281-303, doi:10.1175/1520-0493(1998)126<3303:SOTGTP>2.0.CO;2.

Holton, J. R., P. H. Haynes, M. E. McIntyre, A. R. Douglass, R. B. Rood, and L Pfister (1995), Stratosphere-troposphere exchange, *Review of Geophysics*, 33, 403–439, doi:10.1029/95RG02097.

Jäger, H., and D. Hofmann (1991), Midlatitude lidar backscatter to mass, area, and extinction conversion model based on in situ aerosol measurements from 1980 to 1987, *Applied optics*, 30, 127-138, doi:10.1364/AO.30.000127.

Junge, C. E., C. W. Chagnon, and J. E. Manson (1961), Stratospheric aerosols, *Journal of Atmospheric Science*, 18, 81–108, doi:10.1175/1520-0469(1961)018<0081:SA>2.0.CO;2.

Kettle, A. J., U. Kuhn, M. von Hobe, J. Kesselmeier, M. O. Andreae, (2002) The global budget of atmospheric carbonyl sulfide: Temporal and spatial variations of the dominant sources and sinks, *Journal Geophysical Research*, 107, D22, 4658, doi:10.1029/2002JD002187.

Kiehl, J. T., and B. P. Briegleb (1993), The relative roles of sulfate aerosols and greenhouse gases in climate forcing, *Science*, 260, 311-314, doi:10.1126/science.260.5106.311.

Kosch, M., S. Mäkinen, F. Sigernes, and O. Harang (2003), Absolute optical calibration using a simple tungsten light bulb: Experiment, *Proceedings of the 30th Annual European Meeting on Atmospheric Studies by Optical Methods*, 50-54.

Kovilakam, M., and T. Deshler (2015), On the accuracy of stratospheric aerosol extinction derived from in situ size distribution measurements and surface area density derived from remote SAGE II and HALOE extinction measurements, *Journal Geophysical Research Atmospheres*, 120, 8426–8447, doi:10.1002/2015JD023303.

Kozun M. N. (2015), *Optical Pointing System For Stratospheric Balloon-Borne Multi-Slit OSIRIS-DM*, Master's Thesis, University of Saskatchewan.

- Kremser, S., L. W. Thomason, M. von Hobe, M. Hermann, T. Deshler, C. Timmreck, M. Toohey, A. Stenke, J. P. Schwarz, R. Weigel, S. Fueglistaler, F. J. Prata, J.-P. Vernier, H. Schlager, J. E. Barnes, J.-C. Antuña-Marrero, D. Fairlie, M. Palm, E. Mahieu, J. Notholt, M. Rex, C. Bingen, F. Vanhellemont, A. Bourassa, J. M. C. Plane, D. Klocke, S. A. Carn, L. Clarisse, T. Trickl, R. Neely, A. D. James, L. Rieger, J. C. Wilson, and B. Meland (2015), Stratospheric aerosol—Observations, processes, and impact on climate, *Reviews of Geophysics* 54, doi:10.1002/2015RG000511.
- Lacis, A., J. Hansen, and M. Sato (1992), Climate forcing by stratospheric aerosols, *Geophysical Research Letters*, 19, 1607–1610, doi:10.1029/92GL01620.
- Levenberg, K. (1944), A method for the solution of certain non-linear problems in least squares, *Quarterly of Applied Mathematics*, 2(2), 164-168.
- Llewellyn, E., N. D. Lloyd, D. A. Degenstein, R. L. Gattinger, S. V. Petelina, A. E. Bourassa, J. T. Wiensz, E. V. Ivanov, I. C. McDade, B. H. Solheim, J. C. McConnell, C. S. Haley, C. von Savigny, C. E. Sioris, C. A. McLinden, E. Grifoen, J. Kaminski, W. F. J. Evans, E. Puckrin, K. Strong, V. Wehrle, R. H. Hum, D. J. W. Kendall, J. Matsushita, D. P. Murtagh, S. Brohede, J. Stegman, G. Witt, G. Barnes, W. F. Payne, L. Piche, K. Smith, G. Warshaw, D. L. Deslauniers, P. Marchand, E. H. Richardson, R. A. King, I. Wevers, W. McCreath, E. Kyrölä, L. Oikarinen, G. W. Leppelmeier, H. Auvinen, G. Megie, A. Hauchecorne, F. Lefevre, J. de La Noe, P. Ricaud, U. Frisk, F. Sjoberg, F. von Scheele, and L. Nordh (2004), The OSIRIS instrument on the Odin spacecraft, *Canadian Journal of Physics*, 82, 411-422, doi:10.1139/p04-005.
- Marquardt, D. W. (1963), An algorithm for least-squares estimation of nonlinear parameters, *Journal of the society for Industrial and Applied Mathematics*, 11(2), 431-441.
- McLinden, C. A., J. C. McConnell, C. T. McElroy, and E. Griffioen (1999), Observations of Stratospheric Aerosol Using CPFM Polarized Limb Radiances, *Journal of the Atmospheric Sciences*, 56:2, 233-240, doi:10.1175/1520-0469(1999)056<0233:OOSAUC>2.0.CO;2.
- McCormick, M. P., and T. J. Swissler (1983), Stratospheric aerosol mass and latitudinal distribution of the El Chichon eruption cloud for October 1982, *Geophysical Research Letters*, 10(9), 877–880, doi:10.1029/GL010i009p00877.
- McCormick, M. P. and R. E. Veiga (1992), SAGE II measurements of early Pinatubo aerosols, *Geophysical Research Letters*, 19(2), 155-158, doi:10.1029/91GL02790.
- McCormick, M. P., L. W. Thomason, and C. R. Trepte (1995), Atmospheric effects of the Mt Pinatubo eruption, *Nature*, 373(6513), 399-404, doi:10.1038/373399a0.

McElroy, C. T., C. R. Nowlan, J. R. Drummond, P. F. Bernath, D. V. Barton, D. G. Dufour, C. Midwinter, R. B. Hall, A. Ogyu, A. Ullberg, D. I. Wardle, J. Kar, J. Zou, F. Nichitiu, C. D. Boone, K. A. Walker, and N. Rowlands (2007), The ACE-MAESTRO instrument on SCISAT: description, performance, and preliminary results, *Applied Optics*, 46, 4341-4356, doi:10.1364/AO.46.004341.

Mie, G. (1908), Considerations on the optics of turbid media, especially colloidal metal solutions, *Annalen der Physik (Leipzig)*, 42, 377.

Mishchenko, M. I., L. D. Travis, and A. A. Lacis (2002), *Scattering, Absorption, and Emission of Light by Small Particles*, 3<sup>rd</sup> edition, Cambridge, UK: Cambridge University Press.

Murphy, D. M., K. D. Froyd, J. P. Schwarz, and J. C. Wilson (2014), Observations of the chemical composition of stratospheric aerosol particles, *Quarterly Journal of the Royal Meteorological Society*, 140, 1269-1278, doi:10.1002/qj.2213.

Neely, R. R., P. Yu, K. H. Rosenlof, O. B. Toon, J. S. Daniel, S. Solomon, and H. L. Miller (2014), The contribution of anthropogenic SO<sub>2</sub> emissions to the Asian tropopause aerosol layer, *Journal of Geophysical Research*, 119, 1571-1579, doi:10.1002/2013JD020578.

Notholt, J., Z. Kuang, C. P. Rinsland, G. C. Toon, M. Rex, N. Jones, T. Albrecht, H. Deckelmann, J. Krieg, C. Weinzierl, H. Bingemer, R. Weller and O. Schrems (2003), Enhanced Upper Tropical Tropospheric COS: Impact on the Stratospheric Aerosol Layer, *Science*, 300, 307-310, doi:10.1126/science.1080320.

Oikarinen, L., E. Sihvola, and E. Kyrölä (1999), Multiple scattering radiance in limb-viewing geometry, *Journal of Geophysical Research*, 104, 31,261-31,274, doi:10.1029/1999JD900969.

Plumb, R. A. and J. Eluszkiewicz, (1999), The Brewer–Dobson Circulation: Dynamics of the Tropical Upwelling, *Journal of Atmospheric Science*, 56, 868–890, doi:10.1175/1520-0469(1999)056<0868:TBDCCO>2.0.CO;2.

Prata, A. J., G. Gangale, L. Clarisse, and F. Karagulian (2010), Ash and sulfur dioxide in the 2008 eruptions of Okmok and Kasatochi: Insights from high spectral resolution satellite measurements, *Journal of Geophysical Research*, 115, D00L18, doi:10.1029/2009JD013556.

Rault, D. F., and R. P. Loughman (2013), The OMPS limb profiler environmental data record algorithm theoretical basis document and expected performance, *IEEE Transactions on Geoscience and Remote Sensing*, 51, 2505-2527, doi:10.1109/TGRS.2012.2213093.

Ridley, D. A., S. Solomon, J. E. Barnes, V. D. Burlakov, T. Deshler, S. I. Dolgii, A. B. Herber, T. Nagai, R. R. Neely, A. V. Nevezorov, C. Ritter, T. Sakai, B. D. Santer, M. Sato, A. Schmidt, O. Uchino, and J. P. Vernier (2014), Total volcanic stratospheric aerosol optical depths and implications for global climate change, *Geophysical Research Letters*, 41, 7763-7769, doi:10.1002/2014GL061541, 2014GL061541.

Rieger, L. A., A. E. Bourassa, and D. A. Degenstein (2014), Stratospheric aerosol particle size information in Odin-OSIRIS limb scatter spectra, *Atmospheric Measurement Techniques*, 7, 507-522, doi:10.5194/amt-7-507-2014.

Rieger, L. A., A. E. Bourassa, and D. A. Degenstein (2015), Merging the OSIRIS and SAGE II stratospheric aerosol records, *Journal of Geophysical Research*, doi:10.1002/2015JD023133, 2015JD023133.

Rodgers, C. (2000), *Inverse Methods for Atmospheric Sounding: Theory and Practice, Series on atmospheric, oceanic and planetary physics*: 1999, World Scientific, River Edge, NJ, USA.

Rogers, R. R., C. A. Hostetler, J. W. Hair, R. A. Ferrare, Z. Liu, M. D. Oblad, D. B. Harper, A. L. Cook, K. A. Powell, M. A. Vaughan, and D. M. Winker (2011), Assessment of the CALIPSO lidar 532 nm attenuated backscatter calibration using the NASA LARC airborne high spectral resolution lidar, *Atmospheric Chemistry and Physics*, 11, 1295-1311, doi:10.5194/acp-11-1295-2011.

Rosen J. M. (1971), The Boiling Point of Stratospheric Aerosols, *Journal of Applied Meteorology*, 10, 1044–1046, doi:10.1175/1520-0450(1971)010<1044:TBPOSA>2.0.CO;2.

Russell, P., and M. McCormick (1989), SAGE II aerosol data validation and initial data use: An introduction and overview, *Journal of Geophysical Research*, 94, 8335-8338 doi:10.1029/JD094iD06p08335.

Saito K., A. W. and T. Yano (1976), Acousto-optic filter. Patent.

Sawamura, P., J. P. Vernier, J. E. Barnes, T. A. Berko, E. J. Welton, L. Alados-Arboledas, F. Navas-Guzmn, G. Pappalardo, L. Mona, F. Madonna, D. Lange, M. Sicard, S. Godin-Beekmann, G. Payen, Z. Wang, S. Hu, S. N. Tripathi, C. Cordoba-Jabonero, and R. M. Ho (2012), Stratospheric AOD after the 2011 eruption of Nabro volcano measured by lidars over

the northern hemisphere, *Environmental Research Letters*, 7, 034,013, doi:10.1088/1748-9326/7/3/034013.

Schutz, B., H. Zwally, C. Shuman, D. Hancock, and J. DiMarzio (2005), Overview of the ICEsat mission, *Geophysical Research Letters*, 32, doi:10.1029/2005GL024009.

Sioris, C. E., C. D. Boone, P. F. Bernath, J. Zou, C. T. McElroy, and C. A. McLinden (2010), Atmospheric chemistry experiment (ACE) observations of aerosol in the upper troposphere and lower stratosphere from the Kasatochi volcanic eruption, *Journal of Geophysical Research*, 115, doi:10.1029/2009JD013469, d00L14.

Smith, W. J. (2000), *Modern Optical Engineering*, New York: McGraw-Hill.

Sneep, M., and W. Ubachs (2005), Direct measurement of the Rayleigh scattering cross section in various gases, *Journal of Quantitative Spectroscopy and Radiative Transfer*, 92(3), 293-310, doi:10.1016/j.jqsrt.2004.07.025.

Soden, B. J., R. T. Wetherald, G. L. Stenchikov, and A. Robock (2002), Global cooling after the eruption of Mount Pinatubo: A test of climate feedback by water vapor, *Science*, 296(5568), 727–730, doi:10.1126/science.296.5568.727.

Solomon, S., D. Qin, M. Manning, Z. Chen, M. Marquis, K. B. Averyt, M. Tignor, and H. L. Miller (2007), Contribution of Working Group I to the Fourth Assessment Report of the Intergovernmental Panel on Climate Change, *Tech. rep.*

Solomon, S., J. S. Daniel, R. R. Neely, J.-P. Vernier, E. G. Dutton, and L. W. Thomason (2011), The persistently variable background stratospheric aerosol layer and global climate change, *Science*, 333, 866-870, doi:10.1126/science.1206027.

Stocker, T. F., D. Qin, G.-K. Plattner, M. M. Tignor, S. K. Allen, J. Boschung, A. Nauels, Y. Xia, V. Bex, and P. M. Midgley (2013), *Climate Change 2013 The Physical Science Basis*, Cambridge University Press, Cambridge, UK, and New York, NY, USA.

Suhre, D. R., L. J. Denes, and N. Gupta (2004), Telecentric confocal optics for aberration correction of acousto-optic tunable filters, *Applied Optics*, 43, 1255-1260, doi:10.1364/AO.43.001255.

Taylor B. J. A. (2015), *The Upgrade, Calibration, and Evaluation of the Multi-Slit OSIRIS-DM for Stratospheric Balloon Flight*, Master's Thesis, University of Saskatchewan.

Thomason, L. W. (1991), A diagnostic stratospheric aerosol size distribution inferred from SAGE II measurements, *Journal of Geophysical Research*, 96(D12), 22,501-22,508, doi:10.1029/91JD02521.

Thomason, L. W., and G. Taha (2003), SAGE III aerosol extinction measurements: Initial results, *Geophysical Research Letters*, 30, doi:10.1029/2003GL017317.

Thomason, L. W. and T. Peter (2006), Assessment of Stratospheric Aerosol Processes (ASAP), *World Climate Research Program*, 1–322.

Thompson, D. W., J. M. Wallace, P. D. Jones, and J. J. Kennedy (2009), Identifying signatures of natural climate variability in time series of global-mean surface temperature: Methodology and insights, *Journal of Climate*, 22(22), 6120–6141, doi:10.1175/2009JCLI3089.1.

Thomason, L. W., and J.-P. Vernier (2013), Improved SAGE II cloud/aerosol categorization and observations of the Asian tropopause aerosol layer: 1989-2005, *Atmospheric Chemistry and Physics*, 13, 4605-4616, doi:10.5194/acp-13-4605-2013.

Uchida, N. (1971), Optical properties of single-crystal paratellurite ( $\text{TeO}_2$ ), *Physics Review B*, 4, 3736-3745, doi:10.1103/PhysRevB.4.3736.

Van de Hulst, H. C. (1962), *Light Scattering by Small Particles*, New York: Wiley and Sons Inc.

Vanhelmont, F., C. Tetard, A. Bourassa, M. Fromm, J. Dodion, D. Fussen, C. Brogniez, D. Degenstein, K. L. Gilbert, D. N. Turnbull, P. Bernath, C. Boone, and K. A. Walker (2008), Aerosol extinction profiles at 525 nm and 1020 nm derived from ACE imager data: comparisons with GOMOS, SAGE II, SAGE III, POAM III, and OSIRIS, *Atmospheric Chemistry and Physics*, 8, 2027-2037, doi:10.5194/acp-8-2027-2008.

Vernier, J.-P., L. Thomason, and J. Kar (2011a), CALIPSO detection of an Asian tropopause aerosol layer, *Geophysical Research Letters*, 38, doi:10.1029/2010GL046614.

Vernier, J.-P., L. W. Thomason, J.-P. Pommereau, A. Bourassa, L. Blanot, C. Trepte, D. Degenstein, and F. Vargas (2011b), Major influence of tropical volcanic eruptions on the stratospheric aerosol layer during the last decade, *Geophysical Research Letters*, 38, L12807, doi:10.1029/2011GL047563.

Vernier, J.-P., L. W. Thomason, T. D. Fairlie, P. Minnis, R. Palikonda, and K. M. Bedka (2013), Comment on "Large volcanic aerosol load in the stratosphere linked to Asian monsoon transport", *Science*, 339, 647, doi:10.1126/science.1227817.

- Volk, C. M., J. W. Elkins, D. W. Fahey, G. S. Dutton, J. M. Gilligan, M. Loewenstein, J. R. Podolske, K. R. Chan, and M. R. Gunson (1997), Evaluation of source gas lifetimes from stratospheric observations, *Journal of Geophysical Research*, 102(D21), 25543–25564, doi:10.1029/97JD02215.
- Voloshinov, V. (1996), Spectral and polarization analysis of optical images by means of acousto-optics, *Optics Laser Technology*, 28, 119-127, doi:10.1016/0030-3992(95)00079-8.
- Voloshinov, V. B., and J. C. Mosquera (2006), Wide-aperture acousto-optic interaction in birefringent crystals, *Optics and Spectroscopy*, 101, 635-641, doi:10.1134/S0030400X06100225.
- Voloshinov, V. B., K. B. Yushkov, and B. B. J. Linde (2007), Improvement in performance of a TeO<sub>2</sub> acousto-optic imaging spectrometer, *Journal of Optics A: Pure and Applied Optics*, 9, 341-347, doi:10.1088/1464-4258/9/4/006.
- von Savigny, C., F. Ernst, A. Rozanov, R. Hommel, K.-U. Eichmann, V. Rozanov, J. P. Burrows, and L. W. Thomason (2015), Improved stratospheric aerosol extinction profiles from SCIAMACHY: validation and sample results, *Atmospheric Measurement Techniques*, 8, 8353-8383, doi:10.5194/amtd-8-8353-2015.
- Wang, P.-H., M. P. McCormick, T. J. Swissler, M. T. Osborn, W. H. Fuller, and G. K. Yue (1989), Inference of stratospheric aerosol composition and size distribution from SAGE II satellite measurements, *Journal Geophysical Research*, 94(D6), 8435–8446, doi:10.1029/JD094iD06p08435.
- Winker, D. M., W. H. Hunt, and M. J. McGill (2007), Initial performance assessment of CALIOP, *Geophysical Research Letters*, 34, doi:10.1029/2007GL030135.
- Wiscombe, W. J. (1980), Improved Mie scattering algorithms, *Applied Optics*, 19, 1505-1509, doi:10.1364/AO.19.001505.
- Xu, J., and R. Stroud (1992), *Acousto-optic devices: principles, design, and applications*, Wiley-Interscience.
- Young, S. A., and M. A. Vaughan (2009), The retrieval of profiles of particulate extinction from cloud-aerosol lidar infrared pathfinder satellite observations (calipso) data: Algorithm description, *Journal of Atmospheric and Oceanic Technology*, 26, 1105-1119, doi:10.1175/2008JTECHA1221.1.

Zawada, D. J., S. R. Dueck, L. A. Rieger, A. E. Bourassa, N. D. Lloyd, and D. A. Degenstein (2015), High resolution and Monte Carlo additions to the SASKTRAN radiative transfer model, *Atmospheric Measurement Techniques*, 8, 3357-3397, doi:10.5194/amtd-8-3357-2015.

## APPENDIX A

# ALI HARDWARE COMPONENTS

The section will list and give specifications for all of the major ALI hardware components.

Each section will have a brief description followed by a table of the specifications.

### A.1 Optical Components

#### A.1.1 Optical Lenses

All lenses used in the ALI system were purchased from Newport and were coated with anti-reflective coating AR.16 which covers 650-1000 nm range with an average reflectance of 0.5% and a maximum of 1.5%. All the lens in the system were made from N-BK7 glass and the specification and model number of each lens is located in Table A-1.

**Table A-1:** Lens used in ALI and their specifications.

Model Number	Effective Focal Length (mm)	Diameter (mm)	Center Thickness (mm)	Radius (mm)	Type of Lens
KPX100AR.16	150.0±1.5	25.4+0/-0.1	4.0±0.1	77.520	Plano-Convex
KPX187AR.16	100.0±1.0	50.2+0/-0.1	9.7±0.1	51.680	Plano-Convex
KBX052AR.16	50.2±0.5	25.4+0/-0.1	6.2±0.1	50.806	Bi-Convex

#### A.1.2 Polarizers

ALI needed two linear polarizers to help remove unwanted signal and reduce stray light in the system. These polarizers required a high extinction ratio over the range of the CCD sensitivities. The polarizers chosen were model number LPVIS100 from Thorlabs. The extinction ratios and transmission of the device can be seen in Figure A-1.

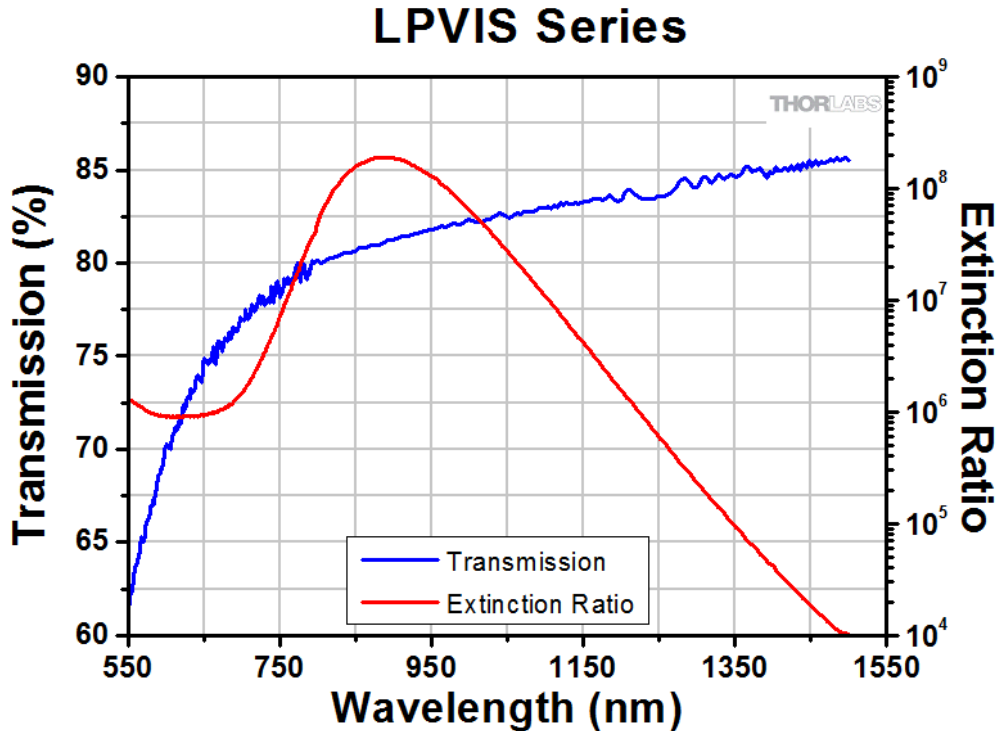


**Figure A-1:** The transmission and extinction ratios of the LPVIS100 used in ALI.

### A.1.3 AOTF

The AOTF in ALI is made by Brimrose of America (model number TEAFI10-0.6-1.0-MSD).

The specifications of the device can be seen in Table A-2. The separation angle is defined as the angle between the input source and the desired refracted polarization and the acceptance angle is measured from the normal of the face of the crystal.

**Table A-2:** AOTF Specifications.

Parameter	Value	Parameter	Value
Material	$\text{TeO}_2$	Polarization	Linear vertical
RF Range (Mhz)	75-156	Tunable Range (nm)	600-1200
Optical Aperture (mm)	10x10	Angular Aperture ( $^\circ$ )	4.0
Acceptance Angle ( $^\circ$ )	2.0	Separation Angle ( $^\circ$ )	6.4
Output Angle ( $^\circ$ )	2.7	Diffraction Efficiency (%)	~60
RF Power (W)	2.0	Damage Threshold (W)	5.0

## A.2 Opto-Mechanical and Electrical Components

### A.2.1 RF Driver

The driver for ALI is made by Gooch and Housego (model number 64020-200-2ADMDFS-A). It had no internal control mechanism and required additional control hardware to operate the device. In order to pick the frequency, a 30-bit digital value is inputted into the device to pick a frequency as well as manage several control lines to the device. The control word is used to determine a specific frequency which is given by

$$K_{10} = \frac{F2^{n+1}}{F_{clk}} \quad (\text{A.1})$$

where  $K_{10}$  is the 30-bit control word in base 10 rounded to the nearest integer,  $F$  is the desired RF to be outputted by the driver,  $F_{clk}$  is the internal clock of the driver which is 1000.059 MHz for ALI, and  $n$  is the number of bits in the control word for ALI (*i.e.*  $n = 30$ ). The control word is converted to binary and sent to the device to get the desired RF.

### A.2.2 QSI CCD Camera

The CCD camera was a QSI 616s with a Kodak KAP-1603ME sensor with a mechanical shutter and a 16-bit digital readout. The spectral response of the device can be seen in Figure 3-8 and the camera specification can be seen in Table A-3.

**Table A-3:** QSI CCD camera specifications.

Parameter	Value	Parameter	Value
Imager Size (mm)	13.8 x 9.2	Imager Size (pixels)	1536 x 1024
Pixel Size ( $\mu\text{m}$ )	9 x 9	Read Noise RMS (electrons)	15
Mass (kg)	0.95	Power Consumption (W)	24
Operating Temperature ( $^{\circ}\text{C}$ )	-20 to 30	Full Well Depth (electrons)	100,000

### A.2.3 OCELOT Computer

The on board computer for the ALI instrument was the Ocelot VL-EPMs-21 computer made by VersaLogic. Its architecture is based on the Intel Atom Z5 processor and had 2 GB of DDR2

memory. It had low power draw and fanless operation. It had a temperature range of -40 to 85 °C.

The system run a bare-bone version of Debian Linux.

#### A.2.4 Opto-Mechanical Pieces

In this section is a brief list of all the opto-mechanical components used within the final version of ALI. Listed is the model number of the components and the quantity in the design with a short description. All components were purchased from Thorlabs.

**Table A-4:** Opto-mechanical components used in ALI

Model Number	Quantity	Description
XT95SP-1000	1	1000 mm length optical rail, 95 mm width
XT95P11/M	4	95 mm width optical rail drop-on carriage
RS2P4M	2	Pedestal post, 50 mm long, 25.4 mm width, metric, M4
RS2P/M	2	Pedestal post, 50 mm long, 25.4 mm width, metric, M6
RS2M	2	Pedestal post spacer, 2 mm long, 25.4 mm width
RS7M	2	Pedestal post spacer, 7 mm long, 25.4 mm width
LCP01B	2	60 mm cage clamp
CP02T/M	1	30 mm cage plate, 1" lens holder, square, metric
CP07	3	60 mm cage plate, 1" lens holder, round, metric
LCP01/M	1	60 mm cage plate, 2" lens holder, square, metric
LCP02/M	4	30 mm to 60 mm cage converter, metric
ER1-P4	3	Cage assembly rod, 1" long, 4 pack
ER2-P4	2	Cage assembly rod, 2" long, 4 pack
ER4-P4	1	Cage assembly rod, 4" long, 4 pack
ER8-P4	2	Cage assembly rod, 8" long, 4 pack
LC1A/M	1	Swivel mount, 60

## APPENDIX B

### ALI SOFTWARE COMMANDS

#### B.1 List of Commands for ALI Software

Following is a list of the commands that can be used in the ALI software for operational control during flight through the ground based communication program. A complete list will be presented then a description of each function will follow, all are case sensitive.

- `EnableScience`
- `DisableScience`
- `EnableRF`
- `DisableRF`
- `EnableAutoSendStats`
- `DisableAutoSendStats`
- `SetScienceMode`
- `ReloadConfig`
- `LdCusCnf`
- `LdCusExp`
- `GetFile`
- `EndCurrentScienceCycle`
- `SetExposureScaleFactor`
- `UpdateExposureTimeCurve`
- `EnableCheckRfTemps`
- `DisableCheckRfTemps`
- `ResetHousekeeping`

- `DumpConfig`
- `SetBitsPerSecond`
- `EnableAutomation`
- `DisableAutomation`
- `SetAutomationTimeout`
- `EnableGps`
- `DisableGps`
- `EnablePulse`
- `DisablePulse`

### **B.1.1 EnableScience**

Full Command: `EnableScience`

This command enables science data acquisition and enables the RF driver. If the current mode is invalid, the system reports the error to the user. By default, science mode data acquisition is disabled and must be enabled.

### **B.1.2 DisableScience**

Full Command: `DisableScience`

This command disables science data acquisition at the end of the current science mode cycle. This mode does not disable the RF driver. Disabling the RF driver only pauses the cycle and does not terminate it. By default, science data acquisition is disabled.

### **B.1.3 EnableRF**

Full Command: `EnableRF`

This command turns on the RF driver by enabling the relay that controls the power to the device. It has a heavy power draw and by default is disabled.

### **B.1.4 DisableRF**

Full Command: **DisableRF**

Disables the RF driver during science mode acquisition. This only pauses the science acquisition cycle mode and will continue once the driver is enabled again. By default, the RF driver is disabled due to the high power draw.

### **B.1.5 EnableAutoSendStats**

Full Command: **EnableAutoSendStats**

Enables the sending of statistics for each image taken and includes five vertical columns of measured data and housekeeping information. By default, this is enabled.

### **B.1.6 DisableAutoSendStats**

Full Command: **DisableAutoSendStats**

Disables the sending of statistics for each image taken. It is not recommended to disable sending the statistics. .

### **B.1.7 SetScienceMode**

Full Command: **SetScienceMode scienceMode,exposureMode**

Parameter: **scienceMode** is a numerical value of the science mode to be run.

Parameter: **exposureMode** is a numerical value of the science mode to be run.

Allows the user to change science mode and exposure modes that ALI is performing. The science mode is a predetermined cycle of images to perform a specific scientific goal and Table **B-1** contains a list of all of the modes available and a complete description of each cycle is presented in section B.2. The exposure mode is a predetermined exposure time length to be used for each wavelength and Table B-6 contains a list of all of the modes available and a complete description of each mode is presented in section B.3. The next mode will be loaded once the current mode is complete. By default the program is set in Invalid Mode.

### **B.1.8 ReloadConfig**

Full Command: **ReloadConfig**

Upon completion of the current science cycle, the science mode cycle will be reloaded from the configuration files.

### **B.1.9 LdCusCnf**

Full Command: **LdCusCnf IsOneExp,NumExp,wavelength,RFPower...**

Parameter: **IsOneExp** is either a 0 or a 1. A 0 states that the exposure time will be scaled to the calibration curve. A value of 1 states the exposure time will be constant.

Parameter: **NumExp** is the number of images in the custom science mode.

Parameter: **wavelength,RFPower...** is a pair of values for each image in the cycle as defined by **NumExp** consisting of a wavelength in nanometers and a RF power ranging from zero to one.

This function uploads values for a custom science mode. The first value is whether a constant or varying exposure time is to be used for the cycle followed by the number of exposures. For each exposure, a pair of values that consists of a wavelength in nanometers and RF power are required for the specifications. There is no check on the values of the wavelength and RF powers and the user must verify that the wavelength range is in between 600 and 1000 nm and the RF power is between zero and one.

### **B.1.10 LdCusExp**

Full Command: **LdCusExp numTimes,time...**

Parameter: **numTime** is the number of exposure times to be entered.

Parameter: **time...** is a series of times in seconds separated by commas to match the number of exposure times loaded into the custom mode.

This function uploads values for a custom exposure time series. The first value is the number of exposure times followed by a series of time in seconds. If custom exposure time is used, the number of exposures must match the number of exposure times or an error is sent to the user.

### **B.1.11 GetFile**

Full Command: `GetFile filename`

Parameter: `filename` is the image file to be downloaded from ALI with the full path.

Sends a filename into the queue to be downloaded from ALI if the filename exists. This entered file is added to the top of the queue.

### **B.1.12 EndCurrentScienceCycle**

Full Command: `EndCurrentScienceCycle`

Ends the current science operation mode immediately.

### **B.1.13 SetExposureScaleFactor**

Full Command: `SetExposureScaleFactor scaleFactor`

Parameter: `scaleFactor` is a number greater than zero that scales the default calibrated exposure time curve seen in **Error! Reference source not found..**

Sets a scaling factor for the exposure times. Value must be greater than zero or an error is returned. Default is 1.0.

### **B.1.14 UpdateExposureTimeCurve**

Full Command: `UpdateExposureTimeCurve time...`

Parameter: `time...` is a series of 13 times separated by commas with minimum values of 0.05 seconds and a maximum of 60 seconds. The 13 values correspond to exposure times for wavelengths from 650-950 nm in 25 nm intervals.

This function changes the default values in the calibrated exposure time curve. Default values can be seen in Table 4-2.

### **B.1.15 EnableCheckRfTemps**

Full Command: `EnableCheckRfTemps`

Enables a check to verify that the RF driver is not operating outside its rated temperature range.

At 0 degrees Celsius the RF driver is powered on and at 50 degrees it is powered off. By default the check is enabled.

### **B.1.16 DisableCheckRfTemps**

Full Command: `DisableCheckRfTemps`

Disables the temperature check for the RF driver. By default the check is enabled and it is not recommended to disable the check unless an issue with the temperature sensors arises.

### **B.1.17 ResetHousekeeping**

Full Command: `ResetHouseKeeping`

Resets the housekeeping module to reacquire the voltage and temperature sensors. To only be used if there is a problem occurs with the housekeeping module.

### **B.1.18 DumpConfig**

Full Command: `DumpConfig`

Prints the current configuration loaded into the science module. It is used for debugging purposes.

### **B.1.19 SetBitsPerSecond**

Full Command: `SetBitsPerSecond bitsPerSecond`

Parameter: `bitsPerSecond` is the value to change the download speed during operation in bits per second.

Changes the bitrate limit for the ALI operation program. Minimum value is 32000 bits per second and the default is 50000 bits for second.

**B.1.20 EnableAutomation**

Full Command: **EnableAutomation**

Enables the automatic timeout process in case of a loss of communication during the launch.

Enabled by default and after 90 minutes of inactivity it puts the system in aerosol mode.

**B.1.21 DisableAutomation**

Full Command: **DisableAutomation**

Stops the process that automatically starts ALI in an aerosol mode science operation after 90 minutes. This process should be disabled if the user has control of the system at float altitude.

**B.1.22 SetAutomationTimeout**

Full Command: **SetAutomationTimeout time**

Parameter: **time** is the new time in minutes to set the timeout value.

Changes the default timeout time to the time given in minutes. Default is 90, minimum is 5 and maximum is 240 minutes.

**B.1.23 EnableGps**

Full Command: **EnableGps**

Starts the GPS process if it is not already started.

**B.1.24 DisableGps**

Full Command: **DisableGps**

Stops the GPS process if it is not currently running.

**B.1.25 EnablePulse**

Full Command: **EnablePulse**

Starts the pulse per second process if it is not already started.

**B.1.26 DisablePulse**

Full Command: **DisbalePulse**

Stops the pulse per second process if it is not currently running.

## B.2 List of ALI Science Modes

The following section will give a brief description of each of the programmed science operational modes that exist on the ALI platform. A complete table of the modes can be seen in Table B-1.

**Table B-1:** ALI operational science modes.

Mode Number	Mode Name
0	Invalid Mode
1	Calibration Mode
2	Aerosol Mode
3	H <sub>2</sub> O Mode
4	O <sub>2</sub> Mode
5	Custom Mode
6	Aerosol Constant Exposure Time Mode

### B.2.1 Invalid Mode

This mode is a nonexistent mode that has no operational function and will not allow the science module to operate. No images in the mode.

Mode Number: 0

Number of Images: N/A

### B.2.2 Calibration Mode

This mode runs with the shutter opened and the AOTF off. The scaling factor does not work on this function and the values are hard coded into the system. This mode does not use any wavelength values and the RF power is set at 0.

Mode: 1

Number of Images: 8

**Table B-2:** ALI calibration science mode specifications.

Image Number	Exposure Time (s)	Image Number	Exposure Time (s)
1	0.05	5	2.00
2	0.10	6	3.00
3	0.50	7	5.00
4	1.00	8	10.00

**B.2.3 Aerosol Mode**

This mode runs with the standard aerosol mode. An AOTF off image is taken between each exposure. Custom exposure times and scale factor can be used. Exposure time is based off the standard calibration curve which can be seen in Table 4-2.

Mode Number: 2

Number of Images: 26

**Table B-3:** ALI aerosol science mode specifications.

Image Number	Wavelength (nm)	RF Power	Image Number	Wavelength (nm)	RF Power
1	650	0.0	14	800	1.0
2	650	1.0	15	825	0.0
3	675	0.0	16	825	1.0
4	675	1.0	17	850	0.0
5	700	0.0	18	850	1.0
6	700	1.0	19	875	0.0
7	725	0.0	20	875	1.0
8	725	1.0	21	900	0.0
9	750	0.0	22	900	1.0
10	750	0.9	23	925	0.0
11	775	0.0	24	925	1.0
12	775	0.9	25	950	0.0
13	800	0.0	26	950	1.0

**B.2.4 H<sub>2</sub>O Mode**

This mode is used to measure water vapor lines. An AOTF off image is taken at the start and end of each cycle. Custom exposure times can be used, as well as a scale factor can be used. Exposure times are based off of the standard calibration curve for the first wavelength of the cycle and is constant for every image.

Mode Number: 3

Number of Images: 28

**Table B-4:** ALI H<sub>2</sub>O science mode specifications.

Image Number	Wavelength (nm)	RF Power	Image Number	Wavelength (nm)	RF Power
1	920	0.0	15	946	1.0
2	920	1.0	16	948	1.0
3	922	1.0	17	950	1.0
4	924	1.0	18	952	1.0
5	926	1.0	19	954	1.0
6	928	1.0	20	956	1.0
7	930	1.0	21	958	1.0
8	932	1.0	22	960	1.0
9	934	1.0	23	962	1.0
10	936	1.0	24	964	1.0
11	938	1.0	25	966	1.0
12	940	1.0	26	968	1.0
13	942	1.0	27	970	1.0
14	944	1.0	28	970	0.0

### B.2.5 O<sub>2</sub> Mode

This mode is used to measure O<sub>2</sub> lines. An AOTF off image is taken at the start and end of each cycle. Custom exposure time and scale factor can be used. Exposure times are based off of the standard calibration curve for the first wavelength of the cycle and are constant for every image.

Mode Number: 4

Number of Images: 20

**Table B-5:** ALI O<sub>2</sub> science mode specifications.

Image Number	Wavelength (nm)	RF Power	Image Number	Wavelength (nm)	RF Power
1	755	0.0	11	764	1.0
2	755	1.0	12	765	1.0
3	756	1.0	13	766	1.0
4	757	1.0	14	767	1.0
5	758	1.0	15	768	1.0
6	759	1.0	16	769	1.0
7	760	1.0	17	770	1.0
8	761	1.0	18	771	1.0
9	762	1.0	19	772	1.0
10	763	1.0	20	772	0.0

### B.2.6 Custom Mode

This mode lets the user upload a configuration to an extra configuration file on the ALI platform. The command is sent up via the `LdCusCnf` command. Details can be located in section B.1.9.

Mode Number: 5

Number of Images: N/A

### B.2.7 Aerosol Constant Exposure Time Mode

This function is the same as the aerosol science mode (section B.2.3) except the exposure time has been set to two seconds for all exposures. The scaling factor is applied to this mode. A table of the specifications can be seen in Table B-3.

Mode Number: 6

Number of Images: 26

## B.3 List of ALI Exposure Modes

ALI had two usable exposure modes during the campaign, a calibrated mode and a custom mode which can be configured by the user. An automatic exposure mode was planned but due to time constraints was never implemented. A brief description of the modes will follow.

**Table B-6:** ALI operational exposure time modes.

Mode Number	Mode Name
0	Invalid Mode
1	Calibrated Exposure Mode
2	Automatic Exposure Mode ( <i>Not Implemented</i> )
3	Custom Exposure Mode

### B.3.1 Invalid Mode

This mode is a nonexistent mode that has no operational function and will not allow the science module to operate. No exposure times are associated with this mode.

Mode Number: 0

### B.3.2 Calibrated Exposure Mode

Using the method outlined in section 4.4.1, a table of calibrated exposure times were determined for a stratospheric balloon geometry. Table 4-2 contains the calibrated exposure times. For any wavelength requested that is between two of the calibrated wavelengths, the exposure time is linearly interpolated between the two wavelength's exposure times. For wavelengths less than 650 nm the exposure time for 650 nm is used, and for wavelengths greater than 950 nm the exposure time for 950 nm is used.

Mode Number: 1

### B.3.3 Custom Exposure Mode

This mode lets the user upload a series of exposure times on the ALI platform to be used instead of the calibrated exposure mode. The command is sent up via the LdCusExp command. Details can be located in section B.1.10.

Mode Number: 3